

Towards magnetic engineering at metal surfaces

*A dissertation submitted to the
SWISS FEDERAL INSTITUTE OF TECHNOLOGY
LAUSANNE*

*for the degree of
Docteur ès Sciences*

*presented by
Paolo Messina
Laureato in Fisica, Università di Pavia*

*examining board:
Prof. K. Kern, directeur de thèse
Dr. C. Carbone, rapporteur
Prof. W. Dieter Schneider, rapporteur
Prof. H. Vogel, rapporteur*

March 2003

Version abrégée

Cette thèse s'articule autour de deux axes principaux : d'une part la mise au point d'une nouvelle méthode d'élaboration de nanostructures magnétiques supportées en surface et d'autre part la construction d'un nouveau microscope effet tunnel fonctionnant en ultra haut vide et basse température (1K), destiné à coupler la résolution spatiale du STM avec la capacité de détecter le magnétisme.

Le premier chapitre porte sur la construction du système complet comprenant le microscope STM. Un accent particulier est mis sur le design et les fonctionnalités. Le système est un STM UHV LT de type Eigler. Cette classe de STM basse température est basée sur un mécanisme pendulaire qui découple mécaniquement le STM du reste du système UHV. La stabilité mécanique est grandement améliorée grâce à ce dispositif. En outre, ce design permettra de développer un système permettant de contrôler précisément la température entre 1 et 80 K.

A la différence des STM de type Eigler de première génération, la température peut être abaissée en dessous de 4,2 K par l'utilisation d'un cycle de détente fermé de type Joule-Thomson. De l'hélium 3 se détend dans la cavité autour du pendule. La température du microscope peut descendre jusqu'à 0,5 K grâce à la circulation du gaz autour du pendule.

Le design du STM est adapté d'une configuration originale proposée par Pan et développée par Pietzsch. Ce design est compact, stable et procure une bonne stabilité thermique, il permet aussi la rotation de l'échantillon in situ sur 180°.

Différentes propositions pour la détection du magnétisme par STM sont présentées à la fin de ce chapitre.

Le deuxième chapitre est centré sur l'élaboration de nanostructures de surface en conditions UHV.

Le STM-VT est utilisé pour caractériser des structures organométalliques formées sur Cu(100). Un atome magnétique, le fer, et une molécule organique, le TMA, sont déposés sur la surface. Une réaction chimique a lieu entre ces deux adsorbats.

Les molécules de TMA présentent trois groupes carboxyliques susceptibles de former une liaison latérale avec les atomes de fer. Ainsi, l'interaction coordinante entre les groupes carboxyles et les atomes de Fe peut être astucieusement utilisée pour construire toute une gamme de nanostructures en contrôlant la stœchiométrie, la séquence de déposition des adsorbats et la température du substrat.

Les complexes $Fe[TMA]_4$ se développent pour de faibles valeurs de $\frac{[M]}{[L]}$ mononucléaire. Ces complexes sont chiraux. Des liaisons multiples des molécules de TMA sont observées quand le rapport $\frac{[M]}{[L]}$ augmente. On observe des complexes polynucléaires sur des terrasses planes en inversant l'ordre de déposition des adsorbats.

Suite à un recuit le nombre de structures 1D et 2D formées augmente. Les assemblages 2D sont constitués d'arrangements chiraux de structures 1D.

Les assemblages 2D pourraient provenir d'un effet hiérarchique d'interactions chimiques l'intérieur et entre les structures 1D, c'est-à-dire de liaisons coordinantes et de liaisons hydrogène. Ici, contrairement à l'ingénierie des cristaux l'interaction adsorbat-substrat a un rôle non négligeable.

Une discussion approfondie des applications possibles de cette technique pour reproduire des résultats de magnéto-chimie est aussi abordée.

Abstract

The aim of this thesis is twofold: on the one hand to demonstrate a new method of building magnetic nanostructures at surfaces and on the other hand to present the construction of a new 1K UHV Low Temperature STM aimed at coupling the spatial resolution of the STM microscope with the capability to detect magnetism.

The focus of the first chapter is the construction of the entire system incorporating the STM microscope. Design and the functionalities of the instrument are emphasized. The system is an Eigler type UHV LT STM. This class of low T STM relies on a pendulum mechanism which mechanically decouples the STM from the entire UHV system. As a result the mechanical stability of the microscope is particularly improved. Besides, this design will allow eventually to develop a temperature control allowing the instrument to work between 1 and 80 K.

Unlike the first generation of Eigler type STM, the temperature can be lowered below 4.2 K by the use of a Joule-Thompson expansion closed cycle. He^3 is let to expand into the cavity allocating the pendulum. Upon circulation of the gas around the pendulum the microscope is cooled down to a temperature as low as 0.5 K.

The STM microscope itself is adapted from a design originally proposed by Pan and then developed by Pietzch. This design is compact, stable, provides a good thermal stability and allows for in situ 180° sample rotation.

Different proposals for the detection of magnetism with the STM are described at the end of the chapter.

The second chapter is inherently focused on the construction of magnetic nanostructures at surfaces under UHV conditions.

A VT-STM is used to characterize organo-metallic assemblies formed on Cu(100). A magnetic atom, Fe, and an organic molecule, TMA, are deposited on the surface. A chemical reaction between the two adsorbates takes place.

The TMA molecules offers three carboxyle moieties for lateral linkage to the Fe atoms. In this respect the coordinative interaction between the carboxyle

moiety and the Fe atom can be suitably used to build a range of different nano structures. By tuning the reciprocal amount of ligand $[L]$ and metal $[M]$ i.e. $\frac{[M]}{[L]}$, the sequence of adsorbates deposition, the substrate temperature, a number of different structures can be synthesized.

At low values of $\frac{[M]}{[L]}$ mononuclear $Fe[TMA]_4$ complexes evolve. These complexes are chiral. For increasing values $\frac{[M]}{[L]}$ multiple linkage of TMA molecules is observed. By inverting the order of adsorbates deposition polynuclear complexes are observed at flat terraces.

Upon annealing the formation of 1D and 2D structures arises. The 2D assemblies comprise chiral arrangements of 1D structures.

The 2D assemblies may result from an hierarchical effect of chemical interactions within and among 1D structures, i.e. coordinative bonding and hydrogen bonding. Unlike crystal engineering the adsorbate-substrate interaction still plays a relevant role in this scenario.

A thorough discussion of the possible applications of this technique to reproduce results of magneto chemistry is also presented.

Abbreviations and Common Symbols

LITD	Laser Induced Thermal Desorption
RAIRS	Reflection Adsorption Infrared Spectroscopy
HREELS	High Resolution Electron Energy Loss
(L)DOS	(Local) Density Of States
PES	PhotoEmission Spectroscopy
STM	Scanning Tunneling Microscopy
STS	Scanning Tunneling Spectroscopy
2D	Two-Dimensional
2DEG	Two-Dimensional Electron Gas
UHV	Ultra-High Vacuum
SMM	Single Molecular Magnets
VT-STM	Variable Temperature STM
LT-STM	Low Temperature STM
CVD	Chemical Vapor Deposition
TMA	1,3,5 Tricarboxylic Benzoic Acid
HtBDC	3,5-di-ter-butyl-phenyl-porphyrin
TTBPP	Tetrakis porphyrin
TCNE	Tetracyanoethylene
J-T	Joule Thompson expansion
PI	Proportional Integrative controller
P	Proportional controller
D	Derivative controller: Dipolar Field splitting operator
δ	delta function
dI/dV	differential conductance
ΔV	sinusoidal peak-to-peak bias modulation
E	energy with respect to the Fermi energy (if not otherwise stated)
e	protonic charge, $e = 1.6 \cdot 10^{-19}$ C
E_F	equilibrium Fermi energy
$f(E, T)$	equilibrium Fermi function
G	Free energy

S	Entropy: Spin operator
H	Enthalpy
J	Exchange interaction: rotational quantum number
B	Magnetic Field
k_B	Boltzmann constant, $k_B = 0.087$ meV/K
m_e	free electron mass, $m_e = 9.1 \cdot 10^{-31}$ kg
m^*	effective electron mass
n	electron density
ρ_b	bulk electron contribution to the density of states at the surface
ρ_s	electronic density of states at the surface
s	tip-sample distance
T	temperature
T_0	temperature in the J-T expansion chamber
P	Pressure
P_0	Pressure in the J-T expansion chamber
Q	Gas Flow
Q_m	Mass Flow
F	Tube impedance
V	electric potential of sample with respect to tip
W	work function
z	tip height
S	tip height
δI	AC tunnelling current component
ΔI	Fluctuations of tunnelling current component
I_ω	tunnelling Current Fourier Transform
Γ	Tunnelling Matrix
l_i	Pumping line section i length
a_i	Pumping line section i cross section
a	Activity
f	Activity coefficient
c	Molar concentration
E_n	Normal component adsorbate translational energy

Contents

Abbreviations and Common Symbols	8
1 A UHV LT STM for spin sensitive...	17
1.1 Construction of the instrument	17
1.2 Damping, UHV Chamber...	18
1.3 Interior Parts specially designed	27
1.4 Microscope	32
1.5 Cryostat and Refrigeration	36
1.6 Electronics Parts	50
1.7 Future technical improvements.. . . .	54
1.8 Andreev Tunnelling Reflection STM	57
1.9 Spin polarized injection by.. . . .	63
1.10 Electron Spin Resonance Scanning...	66
2 Metal-Organic Self Assembly at Cu(100)	75
2.1 Introduction	75
2.2 Experimental	75
2.3 Metal hetero epitaxy	77
2.4 Principles of Metal-organic 3D Synthesis	81
2.5 Serendipitous Approach to metal-organic.....	86
2.6 Bonding and Dynamics of large adsorbates	98
2.7 Metal-organic Chemistry at metal surfaces...	102
2.8 Chemistry of carboxylic acids...	104
2.9 ..Synthesis at surfaces: first results	111
2.10 ..Synthesis at surfaces: Mononuclear complexes	115
2.11 ..kinetics of complex formation	126
2.12 Kinetics of adsorption processes	134
2.13 ..synthesis at surfaces: Polynuclear complexes	139
2.14 ..Synthesis at surfaces: 1D and 2D structures	143
Curriculum vitae	185

acknowledgements

187

Introduction

Magnetism has fascinated scientists for a long time. In the 19th century the debate on the nature of electrical and magnetic phenomena culminated with the establishment of the electromagnetic theory. The Maxwells equations represent the summary of studies in this field in that century. The symmetry of those equations describing Electric and Magnetic Field is broken at the level of the origin of the two fields. The divergence of the vector \mathbf{E} (Electric field) is connected to the electric charge, however the divergence of the vector \mathbf{B} is equal to zero. As a result, no source of the magnetic field really exists. The reason has been explained in the theory of relativity.

Basically the search for magnetic monopole has been a long aimed goal of physics. Today physics rather than searching for magnetic monopole aims at measuring the smallest magnetic dipole of the smallest stable aggregate of matter known, i.e. the magnetic moment of a single atom, absorbed on a surface or embedded among electric leads.

The magnetic moment of a single atom and inherently of single molecules has a spin contribution and an orbital contribution. The measure of the magnetization on a smallest possible scale would give information on these two quantities and those ones related. The further possibility of direct access to the spin of single atoms (molecules) would give the possibility to distinguish between the intrinsic magnetic properties of a microscopic system and the effect due to the surroundings manifesting itself through effects on the angular moment.

Surface science offers an invaluable opportunity to provide atomically flat and clean surfaces on which studies of single magnetic adsorbates become feasible. The development of nano-probes also offers a number of techniques that can couple spatial resolution with physical sensitivity to different phenomena. However, the outermost spatial resolution is achieved routinely only from the Scanning Tunnelling Microscope (STM). Accordingly, the coupling of the spatial lateral resolution offered by the STM and the capability of detecting Magnetism is of paramount fundamental and technological importance[1, 2, 3].

The first part of this thesis focuses on the construction of a UHV LT-STM aimed at detecting magnetism on a nano-scale. Only two groups in the world are known to have achieved sub nanometric magnetic resolution by using ferromagnetic tips[4, 5, 6]. This technique enables to measure the magnetization of the nanostructure placed underneath the STM tip. Nevertheless, the stray field generated from the ferromagnetic tip can severely affect the orientation of the magnetic moments of atomic or molecular adsorbates. The former is a major drawback of this technique that limits its range of applications. Different proposals for circumventing this limitation have appeared in the specialized literature including the use of Mott insulating tips [7] and ferromagnetic-superconductor tips [8].

However, large echo in the nano probes scientific community has been granted to the use of superconducting tips [9, 10, 11, 12] and the detection of high frequency components of the tunnelling current[1].

Recent experiments have proven that Andreev reflection on the interface between a ferromagnetic single point contact and a superconductor can be used to assess quantitatively the degree of spin polarization of the ferromagnet[13]. As matter of a fact there are no constraints that would prevent to apply this method to the STM microscope. In this way the magnetism of a nanostructure on surfaces would be proven by measuring the suppression of the tunnelling current flowing across the sample and the superconducting tip. Moreover it has been recently proved that a magnetic impurity suppresses locally superconductivity [14]. This effect can be exploited to produce a spin polarized current[15]. The stray field generated from the magnetic impurity on the very apex of the STM tip is expected to be much lower than the one used for ferromagnetic tips.

The possibility of coupling magnetic resonances and nanoprobe has been validated in the case of Atomic Force Microscope (AFM) about one decade ago [16]. Also, the very first experiment coupling STM and a magnetic resonance technique was accomplished by Manassen and coworkers at IBM more than one decade ago[17]. The experimental set up (ESR-STM) was able to detect the gyromagnetic ratio g through a mechanism that is still matter of debate[18]. In spite of several critics, some new experimental evidences have been brought about over the last years[19, 20]. In particular the last experiment has been performed using ESR standard radicals in air. The latter opens up the possibility of studying magnetic molecular adsorbates on surfaces[21, 22, 23].

Particularly intriguing would be the study of systems which exhibit the low rate relaxation of the magnetization such as Single Molecular Magnets (SMM)[24, 25] or 1D spin chains[26]. Besides, a number of intriguing quantum phenomena such as the Tunnelling of the Magnetization (MQT) and quantum phases

[27] could be studied at single molecular level.

Another class of magnetic molecular systems that may be studied at the single molecular are endohedral fullerenes [28]. As the magnetic atom comprised in the carbon cage is insulated from the surface, these systems may be particularly interesting to probe the effect of dipolar interactions on different type of surfaces. Among endohedral fullerenes a new class of N,P magnetic doped fullerenes have been recently reported [29]. This class is interesting in term of applications to quantum computing[30] as the magnetic atom included in the carbon cage does not interact with the cage in itself. A current challenge is bringing these molecule on to surfaces as their degradation temperature exceeds the sublimation point [31].

The possibility of studying the magnetism of molecular adsorbates may turn to be of fundamental importance to understand the physical properties of molecular-solid state systems as well as for implementing solid state electron spin single molecular quantum computing [32, 33, 34, 35].

There is a different approach to study molecular magnetic adsorbates on surfaces instead of building them for i.e. directly on the surface. This is the approach explained in the second part of the thesis.

Supramolecular chemistry has revealed to be an invaluable tool to build complex structures [36]. It is also expected to provide major solutions to shrink the sizes of basic computer components [37] [38] [36].

Particularly, coordinative interaction offers many advantages in the design of complex structures over other noncovalent interactions[39].

Noncovalent interactions, such as hydrogen bonding, have been already used to build nano structures on metal surfaces[40, 41]. By contrast, the use of coordinative interaction has occurred only very recently [42]. Lin and coworkers have reported the observation of complex formation at Cu(100) [42] although the weak stability of the formed complexes indicates that the strength of the interaction is not as high as in normal coordination compounds.

Basically coordinative complexes of Fe and 1,3,5 tricarboxylic benzoic acid(TMA) have been obtained in this work [43]. Very recently the cast for shrinking the size of transistor[44] has lead to build devices comprising a single dinuclear complex [45] or even a single atom comprised in organometallic complex [46]. In these works the coupling between the leads and the magnetic molecular adsorbate is enhanced in order to let evolve a Kondo effect.

Building organometallic complexes on surfaces in a similar way opens up the possibility of studying a range of different couplings between the electron gas on the surface and the magnetic atom within the complex. However, coordinative interaction can be used also for building polynuclear clusters and chains. In this respect a major challenge is to tailor directly the magnetic properties of 0D and 1D assemblies pretty much like the case of SMM[24]and

magnetic Co chains [26].

In coordinative crystal engineering coordinative bonding is used alongside with noncovalent interactions to try the production of certain structures. On the surface the presence of adsorbate-substrate interaction and noncovalent interactions among adsorbates such as hydrogen bonding may result in intriguing 2D arrangements.

Within the framework of this thesis the former concepts are explored and reveal to be applicable to the direct construction of nanostructures on surfaces under UHV conditions.

Chapter 1

A UHV LT STM for spin sensitive tunnelling spectroscopy

1.1 Construction of the instrument

The scanning tunnelling microscope [47] is an instrument which allows to image the morphology of a surface. It also allows to do local electron spectroscopy at low energy ($|E - E_F| \leq 2$ eV) [48]. The STM has also been used to manipulate atoms [49] and molecules [50]. It is inherently a multifunctional tool for surface investigation. Usually a metallic tip is brought close to the surface by means of an electro-mechanic mechanism. This mechanism is called STM microscope. If the tip is brought close enough to the surface so that the empty states on the tip can overlap the occupied states on the surface, a tunnelling current can flow from the surface towards the tip [51]. The amount of the current which flows from the surface to the tip is exponentially proportional to the surface tip separation (typically of the order 5-10 Å). In UHV conditions the surface can be prepared in order to become atomically flat and clean. If the microscope operates in ultra high vacuum conditions atomically flat and clean surfaces can be routinely imaged. Lowering the temperature allows also a further stability, as the thermal drift of the instrument is reduced. Besides, low temperature operation results in a better energy resolution during the scanning tunnelling spectroscopy **STS**. The combination of UHV with cryogenic technology and the construction of the microscope are the object of the following pages. There are a number of different examples of instruments which combine the afore mentioned capabilities. For instance the system constructed by Pietzsch et. al. [52]

is designed for sample and tip exchange. However, this system is only able to reach temperatures as low as 11 K. The former is due to the limitation introduced by the presence of a view port in the sample area which allows radiation to warm up the sample even though shields are present. Other designs emphasize the low temperature performance reducing then the amount of irradiation at the sample. In this configuration the sample region is not observable during standard load operations. As a result the degree of precision requested in all the mechanical movements during the sample exchange transfer is increased. This suggests that the STM microscope, to be incorporated in the system, should be simple and easily operated. A simple ^3He design is provided by Hudson et al. [53]. Nevertheless the latter design does not provide a UHV environment for sample preparation limiting the range of application of the microscope. Another design of a UHV STM (reaching 300 mK) has been published recently by Kugler et al. [54]. In this design the authors use a ^3He sorption pump refrigerator. The STM microscope shuttles from the sample preparation area to the experimental location. The former requirement implies a certain degree of risk that one of the connections to the STM can break from time to time reducing therefore the maintenance time interval. We opted for a top loaded design based on Joule-Thompson refrigeration cycle following the construction outlined by Heinrich and Eigler at IBM Almaden research Center [55].

1.2 Damping, UHV Chamber and other Vacuum parts

In Fig. 1.1 the general construction of the entire instrument is shown. The system consists of a cryostat, the UHV chamber and accessories, the microscope, the damping system and the control electronics and related instrumentation. There are two UHV chambers mounted on a rigid frame. The two chambers are divided by a gate valve. The horizontal manipulator is mounted on the sample preparation chamber allowing the sample to be transferred from the preparation area to the second chamber named **STM chamber**. In the former chamber the sample can be transferred to the vertical manipulator and then loaded in the STM. The **STM chamber** is connected to the STM microscope through a **UHV Tube** which goes all the way through the cryostat and is mechanically decoupled from both the chamber and the cryostat. There are two different strategies of providing an appropriate damping insulation of the STM microscope. The first one is to make the microscope as rigid as possible. The second one is to provide a number of mechanical

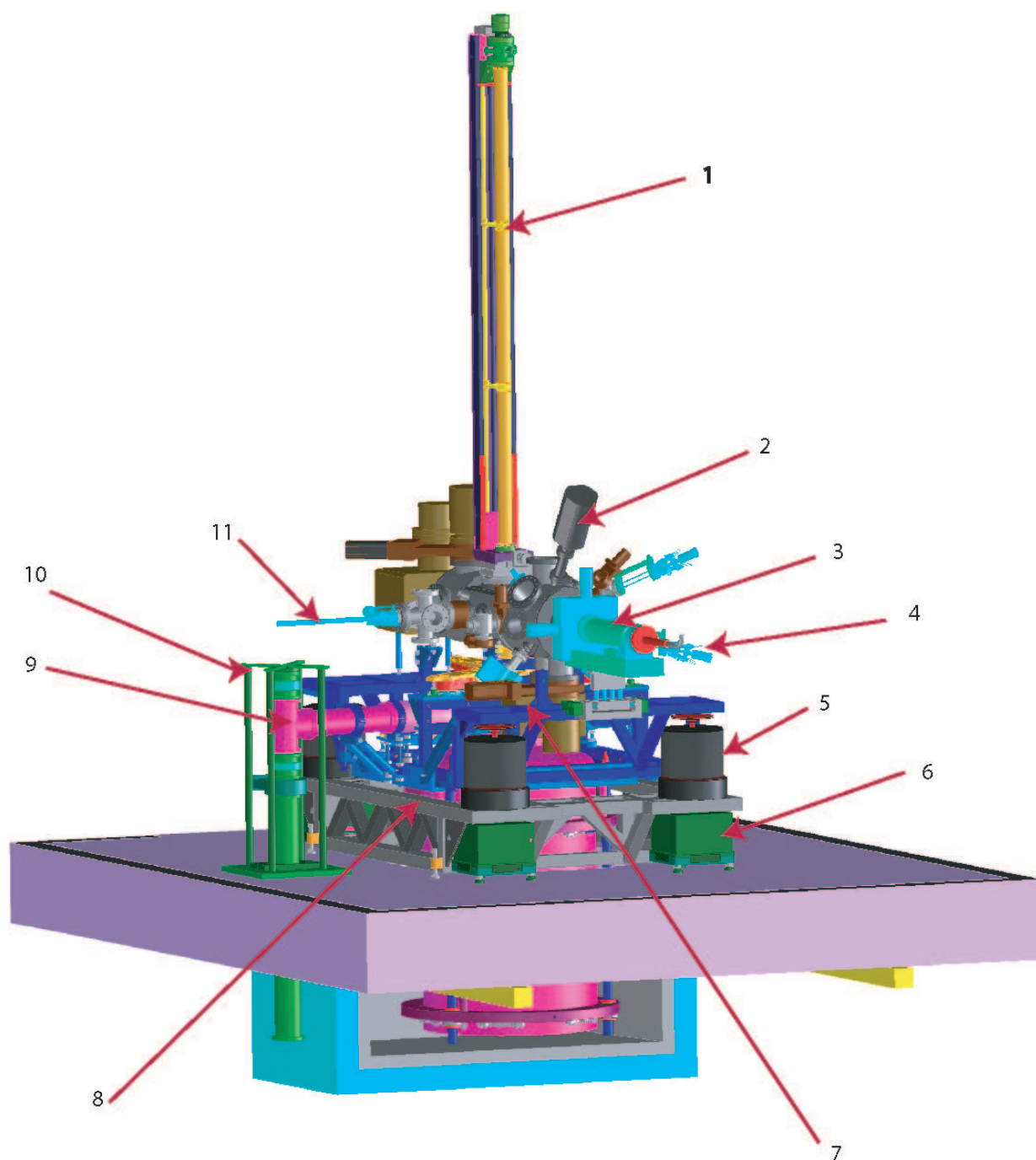


Figure 1.1: 1) *Vertical Manipulator*; 2) *Mass spectra*; 3) *Horizontal manipulator*; 4) *Evaporators*; 5) *Passive damping elements*; 6) *Active damping elements*; 7) *Frame upper part*; 8) *Frame lower part*; 9) *Pumping Line*; 10) *Pumping line damping*; 11) *Load Lock*;

damping stages. The constraints described in Par. 1.10 require that the microscope is compact and light. As a result the STM microscope must be mechanically insulated from the external environment through a number of mechanical damping stages. The main sources of vibrations are the low frequency floor vibrations as well as high frequency environmental vibrations. However, also the acoustic noise propagated by the stainless steel walls of the UHV chambers and equipment may be detrimental for the microscope stability. Because of the former reason, the entire system is allocated in an acoustically insulated chamber. Okano has studied the effectiveness of the number of damping stages introduced in a STM system to increase the vertical stability of the microscope [56]. Increasing the number of damping stages leads to the increase of stability as long as the resonance frequencies of each stage are well separated from each other. Practically this requirement means that the masses of the two damping stages must be sufficiently diverse from each other. Further comments on the requirements that the damping system should satisfy can be found in ref [57].

Fig. 1.2 describes the principle of the damping configuration that has been chosen for the system being described. The damping is performed through three different stages. The entire system rests on four active dampers. They act against low frequency excitations coming from the building. The second stage consists of the UHV chambers and the Cryostat which are connected to the stainless steel frame. These parts rest on four passive Newport **damping elements**. The former is a design strategy particularly rewarding as it allows to concentrate almost the entire weight of the system on this second stage. In turn it makes more complex the decoupling of the third and last damping stage. The last stage is aimed at decoupling the STM microscope from the rest of the system.

This is achieved as follows: The **UHV Tube** departing from the **UHV STM Chamber** is decoupled from the chamber by means of a bellow connected to a special flange anchored at the **T Pendulum**. A closer view to this mechanism is offered in Fig. 1.3. From the flange mounted to the **T Pendulum** the **UHV Tube** goes all the way through the cryostat till reaching the experimental region where the magnetic Field is located. The **UHV Tube** is further decoupled from the cryostat by mean of a second bellow connected to the **Pumping line Knee**. Through this mechanism the **T Pendulum** is mechanically decoupled both from the Chamber and from the Cryostat. It sits on three flat passive damping elements which are anchored at the second stage. The **T Pendulum** is herewith free to swing within the cryostat inlet Fig. 1.2. As The STM microscope is placed in the last part of the **UHV Tube**, Fig. 1.3, this particular arrangement provides a final insulation of the microscope from the other parts. Besides as the

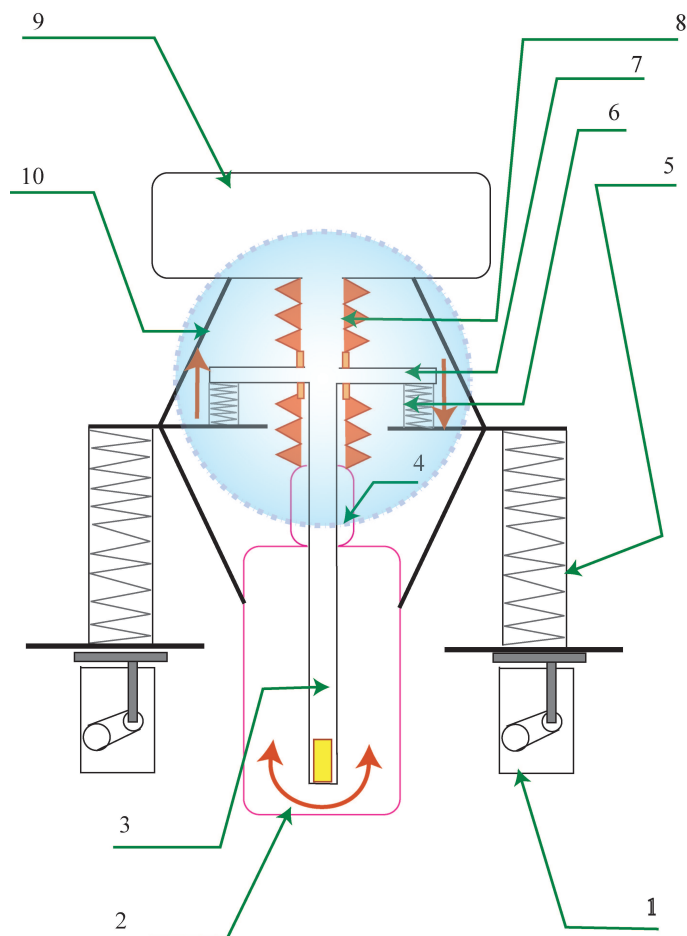


Figure 1.2: Schematic overview of the three damping stages. 1) Active dampers 2) Cryostat; 3)UHV insert acting as a pendulum; 4)Pumping line Knee; 5)New Port Passive damping elements; 6)Passive damping elements holding the pendulum mechanism; 7)T shaped pendulum holder; 8)System of decoupling bellows; 9)UHV Chamber; 10)Frame

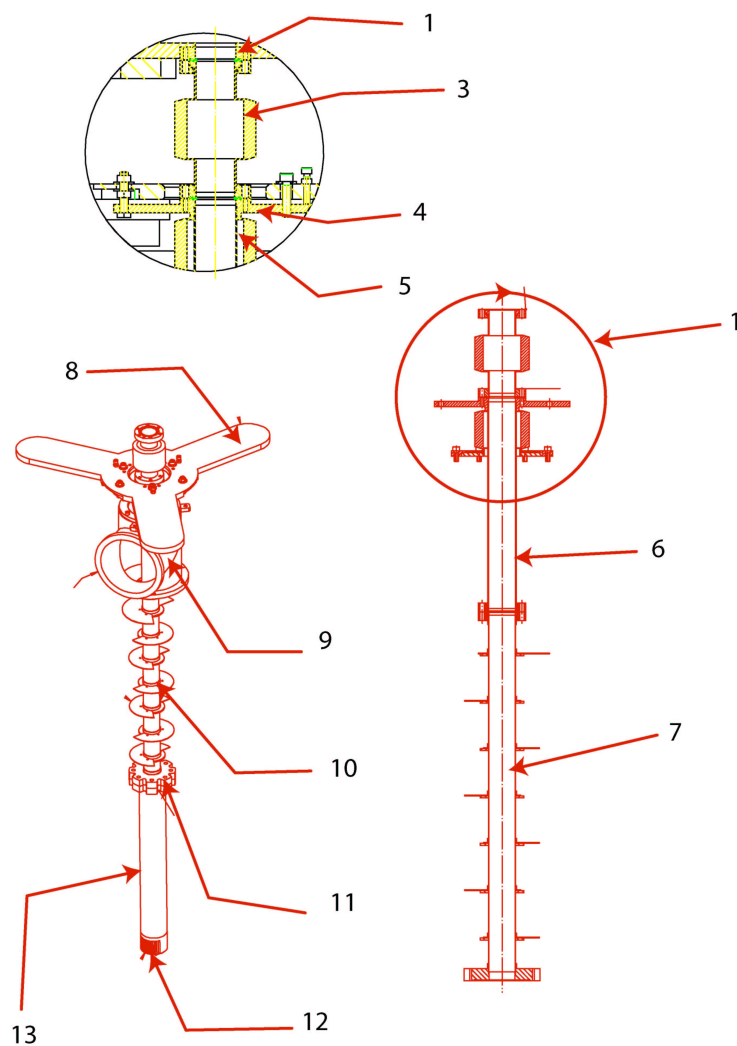


Figure 1.3: 1)Overview damping mechanism; 3)Bellow; 4)Special Flange; 5)Bellow; 6)Top section of UHV Tube; 7)Middle section UHV Tube; 8)T Holder for Pendulum Mechanism; 9)Pumping line Knee ; 10)Radiation shielding; 11)Special Flange; 12)Heat Exchanger; 13)Bottom Part UHV Tube containing The STM Microscope;

tube and the microscope under UHV conditions weigh less than 100 kg, this arrangement provides a decoupling between a very heavy stage and a light one. The former ensures that the resonance frequencies of the two last stages are well separated to prevent any amplification.

The main criteria followed in designing the UHV chamber and the related pumping system has been to divide the chamber in two parts: *preparation chamber* and *UHV STM Chamber* [58]. The former is suited to prevent contamination of the cold region during sample preparation. Fig. 1.4 shows the two lateral views of the UHV chambers. The two chambers are divided by a gate valve welded between the two. The sample transfer operations are ensured through the use of two Manipulators, the first one mounted horizontally and the second one vertically. The *horizontal manipulator* allows for sample cooling during evaporation and sample transfer from the *preparation chamber* into the *UHV STM Chamber*. The *long vertical*¹ manipulator allocated on the top of the second chamber allows sample loading into the STM microscope. Further details concerning the sample transfer and the interior components will be described below.

The *preparation chamber* is equipped with instrumentation for surface analysis and deposition. The Auger, LEED apparatus is placed on the flange on the top of the chamber. This system enables both surface structure characterization as well as qualitative recognition of surfaces and adsorbates [59]. The QMS Analyser is also allocated in this chamber allowing UHV leak test and low mass thermal desorption detection. Two different sets of evaporators can be included in this chamber. The first set can be positioned on a battery of flanges perpendicular to the *sample preparation position*. It consists of MBE metal evaporators. At present only one single Fe evaporator has been mounted on this chamber. The second set consists of two crucible evaporators pointing towards the *sample preparation position* with an angle between 90° and 60°. This technical solution became compulsory because the size of the crucible evaporators did not allow to position them in the perpendicular direction to the *sample preparation position*. The chamber allocates also a sputter gun for sputtering cycles during preparation.

The *STM Chamber* has been designed to accomplish three main functions:

- Transfer the sample from horizontal to vertical manipulation.
- Storing samples, filaments, thermal shielding and eventually tips for experimental region.

¹150 cm travelling length

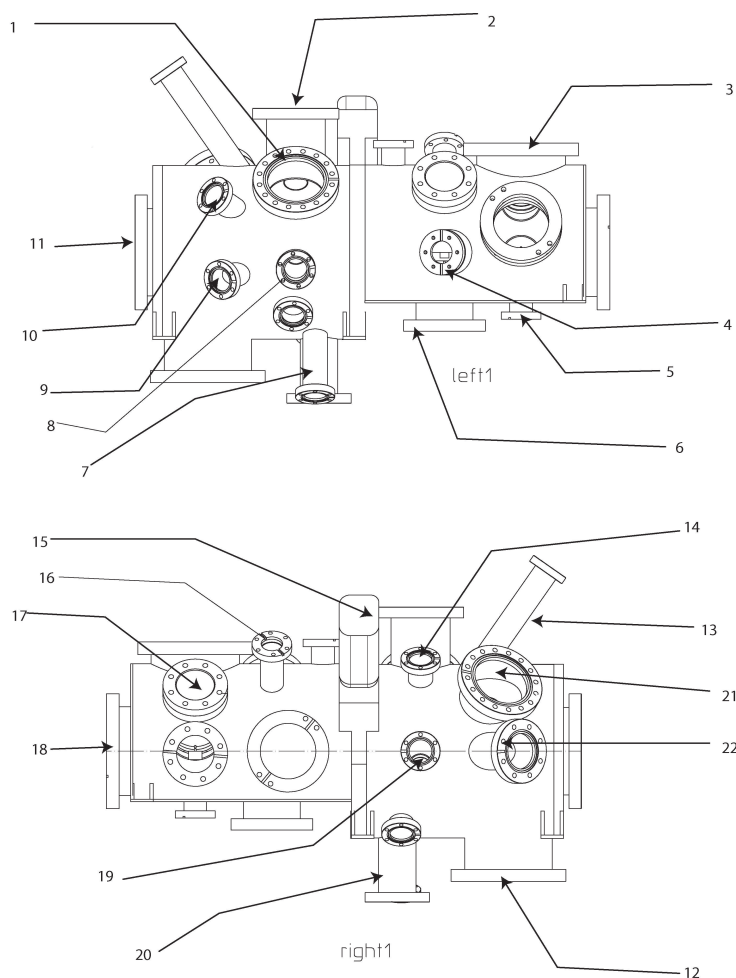


Figure 1.4: *Entire microscope 3D drawing. 1)View port; 2)Turbo molecular pump; 3) Vertical manipulator; 4)wobble stick; 5)UHV Tube; 6)Rotatable carousel; 7)MBE Evaporator; 8)MBE Evaporator; 9)Crucible Evaporator; 10)Crucible Evaporator; 11)Horizontal manipulator; 12)Turbo Molecular Pump; 13)Mass Spectra; 14)Sputter Gun; 15)Ion pump; 16)Gas Inlet Valve; 17)View Port; 18)Ion Pump and Titanium sublimation pump; 19)Load lock; 20)Ion Pump; 21)View port; 22)Ion gauge;*

- Maintaining a clean environment in the experimental region during sample preparation.

This chamber is compact due to the requirement to reduce the vertical manipulator travelling length. The transfer of samples shielding, filaments is performed through the use of a wobble-stick. The connection with the cryostat region is provided by the ***UHV Tube***, Fig. 1.3.

A schematic representation of the pumping circuit is presented in Fig1.5. As explained in [58] one single pumping system cannot provide the best UHV conditions possible, as each pump type has different pumping speed and compression ratio. Besides, each pump gives rise to a certain degree of contamination due to backstreaming and desorption. As a result it is necessary to avoid over dimensioned pumps, that may not provide better performance than the pumps with appropriate specifications. A membrane pump coupled with a small turbo pump provides the rough vacuum ($P = 3 \times 10^{-5} \text{ Torr}$) for all the successive pumping stages. This choice is particular appropriate to an STM microscope system because a membrane pump provides less mechanical vibration and no oil contamination compared to a rotary pump. Each individual chamber is then equipped with a turbo molecular pump and an ion pump providing two independent circuits to reach UHV conditions on both chambers. The sample exchange chamber is also equipped with a Ti sublimation pump to reduce the H_2 concentration in the region where the experiments are performed. The pressure in the ***preparation chamber*** is measured with a ion gauge. The gauge is mounted on a relatively long tube to prevent contamination of chamber walls in the region close to the sample. In fact, gauges desorb impurities during operation. However, the ***STM Chamber*** is equipped with a cold cathode gauge. By using that a further contamination is prevented and this chamber is maintained as clean as possible. Besides, the presence of the cryostat results in a further improvement in the quality of the UHV on this site of the system. Also, two different load lock systems provide sample and filament exchange with the atmospheric pressure environment. The rough vacuum for this circuit is provided by the pre-vacuum system mentioned above. There is a T flange which acts as vacuum reservoir for the two load looks and for the crucible evaporator exchange mechanism as well. A turbo pump is mounted on to the former T and provides pre backing vacuum conditions for the two load looks, for the crucible and for the MBE exchange. Finally, a number of inlet valves are positioned on flanges belonging to both chambers allowing gas injection from outside if experimental reasons require it.

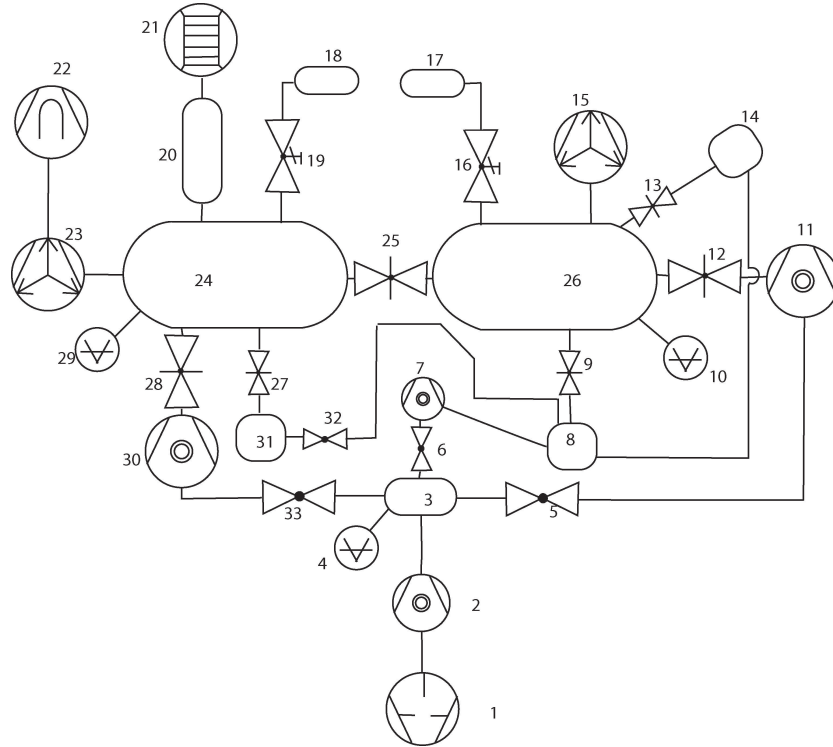


Figure 1.5: Schematic representation of the UHV pumping circuit. 1)View port; 2)Turbo molecular pump; 3) Small chamber; 4)Pirani gauge; 5)Seal valve; 6)Seal valve; 7)Turbo molecular pump; 8)Load lock; 9)Gate valve; 10)Ion gauge; 11)Turbo molecular pump; 12)Gate valve; 13)Gate valve; 14)Bellow for Crucible exchangeable evaporator; 15)Ion pump; 16)Gas Inlet Valve; 17)Gas inlet; 18)Gas inlet; 19)Gas Inlet Valve; 20)UHV Tube; 21)Cryogenic pump; 22)Titanium sublimation pump; 23)Ion pump; 24)UHV STM Chamber; 25)Gate valve; 26)UHV Sample Preparation Chamber; 27)Gate valve; 28)Gate valve; 29)Cold cathod gauge; 30)Turbo molecular pump; 31)Load lock; 32)Seal valve; 33)Seal valve;

1.3 Interior Parts specially designed

The transfer of the sample as well as the mechanical parts occurring in this process are described here. The sample is mounted into a sample holder. The preparation stage is mounted on the Horizontal manipulator which has an end piece specially designed. A cryostat is mounted in the horizontal manipulator allowing to cool down up to ^4He temperatures. The sample is then transferred to the **STM Chamber** and grabbed with the wobble stick. At this stage, it is transferred to the vertical manipulator through the wobble stick and grabbed vertically with a bayonet mechanism. The vertical manipulator transfers then the sample into the STM jack. Inside the **STM Chamber** there is a carousel storing sample holders, filament holders and radiation shields. Once the sample is in the right position a couple of shielders are grabbed from the carousel with the wobble stick and stuck on the vertical manipulator. They are successively transferred into the **UHV Tube** where they are fixed at the ^4He level and right at the flange connecting the bottom part of the **UHV Tube**.

The sample holder is depicted in Fig. 1.6. It has been designed to accomplish the following functionalities:

- Allowing UHV standard preparation (Sputtering and annealing)
- Horizontal grabbing
- Vertical grabbing
- Fitting the sample jack into the STM microscope

The first functionality requires that the sample holder can allocate a filament for electron bombardment of the sample and also that two thermocouples can be incorporated into the holder. Besides, the holder must have a location to allow the wobble stick to grab it along the horizontal axis. Moreover the holder must have a location and a system for the vertical grabbing and the compactness in order to avoid the hindrance of the rotative motion in the sample jack down in the STM microscope. All these requirements represent a challenging task to address.

The holder main body consists of a titan cylinder. There is an opening on the rear front that allows the filament for the sputtering to sit in. Along the vertical axis there are 2 holes all the way through allocating the ceramics for the thermocouple. A thermocouple is necessary to monitor the sample temperature during the sputtering or the deposition. On the top of the main body there is a pole which is used as protrusion to grab the holder with the vertical manipulator. This operation is performed with a fork mechanism

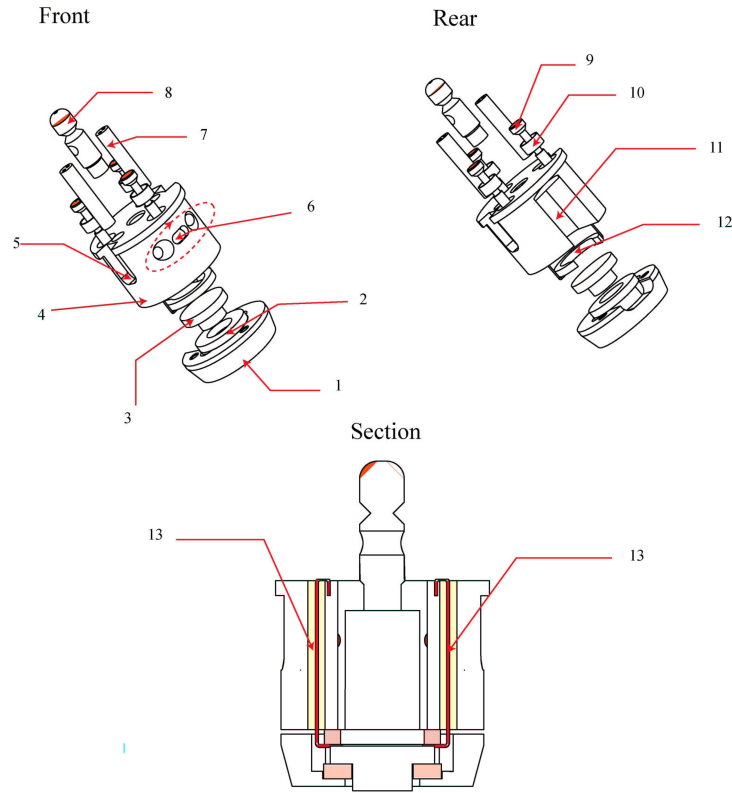


Figure 1.6: *Schematic representation of the sample holder. 1)Bottom holder; 2)Sapphire ring (electrical insulation); 3)Sample; 4)Sample holder main body; 5)Cleavage for fork mechanism; 6) Guide holes for wobble stick grabbing; 7)Thermocouple insulation ceramic; 8)Pole for clamping mechanism; 9)Screw; 10)Screw ceramic insulation; 11)Opening for filament; 12)Sapphire wash insulating thermocouple; 13)thermocouple;*

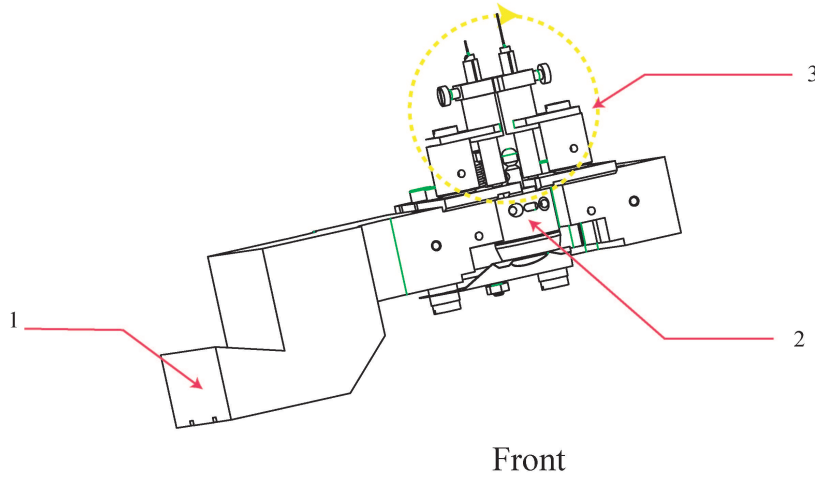


Figure 1.7: 1)Main body; 2)Sample holder; 3)Thermocouple connections area;

described below. The two legs of the fork fit in two cleavages positioned at the main body sides. The bottom part of the holder consists of a cone with an inner slot, designed to allocate the sample. The conic shape is due to the fact that the entire sample holder must enter the jack into the STM microscope being driven by a long manipulator. This operation is performed without visual control from the operator and therefore it is requested a self centering mechanism which is provided by the conical shape of the bottom part of the sample holder alongside the bottom part of the jack hole. The sample has the shape of a hat stuck one to one another.

The sample preparation stage is illustrated in Fig. 1.7. It has been designed for allowing annealing, sputtering and cooling operations. The design strongly depends on the sample holder shape which is imposed by the constraints enumerated above. The main body is built in copper and mounted

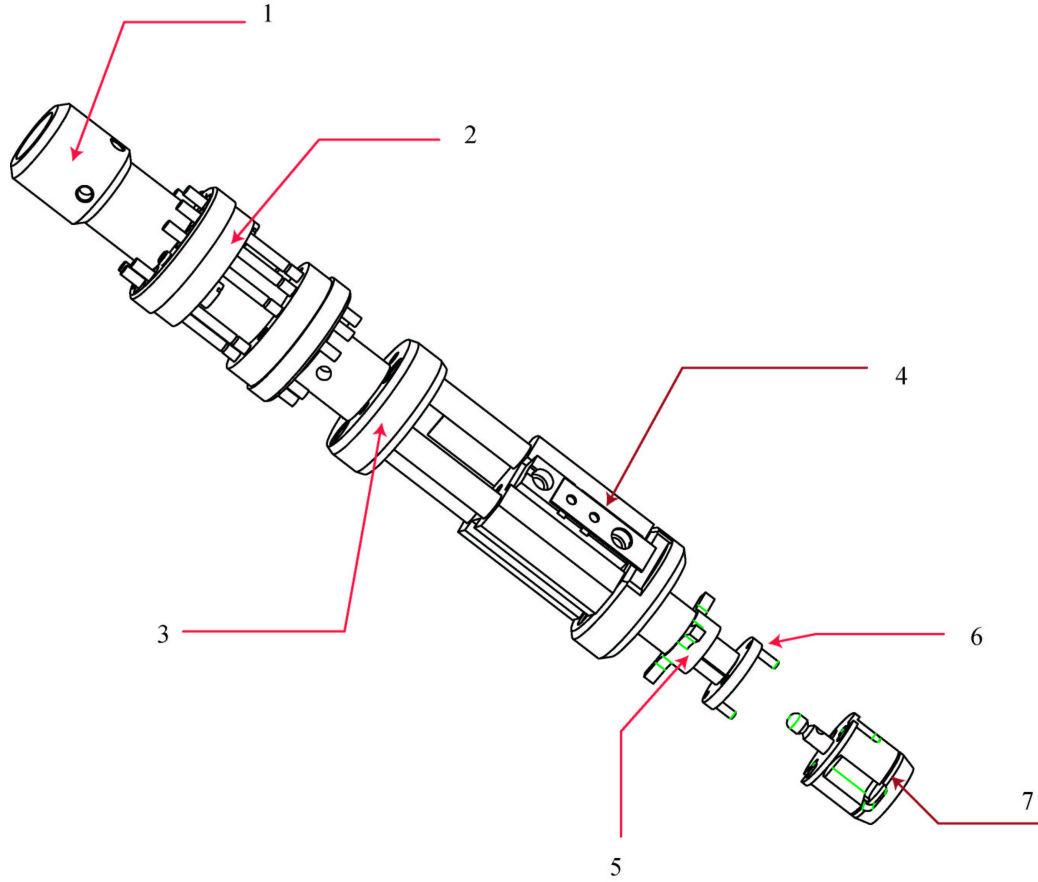


Figure 1.8: *Vertical manipulator final part. 1)Connection to the vertical manipulator; 2)System for sample holder fine positioning; 3)Damper Mechanism frame; 4)Damper mechanism slide; 5)bayonet system; 6)Fork; 7)Sample holder;*

on the horizontal bar. The sample holder is fit into a special overture. On the rear front there is a system, which holds the filament, and a stop. The stop prevents the filament from being damaged during the sample load operation. The high voltage is applied through a plate mounted underneath the main body. The temperature is measured through a contact to the two thermocouple on the top of the sample holder.

The transfer along the vertical direction is performed by the vertical manipulator whose last part is illustrated in Fig. 1.8. The part is insulated by the main bar by a piece of teflon. Following the latter there is a system which allows the final part to slide backwards and damp pushes against the STM microscope. The damper consists of three poles on which three springs are

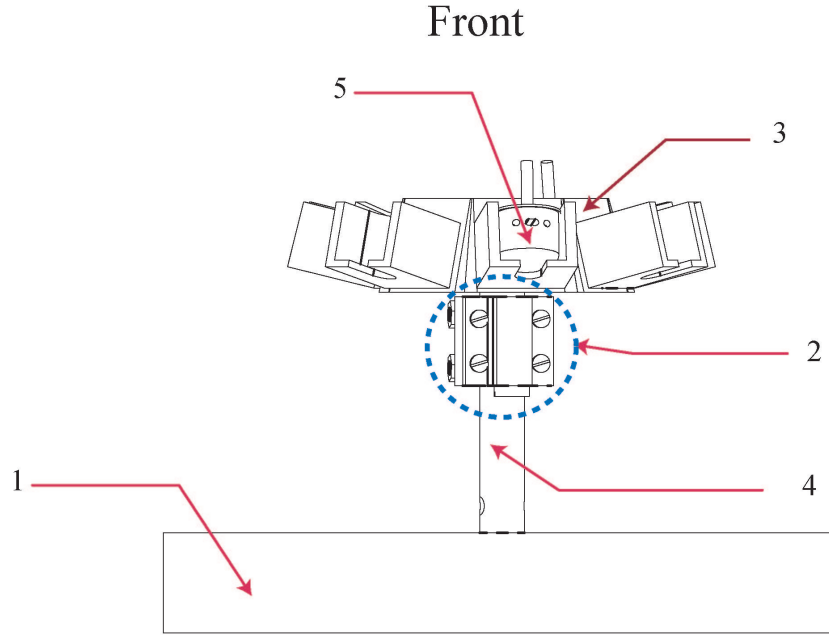


Figure 1.9: 1)Connection to the central manipulator tube; 2)Thermal insulation in teflon; 3)Main body; 4)Axis; 5)Sample holder slot;

threaded and a slide which is free to move backwards, but still mechanically connected to the damper. The head of this piece is composed of two parts. The first one is a bayonet which is used to clamp the shielders. The second one is a fork used to grab the sample holder. The fork has two external legs that simply drive it to the holder pole. It also includes a center cylinder which can clamp the pole through a spring.

The carousel is depicted in Fig. 1.9. It is fixed on a UHV tight CF100 flange. An axis is screwed into the flange and holds the main body. The main body has a circular opening in the middle allocating a ball bearing. The main axis is fit into the internal hole of the ball bearing and fixed on to it. This mechanism allows the main body to move around the axis. The main body is made of aluminum. It can allocate seven sample slots. The slots are hollow parallelepiped-like bodies which can allocate sample holders, filament holders and radiation shielders too. The rotational movement is provided by the wobble stick which can drive the main body rightwards or leftwards. Moreover this rotational mechanism is controlled by a system placed underneath the main body and fixed to the axis. The former consists of a mechanism which press a ball against holes placed at the right angle location.

1.4 Microscope

The design of the *STM Microscope* must match a number of requirements which are listed below.

1. Mechanical stability
2. Thermal stability and homogeneity
3. Space availability
4. UHV compatibility

The perfect microscope is as mechanically rigid as possible. This means that the best design would be a single piece STM as heavy as possible [48]. This is obviously not feasible under the constrain of UHV and low temperature compatibility. A realistic microscope will be composed of many parts including a number of vibrational modes which must be damped.

The thermal stability of the microscope is crucial to the quality of the scanned images. Besides, the lower the temperature the lower the thermal broadening of the tip and sample electronic levels. This improves the energy resolution in STS measurements. Also if tip and sample are at the same temperature the effect of thermal voltage across the tunnelling junction is minimized. For the former two reasons it is important to ensure that tip and sample have the same temperature. This is a challenging requirement as the tip is mounted on a electromechanical mechanism which ensures mechanical motion and the sample is mounted on an holder which must satisfy different constraints 1.3. The two parts have different functionalities requiring different mechanical design and materials. The former reveals to be a major problem in ensuring the same heat transfer to the sample and the tip. In fact the limiting parameters which affect the transfer of heat through different pieces are the type of interface and the number of interfaces [60, 61, 62, 63]. The mechanical and electrical functionalities of the sample and the tip are different implying a different number of interfaces in the two cases as well as the demand for different materials. The difference in the materials used turns in to different thermal interfaces.

The compatibility with the Cryogenic environment requires a compact design as the amount of space available for the microscope and the electrical connections connected to it is limited.

A further constrain to the choice of materials to be adopted is represented by the UHV conditions under which the microscope is supposed to operate. All materials used must stand baking temperatures and they must have a low vapor pressure [58].

Besides, the overall design of the microscope including mechanical functionalities and electrical connections should be reliable in order to allow a long operational time before maintenance.

Moreover, some special requirements have to be satisfied in order to match the initial goals of this system.

1. Scanning area
2. Atomic deposition at low temperature
3. Magnetic compatibility
4. Easy sample loading

The design of the STM depends on the scanning area required. In this case as the system was mostly thought for atomic manipulation and local spectroscopy on single adsorbates a large scanning area is not a stringent requirement though still a good asset.

A special requirement of this system is the possibility to deposit atoms at low temperature while the sample is in the experimental area on the bottom of the **UHV Tube**. This requirement has a deep impact on the microscope design.

The presence of the 14 T magnetic field is necessary to avoid ferromagnetic materials in all the experimental area and superconductors right close to the sample position. If a ferromagnet was magnetized in the experimental region, the remanence field would be enough to affect the magnetization of single adsorbates in the experimental area. The use of superconductors may lead to unexpected movements during scanning in presence of a magnetic field.

As last requirement, one needs an easy sample loading. This point is quite important as the microscope is located in a region which is not accessible to any view port. Moreover the long manipulator does not offer the same mechanical sensitivity that a shorter one can do. This means that the control of the sample positioning is problematic and therefore the loading system should be as effective and simple as possible. However, this requirement must fit the other requirements listed above, particularly the availability of a sample position for atomic deposition at low T. As we opted for a rotary sample holder, the allocation of the sample into the holder becomes problematic, because a rough movement could severely damage the rotary mechanism (described below).

Considering all these requirements we opted for a vertical STM with a rotative mechanism for the sample holder. The basic idea worked out for the microscope is related to the design mentioned in [52]. Fig. 1.10 illustrates a

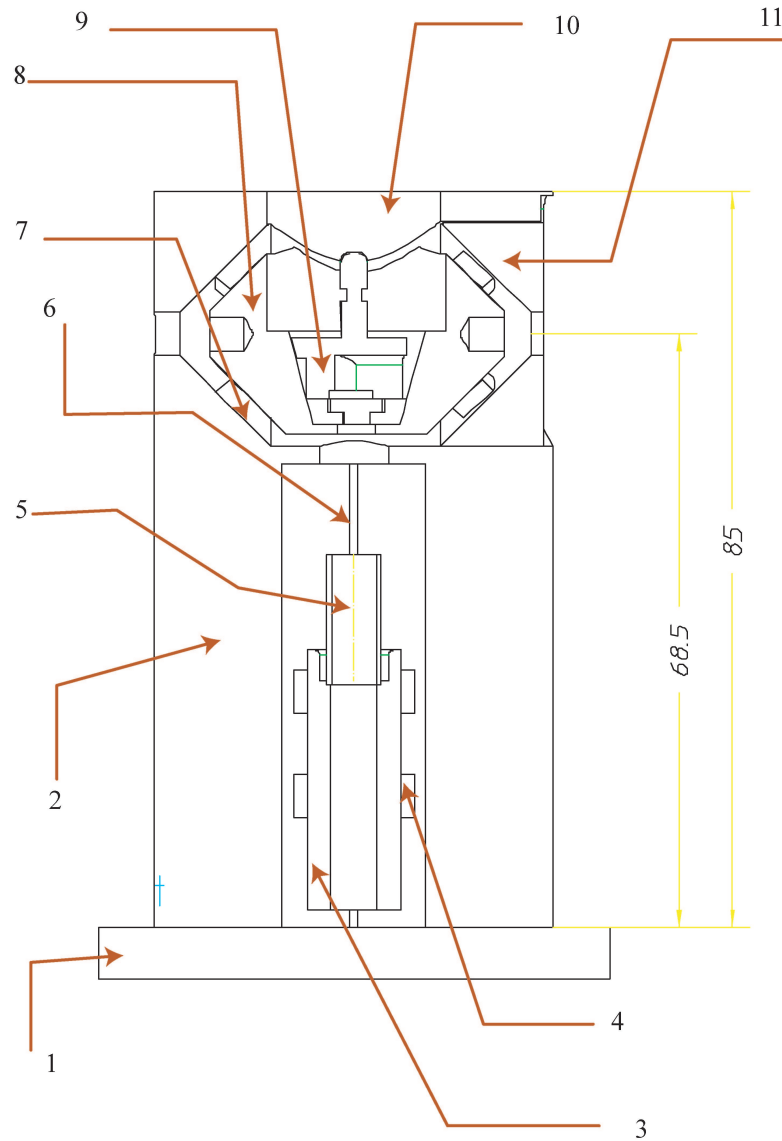


Figure 1.10: *Schematic overview of the STM design. 1) Base plate in Cu; 2) Cu Main Body; 3) sapphire slide and piezo tube glued together; 4) Shear piezo-electrical actuators; 5) Piezo tube; 6) STM tip; 7) Shear piezo for rotary motor [52]; 8) sample jack; 9) Sample holder; 10) Access to the sample jack; 11) Lateral semi-conic staff for rotary motor*

schematic section view of the microscope. It is mounted on a copper plate; the copper plate has three poles connected to a teflon circle on the top. This structure represents a frame which can be inserted into the last part of the ***UHV Tube***. The frame also is used as support for all the wires leaving the STM and reaching the upper part of the tube. All the electrical connections are anchored thermally at the bottom copper plate and on the top of the teflon plate. This design allows both a good thermal anchoring and an easy handling of the wiring that can be fixed once for ever on the frame. On the teflon plate there is a set of electrical pins that can be connected, once the microscope is mounted in the ***UHV Tube***, to the electrical feed through placed on the bottom part of the ***UHV Tube*** Fig. 1.3.

In order to match the requirement of having a good thermal contact the main body has been built in copper [61, 62, 60]. Besides, a single body allows an increasing of the rigidity. This body contains a V shaped groove on which a sapphire prism can slide up and down. The approach mechanism consists of the sapphire slide driven by 6 shear piezoelectric actuators. Four piezoelectric actuators are mounted on the two sides of the groove whereas the last two actuators are mounted on a copper plate placed above the sapphire prism. The copper plate is pressed on to the sapphire prism through a Cu-Be spring fixed on the main body Fig. 1.10. The coarse approach is performed through a quasi-inertial motion allowing the sapphire prism to slide up and down [64]. However, as the main body is heavy and most of the time cooled at the minimum temperature, it can act as thermal reservoir which keeps the temperature of the slide constant. The scanning motion is provided by a tube piezoelectric actuator glued on the top of the sapphire prism. This design offers a smaller scanning area with respect to the beetle type. A special double conical jack is sitting on six piezoelectric actuators which are placed on two copper conic pieces Fig. 1.10.

The two pieces are pressed on the jack by means of two Cu-Be springs fixed on the main body. The jack is rotated through the same quasi-inertial motion as the slide. The rotation operation is necessary if atoms or molecules have to be evaporated at very low temperatures. With respect to the design presented in [52], the one reported here has been modified to match the specific working conditions given in this case. Particularly the sample holder has been redesigned and the jack on which it is allocated has been modified too. The modifications are mostly connected to the mechanism of loading which, in this case, is top based. The sample holder is allocated in the jack through a treed cut inside the jack itself. There are also a number of position sensors determining the position of the moving parts². In order to avoid any

²Useful references in the design of sensors are :[65, 66, 67]

unexpected magnetization effects sample holder and sample jack have been built in Ti.

1.5 Cryostat and Refrigeration

The choice of the refrigeration system [68, 69] for the instrument affects the entire design. There are a number of parameters [70] that have to be taken into account including:

- Cooling time
- Cooling power
- Temperature range
- Temperature stability
- Total power input
- Vibration

The low temperature UHV STM microscope available are mostly working down to temperature as low as 4 K [57, 52, 71, 72, 73]. However, the aim of this project is to reach temperature below 1 K. The STM microscope is an instrument which must be connected to the external world. The number of electrical connections it has, represents a source of heat leaks. Therefore the cryogenic cycle cooling power should take into account the relative high amount of cooling power required below 1 K. The requirement of working under UHV conditions implies that the standard baking procedure could be accomplished. The vibration of the cryostat are crucial to other parts of the design as the STM microscope should be mechanically insulated from the external environment. Finally, also the cost of the cryostat itself is relevant. There are two main different types of refrigeration cycles: open cycle and closed cycle [70]. In the open cycles the refrigerant is used to run a particular thermodynamic transformation after which it is lost in the open air. Open cycles are cryogenic refrigerant consuming i.e. He^4 bath. Closed cycle schemes use the same amount of refrigerant which undergoes a particular thermodynamic cycle. Closed cycle may imply complex construction that along with other requirements of the system construction may make the overall design quite complex. As far as open cycle cryostats are concerned one possibility to reach temperatures below 4K is a pumped 4He cryostat. This type of cryostat is He consuming and the cooling power drops below 1.2

K as superfluidity sets in. N_2 vessel may be required to reduce the radiation heat reaching the 4He bath. Such vessel would subsequently increase vibrations noise related to the N_2 boil off. There are examples of STM constructed using this type of cryostat [57], though from time to time operation must be interrupted in order to enable the pumping of N_2 .

3He sorption cryostat are also capable to reach the range of interesting temperatures. Such type of cryostat are commercially available. Nevertheless they require 3 vessels $N_2/He4/He3$. The former makes the design expensive and complex to be combined with UHV requirements and particularly with the possibility to back up the system at temperatures as high as 150 $^{\circ}C$ or higher. The Cooling power of this refrigerator would be few mW (2-5) at 0.5 K.

Another cryogenic cooling scheme able to reach temperature below 1K is dilution refrigeration. The dilution refrigerator uses a mixture of $^3He - ^4He$ and the internal constructive details are complex [70]. They provide up to 2 mW cooling power at 100 mK. Their price is high. It also increases if the construction of the cryostat has to be modified to include a 4He bath specially designed to host a superconductive magnet. The number of operation to perform before operating the microscope would lead to a substantial rise in temperature because of irradiation and thermal contact with parts coming from the UHV area. Particularly, inserting the sample into the STM and depositing atoms would require the radiation shields to be removed and the cold area to warm up. As the thermal mass of the STM is bigger than normal sample mass in very low temperature experiments, warming up the cold region may lead to long cooling times before the experimental region recovers the lowest operational temperature. In order to understand this, the following simplified formula can be considered³:

$$\Delta t = \frac{mC_p}{\Delta W} \cdot \Delta T \quad (1.1)$$

- C_p = sample specific heat
- m = sample mass
- $\Delta W = W_{refrigeration} - W_{heatleak}$

In order to improve speed in operating the microscope a high cooling power is consequently required. There are a number of static closed cycles that

³The problem is actually more complex. The conductivity of the sample and the different thermal resistances should be considered. The interested reader is referred to [74]

may be used to achieve temperature in the range of interest such as adiabatic demagnetization, and thermoelectric refrigeration which require a certain experience in the design and handling of the system [63, 70]. A simple way of reaching temperatures below 4K is to perform a Joule-Thompson expansion[75, 76] using either ^3He or ^4He . If ^4He it is possible to reach temperatures around 2.2 K with a relative little effort. However, for reaching lower temperatures it is advisable to use ^3He to prevent the superfluid transition in ^4He and related problems. The former refrigerant is expensive and therefore the refrigeration cycle must be **non regenerative** to avoid loss of refrigerant.

^3He Joule-Thompson has been proven to provide cooling power as high as 200 mW at 1.5 K using a flow of 7 lmin^{-1} [77, 78]. In this case the authors provide a design which is based on a N_2 - ^4He pre-cooling stage of ^3He . The design relies on a Joule-Thompson expansion needle which lets the refrigerant into the expansion chamber. The cryostat is proven to work well also without N_2 pre-cooling stage, simplifying then drastically the design.

For these reasons we opted for a Joule-Thompson expansion performed in a normal super insulated ^4He cryostat equipped with a 14T magnet. The microscope is allocated into a UHV tube which goes through the Cryostat opening. The STM microscope is top loaded. The expansion is performed in the interspace between the tube and the Cryostat walls fig 1.17. This technical choice allows high cooling power around 1K and therefore a better performances in the cooling time. For the temperature range between 0.5 K and 1.5 the cooling power provided from this cooling method is among the best performance possible. The vibration insulation is necessary as the refrigerant must be compressed before expansion but, a number of different solutions may be adopted and this will be described in the 1.2. The temperature stability of this method is good and furthermore if ^3He is liquefied, the cycle can be switched off for some hours. The maintenance is relatively easy as the complexity of the entire refrigeration apparatus is reduced. Standard UHV baking procedures are also simplified as described in paragraph 1.2. Finally, the cost of such a system is kept relatively low as only the super insulated ^4He Cryostat must be purchased from sailer.

In order to understand how the refrigeration is performed it is necessary to recall briefly few concepts of thermodynamics. In Fig 1.11 the temperature entropy phase diagram for a typical refrigerant such as ^4He , ^3He , N_2 , O_2 is illustrated. The point A represents the room temperature conditions for the refrigerant. The curve **AE** represents an isobaric transformation from room temperature to the liquefaction temperature at atmospheric pressure. When the refrigerant reaches D it becomes vapor. Along the line **EF** liquid and vapor coexist and E represents the *saturated vapor point* whereas **F** is

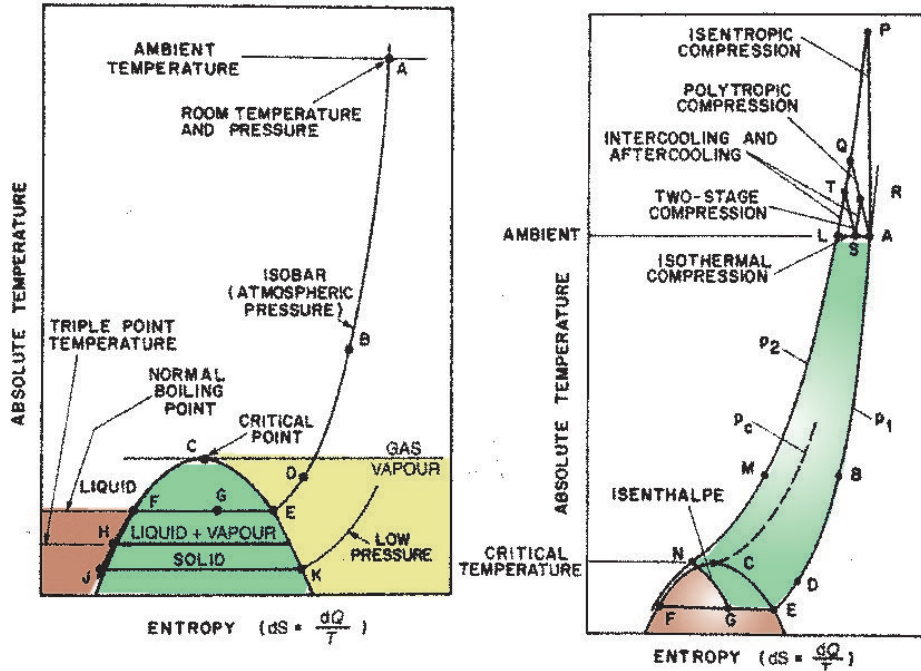


Figure 1.11: Temperature-Entropy phase-diagram for a refrigerant

the *saturated liquid point* (beyond it only the liquid can exist). The region in red is the region where only liquid phase is present and the one in green includes the *Liquid-Vapor* and *solid phase*. The point **C** is the point at a temperature above which the refrigerant cannot anymore be liquefied only by compression, it is called *Critical point*. The area of the temperature entropy diagram underneath a curve indicates the amount of heat exchanged in the transformation described by the curve in itself.

The Joule-Thompson expansion works between two isobaric curves at pressures $p_1 \ll p_2$ as illustrated in Fig. 1.11 b. The refrigerant is compressed from **A** to **L** at room temperature. Ideally this is an isothermal process but, in reality it is carried in a pump which follows a number of polytropic compressions and after-cooling (bringing the gas at the point **L**). At this stage the refrigerant is pre-cooled at a certain temperature (4.2 K in the case we present here) along an isobaric transformation. When the gas reaches the point **N** it is let expand at constant Enthalpy. If the gas temperature is below the Joule-Thompson inversion temperature [79] the expansion will result in a temperature decrease. The heat underneath the line **GE** represents the *refrigeration load* of the process. The gas is then let in heat exchanger and returns to the point **A**. If the cycle is repeated without regeneration of the refrigerant then the process is known as **LINDE-HAMPSON** cycle and

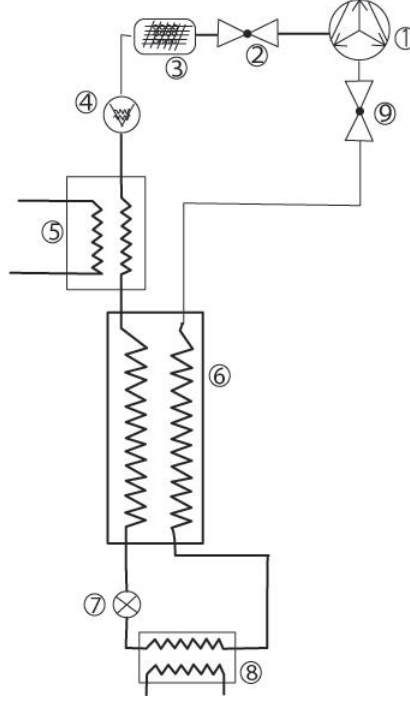


Figure 1.12: *Linde-Hampson scheme: 1) rotary pump compressing the ^3He . 2) Seal valve. 3) Oil Filter. 4) Flux meter. 5) First heat exchanger (^4He). 6) Second heat exchanger (capillary) 7) expansion valve (capillary apex). 8) refrigeration. 9) Seal valve*

the associate cryocooler will be a non regenerative LINDE-HAMPSON.

The cycle is described in Fig 1.12. The compression is performed by a rotary pump and then the ^3He goes through an oil filter and let in to the first heat exchanger where its temperature reaches 4.2 K. The second heat exchanger is placed close to the expansion chamber in such a way that the expanded gas going back to the pump can further refrigerate the ^3He . The scheme shows a needle valve which lets the gas expand. The gas is than expanded in the refrigeration stage and recirculating back to the pump.

The equivalent curve to the Entropy-Temperature diagram is the Enthalpy-pressure diagram. An experimental determination of this curve for ^3He was performed by Kraus [77] and it is illustrated in Fig. 1.13. In this diagram different isothermal curves are reported on the plane H-p. The part of the curve enclosed within the circular curve represents the liquid phase for ^3He . Each isobaric line in this region gives the latent heat of evaporation that is 7Jg^{-1} at 0.3 K.

As the enthalpy is the amount of heat exchanged in a thermodynamical

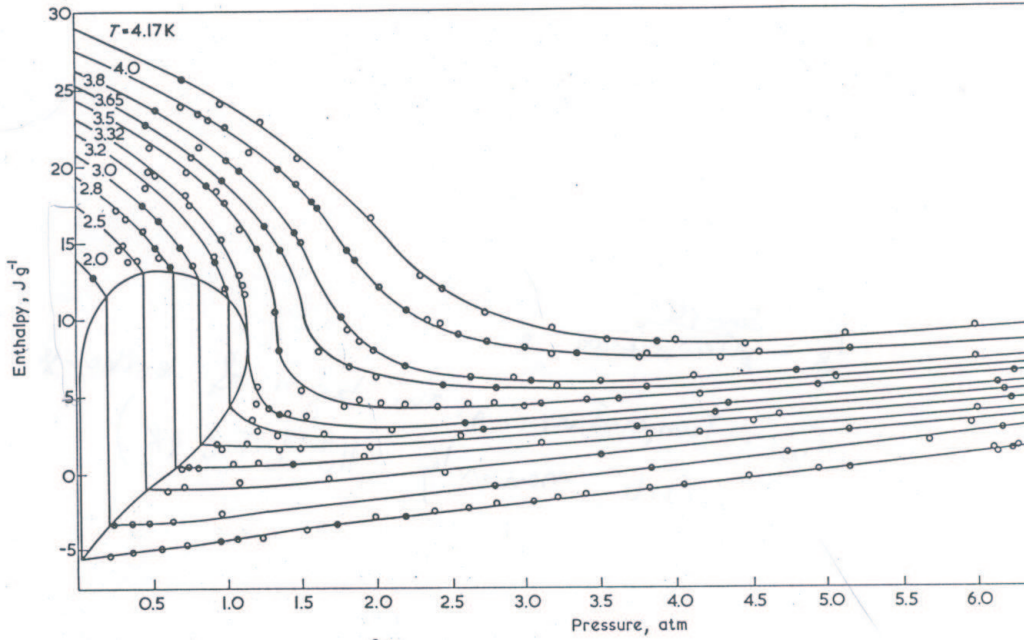


Figure 1.13: *Enthalpy-pressure diagram for ^3He in the temperature range $0.3 \div 4 \text{ K}$ [77]*

process happening at constant pressure the enthalpy can be related to the entropy from simple algebra:

$$dH = dQ_p = C_p dT \quad (1.2)$$

$$dS = \frac{\partial Q}{T} \quad (1.3)$$

$$dS_p = \frac{\partial Q_p}{T} \quad (1.4)$$

From this three equations it follows straightforward that:

$$dH = T \cdot dS_p \quad (1.5)$$

Accordingly, Fig. 1.14 reports a temperature enthalpy diagram from which it is possible to infer in which pressure interval the Joule-Thomson cycle should indicatively be run. In fact, in the diagram different curves at constant pressure are reported. It is possible to see that for liquefying ^3He in the temperature interval $0.3 \div 4 \text{ K}$ the cycle should run with an input pressure superior 1.5 atm and output pressure of a few matm. The maximum amount of cooling power available in the joule-Thomson process is given from the

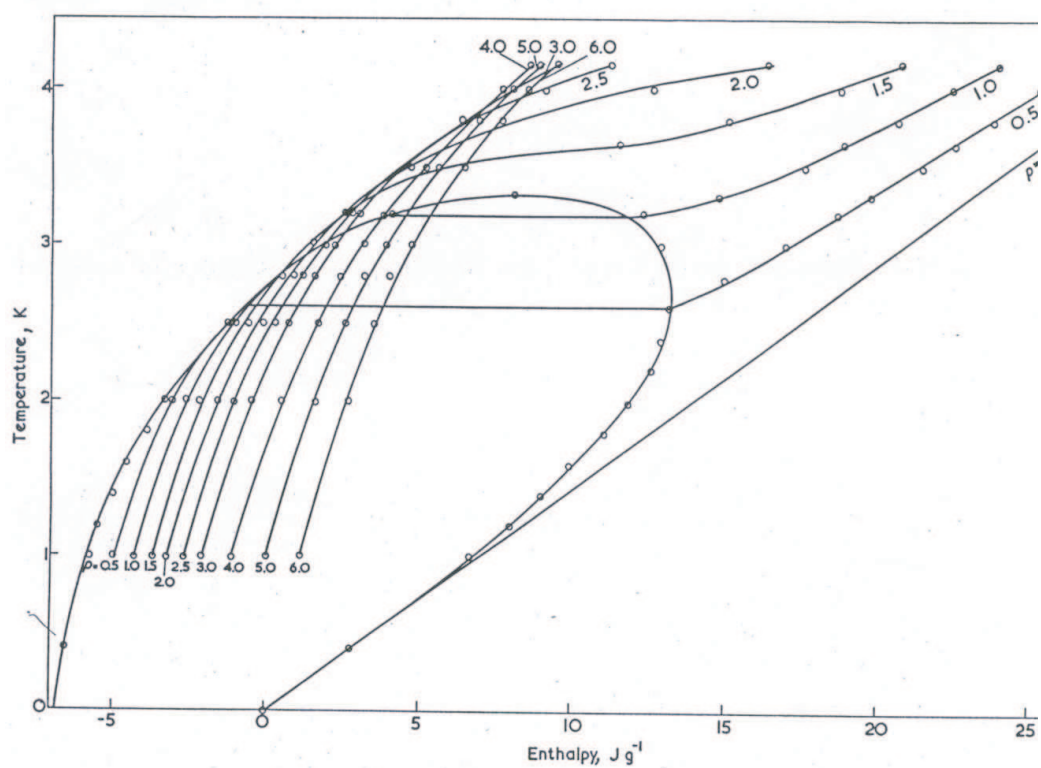


Figure 1.14: *Temperature-enthalpy- diagram for ^3He in the pressure range $0 \div 4 \text{ atm}$ [77]*

latent heat of evaporation of the ^3He time the mass flux of ^3He circulating in the cycle [80]:

$$W_{max} = L_v \cdot Q_m \quad (1.6)$$

Where W is the cooling power, L_v the latent heat of evaporation and Q_m the ^3He mass flow. In real operational conditions the cooling power is less than this theoretical amount as the enthalpy of the returning $^3\text{He}(H_r)$ and the heat leak due to the ^3He pot must be taken into account:

$$W = (x \cdot L_v - H_r) \cdot Q_m - W_{pot-leak} \quad (1.7)$$

($W_{pot-leak}$ being the power dissipated from the pot in which the expansion takes place) and inherently the effective mass flow can be determined as:

$$Q_m = \frac{W - W_{pot-leak}}{x \cdot L_v - H_r} \quad (1.8)$$

The eq 1.8 is useful during the design of the pumping line because it enables to establish the mass flow after having decided the cooling power requested and the difference between latent heat of evaporation and enthalpy of the returning ^3He . For example at 0.3 K the term H_r is 0.85 Jg^{-1} . The meaning of x will be explained below.

As explained before the maximum value of the cooling power is given by the equation 1.6. In reality only a fraction of this amount is really available during the J-T⁴ expansion. The latter can be understood from the analysis of the diagram presented in Fig. 1.15. The picture shows two different isothermal on the H-p plane, the first one concerns ^3He at 4.17 K and the second one ^3He at 1 K. From these two curves it is possible to understand how the J-T cycles work and the effective amount of cooling power available. Some definitions are requested to understand the following:

- $T^{in} = ^3\text{He}$ temperature at the entrance of the cycle (capillary)
- $T^{out} = ^3\text{He}$ temperature right before the expansion (at the apex of the capillary)
- $T^B = ^3\text{He}$ bath temperature on the bottom of the cryostat
- $T^{out} = ^3\text{He}$ temperature when the gas lives the expansion region⁵

⁴Joule-Thompson

⁵In this set up this temperature is roughly the temperature at the last UHV flange (see Fig 1.18)

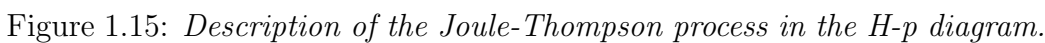
$$\Delta T_W = T^{in} - T^{out} \quad (1.9)$$

$$\Delta T_k = T^{out} - T^B \quad (1.10)$$

There are different cases under which the J-T cycle can be run[77]. In Fig. 1.15 the distance \overline{AB} represents the latent heat L_v whereas the distance \overline{BC} represents the enthalpy of the expanded gas. In the following different examples are analyzed. *Example1*: input 3He pressure $p = 1.4$ atm (point D in the 4.17 K isotherm). The gas is pre-cooled up to the point E. Particularly the variation of enthalpy for the 3He in the capillary is $\overline{DE} = \overline{BC}$. Also the temperature of the gas at the point E, $T(E) > 1K$ $\Delta T_k > 0$ and $\Delta T_W \approx 0$. During the isenthalpic expansion (when the gas comes out of the capillary) the 3He pressure reaches the point named F in Fig. 1.15. The distance \overline{FB} is the actual amount of refrigerating capacity available that in this case is about the 60 % of the overall amount $L_v = \overline{AB}$.

Example2: input 3He pressure $p = 1.77$ atm (point D'). The enthalpy of 3He is reduced in the precooling of an amount $\overline{D'E'} = \overline{BC}$. This time $T(E') = 1K$ $\Delta T_k \simeq 0$ and $\Delta T_W \approx 0$. When the gas is expanded its pressure reaches the point F' . The cooling power will be given from the distance $L_v = \overline{F'B}$ times the mass flow. In this case x is the 81 % of L_v . The case described in this example is a limit case. In fact a further increase in the initial pressure will give counterproductive results.

Example3: input 3He pressure $p = 4.36$ atm (point D''). After cooling the 3He reaches the point E'' which is on the same level as E. This means that the effective amount of refrigerating capacity is the same as in the *Example1*. The latter leads to the conclusion that given a certain T^{in} and T^B it is not reasonable to apply a pressure p bigger than a certain $p_{max}(T^{in}, T^B)$. In particular if $T^{in} = 4.17K$ then $1.77atm \leq p_{max} \leq 2.2atm$, if $1K \leq T^B \leq 3.2K$. However, , if $T^B = 1K$ then $0.2atm \leq p_{max} \leq 1.77atm$, if $2K \leq T^{in} \leq 4.17K$. It will be now explained how the thermodynamical information given above can be used to design the pumping line. Particularly, it will be explained how to use eq 1.8 once the desired cooling power is known to assess the length of different sections of the pumping line. This is relevant in the design of the cryostat. Actually, different parameters enter this design and the result is a compromise between different possible technical solutions. There are two well defined regimes in which a gas can flow through a pipe, molecular and viscous. The flow is viscous when the molecules mean free path is much smaller than the pipe diameter. However, the flow is molecular when the mean free path is longer than the pipe diameter. For 3He the flow is close to be molecular and this will be assumed in the following [80]. The



3He mean free path is given from:

where L is in cm and P in torr. If the gas flows in a pipe or in a line it is important to know how the pressure drops along the line. This is important in order to assess the actual parameters for the J-T expansion. This calculation can be easily performed if the line impedance F is defined:

$$F = \frac{4a^3}{3l} \sqrt{\frac{2\pi KT}{m}} \quad (1.14)$$

where Q is the gas flow and Q_m the mass flow. The eq 1.14 explains as the decay of the pressure is more sensitive to the tube diameter than to the line length l . In this respect it is possible to understand that in general the pumping lines can be long enough to place the pump some meters far away from the cryostat. This is particularly useful in the case the cryostat allocate

an STM as the acoustic and mechanical vibration, due to the pump, can be damped along the line.

Combining together the three former equations it is obtained:

$$Q_m = \frac{4a^3}{3l} \sqrt{\frac{2\pi m}{K}} \left(\frac{P_1}{\sqrt{T_1}} - \frac{P_2}{\sqrt{T_2}} \right) \quad (1.15)$$

This equation is particularly important in the design of the line. In fact is the entire line (cryostat included) is modelled as a series of tubes of different length and section (Fig. 1.16) and assuming that the flow Q_m is constant the equation 1.15 can be rewritten as function of the pressure and the temperature of only the first and last line stage.

$$\left(\frac{P_0}{\sqrt{T_0}} - \frac{P_n}{\sqrt{T_n}} \right) = \frac{3}{4} Q_m \sqrt{\frac{k}{2\pi m}} \sum_{i=1}^n \frac{l_i}{a_i^3} \quad (1.16)$$

Keeping in to account that $T_0 \ll T_n$ the previous equation can be rewritten as:

$$\frac{P_0}{\sqrt{T_0}} = \frac{3}{4} Q_m \sqrt{\frac{k}{2\pi m}} \sum_{i=1}^n \frac{l_i}{a_i^3} \quad (1.17)$$

The equation 1.17 can be transformed in convenient units (P in torr, Q_m g/sec, length in cm):

$$\frac{P_0}{\sqrt{T_0}} = 1.2 Q_m \sum_{i=1}^n \frac{l_i}{a_i^3} \quad (1.18)$$

In reality the equation 1.18 is a constraint equation. That means that if the ultimate cooling power and temperature to be reached are known then the operation pressure is fixed from the inequality:

$$\frac{P_0}{1.2\sqrt{T_0}Q_m} > \sum_{i=1}^n \frac{l_i}{a_i^3} \quad (1.19)$$

where the mass flow Q_m is dependent on the cooling power requested through equation 1.8. The equations 1.8 and 1.19 determine the construction of the cryostat and the pumping line. In the following a few example of modelled cooling power pumping line length for fixed final temperature and input pressure are reported⁶.

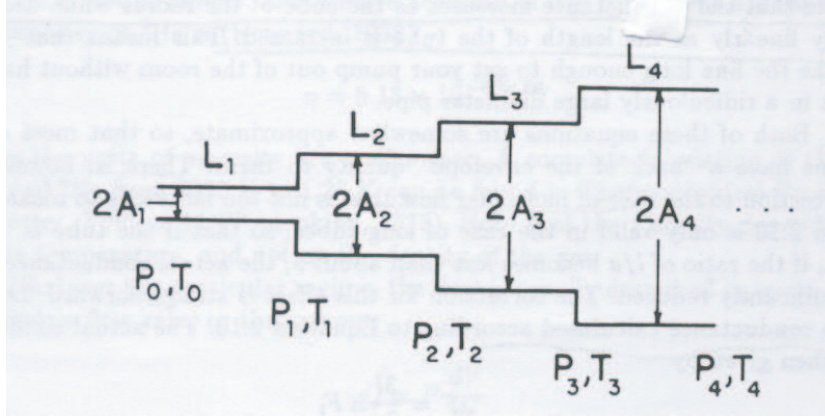


Figure 1.16: Schematic representation of the gas line. Each sector of the line has got its own pressure, temperature, length and diameter.

Pumping line model parameters, $P_0 = 1.848$ atm, $T_0 = 0.5$ K		
L_0 in m	Q_m in ($gs^{-1} 10^{-3}$)	$x \cdot L_v \cdot Q_m$ (mW)
2	11	79
3	7,7	54
4	5.8	41
5	4.7	33

Table 1.1: This table shows as the effective refrigerating capability goes down while increasing the length of the pumping line L_0 . It also shows the order of magnitude of the refrigerating power achievable which is below 100 mW.

Pumping line model parameters, $P_0 = 1.848$ atm, $T_0 = 1$ K		
L_0 in m	Q_m in ($gs^{-1} 10^{-3}$)	$x \cdot L_v \cdot Q_m$ (mW)
2	11	76
3	7,5	52
4	5.7	40
5	4.6	32

Table 1.2: This table shows as the effective refrigerating capability goes down while increasing the length of the pumping line L_0 . The effect of the increased minimum temperature is modeled as a reduction in the mass flow

Pumping line model parameters, $P_0 = 2.178$ atm, $T_0 = 0.5$ K		
L_0 in m	Q_m in ($gs^{-1} 10^{-3}$)	$x \cdot L_v \cdot Q_m$ (mW)
2	13	93
3	9,1	63
4	6,9	48
5	5,5	39

Table 1.3: *This table shows as the effective refrigerating capability goes down while increasing the length of the pumping line L_0 . The increase of the pressure P_0 leads to an increase in the refrigerating capability below the value P_{max} as described in the text.*

Pumping line model parameters, $P_0 = 1.848$ atm, $T_0 = 0.5$ K		
L_0 in m	Q_m in ($gs^{-1} 10^{-3}$)	$-H_r \cdot Q_m - W_{pot-leak}$ (mW)
2	11	22,2
3	7,7	18,4
4	5.8	16,4
5	4.7	15,3

Table 1.4: *This table shows as the internal power consume given from equation 1.7 behaves.*

The cryostat with which the entire machine is equipped follows the Linde-Hampson scheme outlined before, Fig 1.17. It consists of a main body which contains the 4He bath. This part is super-insulated. Particularly the internal surface of the outer stainless steel walls are coated with Silver to reduce the thermal irradiation. The outer part of the 4He bath is super-insulated with Al-Nylon foils which prevent radiation to reach the 4He bath and let the liquid boiling off [63]. The first insert is mounted on the flange on the top of the cryostat. The insert Fig 1.17 has got a frame holding the superconducting magnet on the bottom as well as the pipe for refilling the 4He bath. The second insert consists of 3 different parts. The first part on the top has a diameter of 150 mm and is made up of stainless steel, the second part goes

⁶The interested reader can find further information in the following references: properties of 3He above 1K [81]. 3He vapor pressure [82]. Thermodynamical properties of 3He He^4 mixtures [83, 84, 85]. A review on fluid He^4 [86]. J-T Cryocooler calculations and experiments [75, 87, 88, 89, 90]. Technical details on the expansion valve for a J-T cryocooler [91].

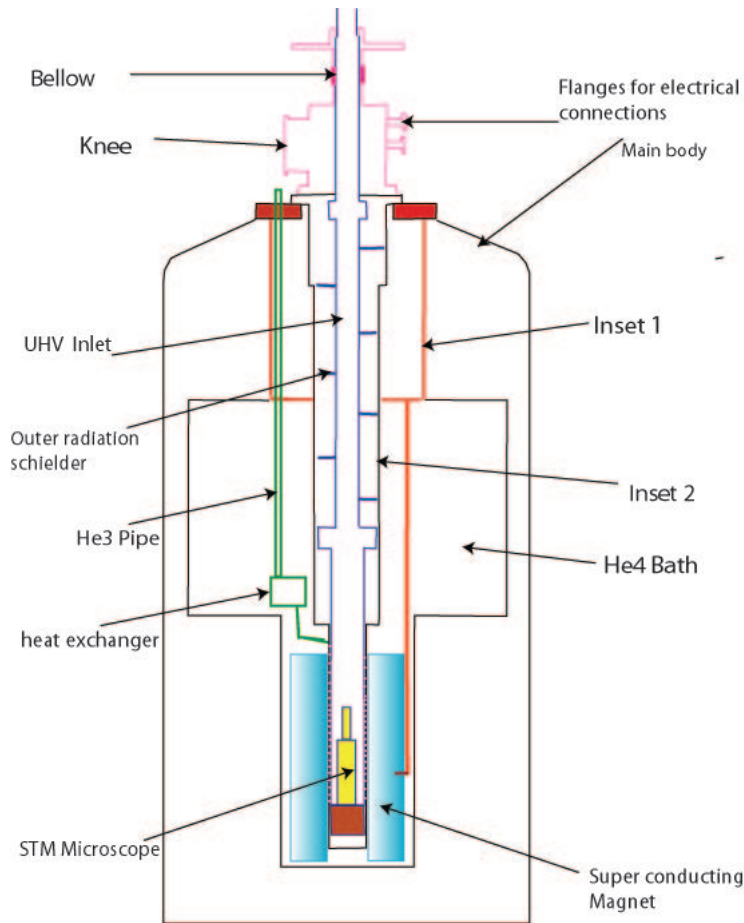


Figure 1.17: *This is a schematic overview of the Cryostat design.*

down to few cm above the magnet and ends up with a flange. This part is made up for the first section of stainless steel whereas in the region where it is in contact with the ^4He bath the material used is Copper. The last part is a 76 mm tube which goes through the magnet and is indium sealed at the upper flange as shown in Fig 1.17. The second insert is mounted on the flange to which the first insert is mounted. The second insert is also mounted on the outer part of the ^3He pipe. Towards the bottom the pipe ends up in a heat exchanger from which a small tube reaches the upper part of the bottom flange. The tube goes through the bottom flange and ends up in a capillary which is wound the inner part of the bottom insert section. This part is better illustrated in Fig. 1.18 and will be described below. On the top of the cryostat there is a big knee 100 mm wide. It is connected to the rotary pump and it is the exit from which the ^3He is pumped out. The knee has got also a number of flanges from which all the electrical connections

go into the cryostat. On the top of the knee there is a special flange which is described in the UHV section. It allows the UHV insert to go through the cryostat. The insert is 38 mm wide and it is divided in three parts connected to each other through standard CF40 UHV flanges. Along with the second part, there is a set of radiation shielding which prevent radiation to reach the coldest part of the second insert. The last part of the UHV tube contains the STM microscope and two sets of electrical UHV feed-through. The latter allows the electrical connections to go from the microscope in UHV conditions to the outer region which has a few mbar pressure. The region where the Joule-Thompson expansion is performed is illustrated in Fig 1.18. The capillary is wound around the UHV tube at a distance of about 1mm from the tube. It ends with a small apex from which the ^3He is let expand into the *expansion chamber* as shown in Fig 1.18. The bottom part of the UHV tube consists of a copper heat exchanger designed to transfer the heat from the STM microscope (mounted inside the UHV tube) to the saturated ^3He gas flowing from the *expansion chamber* to the top of the cryostat. The magnet [63, 92] with which the cryostat is equipped is a single coil Solenoid American Magnetics model A9030-3 capable to reach 9.34 T⁷ at 4.2 K under a current of about 80 A.

1.6 Electronics Parts

The system electronics relies partially on home built components and is PC controlled. It differs therefore from our previous low temperature microscope described in [57]. Fig. 1.19 offers a schematic outline of the electronic design used. The control is provided by a PC which has been equipped with 2 National Instruments boards designed for instrumentation computer communication. The first one is basically an Analogical Digital (A/D) converter [93, 65, 94] which provides 16 single ended channels or 8 double ended channels. The second one is an Input-output (I/O) board.

The central part of the control electronics of any STM microscope is the Feedback loop [48]. The tunnelling current is compared with a reference value (*Set Point*) the resulting signal is processed and used as control signal for the Z movement of the scanning piezoelectric actuator. In this way any variation in the tunnelling current results in variation in the applied high voltage to the Z piezoelectric actuator. In general the feedback loop could be integrative or derivative [95]. However, derivative controller (**D**) is rarely used because of its noisy character whereas integrative controller (**I**) is often combined with a proportional controller (**P**). The basic reason for this is, that

⁷The magnet will be eventually substituted with a new one reaching 14 T.

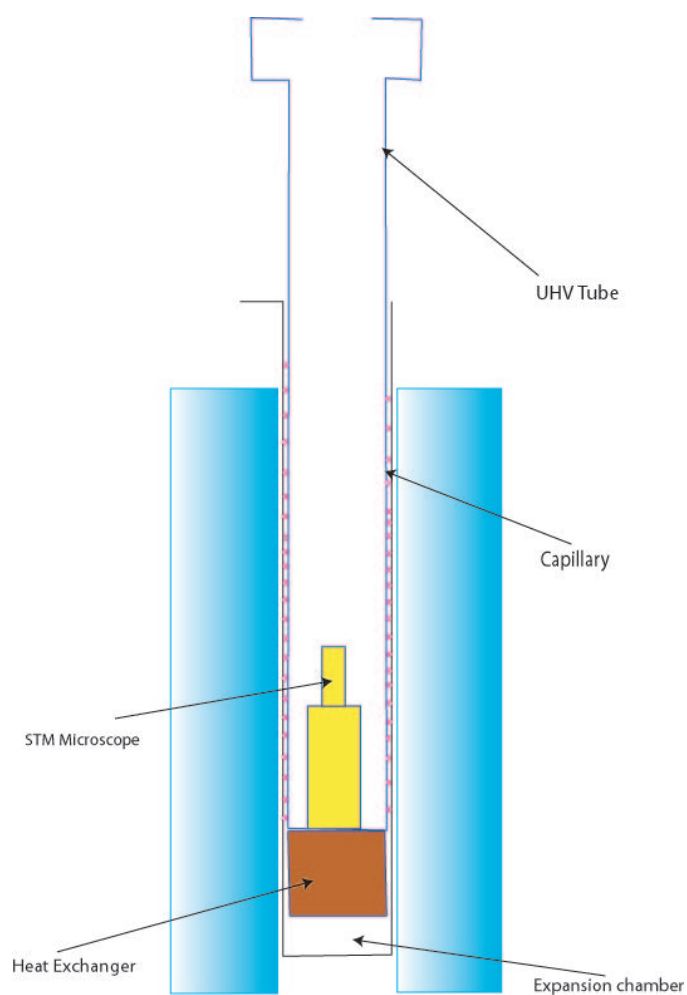


Figure 1.18: *Chamber for the Joule-Thomson expansion. The chamber where the Joule-Thomson expansion takes place is super insulated.*

an integrative-proportional (**PI**) controller has zero steady state error and a faster response time than **I** the controller alone. In the set up described here we also use a **PI** controller. This type of controllers relies on two parameters which are the *total loop gain* and the *relative gain* between **P** and **I**. The two must be appropriately set by the operator to achieve suitable working conditions.

The analogical feedback is in principle the fastest controller possible but, the type of feedback function is fixed and cannot be modified through a computer program. A different approach that will be eventually developed is a digital feedback. In general *Digital Signal Processing* (**DSP**) offers a number of advantages over analogical counterpart [96, 97]:

- The feedback loop parameters are easily controllable by the host computer
- Feedback functions implemented in software are inherently more flexible than hardware circuitry.

This implementation will allow the possibility of introducing special feedback algorithms for atomic and molecular manipulation as well as for special spectroscopies purposes.

Referring to Fig. 1.19 it is possible to outline the main functions of the electronic design. The microscope requires 6 outputs for the scanning tube piezoelectric actuator, particularly (X,-X,Y,-Y,Z,-Z). Besides, it requires one channel for applying the bias voltage between sample and tip. Also two different control channels are requested to drive the coarse approach and the rotative motion of the jack on the top of the STM microscope. The Y and Z signal are feed from the I/O board in to a battery of home built D/A converters. Those converters produce an output of $\pm 10V$. These output signals are feed into an instrumental amplifier. The basic circuitry of these amplifiers consists of two operational amplifiers whose inverting terminals are feed into a variable resistor. The output terminals are feed in the two input terminals of a third operational amplifier. The final gain is proportional to the input signal and depends upon the variable resistance.

However, the X and the bias signal go through the data acquisition card DAQ according to the specifications of the control software. The signals are then sent to the instrumental amplifier described above.

The bias voltage is sent to a home built active filter. This type of filter is known as Multiple Feedback arrangement (**MFB**) [66]. This filter sharply cuts components above 10 KHz accounting for an accurate answer at frequencies below that threshold. Besides, the filter stabilizes the tunnelling current avoiding high frequency components to affect it. As result also the

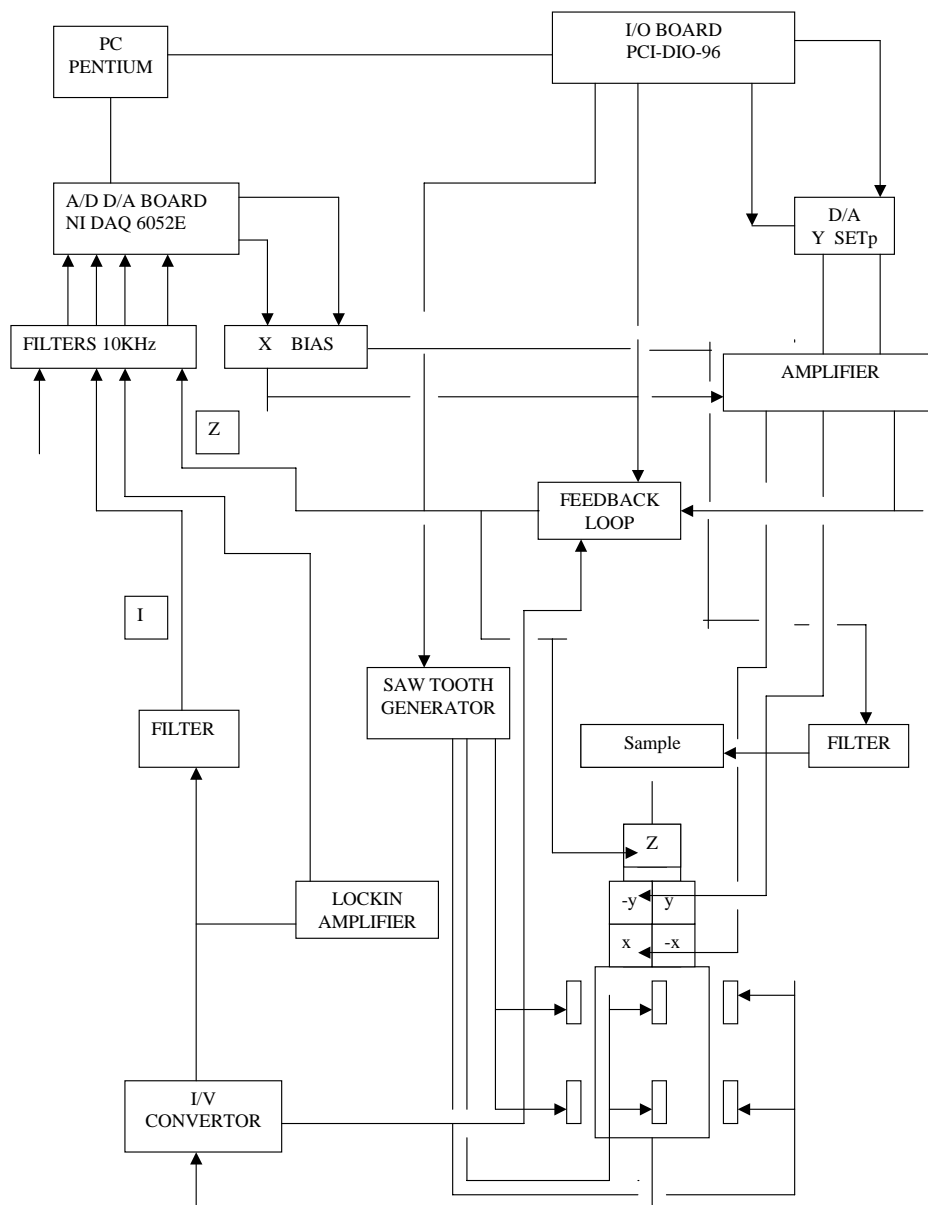


Figure 1.19: *This an overview of the electronics setup for the STM microscope. The DAQ 6052E board is used both to drive the X piezo and the bias voltage (therefore as D/A board) and to read the tunnelling current I signal as well as the Z height of the piezo scanner. The STS signal coming from the Lockin amplifier is also read through this card. The I/O PCI-DIO-96 card is used to drive the set point and the y signal going to the piezo scanner. Two digital signals different from it control the retract movement and the generation of ramps for the coarse approach performed by the six piezoelectric shear displacer placed into the microscope. The high frequency noise is filtered both from the bias voltage and from the tunnelling current signal. The control of the rotor motor is similar to the one of the slide prism used for the coarse approach.*

feedback control turns to be stabilized.

The I/O board provides also digital control output for the coarse approach and rotor. These digital signals are feed into some FET based cards which provide a correct signal amplitude and shape for the shear piezoelectric actuators in the STM microscope.

The tunnelling current is feed into the current voltage convertor I/V. The reason is that the current is small (from pA to nA) and it needs to be amplified as soon as it comes out from the cryostat. The I/V converter is a 3 stages amplifier based on a simple OP27E configuration which provides a 10^8 amplification. It is connected to a small post amplifier which provides another order of magnitude in amplification. One of the terminals of the I/V convertor is feed into the feedback circuit. Another one goes into the lockin amplifier for STS. Finally, one terminal is feed into a multistage filter with cut off frequency above 10 KHz.

The tunnelling current, Z level and Lockin amplifier signals ⁸ are read from the DAQ card. Previously all the 3 signals are feed in to a signal conditioning stage consisting of RC 10 KHz filters. The conditioning stage is useful to avoid any undesired signal or high voltage to enter the computer boards.

1.7 Future technical improvements and developments

In this section it is briefly shown what can be the future developments of this system. There are three goals that seem to be achievable without changing drastically the design that has been described so far:

- Introducing an *in-situ* STM Tip exchange
- Widening the range of operational temperature
- Optical pumping of magnetic adsorbates into excited states

As it will be explained in the following paragraphs a number of proposals for the detection of the single adsorbates magnetization rely on certain properties of the tip. Inherently the possibility to have access to tips made up of different materials, namely different superconductors, is of fundamental importance.

Besides, the possibility of fastening the operations required for exchanging the STM tip may facilitate the access to semiconducting samples. As the

⁸reference notes on our Lockin can be found in [98]

system is equipped with a relatively⁹ high magnetic field (14 T), the study of certain semiconducting surfaces may be interesting to shed light on different intriguing effects,¹⁰ characterizing these materials with a spatial lateral resolution better than 1 nm.

The design described here could be implemented to allocate a tip exchange following Pietsch [4] with a more sophisticated electronic positioning which considers the fact that in our setup there is no possibility of looking at the STM. Nevertheless, the difficulty of this implementation may reveal the goal not reachable. It is possible to follow an intermediate solution instead. It could be possible to insert a gate valve between the STM UHV chamber and the cryostat. The valve can be positioned somewhere along the UHV Tube before the 100 KF knee. In this way it could be possible to close the path between the UHV chamber and the UHV tube. If a small CF 16 lateral flange is adjoint to the UHV tube below the gate valve, the part of the UHV tube inside the cryostat could be vented. The UHV tube may be removed and the STM brought to air. Once the STM and its frame are on air, the exchange of the tip may be performed manually looking directly at the microscope. Once mounted back, the STM on the UHV tube, the tube may be pumped to UHV conditions from a turbo molecular pump connected to the CF 16 flange. After cooling the system to $4 \div 0.5$ K UHV conditions are easily achieved without baking the tube as described in [53]. As UHV conditions set in the gate valve between the knee and the chamber can be opened reestablishing standard operational conditions. This solution would reduce the time requested for tip exchange. However, exchange of special tips prepared in UHV would still not be possible.

Many important results have been achieved lowering¹¹ the operation temperature of STM[102, 103, 104, 105, 106, 49, 107, 14]. However, there are a lot

⁹In the study of high Tc Superconductors magnetic fields of $40 \div 50$ T or even higher are requested to reach the critical field.

¹⁰The reduced mass of a surface state on a metal surface is about $\frac{1}{3}$ of the electron mass. However, in semiconducting surfaces as InAs(110) the reduced mass is some 0.002 times the electron mass. The electrons are less delocalized than in metals, they feel a weaker electron repulsion and inherently the external magnetic field modifies their properties more incisively than it can on metal surfaces.

¹¹The aim of lowering the operational temperature of the STM has recently led to build instruments capable of reaching 20 mK in magnetic fields as high as 6 T [99]. This field of very low nano probes has been reviewed from Nunes [100]. If the UHV ULT STM constructed has to be used in studying, the quantum tunnelling of the magnetization in single molecular magnets or the local magnetic order specially in metal organic structures self assembled on surfaces, temperatures lower than 0.3 K may be required. Such a requirement in the system may be carried out through the magnetic cooling [101]. However, the complexity of such a development may result difficult to implement in the microscope.

of interesting phenomenon such as phase transitions and migrations of single adsorbates that manifest themselves in the temperature interval $1 \div 80$ K. This phenomenon are interesting to be studied with the spatial resolution offered by this type of microscope (known as Eigler type [108]) which is among the most stable through the low T STM microscopes. A way for achieving a temperature control over the range $4 \div 80$ K has been presented recently[109]. In this work a particular property of the gas (He^4) is exploited. Below a certain critical pressure $p_c = 1.5 \times 10^{-3}$ mbar, the mean free path of the gas l^m is longer than the space between the pendulum and the cryostat walls. In these conditions the thermal conductivity is proportional to the gas density and inherently to the pressure $\Lambda \sim n_{He} \sim p_{He}$. Accordingly the thermal conductivity varies linearly with the pressure. If the flux of gas flowing between the UHV tube and the He^4 cryostat is arrested¹² a gradient of pressure from the top to the bottom of the cryostat arises. The He^4 is more concentrated close to the bottom of the cryostat and less on top of the pendulum mechanism. In this respect if a small resistor is positioned close to the STM flange the pressure gradient along the cryostat can be varied. Accordingly the temperature can be modified. Rust and coworkers use a PI controller to stabilize the temperature. The feedback reacts within 2 min and stabilizes in about 10 minutes. Actually this type of control can be implemented also on a system using 3He . The mean free path of the gas depends upon the molecule diameter and this does not change from 3He to He^4 . Therefore, once arrested the J-T expansion, the temperature could be controlled up to 80 K or may be to higher temperatures.

Finally, I remark that studying non linear phenomenon on molecules and atomic structure as well as the coupling between optical and resonance techniques are also within the range of possibilities for further developments of this instrument. One thing that may be achieved reasonably quickly is the optical pumping of adsorbates at surfaces. Large organo-metallic clusters such as SMM [110] or even magnetic radicals [111] may have high value of zero field splitting. Promoting the system into interesting excited levels may turn to be difficult with the STM. Alternatively shading UV light through a wave guide on the sample can match the goal mentioned above. In principle it could be possible to connect optical fibers to the last stage of the UHV tube where the microscope is mounted. A laser can be connected to the set up to provide both high speed pulses or simply to shed light on the scanning area. There are enough feedthroughs and space to reach the experimental

¹²In the design used from Rust and coworkers[109] during operation the flux is arrested and the turbo molecular pump pumping the He^4 is switched off. In this design there is not J-T expansion the He^4 is used only as thermal conducting mean.

area. Technology and electronics necessary are described in [112].

1.8 Andreev Tunnelling Reflection STM

Over the last years it has become possible to use STM tips made of superconducting materials [11]. The former opens up the possibility to extend a number of effects related to superconductor mesoscopic physics¹³ to a smaller scale; i.e. sub-nanometric scale. In this chapter it is briefly described the range of possible application for Andreevs reflection.

The main scientific focus of the instrument built is the detection of magnetism on the atomic scale. In particular the focus of this paragraph is the detection of the magnetization of magnetic nanostructures deposited on to surfaces. The detection of the magnetization gives crucial information about the magnetic anisotropy [128] providing therefore valuable indication on the electronic structure of the system studied and its coupling with the surroundings. One physical effect that may reveal sensitive to the magnetization of a

¹³One effect of mesoscopic superconductivity that is interesting to reproduce with the STM is the Josephsons effect. In superconductor tunnelling junctions a zero voltage current appears due to quantum mechanical effects [113]. The current depends on the SC order parameter and on the magnitude of the tunnelling resistance. This current is known as Josephsons current. Sc Tips have already proven to work with reproducible results in the S/I/N and S/I/S configuration [11, 10, 51]. Developing a Josephsons STM (JSTM) would be of interest because it may provide direct access to SC order parameter, information about its behaviors under application of high magnetic field, nature of the gap in High Tc SC. In order to access the Josephsons regime some physical conditions have to be matched

1. Josephson energy must be bigger then thermal fluctuations[113]
2. The tunnelling resistance must be as low as possible[114]
3. Coulomb energy must be smaller than the SC OP [115, 116]
4. Coulomb energy must be smaller than Josephson energy[117]

The former conditions are difficult to meet in an STM environment. First evidences of JSTM have been reported [9, 118, 119][120]. In particular as far as the experiment reported in [9] is concerned, the temperature was as high as 2K and the Josephsons regime was not reached. The authors study a transition region and give indirect confirmation of the detection of a Josephsons current by applying a 15 GHz microwave field. If a material showing an high T_c is used, the Josephson regime is achieved also at temperature higher than $1 \div 2$ K. Recent experiments done on the new superconductor MgB_2 account for Josephsons Nb/MgB_2 points contact [121] and for the production of small MgB_2 wires[122]. Accordingly MgB_2 may be a good candidate for JSTM. As the junction is formed by the tip and the surface appropriate surface as counterpart of the tunnelling junction must be chosen [123, 124, 125]. Recent studies of MgB_2 surfaces have appeared in literature making this material available for this type of experiments too [126, 127].

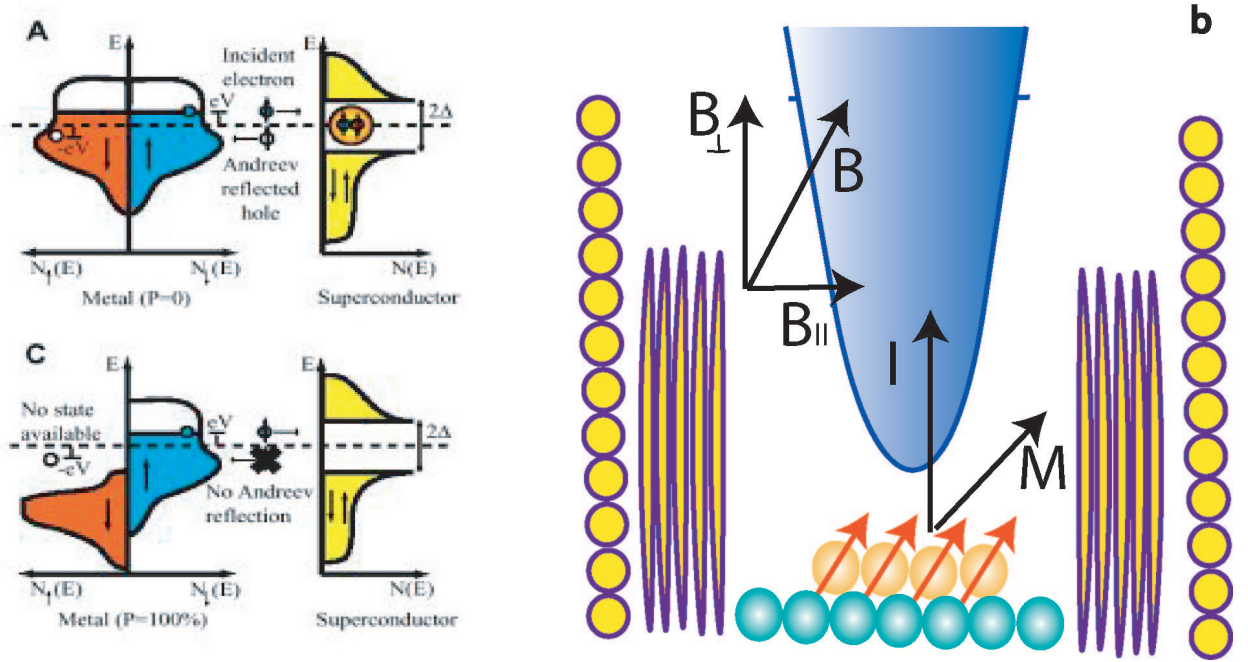


Figure 1.20: **a)** Andreev reflection at normal metal superconductor junction **b)** Proposed Andreev STM set up. **c)** Andreev reflection at ferromagnetic metal superconductor junction. Some parts of the figure are adapted from [13].

nano structure is Andreevs reflection between magnetic nanostructures and a superconducting tip. In mesoscopic physics this effect has been studied in a number of situations [129, 130, 131, 132, 133]. However, it has also been proved that the effect can be exploited in atomic contact [13]. Particularly in this type of experiment an half metal as CrO_2 is contacted to a Nb point electrode. The current flowing from the oxide into the superconductor is dependent on the magnetization of the oxide. In this particular case as the oxide is ferromagnetic the 0 V conductance (Fermi level) of the junction is suppressed. In general the 0 V conductance depends on the degree of magnetization of the magnetic part of the junction. This effect can be used also at the STM level, building a junction between a superconducting tip and a magnetic nanostructure deposited above the metal surface.

The physics of this effect is briefly outlined. If a bias voltage V is applied to a normal metal/superconductor single point¹⁴ contact different mechanism

¹⁴This is actually a good approximation for STM junction as this type of contacts present a tiny tunnelling barrier arising from lattice mismatch, impurities, geometrical irregularities.

lead the current I to enter the superconductor [134, 135]. Quasi particles tunnelling predominates at $V \gg \Delta$. The quasi particles travelling into the superconductor relax eventually in the Cooper condensate. By contrast, if the applied voltage is such that $V \ll \Delta$ there are no available quasi particle states in which the metal quasi particles can tunnel, Fig.1.20 **a**. The quasi particles, in order to enter the superconductor, must be directly converted into Cooper pairs [134]. Accordingly, a charge $2e$ is transferred across the interface and a hole is reflected back. This process is known as Andreevs reflection. The zero bias conductance $G(0)$ results then enhanced to a value $G(0)/G_n = 2$. G_n being the normal conductance for $V \gg \Delta$.

In case the metal is a ferromagnet Fig.1.20 **b** the situation is different. As the d bands of the metal are split in spin up and spin down parts, the amount of quasi particles available for conversion into Cooper pairs will be dependent on the degree of polarization P of the ferromagnet. In general for a polarization P $G(=0)$ is given from:

$$G(0)/G_n = 2(1 - P) \quad (1.20)$$

The former equation indicates a clear reduction of $G(=0)$ down to the limiting value 0 for $P = 1$ (perfect ferromagnet).

The dependence of the tunnelling current on microscopic parameters was studied by Blonder and coworkers [134]. In this study the different irregular contribution to the tunnelling barrier were simulated introducing a δ function interface potential. Its strength is given from a dimensionless parameter Z . The tunnelling current I expression depends upon four coefficients A, B, C, D . A is the Andreev reflection probability, B the normal transmission probability and C, D the related transmission probabilities for an impinging electron with energy E . As $A + B + C + D = 1$ a convenient expression for the current I results to be:

$$I(V, \Delta, Z) = 2eSNv_F \int_{-\infty}^{+\infty} [f(E - V, T) - f(E, T)][1 + A - B]dE \quad (1.21)$$

In Eq.1.21 the dependence upon Z and Δ is included in the coefficients $A = A(E, \Delta, Z)$ and $B = B(E, \Delta, Z)$. The conductance is easily calculated as $G(v) = dI(V)/dV$.

This model becomes a bit more complex if one part of the junction is composed of a ferromagnetic metal. In fact, in this case two contribution to the current are present, the unpolarized I_u and the polarized I_p [135]. The current I will be function of the polarization P :

$$I(V, \Delta, Z, P) = (1 - P)I_u + PI_p \quad (1.22)$$

Where I_u and I_p are calculated by choosing the appropriate probabilities, namely $A_u, B_u, A_p = 0, B_p$. This model correctly foresees the 0 bias enhancement of the tunnelling current as well as the suppression of the Andreevs reflection effect ($I_p \rightarrow 0$) for $Z \sim 1$. Z is the parameter that takes into account, among the other things, the width of the tunnelling barrier. It is then evident that if this Andreevs reflection is to be used to determine the polarization of the tunnelling current P in a STM-Tip/magnetic-nanostructure/surface junction (Fig. 1.20 b) care must be taken in positioning the tip close enough to the structure.

An important point is whether the configuration shown in Fig. 1.20 b can detect more than the simple polarization of the current P , namely the direction and the magnitude of the magnetization \mathbf{M} . In the absence of any symmetry breaking agent there is no reason for Eq.1.21 to depend on \mathbf{M} . However, if a magnetic field \mathbf{B} is present then the magnetization of the nanostructure will be a function of \mathbf{B} . Accordingly the spin part of the wave function describing an impinging electron into the barrier will be function of \mathbf{B} . Presumably the reflection and transmission probabilities may become function of \mathbf{M} such that $A = A(E, \Delta, Z, \mathbf{M})$ and $B = B(E, \Delta, Z, \mathbf{M})$. In this respect Δ is function of \mathbf{B} $\Delta = \Delta(\mathbf{B})$ ¹⁵. The tunnelling current would then depend on \mathbf{B} and \mathbf{M} :

$$I(V, \Delta, Z, P, \mathbf{M}, \mathbf{B}) = (1 - P)I_u(\mathbf{B}) + PI_p(\mathbf{M}, \mathbf{B}) \quad (1.23)$$

. If this was the case the former equation could be inverted numerically to achieve \mathbf{M}). In this respect mapping the tunnelling current as function of the applied magnetic field may lead to the detection of the magnetization of magnetic adsorbates at surfaces. A deep theoretical and experimental study is on demand.

From the discussion above it is evident that it is essential to choose the right material for the tip. Nb and Ta would restrict the experimental conditions to low magnetic Field. Besides, they do not have a large gap, $2meV$ [13, 123, 124]. There are different alternative possibilities coming from High magnetic field magnet technology. Particularly if atomic resolution is not strictly required¹⁶ different materials may be considered. As example NbTi wires or Chevrel phases wires like PbMo6S8 may be used. The recent discovery of MgB2 high SC Tc [121, 122, 136] makes this material a good candidate

¹⁵Proximity effect may prevent the suppression of the superconductivity to field as high as 1,5 T.

¹⁶This is the case for a system as large as several nanometers like endohedral fullerenes [28] or even single molecular magnets [25]. Nevertheless in the study of large molecular adsorbates it may be possible that the tunnelling current I has to be set at high values (e.g.1 eV). In this case is not possible to choice different materials satisfying the condition $V \leq \Delta$.

for Sc tips too.

There are 2 different approaches that can be considered in order to make a superconducting tip. The first one is sticking a SC fiber or single crystal on a metal wire such as W. The second one is using a wire entirely made up of a superconductor material. A good superconducting tip for the experiments described here should have the following characteristics:

- High critical magnetic field B_{c2}
- High transition temperature and therefore a large SC gap $\Delta(0)$
- being not oxidative at the surface
- Good mechanical properties
- Highly oriented chemical bonds

As far as the first approach is concerned there are two materials that may be used, MgB_2 and V_3Si . A comprehensive review on the properties of MgB_2 can be found in [136]. The Tc temperature of this material is around 39 K whereas its critical field B_{c2} can vary up to 40 T¹⁷. STM studies of MgB_2 surfaces have already appeared in literature [126] as well as studies of small grains junctions [127]. Particularly in [126] a gap of 5 meV was measured¹⁸. As for V_3Si recent studies show that it has a gap of about 2.6 meV [137, 138]. Its critical temperature is 19 K, though surface effects may reduce it and the critical field is 20 T. It has already been used by making superconductor wires with a Cu clad [139]¹⁹

Very recently MgB_2 superconductive STM tips have revealed to be usable [12]. In this experiment a piece of MgB_2 single crystal is cleaved and glued onto the tip holder. The holder is inserted into the UHV apparatus and cleaned by Ar sputtering cycles. Scanning imaging of Au(111) is demonstrated up to temperatures as high as 30 K. This experiment actually opens up the way of using special materials for the fabrication of superconductive tips.

¹⁷There are different methods to produce MgB_2 . Recently single fibers [121] have been produced. Their diameter was $160\mu m$ and they were produced by exposing B fibers to Mg vapors at 950 C.

¹⁸. Josephsons current in single point contacts MgB_2 / Nb has been detected too [120] envisaging the possibility to extend this effect to junctions made of superconductive STM tip and MgB_2

¹⁹For studies on tunnelling junctions $V_3Si/SiO/Pb$ the reader is referred to [140, 141]. For an extensive review of the physical properties of the A15 alloys one may refer to [142]. These materials have been known longer than MgB_2 and it is expected to have better mechanical properties and less attitude to oxidation.

A different approach consists of etching superconducting wires, by use of acids that have a protecting clad on the superconducting material. NbTi wires with a Cu clad are available on the market and they can be largely used for this approach. Their T_c is about 9 K and B_{c2} about 14 T. Another possibility is represented by $Pb_{0.2}SnMo_6S_8$ wires whose T_c is about 17 K and B_{c2} as high as 50 T²⁰. Finally, Nb_3Sn wires with T_c 18 K and B_{c2} 24 T may be supplied too and become available for Tip construction. Some of these materials have been tested and analyzed with transmission electron microscopy (TEM). The hard materials gave fragile tips and the images showed that the apex of the tips was not sharp. The Tips fabricated were not tested on the STM. However, NbTi wires showed the best mechanical properties. Pure wires were easily prepared and TEM images showed a sharp tip apex. The discussion above shows that in principle there is a possibility to use special materials whose critical magnetic field and temperature can be as high as 20 T and 40 K. Under these conditions we can envisage more effective methods to detect the actual direction of the magnetization occurring in nanostructures underneath the tip. The proximity effect will enhance even 20 times the critical field. The latter has been recently experimentally proven in a special tunnel configuration made up Pb [144]. Under high magnetic fields it is possible to split the spin up and spin down channel in a superconductor without breaking the superconductivity[145, 146]. In this way a spin polarized current can be produced through which it is possible to determine the magnetization of the underneath magnetic structure.

In general the application of an external magnetic field could be limiting. If the coercively field of the structure put under the tip, were lower than the field applied, the structure magnetization would follow the field direction. In this respect only a theoretical description of the nano structure magnetization dynamics may elucidate the ground state magnetization. As a result, alongside the experimental development of superconductor tip based probes, the development of an appropriate theory is requested.

As described before the application of 3D magnetic field it may be possible to measure the tunnelling current at constant hight mode while varying the direction of the applied magnetic field. The Andreevs reflection would depend on the direction of the magnetic field as the magnetic anisotropy of the studied structure varies with the direction of the applied field. This concept may lose significance at the limit of single atomic adsorbate but, if the probabilities $A = A(E, \Delta, Z, \mathbf{M})$ and $B = B(E, \Delta, Z, \mathbf{M})$ could be calculated then an answer on this point would be available. Accordingly one may decide whether to modify the experimental set up in a way which is able to apply a

²⁰For a review on Chevrel superconductors the reader is referred to [143]

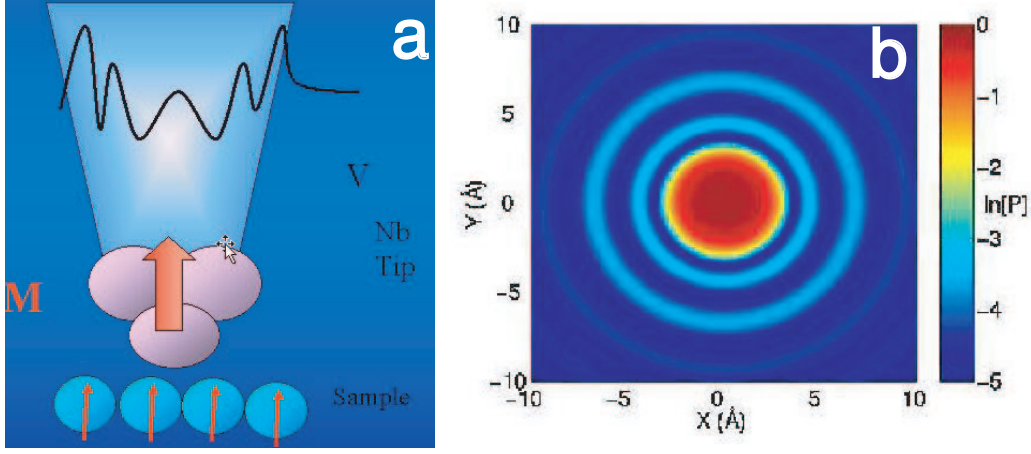


Figure 1.21: **a)** Schematic representation of the tunnelling current polarization. A magnetic impurity is placed on the Superconducting tip. **b)** Calculated STM image of a spin center underneath a tip prepared as in **a)** [15].

3D magnetic field \mathbf{B} .

1.9 Spin polarized injection by using a magnetic impurities on the SC TIP

A single magnetic moment placed on the STM tip may be used as source of polarized electrons [14, 15]. In this respect the STM can be used like in the experiments employing ferromagnetic tip [4] to inlet a spin polarized current into the sample. However, the stray field due to the magnetic impurity is much less than the one produced by a ferromagnetic tip [4]. A schematic representation of this method is presented in Fig. 1.21. Let us suppose that a magnetic impurity is placed on a SC Surface and also that we are able to pick up a magnetic atom on the apex of the STM tip [49, 147]. Can the orientation of the magnetic moment on the surface be measured? The answer is: in theory yes, it can.

The exchange interaction between the magnetic impurity and the cooper condensate is such that in the region close to the magnetic impurity a spin on a polarized state is thermodynamically more favorable than a coopers pair. This effect has been studied by Yadzani [14] on Mn and Gd atoms deposited on Nb(110) surface by means of the STS local spectroscopy. The results show the spatial dependence of the local suppression of the superconductivity. Besides, if a magnetic impurity is placed on the superconductor surface, the

experiment shows evidences of the presence of a resonant status within the SC gap. This resonant status is spin polarized.

The focus of the sequent discussion is on the configuration through which a superconducting tip with a magnetic atom on the apex faces a magnetic nanostructure (even a single atom) placed on a superconducting surface. Will the tunnelling current depend on the respective orientation of the two magnetic moments? As calculated by Balatsky [15] the answer is positive and the effect seems to be relevant and detectable. In fact it is possible to correlate the tunnelling current to the angle between the magnetization orientation of the two spins [15].

$$I(V) = (I_{11} + I_{22}) \cos^2 \frac{\theta}{2} (I_{12} + I_{21}) \sin^2 \frac{\theta}{2} \quad (1.24)$$

The different components of the current in the eq.1.24 are related to the scattering matrixes of the two impurity spins [15]. A representation of the angular dependence of the tunnelling current on the angle θ is shown in Fig.1.22.

This technique is not restricted only to the superconductive surfaces. It can be more generally applicable. For a superconductive surface the enhancement of the tunnelling current at a given voltage within the SC gap would be the maximum possible but, in theory, every metal surface can be used to perform such an experiment.

In order to use one of the state detected in [14] as source for the spin polarized electrons, it should be ensured that the magnetic moment on the tip does not change orientation while letting electrons into the sample. For this reason a possible preparatory experiment has to follow the tunnelling current evolution with the time [15] and has to assess the time constant of the flip process of the spin, which occurs in the magnetic impurity at the very apex of the superconductive tip. Fig. 1.22 shows how the spin decoherence time depends upon the spin diffusion parameter.

In theory at low temperature, the microscope operation temperature is expected to be 1K, the spin could not decay within the observation time allowed by the stability of the microscope. Such a technique is potentially feasible and it may have some advantages on the atomic scale over the one by Wiesendanger and coworkers [4]. Nevertheless it reckons in some complications as picking up an atom and good tip shape. As all the techniques are based on SC, it can be used only within the energies inside the SC gap, setting probably the major drawback of this scheme. Proximity and confined effects on the tip are not accounted in the calculations²¹. It may be better

²¹This means that the geometrical dependence of the superconductor various parameters is not taken into account.

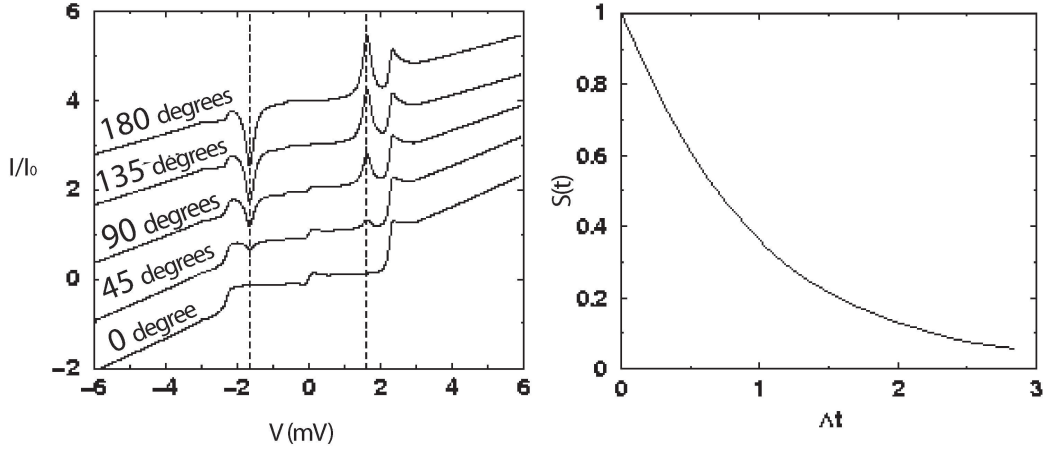


Figure 1.22: *Calculated dependence of the tunnelling current I_0 on the angle θ between the direction of the impurity magnetization and the magnetization of the magnetic adsorbate. The calculation is performed for a Nb surface and Mn atoms as magnetic impurity and adsorbate. The graph on the right refers to the spin correlation function decay. it shows how the spin decoherence time depends upon a spin diffusion parameter Λ that can be measured experimentally. Figure adapted from [15].*

to start with the study of the confinement effects of the impurity intra-gap states on a SC island and eventually the dynamics of magnetic moments on metal surfaces. A typical STM image of a single spin has been calculated in [15] and it is shown in Fig 1.21. It refers to the degree of polarization of the tunnelling current P flowing across the junction:

$$P = \frac{I_{\uparrow\uparrow} - I_{\uparrow\downarrow}}{I_{\uparrow\uparrow} + I_{\uparrow\downarrow}} \quad (1.25)$$

where $I_{\uparrow\uparrow}$ is the spin polarized part of the tunnelling current I_0 and $I_{\uparrow\downarrow}$ is the unpolarized part.

Even though this technique presents some major drawbacks connected to the actual possibility to pick up the right adsorbate at the surface, it is promising in terms of possible spin-electronics experiment at molecular scale. The possibility of probing the magnetism or input polarized tunnelling current in single molecules on surfaces is particularly promising for possible applications to single molecular computers [35].

1.10 Electron Spin Resonance Scanning Tunneling Microscope ESR-STM

One of the most established techniques for the investigation of magnetism in molecular systems and solid state[111] is *Electron Spin Resonance* (ESR). It is particularly used for the study of metal organic systems as complexes of transition metal ions [148, 149] and therefore particularly relevant for the theory argued in the following chapter.

A magnetic atom or molecule in a magnetic field is described by a simple hamiltonian, relating the angular momentum and the spin momentum as follows[111]:

$$\widetilde{H} = \widetilde{H}_0 + g\beta\mathbf{J} \cdot \mathbf{B} \quad (1.26)$$

In the former equation $\mathbf{J} = \mathbf{L} + \mathbf{S}$ commutes with the hamiltonian and inherently its eigenvalue J and M_j are good quantum numbers for the system. In the equation 1.26 g is given from:

$$g = 1 + \frac{J(J+1) + S(S+1) - L(L+1)}{2J(J+1)} \quad (1.27)$$

In presence of a crystal field the mathematical treatment must change in order to make evident the presence of the crystal field itself. This is a typical situation in complexes. As described in the next chapter it occurs also in crystalline solids or magnetic adsorbates on surfaces. If a crystal field is present the energy levels will be split accordingly. There are two extreme situations[111, 150]: the spin orbit interaction within the magnetic center is weaker than the crystal field or the other way around. The first case is typical for the d transition metals where the spin orbit interaction amounts to $10 \div 100$ meV and the crystal field amounts to several eV. However, in case of f transition metals the spin orbit interaction can amount up to 1 eV and the quenching of the angular moment results in small M_j . In this case the spin orbit splitting is predominant with respect to the Zeeman splitting. In presence of a crystalline field the magnetic center can be conveniently described from the spin hamiltonian. It accounts for three terms:

- The Zeeman splitting
- Dipolar splitting
- Hyperfine splitting

$$\mathbf{H} = \beta B \cdot \mathbf{g} \cdot \mathbf{S} + \mathbf{S} \cdot \mathbf{D} \cdot \mathbf{S} + \mathbf{S} \cdot \mathbf{A} \cdot \mathbf{I} \quad (1.28)$$

$$\mathbf{g} = g_e \mathbf{1} + 2\lambda \mathbf{\Lambda} \quad (1.29)$$

$$\mathbf{D} = \lambda^2 \mathbf{\Lambda} \quad (1.30)$$

$$\mathbf{A} = \text{hyperfine} - \text{tensor} \quad (1.31)$$

each of these interactions is associated to a tensor whose component can be determined through ESR spectroscopy. In the former equations λ represents the magnitude of the spin orbit coupling. However, $\mathbf{\Lambda}$ is a complex tensor that considers the effect of the crystal field. The hyperfine interaction is about 3 orders of magnitude smaller than the Zeeman splitting (MHz regime).

A standard ESR Spectrometer is composed of a Klystron generating a microwave field, a resonant cavity, a magnet and detection electronics. Each resonant cavity has a fixed frequency. The operation mode is at constant frequency. A magnetic field placed around the cavity is switched in order to find the peak of the absorption. From the peak position, height and width the hamiltonian parameters of the spin can be inferred.

The technique is improved a lot if the resonant frequency is high, as the fine structures in the absorption peaks can be better inferred [110] determining their different components of the tensor mentioned before. This leads to elucidate the contribution of high order terms in the different magnetic interactions characterizing a particular sample. The technique has proven to give particular insights in the magnetic behavior of SMM [151].

In general sensitivity is proportional to the square of the operational frequency. Increasing the operation frequency is not simple, as the size of the sample must be reduced, the homogeneity of the magnetic field increased and dielectric adsorption from the sample limited.

The focus of this paragraph is to describe a possible coupling between this technique and the spatial resolution offered by the STM. Besides, a standard ESR technique has usually a sensitivity²² limit of $10^{11} \div 10^{10}$ paramagnetic

²²The formula giving the minimum number of spin centers detectable is:

$$N_{min} = \frac{3V_c k_b T_s \Gamma}{2\pi g^2 \beta^2 S(S+1) B_r Q_u} \left(\frac{F k_b T_d b}{P_0} \right)^{\frac{1}{2}} \quad (1.32)$$

where

- V_c = cavity volume
- k = Boltzman constant
- T_s = sample temperature
- Γ = half half-width of the adsorption line
- B_r = magnetic field at the center of the adsorption line

centers [111] whereas there are some experimental evidences that may get this number down to one single spin as described here.

The possibility to detect the ESR signal from a smaller magnetic assembly and even to the level of a single atom placed on a surface is not forbidden by any physical constraint. The reason why the limit in the detection is high is due to the inefficiency of the detection system. However, the STM offers the opportunity to investigate carefully single adsorbates on the surface. The former implies that if a mechanism of magnetic coupling between the tip and the adsorbate is established, it is possible to detect magnetic information at single atomic or molecular level.

Coupling between a single ion in a magnetic field and the tunnelling current have been demonstrated [17, 20, 1]. The authors called this effect ESR-STM. The first experiment was conducted in UHV condition at room temperature on Si(111)(7×7). A schematic representation of the setup is illustrated in Fig. 1.23. This surface present dangling p orbitals which act as paramagnetic centers. In presence of a perpendicular magnetic field the spins in this dangling orbitals precess around the direction of the field (in a classical picture), bringing the tip of the STM close to one Si atom results in the presence of an high frequency signal in the tunnelling current. The position of this signal is proportional to the magnitude of the applied field (few hundreds Gauss) indicating a correct value of the magnetic ratio g . The experiment was repeated under the presence of perpendicular AC field in such a way to modulate the frequency of the precessing spins. Also the experiment was made by detecting induced modulated components of the tunnelling current through a phase sensitive detection scheme [152]. The effect was early explained in terms of oscillating electric dipole induced on the spin center through the precession of the spin [153, 154]. There is also a more complex mathematical analysis of the coupling between the tip and the precessing spin which will not actually be discussed in this chapter [155]. The effect of the oscillating charge on the magnetic center is turned into a modulation of the tunnelling barrier at the precessing frequency inducing a high frequency component in the tunnelling frequency as reported in [157]. Recently the same group reported a new experiment on ESR-STM [17]. The surface chosen was Si(111)(7×7). Fe atoms

-
- Q_u = the effective unloaded Q factor of the cavity
 - T_d detector temperature
 - b = band width of the detecting and amplifying synstem
 - P_0 = microwave power incident on the cavity
 - F = noise figure attributable to sources other than thermal detector noise

as reported by Wertz [111].

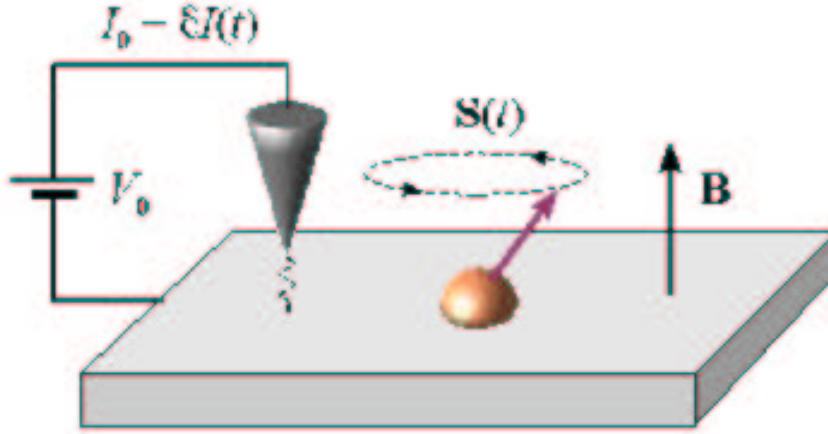


Figure 1.23: *Schematic view of the proposed experimental setup. Figure adapted from [156].*

evaporated on this surface. The surface is then warmed at about 600 C in order to let the Fe atoms to diffuse on the surface. The first monolayer is expected to consist of Si atoms and the Fe atoms are supposed to be located at the center of a tetrahedral cluster of Si atoms. The latter ensures that the magnetic moment of the Fe atoms is preserved. The resonance at the larmor frequency is detected again, demonstrating the validity of the ESR-STM. A much simpler set up has been put together by Durkan and coworkers [20]. The set up works at room temperature under atmospheric pressure condition. The authors use graphite as substrate and a well known radical for ESR spectroscopy, BDPA. The magnetic field was provided by simple magnets placed below the graphite sample. The detection circuit consisted of standard high frequency scheme. This experiment is particularly promising as it would give the possibility of studying SMM [24] on inert chemical surfaces at room temperature. In fact it is possible through self assembly to build molecular cages on metal surfaces and include the SMM[158, 159]. The recent experiments by Durkan [20] have motivated ²³ a new explanation of this effect that will be briefly outlined below[161, 18]. First of all it is necessary to explain how the tunnelling current is connected to a number of different parameters.

A common approximation in STM theory is the *s*-wave approximation for tip wave functions leading to the following expression for the tunnelling current

²³It has also set going a new proposal for single spin detection that is not described here. This proposal is based on *noise spectroscopy* and is described in ref [160].

([51] and references therein):

$$I(V, T, x, y, d) \propto \int_{-\infty}^{\infty} dE \rho_s(E, x, y) \rho_t(E - eV) \times \mathcal{T}(E, V, s) [f(E - eV, T) - f(E, T)], \quad (1.33)$$

where ρ_t is the DOS of the tip, x and y characterize the lateral position on the sample and d the distance between tip and sample measured from a virtual plane passing through the uppermost atoms. ρ_s is the LDOS of the sample in this virtual plane. An often used expression for the tunneling transmission factor $\mathcal{T}(E, V, s)$ disregards the $p_{||}$ dependence of $T_{\mu, \nu}$ and reads [51]:

$$\mathcal{T}_0 = \mathcal{T}(E, V, s) = \exp \left(-2s \sqrt{\frac{m_e}{\hbar^2}} \sqrt{W_s + W_t - 2E + eV} \right). \quad (1.34)$$

For²⁴ low bias voltages the bias and energy dependence of the transmission factor in Eq. (1.34) can be disregarded, leading to the following simplified expression for the current:

$$I(V, T, x, y, s) \propto e^{-2s \sqrt{\frac{m_e}{\hbar^2}} \sqrt{2\overline{W}}} \int_{-\infty}^{\infty} dE \rho_s(E, x, y) \rho_t(E - eV) g(E, V, T), \quad (1.35)$$

where $2\overline{W} = W_s + W_t$ and $g(E, V, T) = f(E - eV, T) - f(E, T)$. The Eq. 1.35 shows how the density of state of tip and sample are convoluted in the tunnelling current expression. It also exemplifies the role of the tunnelling matrix in the determination of the tunnelling current.

During the time of precession $\frac{1}{\omega_L} \sim 2ns$ there are about 20 electrons crossing the tunnelling barrier if it is assumed that the DC tunnelling current²⁵ $I_0 = e/\tau_e = 1$ nA and the tunnelling rate of a single electron $1/\tau_e \sim 10^{10}$ Hz. This is an amount small enough for a fluctuation of the tunnelling current spin polarization to take place [161, 18]. If this happen then it is possible to imagine that the local spin polarized current can be coupled to the precessing spin on the surface, Fig. 1.21, through exchange interaction. The former will affect the tunnelling matrix from Eq. 1.34 in the following way:

$$\Gamma = \mathcal{T}_0 \exp \left[-\sqrt{\frac{\Phi - J\mathbf{S}(t)\sigma}{\Phi_0}} \right] \quad (1.36)$$

Where $\mathbf{S}(t)$ is the precessing spin operator and σ is the spin operator of the tunnelling electrons. J is the exchange coupling and Φ the tunnelling energy

²⁴ W_s surface work function, W_t tip work function

²⁵The notation will be simplified from now on. The DC tunnelling current will be referred as I_0

barrier and Φ_0 is a parameter depending on tip sample separation. Under the reasonable hypothesis that the tunnelling barrier is bigger than the exchange coupling the (Eq. 1.36) can be expanded in JS as follows:

$$\Gamma = \mathcal{T}_0 \exp[-(\frac{\Phi}{\Phi_0})^{\frac{1}{2}}] [\cosh(\frac{JS}{2\Phi}(\frac{\Phi}{\Phi_0})^{\frac{1}{2}}) + \sigma \mathbf{n}(t) \sinh(\frac{JS}{2\Phi}(\frac{\Phi}{\Phi_0})^{\frac{1}{2}})] \quad (1.37)$$

where the dependence of S with respect t has been discharged on $\mathbf{n}(t)$ defined from $\mathbf{S}(t) = \mathbf{n}(t)S$. From Eq.1.37 it is possible to infer that the AC component of the tunnelling current will be proportional to the product $\sigma(t)\mathbf{n}(t)$. In the precession period associated to ω_L , T there will be $\bar{N} = I_0 T$ electrons tunnelling. Besides, the time average current ΔI will be dependent on $\delta I(t)$. The time fluctuation of ΔI give an estimation of the magnitude of the AC component. It is found [161, 18] that $(\overline{\Delta I^2})^{1/2} \sim (I_0 B)^{1/2}$ indicating that the magnitude of the AC component is slightly dependent on the magnitude of the applied magnetic field and DC current. A numerical estimation of the tunnelling current fluctuation leads to asses them to be in the order of 10 pA when $I_0 = 1$ nA and the exchange coupling $J = 0.1$ eV [161, 18]. The former is according to experimental results. It is also possible to estimate the effect of the exchange interaction on the precessing spin $\mathbf{S}(t)$. This effect leads to a decoherence of the precessing spin. The time scale associated to this process is named $1/\tau_s$ and it is estimated to be about 4×10^6 Hz which is sensibly less than $\omega_L/2\pi = 5 \times 10^8$ Hz if the applied field is about 200 Gauss. In this respect it is possible to see that before getting affected from the tunnelling current the precessing spin can encode an AC signal in the current. Finally, in order to estimate the signal to noise ratio the authors calculate the Fourier transform of the tunnelling current and estimate it at ω_L [161, 18]:

$$\frac{\overline{\langle I_{\omega^2} \rangle}}{\langle I_{Shot-noise}(\omega)^2 \rangle} = [\sinh(\frac{JS}{2\Phi}(\frac{\Phi}{\Phi_0})^{\frac{1}{2}})]^2 \frac{1}{\tau_e \gamma} = 2 \div 4 \quad (1.38)$$

This amount corresponds to the experimental magnitude reported in [17, 20]²⁶. It seems that this theory could explain the experiments. It also shows how the DC current, the magnetic field applied, the magnitude of the exchange coupling and Finally, the size of the spin center are all parameters that can be tuned to magnify this effect.

There are two possible experimental setups that can be implemented on the system described. One relying on low temperature high frequency electronics and the other one much simpler relying on standard high frequency electronics. In [19] the experimental setup used was adapted to a room temperature. A splitter was placed close to the tunnel junction and two filters

²⁶ γ is a width entering the fourier transform Loretzian.

were allocated in vacuum. One was a low pass filter for normal STM operation and the other one consists of a high pass filter to be connected to an RF circuit. As the tunnelling junction is normally of the order of MOhm an impedance matching circuit is also required. As explained in [93] up to 1GHz the transmission line for circuit connections can be a coaxial cable though more complex coaxial wires can be used for high frequency low temperature applications [69]. Nevertheless in order to avoid undesirable reflection the impedance of the line, the source and the load must be equal. Furthermore in order to transfer the maximum power from the source to the spectrum analyzer the input impedance of the instrument must be equal to the output impedance of the RF amplifier. As discussed in [162] if a line between a source and a measurement apparatus has to be placed in the circuit some drawbacks may appear:

- Reduction of source quality factor Q
- Degradation of high frequency performance due to the phase shift induced by the line length
- Interference and noise increase.

For these reasons in a cryogenic environment, as in our set up, it may be better to use a configuration which incorporates some parts of the electronics in the low temperature stage. Particularly a high frequency filter and a preamplifier with appropriate matching impedance should be incorporated. Previous to those two components an AC-DC splitter has to be connected to the tunnelling junction to allow the detection of the DC channel. The presence of these components may introduce a heat leak. Kirshman [163] provides some insights about the former issue. The best device to build an high frequency cryogenic amplifier is a GaAs MOSFET whose power consumption can be reduced to $10\ \mu\text{W}$. Thermal conductance of the components used to build the high frequency detection circuit is a relevant parameter, as it can affect the cooling time of the experimental region. Unfortunately GaAs thermal conductance decreases below 77 K. A typical example of high frequency pre amplifier is described in [164]. In the set up described in this chapter a further power consumption of $10\ \mu\text{W}$ should not be a problem as we expect a cooling power at 0.5 K of 3 mW. The circuit is small and there is enough space to place it close to the STM or on the STM frame.

However, a much simpler approach is also possible relying on standard high frequency components connected outside the UHV environment. The former makes the detection problem much easier to handle. A simple circuit consisting of an AC-DC splitter plugged directly on the tunnelling current

line just before the I/V convertor has been assembled and tested. Following the splitter a band pass filter (200-400 MHz) is connected to two amplifiers. The amplifiers have 20 dBm. All the components have an input -output impedance of 50 Ohm that incorporates an easy plugging in the spectrum analyzer. Impedance matching at the tip level is simply ensured by the coaxial cable connected to the tip itself.

The technique described in this section is particularly promising as it can be implemented in simple set up at air pressure, like in [20] and in complex set up as the system described here. Besides, the possibility of studying intriguing magnetic systems as molecular magnets [24, 165] can be also envisaged. Nevertheless clusters of high nuclearity as SMM have usually high zero field splitting D [110], this means that the minimum magnetic field, that has to be applied in order to excite the precession of the spin, is much higher than in the experiments reported so far [20] (D can be as high as $30 \div 40$ GHz). This requirement shows how the technique must be necessarily developed at higher frequencies than those used so far in the detection of the ESR-STM effect.

Also, the magnetism and the coordinative bonding nature of metal-organic self assembled structures at surfaces [43, 166], can be elucidated using a spin sensitive local probe as the one being described. Finally, the use of ESR STM and magnetic molecules for alternative approaches to quantum computation [34, 35, 133] is certainly one of the most intriguing technological applications of the ESR STM. Particularly very recently Harneit and Coworkers have proposed a quantum computing approach based on endohedral fullerenes [30] and ESR detection. This approach can be extended to single molecular level if a resource for local read out was available [167]. In view of this ESR-STM is proposed as the tool for locally addressing the single magnetic adsorbates. Although all the former applications are certainly intriguing, the most straightforward application of this technique may be the study of simple molecules with a relatively low zero field splitting. In this respect radicals are certainly potentially the best candidates. Different types of employable radicals may be inferred from the well established work in this field [168, 169].

Chapter 2

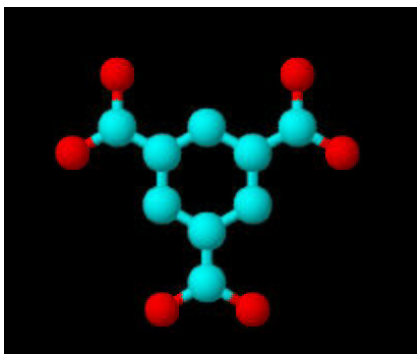
Metal-Organic Self Assembly at Cu(100)

2.1 Introduction

In this chapter is described a new method to produce nanostructures on surfaces. The first paragraphs elucidate the difference between metal hetero epitaxy on metals and metal-organic self assembly at metal surfaces. A quick review of programmed self assembly is presented. Also, in the fourth paragraph concepts of magnetochemical synthesis, such as synthesis of polynuclear magnetic clusters and magnetic chains, are presented and discussed in view of applications on the direct metalorganic synthesis on surfaces. The next sections describe the adsorption and the surface dynamics of large adsorbates. A survey of metalorganic chemistry on surfaces including the behavior of TMA at Cu(100), is presented in paragraph 6. Following results on mono nuclear complex and analysis (including chemical kinetic) are reported. Results and discussion on polynuclear clusters are reported. Besides a foregoing on the kinetics of adsorbate adsorption follows. The last part of the chapter describes the formation of 1D and 2D metalorganic structures. Results are interpreted in view of concepts of metalorganic chemical engineering. Particular relevance is given to the hydrogen bond as tool to tune the shape of longrange ordered metalorganic structures.

2.2 Experimental

Iron and 1,3,5 tricarboxylic benzoic acid (TMA) Fig.2.1 have been coevaporated on a Cu(100) surface in ultra high vacuum of 5×10^{-10} mbar. Under these conditions the surfaces can be prepared such to become clean and atom-

Figure 2.1: *1,3,5 tricarboxylic benzoic acid.*

ically flat, no oxide or impurity layers are present. A scanning tunnelling microscope is used [170] to study the resulting structures at the single-molecule level. Cu(100) clean surfaces were prepared through standard cycles of sputtering with Ar and annealing up to 800 K. TMA molecules were evaporated from a Knudsen type evaporator. The temperature of the cell was constantly kept at 463 K during the evaporation. Fe atoms were evaporated from an e-beam heating evaporator. For some measurements both the TMA and Fe deposition were performed keeping the temperature of the substrate at about 100K. The latter ensures that the adsorbates mobility is drastically reduced at deposition and that intermixing of Fe adatoms into the Cu(100) surface is suppressed. The samples were annealed to room temperature for STM measurements. However some experiments have been accomplished depositing adsorbates at room temperature. In this case the above mentioned adsorbates are expected to freely move on the surface.

The UHV STM has been extensively described in precedent works [170, 171, 172]. Accordingly, only some general features are here outlined. The instrument consists of a main UHV chamber fixed on a frame. During operations the frame is suspended on four springs attached to the lab ceiling. The external damping consists in a single damping stage implemented through rigid springs. The chamber is equipped with standard UHV instrumentation. Fig. 2.2 sketches a side view of the experimental area. The sample holder is mounted on a copper support. This support is, in operation, mechanically decoupled from the precision tube of the manipulator. However, the copper support rests on a stack of Viton damped Cu plates Fig.2.3. The latter represent a second damping stage. The STM is a beetle type. In operation, it is placed on a ramp mounted on top of the sample holder. The beetle de-

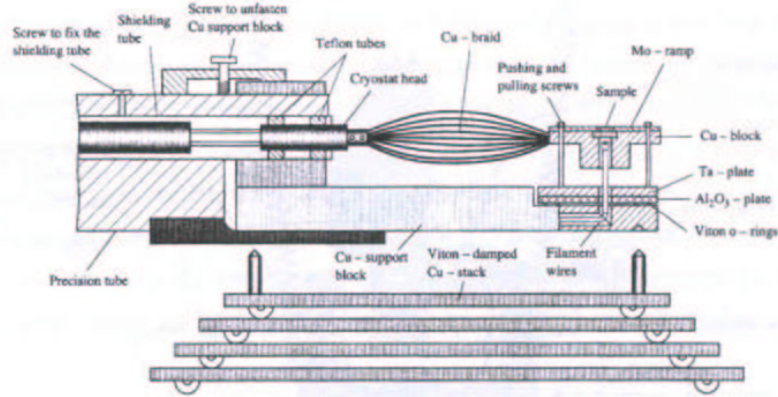


Figure 2.2: *Side view of the manipulator and the sample holder. Adapted from [173]*

sign allows a large¹ scanning area along side with a good thermal dilatation compensation. The former is relevant for studying growth phenomenon, as a statistical sampling of images on the same experimental session may be requested. The latter is important because the thermal drift due to dilatation of the scanning tube piezoelectric actuators and the contraction of the support, is limited in this construction. The horizontal manipulator incorporates a flux cryostat that can work both with ^4He and N_2 . The thermal contact with the sample is ensured by a copper braid connection. The control electronics is a commercial one bought by RHK. Further details concerning the UHV variable temperature STM can be easily retrieved in [171]. All the images presented in this thesis were achieved in constant current mode.

2.3 Metal hetero epitaxy

In the framework of this experimental work it is relevant to make a parallel between the current knowledge in growth processes at surfaces[174] and the case that will be described in the next chapter, i.e. metalorganic synthesis at surfaces.

Metal hetero epitaxy in metal-on-metal growth is a kinetic process as no growth is possible at thermodynamic equilibrium [171]. When an adsorbate reaches the surface, it can take part to a number of processes² as illustrated

¹The tripod approaching mechanism can be used for lateral displacement of the tip along distances as long as 2 mm. In other design types, such as the Pan design[53], the approach mechanism does not permit a long lateral displacement.

²All these processes depend on the temperature.

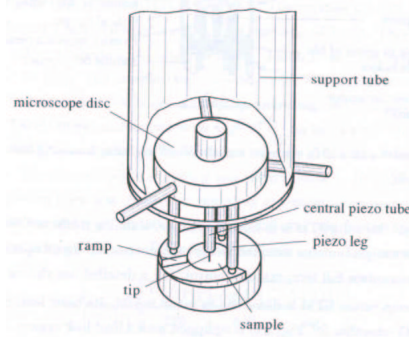


Figure 2.3: 3D view of the Variable temperature STM, adapted from [173].

in Fig. 2.4. In the first process the adatom can undergo desorption. Besides the adatom can meet other free adatoms and form nucleation centers. Nucleation centers can grow up to a certain critical size above which a stable cluster is formed. The adatom can also be captured from a stable aggregate. The former description is the picture given from the nucleation theory [175] verified experimentally [176]. Each of these processes is associated with a characteristic time scale, namely: time constant for nucleation τ_n , desorption τ_d , capture τ_c .

The kinetic of the growth evolves according to the magnitude of these constants. The magnitude of these constants depends on a number of parameters that can be appropriately varied from outside. The nucleation process depends primarily on the diffusion of single adsorbates on the surface, on the concentrations of adsorbates on the surface and their mutual interaction energy. The concentration of adsorbates is given by the deposition rate which is an important parameter of the growth scenario and which can be tuned from outside. In order to understand which are the other external parameters which act on the growth process, a brief description of diffusion on the surface is on demand. An atom can undergo a transition on a surface from one site to another one only if the thermal agitation is sufficient to overcome the migration energy barrier E_m . In general the substrate temperature T_s is such that $kT_s \ll E_m$; this means that an atom spends most of its time in the site before jumping. Therefore from one jump to the next one the memory of the process is lost and a random migration evolves. The diffusion during random processes is well described by the relation $\langle \Delta x^2 \rangle = 2Dt$ as explained in [177, 171]. The mean square displacement along one direction $\langle \Delta x^2 \rangle$ is proportional to the time diffusion interval t and diffusivity D . The diffusivity is connected to the free energy of the diffusion process. Under the simple approximations that the entropy term is negligible the diffusivity will

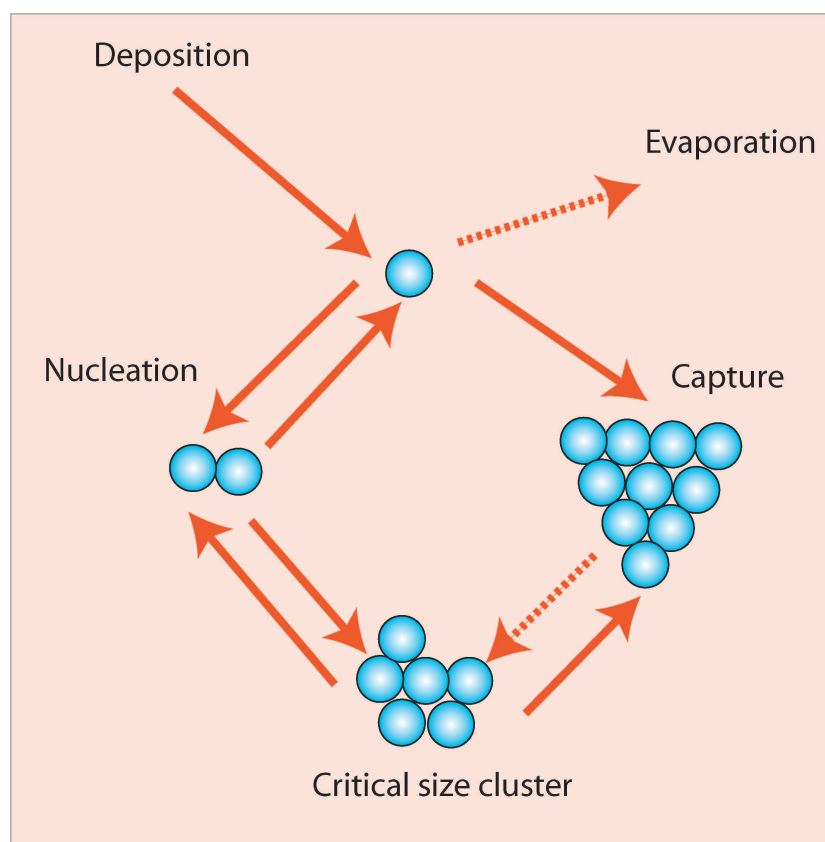


Figure 2.4: *Schematic representation of the relationships between different populations in early stages of film growth*

depend exponentially on the ratio between the migration energy E_m and the substrate temperature T_s ³. The connection with the migration E_m energy clarifies how the chemical nature of adsorbates and substrate may affect the growth scenario. However, the geometrical structure of the surface will also affect the diffusion accounting for a variation of the pre-factor constant. Finally the adsorbate-adsorbate interaction will determine the critical size of stable clusters, for a given temperature. Summarizing a number of external parameters can be appropriately tuned to control the growth scenario [172]. As shown in Fig. 2.5 the control on these parameters lets form nanostructures whose study enables to elucidate the dependence of growth on microscopical parameters. The former lead to a better choice of the external parameters in order to shape the desired nanostructure.

The external parameters tunable from the operator are:

- Deposition rate
- Substrate temperature
- Substrate, adsorbate material and symmetry

These parameters are extremely relevant to the discussion in this thesis as they are not the only ones relevant when two different adsorbates are deposited on the surface. Particularly if the second adsorbate is an organic molecule other degrees of freedom come into play. Besides if a chemical reaction between the two adsorbates takes place the nanostructure growth process is intimately modified.

As matter of fact in normal metal epitaxy growth adsorbate-substrate interaction is the most relevant interaction, however in the case discussed in the following adsorbate-adsorbate interaction is sensibly enhanced. In some cases, as for instance at Cu(100), self diffusing process[178] can affect the growth scenario leading to surfaces alloys. Migration of Cu adatoms from the step edges to the terraces at Copper surfaces is a well established phenomenon and has been the object of different theoretical and experimental studies [178, 179, 180, 181, 182, 183, 184]. This is a process which certainly takes place in the experiments performed in this thesis when the substrate temperature approaches room temperature.

Other relevant surface processes which are of importance to the experiments performed here are the migration of Fe adatoms to the step edges [185, 186] and the exchange of Cu surface atoms with Fe adatoms [185]. Fe adatoms are also known to dig into the first layer of Cu(100) [187]. Such phenomenon

³in this picture the diffusivity will depend linearly on a specific constant

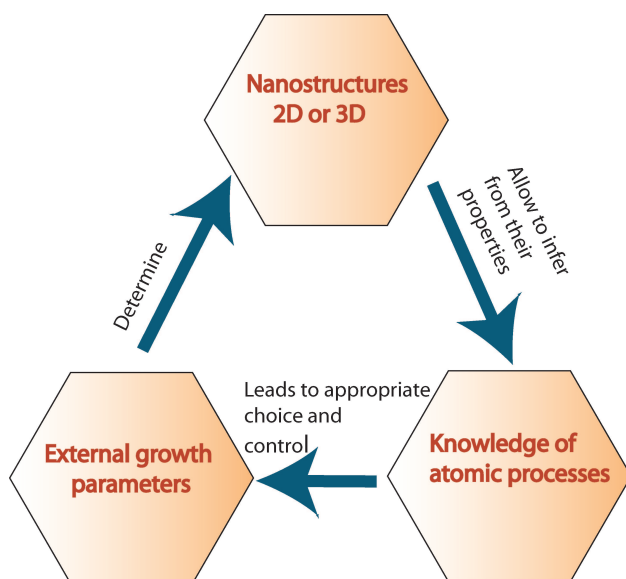


Figure 2.5: *Mutual dependencies between different aspects involved in nanostructure formation, as outlined in [172]*

are not observed if deposition of adatoms is performed at low T [188].

2.4 Principles of Metal-organic 3D Synthesis

Supramolecular chemistry has revealed to be an invaluable tool to build complex structures [36]. It is also expected to provide major solutions in the race for shrinking the sizes of computer industry basic components [37] [38] [36]. There are several reasons why the self assembly approach driven by non covalent interactions has revealed an invaluable tool in the design of complex structures[39]:

- A highly convergent synthetic protocol based on the simultaneous assembly of the predetermined building blocks, whose preparation requires significantly fewer steps than the comparable covalent synthesis.
- Fast and facile formation of the final product since noncovalent interactions are usually established very rapidly
- Inherent defect free assembly as the equilibria between the constituents and the final products contribute to the self rearrangement of the components within the assembled structure and thus to the self correction of defects.

Among the non covalent interactions used in self assembly chemistry, coordination bond represents a pillar [189]. The high directionality of this chemical bond has enabled scientists to build a number of 2dimensional structures as widely discussed in several review articles [190] [191] as well as several recent works [192] [193]. The strategies for building 2D cages may be relevant to the design of wave guides or resonant cavities for the surface electrons at metal surfaces.

Coordination interaction is also important to build cages and complex 3D structures as reported in a number of relevant works [194] [195] [196] [197] [198] [199].

Most relevant for this work are two important aspects of metal-organic supramolecular chemistry:

- The possibility of programming the final structure by encoding information on the type of chemical bond into the metal ion keeping the type of ligand unchanged (see below).
- Time dependent synthetic strategy with the possibility of time evolution into multiple self-organization processes.

A remarkable example [200] [201] of the first properties is given by the possibility of building double or triple helicate with the same ligand by changing the metal ion from Cu^+ to Ni^{2+} . This process is schematized in Fig.2.6. The second aspect is important, as, once achieved a first synthetic species it is possible to induce a rearrangement of its structures by means of external modifications. This is known as *post self assembly* modification [202]. In the framework of this thesis it will be shown as annealing following self assembling is a valuable tool to build structures at surfaces.

Last, proper metal ions have been used to encode magnetic information into the self assembling process [203]. In this work Breuning and coworkers were able to synthesize a system based on $[2 \times 2]$ Fe grids which shows Spin Crossover. Spin crossover is one of the most appealing molecular bistability as it may be used for implementing logic operations and store information [204, 205] in nanometric electronic devices. The compounds synthesized in the afore mentioned work [203] showed bistability to a number of external triggering factors including temperature, pressure and light. Self assembling through coordinative interaction proves accordingly a capability of synthesizing magnetic structures.

The goal of this work is to show that the concepts mentioned in the above are valuable tools to build nanostructures at surfaces and particularly nanostructures showing intriguing novel magnetic properties. There are some major remarks that are requested to be addressed when extending the con-

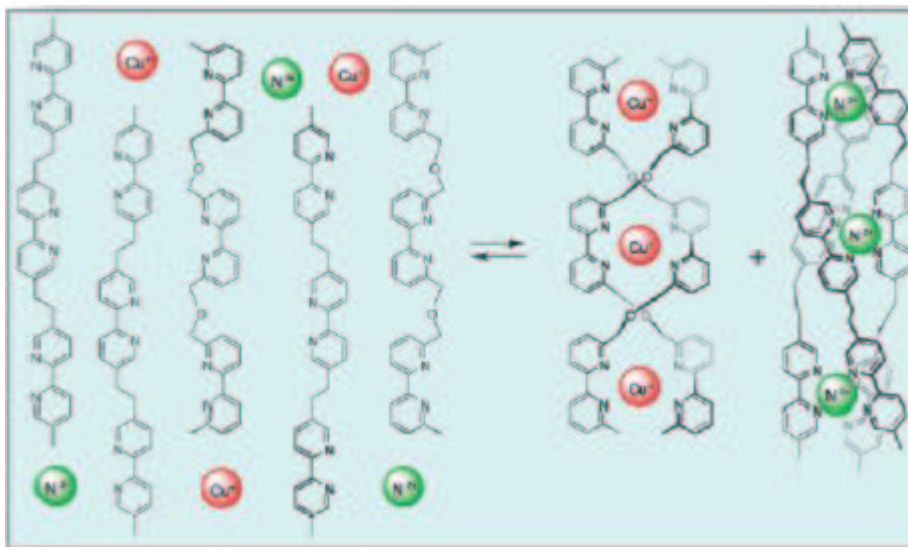


Figure 2.6: *Two different metal ions can encode different structural information. The Cu^+ leads to the formation of double chain helicates whereas Ni^{2+} leads to the formation of triple chain helicates. The picture is taken from [36].*

cepts of coordinative supramolecular chemistry to the surface. As shown before, different structures can be programmed by an opportune choice of the metal atom. The former statement holds also at metal surfaces but, the programmed information is also encoded through the choice of the surface. In fact, different surfaces show either a different chemical potential or a different surface potential profile due to different surface geometries. Besides, self assembly 3D molecular chemistry is based on the use of ions whereas in this thesis work atoms are deposited on to the surface in UHV conditions. The atoms are expected to be in their zero oxidation state, at least before a chemical reaction takes place. The former means that the type of chemistry going on in this scenario is different from solution chemistry. A parallel could be made with the chemistry of free atoms [206] which is a well established field. Particular the metal atom used in this thesis is Fe. Some experiments have been performed evaporating Fe atoms and making them reacting with cyclooctadiene COD and PH_3 [207]. In this configuration Fe is in the oxidation state 0 and it gives an unstable paramagnetic four square planar complex and a square pyramidal complex. However, the most important point to be stressed in this context is the following: Both structural and electronic information encoded into a metal atom deposited at surfaces are slightly different from those encoded in solution chemistry. The reason

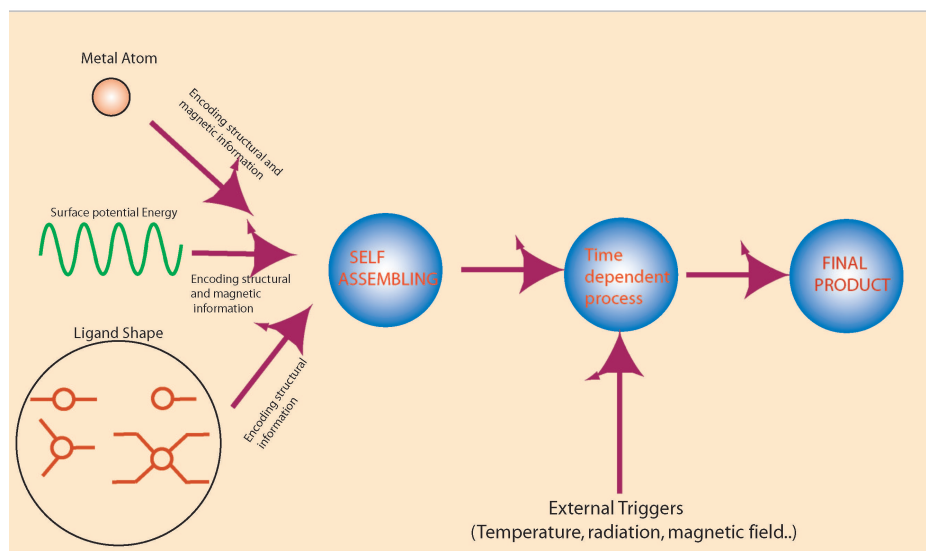


Figure 2.7: A number of different information can be encoded in the initial reactants. The surface potential energy as well as its chemical activity contributes to the information encoding too. Post self assembly modifications can be induced by external triggers, notably annealing.

is that in the reaction at a surface the atom is in its zero oxidation state and therefore it reacts accordingly. For instance Fe has an outer shell electronic configuration $3d^6 4s^2$ which resembles much more the electronic configuration of Ni^{2+} ($3d^8$) rather than Fe^{2+} ($3d^6$). This is an important point which will be reconsidered in the next paragraphs.

The concept of time dependence can be also valuably implemented through annealing the sample at different temperatures for different time lengths. This **post self assembly** modification was the easiest external trigger to be applied in our experimental set up. However a number of other triggers could be used including light sources and magnetic fields. **Fig 2.7** elucidates the concepts of programmed assembling. Structural information are encoded mostly through the choice of appropriate metal atom and substrate as well as ligand shape. The concept of ligand shape is also crucial to the determination of the final self assembled structure [190]. As shown in Fig. 2.7 some ligand shapes are more appropriate to build mono dimensional structures, others can simply generate complexes, and others 2D assemblies. Nevertheless even a simple linear ligand can generate 2D assemblies and this strongly depends on the structural information encoded through the metal atom used in the synthetic process. Also, the surface contributes to the encoding of the magnetic information as it opens up a channel of interaction between magnetic

center. This will be described in the next section.

2.5 Serendipitous Approach to metal-organic magneto chemistry

It may turn a bit contradictory to address the concept of serendipity self assembly in this section. Nevertheless though a programmed self assembly is certainly an asset of supramolecular chemistry, the same does not hold for magnetic metal-organic chemistry. In the world from Siegel and coworkers” the concept of an accessible and controllable molecular program, even within the limited arena of metal coordination structure, seems to be premature” [208]. For this reason it will be stressed in this paragraph that the concept of programmed self assembly at metal surfaces is a valuable goal but, results arise also from a certain degree of serendipity.

The tentative to build structures by attempting the use of different ligands, atoms, and surfaces will certainly predominate the first phase of the search for magnetic nanostructures at metal surfaces. This process of serendipitous self assembly has characterized the search for Single Molecular Magnets (SMM) so far [209].

This paragraph is also intended to give the reader a guideline to understand some major achievements in metal organic magnetic chemistry and how the philosophy behind these results can be extended to surfaces in order to build magnetic nanostructures. There are four main magnetic objects that are interesting to be addressed: *Single molecular magnets* SMM , *1D spin chains*, *2D spin chains*, *Spin ladders*. Trying to build such structures at metal surfaces is extremely interesting as the development of the magnetic sensitive nanoprobe described in the former chapter may open up the possibility of studying the magnetic properties of these structures with sub nanometric spatial resolution. Nevertheless, it should not be neglected the possibility to generate a new class of magnetic material that may arise from the coupling between nanostructures and surfaces. It is therefore suggested that a certain degree of serendipity in the search for 0D 1D, 2D magnetic structures at metal surface is certainly desirable. The reason is that confining the study of magnetic nanostructures only for the mere tentative to reproduce systems already known will live out alternatives that may not be known at the moment.

The tentative to build molecular magnets directly on a surface is not absolutely new, though results are very scarce. Experiments under UHV conditions are not present in literature. However, there are some successful attempts to build molecular based magnetic material in high vacuum conditions [210] and by *Chemical Vapor Deposition (CVD)* [211] [212] [213]. The method in high vacuum leads to the production of well ordered layers whose

thickness amounts to some μm . Though this technique is different from the one used here, the method for the deposit of the layer is to heat the powder in a crucible. This important point reveals that some magnetic material precursors have a sublimation temperature lower than the degradation temperature, a property that is paramount in view of UHV applications. Some material showing high Curie temperature (above RT) have been synthesized. For instance the synthesis and magnetic characterization of $\text{Cr}(\text{TCNE})_x$ [214] (TCNE=tetracyanoethylene) and $\text{V}(\text{TCNE})_x$ [215] have been recently reported. The formation of the above mentioned complexes takes place in flight after evaporation of reactants. Subsequently a thin film develops. The method is different from the one used here, according to which the reaction among reactants occurs on the surface. Despite this difference the evaporation process can be made to illustrate that two or more different precursors of a magnetic compound can be separately evaporated from a crucible.

Single Molecular Magnets (SMM) were discovered in 1993 [24] but, synthesized earlier. These systems are large metal organic polynuclear clusters showing a slow relaxation rate of the magnetization [25]. The clusters have a high spin ground state, for instance the Mn_{12} which was the first cluster to be synthesized [216] has $S = 10$. A schematic representation of Mn_{12} cluster is given in Fig. 2.8. The magnetic ions within the clusters are bridged from O atoms; the high spin arises from a balance of ferro and ferri-magnetic coupling within the clusters. The clusters show also an axial zero field splitting D amounting to less than 1K. The presence of the zero field splitting gives rise to an energy barrier between the state with $m_s = S$ and $m_s = -S$ (m_s is the eigenvalue of the operator \mathbf{S}) resulting in a low rate relaxation of the magnetization [25]. The presence of this energy gap (Fig. 2.9) for the reversal of the magnetization is particular as the molecules can work like magnetic bistable switch, a property that makes such molecules interesting in view of possible applications in nano scale magnetic storage. Also, some related molecules, such as the Fe_8 clusters, show an interesting quantum phenomenon i.e. the tunnelling of the magnetization. Fig. 2.10 schematically illustrates this phenomenon. The two halves of the potential energy diagram can be coupled through quantum tunnelling. The magnetization of the single cluster tunnels only when the applied magnetic field is such that the level occupied in one half is at the same energy of the level unoccupied in the other half. In some clusters, like Fe_8 , this phenomenon can be modulated from a transversal magnetic field. The application of a transverse magnetic field gives rise to oscillations with quenching of the tunnelling for critical values of the field where destructive interference between the tunnelling pathways occurs. This effect is related to the berry phase and was definitively established in 1999 [217]. This property is a beautiful proof of how, purely quantum me-

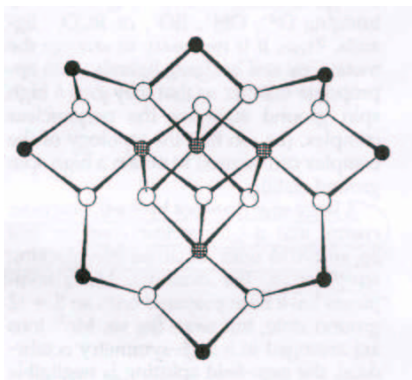


Figure 2.8: Drawing of the Mn_{12} complex. Mn^{IV} ions (shaded circles), Mn^{III} ions (open circles). Figure taken from [25].

chanical effect can manifest themselves through the measure of macroscopic properties. The effect of nuclear spin on the magnetization properties of the SMM were finally established recently [218]. The interplay between nuclear spins and electron spins is at the basis of a proposal for the applications of these systems for *quantum computing* applications. All these reason can be basically applied to bring those systems on the surfaces and to investigate their magnetic properties at the single molecular level. Nevertheless the requirements imposed by the UHV compatibility could limit drastically the possibility of inserting these molecules within a UHV chamber. An alternative approach is the one investigated in this thesis. This is the attempt to exploit metal ligand interaction to build polynuclear clusters directly on the metal surfaces. The properties of these clusters may be different from the ones described before, although still extremely interesting in view of *quantum computing*, *magnetic recording* and the search for the *cross over between classical and quantum world* at the nanoscale.

In this respect it may be interesting to describe briefly the synthetic strategies used to build the SMM. One strategy is a programmed approach. It has been reviewed by Aromi [219]. The starting point of the synthesis is to bridge together complexes made of few metal centers. One of the bridges is opened and a new ligand bridges two smaller complexes. The groups that are usually used are: carboxylic, hydroxylic, ethylic etc.. The approach we use, resembling possibly closer to the approach described recently by Winpenny [220, 221]. This approach is defined "Serendipitous" like the philosophy behind. It is addressing the synthesis by the use of different ligands without programming a priori the final structure of the complex. The approach relies on the flexibility of a class of ligands known as pyridonate. These ligands

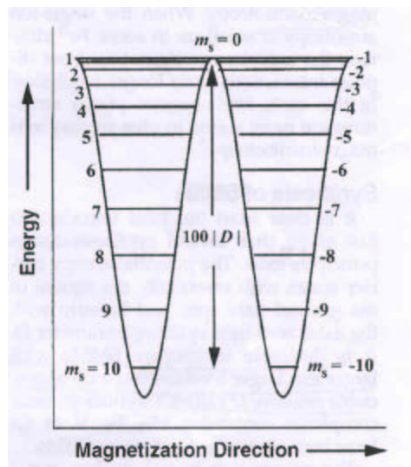


Figure 2.9: Plot of the potential energy versus the Magnetization direction for a single-molecule-magnet with an $S=10$ ground state. Figure taken from [25].

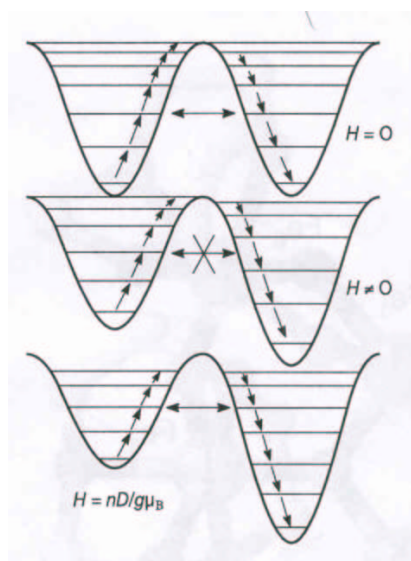


Figure 2.10: Schematic representation of how the potential energy of an SMM changes when the magnetic field is swept of an amount $H = \frac{nD}{g\mu_B}$. The tunnelling of the magnetization can occur only when the energy levels in the two halves of the diagram are aligned. Figure taken from [25].

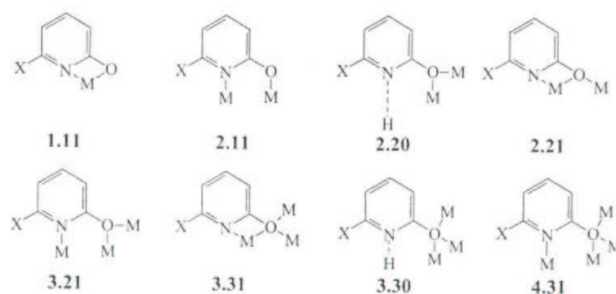


Figure 2.11: *Different ligand mode of the Pyridonate. Figure taken from [209].*

offer N and O donor sites that can bridge the metal atom in different configurations as shown in Fig. 2.11. The flexibility of the ligand can lead to clusters comprising a high number of spin centers. The exploitation of the ligand flexibility is a bit in contradiction with respect of the idea shown in the former paragraph i.e. encoding structural information by changing the metal atom and keeping the same ligand. However, in the future it will be interesting to explore this approach also at surfaces. A number of different polynuclear complexes have been synthesized following the "serendipitous method" and a few examples are shown in Fig. 2.11. . The possibility of exploiting the

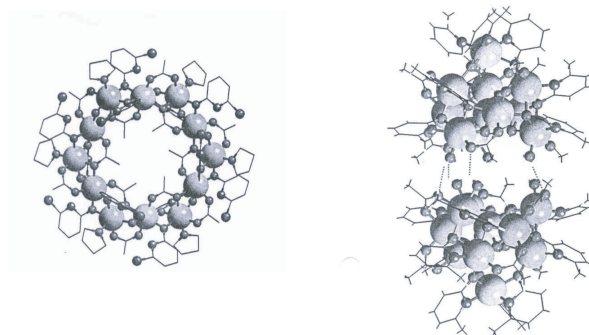


Figure 2.12: *Examples of different clusters synthesized. Figure adapted from [209].*

knowledge developed in the synthesis of polynuclear metal cluster, especially SMM, is considerably promising. A number of ligands have already been put on the surfaces in UHV conditions including benzene thiol on different Au surfaces [222], phenoxy species on Cu(110)[223], phenol on Ag(111) [224] representing a reservoir of ligands available for the direct synthesis of magnetic clusters on surfaces.

The magnetic cluster described above can be considered as quasi **0D** system.

However a number of interesting magnetic properties are expectable also for purely **1D** systems[150]. There are a number of theoretical model which describe the ground state and the excitations of magnetic ordered systems. The most common is the Heisenberg's model which describes spin systems with only neighbor interaction. The hamiltonian of this model is:

$$H = \sum_{ij} J \vec{S}_i \cdot \vec{S}_j \quad (2.1)$$

There are different constraints that can be added to this model. Particularly there are degrees of freedom concerning the spins and their dimensionality usually indicated as $D = 1, 2, 3...$ indicating the directions which the spins are allowed to align to. Also the space dimensionality of the physical system supporting each individual spin can change. This degree of freedom is referred to $d = 1, 2, 3$, $d = 1$ meaning monodimensional and so on. There are clearly many combinations of d and D possible and only for few of these a solution is known [150]:

- All the cases for $d = 1$
- All the cases for $d \geq 4$
- All the case for long range interactions, which give mean field solutions.
- The case $d = 2$ and $D = 1$ (Ising model $H = \sum_{ij} J \vec{S}_i^z \cdot \vec{S}_j^z$)
- The case $D = infinity$ for any d .

The **1D** case is extremely interesting as it represents a benchmark to test fundamental quantum mechanical behavior. There are a number of inorganic systems that have been synthesized to test the magnetic behavior of **1D** magnetic systems, these include $CsCoCl_3$, $KCuF_3$.

The focus of the research in this subject is to study the excitation spectrum of these materials. There are two cases of interest: the case in which the spins are half-integer and the case in which spins in the chain are integer. In the former excitations are known as **spinons** and their energy dispersion is gapless. In the latter the chains are known as **Haldane chains** ($CsNiCl_3$, $Ni(C_2H_8N_2)_2NO_2ClO_4$) and their excitations show a gap. The possibility of building such systems at surfaces would certainly open up a path for the study of magnetic exciations in **1D** through the use of the methods described in the former chapter. Also, it is relevant to mention that copper benzoate has been applied in the study of **1D** magnetic systems a number of times [225, 226, 227, 228]. This indicates that the 1,3,5 tricarboxylic benzoic acid (TMA) molecule is a good candidate to produce magnetic nanostructures.

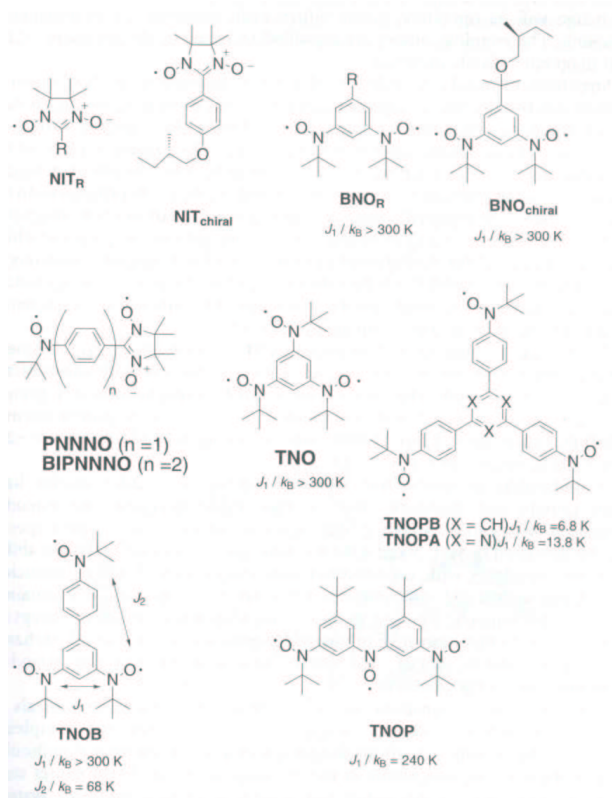


Figure 2.13: Examples of different Nitroxide radicals. Figure taken from [229].

Mono dimensional magnetic systems have been also synthesized through the use of molecular systems [229]. The synthetic strategy in this case is based on the use of Nitroxyl radicals. This is a family of radicals that show a high internal ferromagnetic exchange, a number of radicals belonging to this class are reported in Fig. 2.13. The reason why these radicals are used, can be easily clarified through the scheme in Fig. 2.15. The coupling between the radical and the metal center is antiferromagnetic. If this building unit is repeated in one dimension or more then ferromagnetic 1D and 2D assemblies can be built. A schematic representation of this structural motif is shown in Fig. 2.14. However, even if different attempts to make 1D systems with this method have resulted to be successful as for Mn [230] the slow relaxation rate of the magnetization was observed only recently [26] as the strong requirement for this affect is that the intra-chain exchange J_{intra} must be at least four order of magnitude larger than extra chains interaction J_{extra} . The possibility of having long chains behaving as single magnets would be ex-

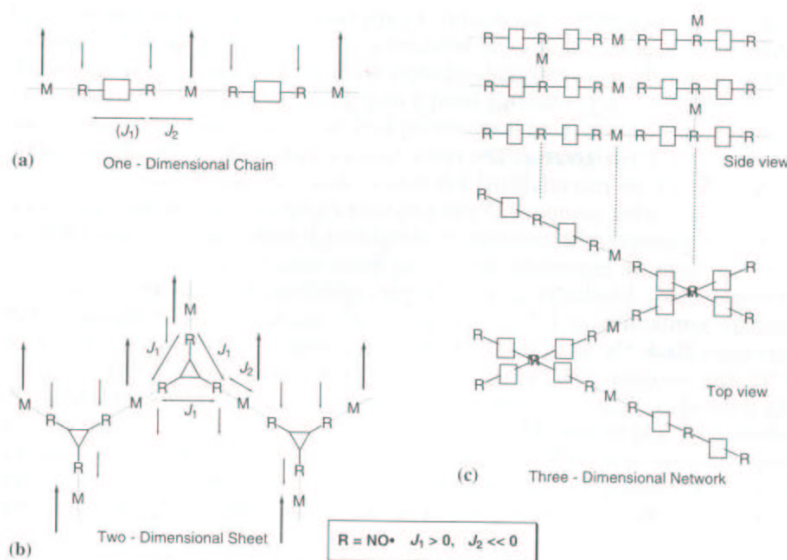


Figure 2.14: *Schematic representation of the coordination network of metal ions and nitroxyl radicals. Figure taken from [229].*

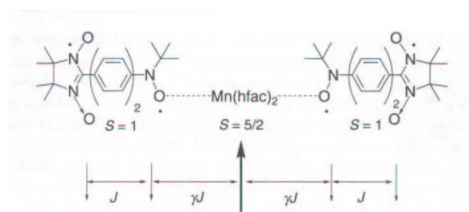


Figure 2.15: *Schematic representation of the antiferromagnetic coupling between the metal ion and the Nitroxyl radical. Figure taken from [229].*

tremely interesting for magnetic recording application on surfaces, as a chain is much more accessible than a small cluster. The direct building of such chains on surfaces would offer the opportunity to make the distance among the chains sufficiently large to avoid lateral coupling. The method developed here could be applied to reach this goal. In fact recently Nitroxyl radicals have been deposited in high vacuum condition on metal substrates[231, 210]. The deposition technique follows the standard path to heat a powder in a crucible evaporator resulting in a possible applicability in UHV condition. The latter experiments open up the possibility of a direct synthesis of **1D** single molecular magnets at surfaces.

As last example for possible targets of the direct exploitation of coordinative interaction at surfaces, the attempt to build spin ladders [232] is suggested. As it will be shown through this thesis we succeeded in attempting the reproduction of the structural motif of spin ladders on metal surfaces.

Spin Ladders are magnetic systems at the crossroad between 1D and 2D ordering. They consist of ordered spin legs connected through rungs as shown in the Fig. 2.16. The interest towards these systems raised at the begin of the last decade when Dagotto et al. predicted a number of quantum mechanical effects that are associated with sharp transitions when going from 1D $\frac{1}{2}$ spin chains to quasi 2D systems [233]. The subject has been recently reviewed by the same author [234] and has been the center of the National Science Council in the review of the last decade achievements in condensed matter physics[235]. Here, the properties of these systems will be briefly listed. However the interested reader can refer to the afore mentioned literature for a detailed explanations. A spin ladder where each site carries a spin $\frac{1}{2}$ is described by the following hamiltonian 2.2

$$H = J_{\parallel} \cdot \sum_{a=1,2} \sum_{i=1}^L \vec{S}_{i,a} \cdot \vec{S}_{i+1,a} - J_{\perp} \cdot \sum_{i=1}^L \vec{S}_{i,1} \cdot \vec{S}_{i+1,2} \quad (2.2)$$

where $\vec{S}_{i,a}$ is the spin operator at the site ($i = 1, 2, \dots$) on the leg a ($a = 1, 2, \dots$) of a ladder with L rungs. The constant J_{\parallel} and J_{\perp} refer to the inter rung and intra rung magnetic exchange[232]. There are two different behaviors according to the parity of the number of legs. Spin ladders with an even number of legs are predicted to give rise to a spin liquid ground state, where couple of spins are coupled anti-ferromagnetically along the rungs. However, spin ladders with an odd number of legs are predicted to behave in a similar way like the 1d chains. Two legs spin ladders are a good benchmark through which all the theories concerning excitations and quantum effects can be tested. There are two limiting cases [232]:

1. isolated dimers, when $J_{\perp}/J_{\parallel} \longrightarrow \infty$

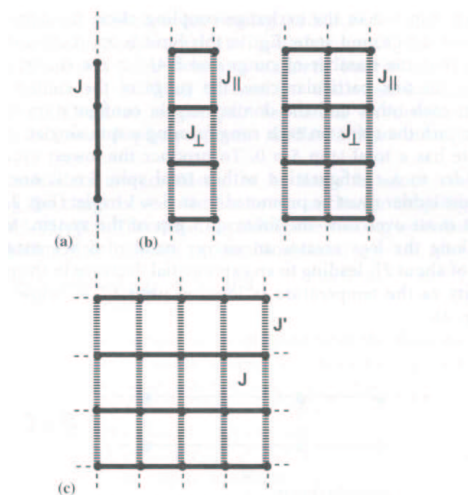


Figure 2.16: *Schematic illustration of different type of spin systems. The black dots denote spin $\frac{1}{2}$ (a) 1D chain. (b) two-leg, three-leg spin ladders. (c) 2D spin lattice with different longitudinal J and horizontal J . Figure taken from [232].*

2. isolated 1D chains, when $J_{\perp}/J_{\parallel} \rightarrow 0$

The real experimental cases lie somewhere between these cases. Nevertheless, the first case can be somehow approached. Theoretical predictions foresee that the ground state is composed of spin couples along the rung having a net $S = 0$. In order to create an excitation in this system an energy gap must be overcome. If this is done, as shown in the Fig. 2.17 (a), a spin singlet $S = 1$ can be created and magnons can travel along the ladder. This travelling quantum object manifests itself through the variation of some thermodynamical properties, by contrast the direct synthesis at surfaces of spin ladders would give the possibility of studying excitation of this type at the most possible intimate level. Besides, as shown in 2.17 (b), the effect of inter ladder exchange can influence the behavior of the single ladder. In this respect the direct synthesis on the surface may be particularly promising to create really insulated ladder.

There are two approaches in the synthesis of spin ladders. The first one consists in bridging 1D chains already made whereas, the second one attempts to connect single dimers in pile. A number of starting building blocks can be used as TTF derivatives, namely DT-TTF, and TCQN derivatives (Fig 2.18). Also, this type of molecule have already been deposited in high vacuum and UHV conditions at surfaces [236].

In conclusion, in this section the relevance that the direct exploitation of

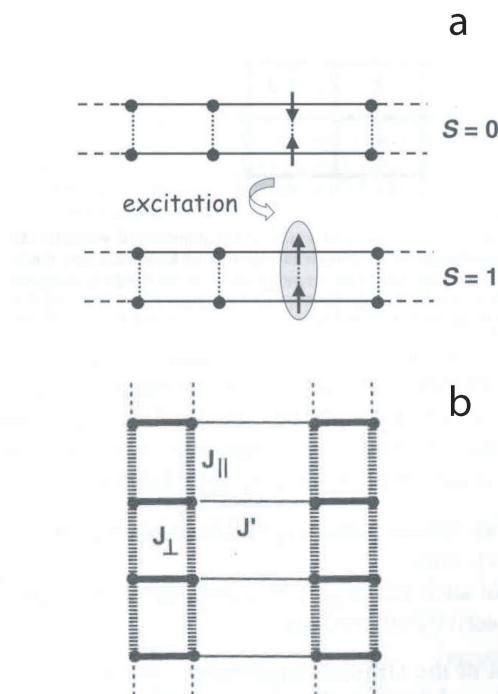


Figure 2.17: **(a)** Scheme of an excitation propagating in spin ladders where the spin on each single site is $\frac{1}{2}$. **(b)** Effect of inter ladder exchange Figure adapted from [232].

coordinative bonding on the surfaces could have in the near future has been shown. However, a number of cases considered here do not take into account the effect that the surface could have for the electronic and magnetic properties of the synthesized structures. The surface will certainly act on the magnetic anisotropy of each single metal atom. The effect will probably include shape and orbital contribution. Moreover, it has been often cited the exchange interaction. Once the magnetic atoms are adsorbed at the surface the exchange interaction among them will be not only mediated by the molecule bridging them but the surface will also contribute. The scenario on the surface resembles more to a double channel phenomenon. Interactions among magnetic centers will be mediated by the molecules (**channel 1**) and the surface (**channel 2**). The relative coupling between molecule and surface will probably affect the interacting channels, as charge transfer into or from molecular orbitals may affect the electronic properties of the chemisorbed molecule. In this thesis the first attempts to synthesize a plethora of interesting structures at surface are demonstrated to be successful.

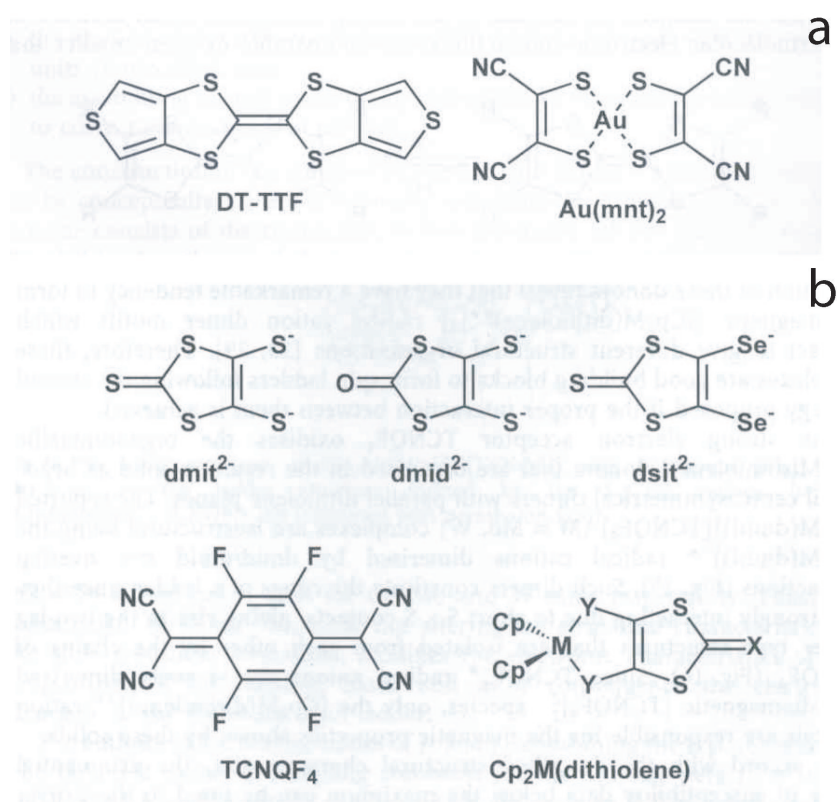


Figure 2.18: *(a)*DT-TFF molecule used in purely organic ladders and the magnetically inert Au(mnt)₂. *(b)* Figure adapted from [232].

2.6 Bonding and Dynamics of large adsorbates

One of the major goals of this thesis is to individuate the control parameters for the self assembling process at metal surfaces involving the direct exploitation of the coordinative bonding between two chemical species. For this reason it is important to understand to what extent the processes, which take place at surface, affect the synthesis of metal organic nanostructures. In the first part of this chapter dynamical effects during deposition will be ignored, though they may be extremely relevant in determining the kinetics of the reaction between TMA molecules and Fe atoms.

The strength of the molecule-substrate interaction is one of the relevant parameters though, as it will be stressed in the foregoing, molecule-metal adatom coordinative interaction seems to be decisive for 2-dimensional ordering. Particularly molecule-substrate interaction is expected to play a role in the ability of the molecule to be effectively integrated in supramolecular assemblies. This is important for the kinetics of complexes formation and also when a post modification is induced by an external trigger as for instance annealing. Besides molecule-substrate interactions may be relevant to determine the kinetic of the reaction with the metal adsorbates through the control of the adsorbate diffusivity. Diffusivity is important because it determines both the preferential direction on which the molecules diffuse and the type of diffusion mechanism they undergo. The two former features may considerably affect the reaction kinetics. Unfortunately the instrument used in these studies does not allow an easy sample exchange and therefore only the Cu(100) surface has been employed. Also, measurements of the diffusivity of TMA molecules on Cu(100) were not systematically performed ⁴.

In view of these reasons a brief account of physisorption and chemisorption[237, 238, 59], with a particular emphasis to large organic molecules, will be provided.

Physisorption is a process according to which the long range dipolar interactions between the adsorbate and the surface take place[59]. The interaction is of the order of few tenths of meV and is typical for passivated surfaces as hydrogenated Si or highly oriented pyrolytic graphite (HOPG). At metal surfaces the phenomenon can occur if the outer shell atomic or molecular orbitals of the adsorbate are substantial higher in energy (several eV) than the metal surface Fermi energy. It can also occur if the surface is somehow passivated, for instance with an oxide. As in this study surfaces are atomically clean and flat, transition metals, molecules are expected to be chemisorbed.

⁴Molecules can be imaged on the Cu(100) surface at 100 K.

Chemisorption is a much more predominant physical phenomenon than physisorption. It involves energies of some eV. A simple description of this phenomenon can be done in terms of frontier orbitals [239]. Some of the molecular orbitals of the adsorbate species lie slightly above the Fermi level. In a simple picture the chemisorption process can be imaged as a two stage process[59]. The afore mentioned molecular orbital interacts with the sp bands of the surface and give rise to a slightly broadened new orbital which lies slightly below the Fermi energy. This process is common to all the metal surfaces and results in a attractive interaction between the adsorbate and the surface. In the case of transition metal surfaces also the d bands play a role. The state formed between adsorbate orbitals and sp band interacts with the d bands(these are much less broadened than the sp bands) forming a two level state (slightly broadened) as illustrated in Fig. 2.19. The resulting interaction between the adsorbate will be attractive or repulsive according to the degree of filling of the antibonding orbital generated. There are three main factors characterizing the strength of the chemisorption interaction [238, 240]:

- Filling of the d bands
- Strength of the adsorbate d-bands coupling
- Position of the d band, ε_d , with respect the Fermi energy, ε_F

The position of the d band, ε_d , is very important to determine the level of the antibonding state with respect to the Fermi level. If the antibonding state lies above the Fermi level, it turns to be empty and the adsorbate-surface interaction is inherently strong (several eV). Conversely, if the antibonding levels lies below the Fermi level, Fig. 2.19 (b), the level will be filled up and the resulting adsorbate-surface interaction will be weak. For most transition metal surfaces the antibonding level lies just across(accounting for its broadening) the Fermi level. The filling of the d bands determines how many electrons will occupy the antibonding orbital. The higher is this number the less stable is the resulting chemical bond. Finally, the strength of the adsorbate d bands coupling is also relevant to the stability of the adsorbate-surface interaction. For instance Cu is more reactive (respect to adsorbates) then Au as the 3d bands are stronger coupled to the adsorbates molecular orbitals than in Au. The chemisorption of small molecules on different substrates is a well established domain of surface science[59],e.g. the behavior of CO on Cu(100) [241], O_2 on Pd(111)[242] are well known. However a few studies are present in the literature concerning large molecules. It is known benzene sticks flat [243]. Some calculations [244] shows that TMA

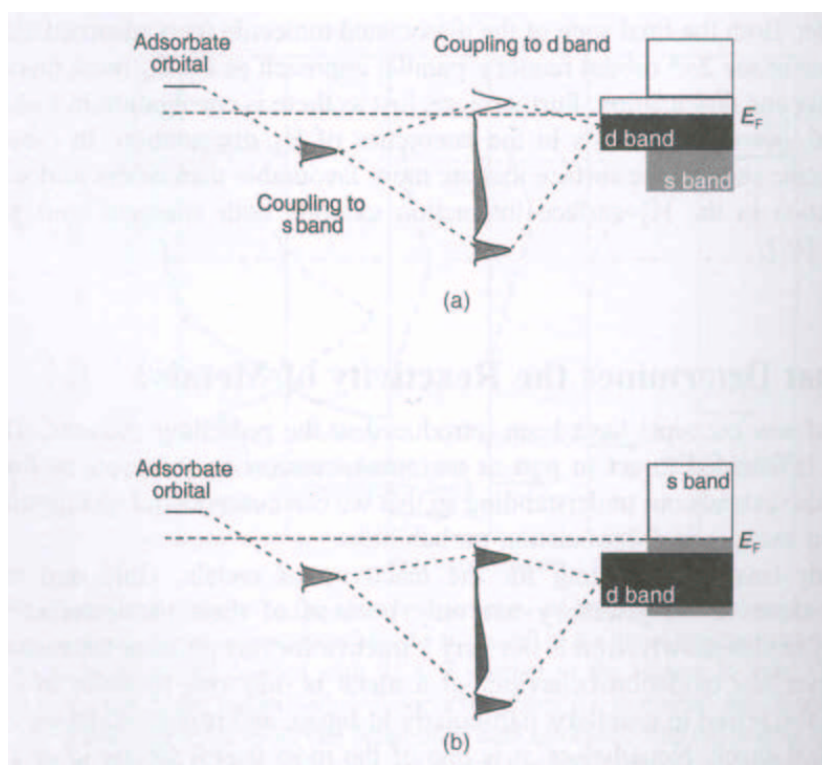


Figure 2.19: The two step concept of chemisorption on a transition metal surface. First the interaction with sp bands and then d bands. (a) Early transition metals ϵ_d is close to the Fermi energy and the antibonding orbitals lie above the Fermi Energy. (b) Late transition metals. In this case ϵ_d lies well below the Fermi energy. Figure adapted from [59]

most favorable adsorption orientation on Cu(100) is lying flat. A possible explanation is that the π orbitals of the phenyl ring can overlap easily with the d bands of the underlying Cu surface. Molecules containing two phenyl rings such as PVBA and PEBA show as well a preferential flat lying adsorption at surfaces like Pd(110) and Ag(111) [245, 246]. Nevertheless the argument that the π orbitals overlap with the surface bands is not always true. If, for instance, a N atom is included in the phenyl ring the situation. For e. g. for pyridine the most stable configuration on Au(111) is expected to stand upright [247]. Besides, some of big molecules including a big aromatic unit connected to different legs type molecules have been studied by using STM. For instance hexa-tert-butyl-decacyclene molecules (**HtBDC**) adsorbs with the main aromatic (π system) group parallel to the surface of Cu(110)[248] as well as Lander molecules do [249]. Also, the same molecule can have different restructuring adapting itself to different surface substrates as for tetra-3,5-di-ter-butyl-phenyl-porphyrin (**TBPP**) at Cu(100), Cu(111) and Cu(211) surfaces [250]. The former example clarifies how the presence of an aromatic (or more then one) ring is not a sufficient condition for flat adsorption.

Another well known process is chemisorbed induced dissociation. Hydrogen molecules are an example of well studied system which dissociate for the effect of the surface [251]. In fact, the presence of the surface not only causes a chemisorption process but, it also induce an electron transfer into the antibonding empty orbitals. The latter process results in a weakening of the interatomic bond strength which, in certain cases, breaks. Here below it would be important to know whether Cu(100) can break, at proper temperature, the OCO-H bond. This point will be addressed briefly in the next paragraph. However, it would be relevant to have access to calculations that addressed this point. Particularly, in this case, the dissociation process could be of dynamic nature.

Last, the diffusion of large molecule is scarcely studied in literature [252]. A number of studies using *Laser Induced Thermal Desorption*(**LITD**) have been carried on n alkane on Ru(0001) [252] demonstrating that the binding energy (0.48-0.65 eV) (of the adsorbed molecule) grows with the length of the molecule. Besides, it was proposed that the mechanism of diffusion of such molecules could follow a long jumps (40-50 Å) diffusion [253]. Very recently Schunack and collaborators [254] have analyzed the diffusion mechanism of two big molecules on Cu(110), decacyclene (**DC**) and hexa-tert-butyldecacyclene (**HtBDC**). They found in both case a long jumps mechanism for the diffusion though for **DC** (where π stacking still prevails [255, 256], the jumps amount to about 4 neighbor sites whereas for **HtBDC** they amount to 7 neighbor sites. Also the diffusion attempt frequency showed

a difference of four orders of magnitude between the two molecules. As studies of diffusivity were not accomplished for TMA on Cu(100), it is interesting to attempt a parallel with the former study. The DC is the molecule that is closer in shape to TMA, as it presents a flat aromatic multi ring adsorbing on the surface. However, DC does have some 7 phenyl rings. It is significantly larger than TMA and it is in theory not possible to draw any direct association between the diffusion of DC and TMA. Besides, studies of the diffusion of PVBA and C_{60} on Pd(110) [252, 173, 257] demonstrate that the prevailing mechanism for diffusion (for this molecule) is based on short jumps. Weckesser [173] determines the migration energy of PVBA on Cu(110) to be 0.83 eV and estimates the binding energy in about 2.8 eV. TMA is closer to the PVBA molecule in Shape. Accordingly (in a very first rough approximation) its dynamics on the surface is expected to resemble closer to the one of PVBA rather than DC.

2.7 Metal-organic Chemistry at metal surfaces under UHV conditions

Noncovalent interactions have been exploited to form self assembled nanostructures at different metal surfaces [40, 258, 259, 260]. Interactions such as dipole-dipole, Van der Waals, Hydrogen bonding have been proven to have magnitude comparable to chemisorption interactions[252]. The final stage of self assembling processes is the result of the competition between the afore mentioned surface adsorbate interactions and the adsorbate-adsorbate interaction[40, 261]. This type of interactions give assemblies that are weakly linked and inherently not very stable.

Metal-ligand interaction is one of the pillar of supramolecular chemistry[189]. Attempts to use this interaction for self-assembly at surfaces are restricted to a number of approaches at atmospheric pressure and few in Ultra high vacuum (UHV).

Metalorganic complexes have been deposited on metal surfaces through evaporation. A remarkable example of STM studied metal-organic molecules is the class of porphyrins [262]. Porphyrins are interesting to be studied as they are very well spread in biology and can act as catalysts. Particularly phtalocyanines have been used to identify different metals included in their hollow cavity [263]. Also, through the study of the tunnelling current at the metal site it was possible to distinguish between Cu(II) and Co(II) phtalocyanin deposited on Au(111) in UHV. There have been also several attempts to decouple the central metal atom of the phtalocyanine (described in [263])

from the surface. These attempts consisted in inserting appropriate legs into the macrocycle[264, 265]. The former studies were extended to STM investigation of Ni(II) /Co(II) tetrakis-porphyrin **TTBPP** [266, 267]. In these studies the two different chemical species Ni-**TTBPP** and Co-**TTBPP** were deposited on Au(111) at sub-monolayer coverage. The two macrocycles could be identified through difference in their respective tunnelling currents. The difference in the tunnelling current through the central metal atoms was observed, even though the metal atom in the center of the complex were decoupled from the surface. Very recently, complexes of Xe and Cu(II) Etiolporphyrin were formed directly in a UHV environment [268]. The authors use atomic manipulation to detach Xe atoms from the macrocycle after Xe deposition. The experiments were carried on Cu(100) and formation of Cu-Xe as well as Cu-Xe₂ were observed⁵.

The class of **diketonate** compounds are very common in the research area of electro luminescent solar cells thanks to their optical properties [271]. The structure of these complexes is such that the two oxygen atoms of the diketon molecule are bounded to a metal atom. The metal Oxygen bond is coordinative. In some cases the complexation cage of the metal is completed with further covalent bonding to multi ring pyridine compounds [272, 273]. The molecules are such that they provide a closed sheath for the ion inside. No particular functional groups can be attached to the outer part of the diketonate. The former implies that this class of molecules are not expected to form any supra molecular structure as the interacting chemical groups lie inside the compound. Octahedral coordination compounds with diketonate ligands have also been deposited on metal surfaces. As result of the adsorption process the ligand out of the surface plane is dissociated. Moreover the complexes on the surface do not tend to form any ordered supramolecular assemblies [274]. Besides, some studies have been preformed on **HOPG** in air by depositing Cu(II) diketonate [275]. The study was aimed at comparing topography and theoretical calculations.

The rare tentative to assemble supramolecular structures comprising metal organic complexes involves mostly the use of hydrogen bonding through different complexes [261]. Supramolecular aggregates of transition metal complexes on metal surface in UHV conditions have been achieved by deposition of Bis terpyridine derivative octahedral complexes of Co and Zn on **HOPG** [276, 277, 278]. However this case accounts also for lateral hydrogen bonding linkage among Bis terpyridine derivative ligands. The lateral linkage results in supramolecular aggregates linking single complexes. The cases listed above

⁵Some other exotic studies on the formation of water and other monolayer have been reported too [269, 270].

reckons in a quite restrict scenario in the use of coordinative interaction to build nanostructures at surfaces. The case of Chemical Vapor Deposition (**CVD**) in UHV conditions, considering a huge number of applications in microelectronics is not included here. In the cases above mentioned, the oxidation state of the central metal atom is known, as the metal atom is part of a complex prepared outside the UHV environment. By contrast, in the case described in the next paragraphs, the metal atom within the complexes interacts with the surface. As result the oxidation state cannot be unambiguously determined.

2.8 Chemistry of carboxylic acids at metal surfaces

The chemistry of carboxylic acids on Copper, Palladium and Nickel has been the object of some experimental studies due to the interest towards the catalytic properties of these metal surfaces [279, 182, 183]. Also, early studies of carboxylate formation on copper were motivated by the intent of understanding the bonding structure of polyimide precursors [280, 281]. The goal of these studies was to grow ordered monolayers through CVD. Only recently carboxylic bonding has been used to build nanostructures at surfaces exploiting directly their ability to form coordinative bonds [42, 166].

Previous studies of benzoate at Cu(110) and Cu(111) [184, 282, 183], acetate on Cu(110) [283, 284], formate on Cu(100) and Cu(110)[285], have elucidated that the carboxylic group of the carboxylate species tends to interact either with the surface or with the self diffusing Cu adatoms.

Particularly relevant to this work are the previous studies on the behavior of benzoate at Cu(111) and Cu(100) investigated by STM imaging, **HREELS** (*High Resolution Electron Energy Loss Spectroscopy*) and **RAIRS** (*Reflection adsorption infrared spectroscopy*) [184]. These studies have established a relationship between the surface and the type of adsorption. The benzoate species adsorbs always in the upright standing configuration at Cu(111)⁶. However, at Cu(110) the benzoate species is flat lying even at temperature above 300 K. As benzene is known to desorb on this surface at below room temperature [286] the π orbitals surface interaction alone cannot account for the stability of the flat lying benzoate. However two different explanations have been provided for the benzoate adsorbed on Cu(111) and on Cu(110). It is suggested that on Cu(111) the benzoate is upright standing (Fig. 2.20) with the two oxygen of the carboxyle group linking to two adjacent Cu

⁶At least in the temperature interval addressed in the study

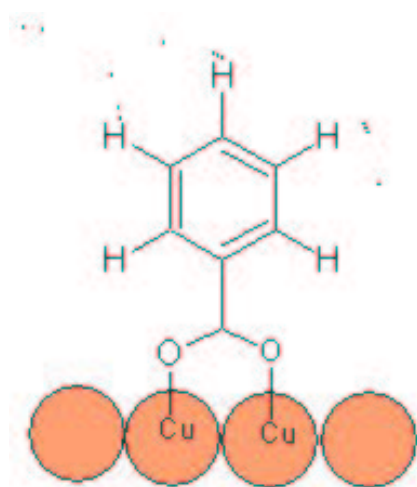


Figure 2.20: *Scheme of the chemisorption geometry of benzoate at Cu(111)*

atoms of the substrate. In this configuration the carboxyle moiety results deprotonated. Besides, theoretical calculations and experimental evidences indicate that the preferred chemisorption configuration for carboxylate at Cu(100) consider the two oxygens bridging two adjacent atoms [287, 288]. The chemisorption energy of the carboxylate adsorbed on Cu(100) amounts to 2 eV. The study reported by Perry and coworkers does not reveal any detail on the mechanism of deprotonation for the chemisorbed benzoic acid [184]. However it will be explained below that this mechanism may be relevant to interpret the results presented in the following sections. In the case of benzoate formation on Cu(110) it was proposed that the carboxylate lies flat on the terrace because dimers are formed with Cu adatoms self diffusing from the step edges into the flat terraces, at appreciable temperature. The dimer is depicted in Fig. 2.21. Copper surfaces are known to give rise to an equilibrium between atoms diffusing from the step edges into flat terraces and viceversa [185, 181, 289]. The mechanism of surface diffusion is different for Cu(100) from the (111) and (110) surface. In the latter an exchange mechanism is foreseen [185, 181], while in the former a simple hopping mechanism is expected. There is no clear evidence whether this difference can provide a different behavior of Cu(100) in the process of deprotonating the carboxylate moiety. However the free energy of adatom formation is expected to be the relevant parameter [184, 290] in governing the self diffusion process at Copper surfaces as long as entropy contribution due to lattice vibration can be neglected [179]. According to the calculation by Hansen and Coworkers [290] the amount of self diffusing Cu atoms on Cu(110) is 500 times higher

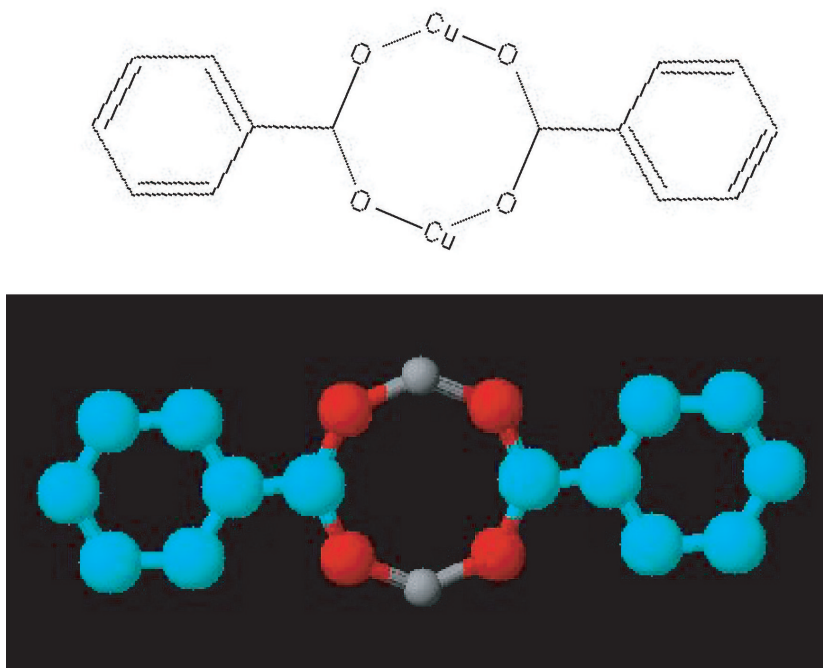


Figure 2.21: *Cu benzoate dimer formed on Cu(110)*

than on Cu(100) and 10000 higher than on Cu(111)⁷. These numbers explain why benzoate lie flat at Cu(110) and are upright standing on Cu(111). In fact, on the first surface there are enough Cu adatoms available for lateral linking to carboxylate moieties whereas, on the latter surface, the amount of self diffusing Cu adatoms cannot account for a lateral carboxyl linkage. Also, the upright standing benzoate is found with the phenyl ring oriented in plane with the carboxylate moiety, as this is the most stable configuration. This picture is quite consistent with experimental observations although it explains very little about the process of deprotonation and the stability of the deprotonated molecule.

The study of the adsorption of TMA on Cu(100) was performed by Dimitriev and coworkers [41]. At low temperature the TMA molecules were found to give rise to a honeycomb structures. The structures were held together by hydrogen bonding. The TMA molecules lie flat on the surface. The distance between two oxygen of two next molecule is about 3.7\AA about 1\AA larger than in normal hydrogen bonded 3d carboxylate solids. This indicates that substrate-adsorbate interaction (π stacking) are still the most relevant

⁷The temperature dependence of this process is relevant. As the number of self diffusing adatoms depends exponentially on the related free energy, this effect is suppressed at low T.

interaction due to the adsorption energies of some of eV ($2 \div 2.5$). However, as the temperature increases to the room value, a new ordering phase takes place. Long stripes are imaged in four different directions indicating that a different adsorption configuration takes place. In this case the TMA molecules are adsorbed in the upright standing configuration. The authors mention that in this configuration all the three carboxylate moieties are still free to rotate with respect to the axis going from the carbon on the carboxyl group to the carbon on the phenyl ring.

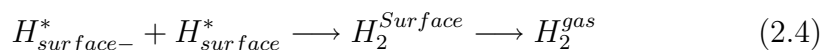
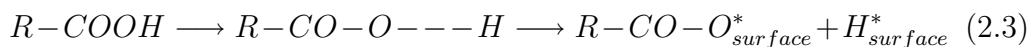
At higher temperatures Lin and coworkers report [42] the set in of a new species. The TMA molecules are found flat again. Complexes of Cu and four TMA molecules are clearly imaged on the flat terraces. As for the case mentioned in [184], the amount of self diffusing Cu atoms rises considerably and the molecules are able to link laterally to them. The study conducted by Lin [42] is the first direct evidence of formation of coordinative bond at metal surface. Nevertheless, the bond energy estimated from the life times of this complexes results to be about 0.31 eV⁸ which is considerably smaller than coordinative bonding energies (1-3 eV) [291]. Besides, the O-Cu bond length is estimated to be about 3 Å, appreciably longer than in normal Cu carboxylate (about 2 Å). These dates show that even in this case the adsorbate-substrate interaction is predominating with respect to the adsorbate-adsorbate interaction. In fact a rough estimation of the adsorbate binding energy can be done by the cohesive energy that is 3.49 eV in the bulk Cu. On the flat terraces the Cu adatom has 4 neighbors and counts a binding energy of about 1.2 eV that is still much larger than the one reported by Lin [42] for the copper complexes. Besides the life time of a single complex is about 35 s. Monitoring the process of formation and dissociation of complexes Lin finds that TMA molecule tends to return to their preferential adsorption site at the hollow site of the Cu(100) substrate, indicating again that the adsorption energy of TMA molecule is of magnitude comparable or higher than the complex formation energy. As it will be seen in the following this scenario is much different in the case of Fe, as coordinative bonding seems to be more pronounced with respect adsorbate-substrate interaction in copper TMA complexes.

An important point that is not addressed by Lin and Coworkers [42] is whether the TMA molecules offer really three deprotonated moieties to the Cu atoms or not. There are three different processes in the deprotonation that can be envisaged. The experiments conducted by Perry [184] on benzoate deposited on Cu(111) demonstrate that when the thermal energy is sufficiently high to break the π – *interaction* between the phenyl ring and the substrate the

⁸The rotation barrier is also included in this value

molecule is free to rotate out of the surface plane. In this process the p orbitals on the O linking the H atoms overlap more consistently with the d electrons of the Cu surface atoms. The surface atoms have 9 neighbors against the 12 in the bulk. This means that they are less coordinated and offer still some sharp localized d orbitals along the z axis. Because of the spherical symmetry of the s orbitals, the hydrogen atom can still bond to the oxygen atom even though the molecule is tilt towards the upright standing position. Accordingly, while the molecule reaches the upright standing position the overlap between the p orbitals on the O atom and d bands of the surface increases. The overlap between the s orbitals of H and the d Cu surface atoms orbitals increases as well. This possible mechanism accounts for a charge transfer in the O-H bond which ultimately results in the break of the O-H bond with the formation of O-Cu and H-Cu bonds. In this way, a thermal activated surface dissociative chemisorption is suggested. In fact, the thermal energy at room temperature amounts to 25 meV, a value which could not support a direct thermal dissociation of the O-H bond, which is weak but still considerably stronger than 25 meV. However, 25 meV is the order of magnitude of rotation excitation at low J. The mechanism proposed could also explain the results achieved by Dimitriev on TMA [41] at room temperature. The Cu(100) surface atoms have 8 neighbors and the comments outlined before are still valid. The TMA molecule are found to stick in the upright position at room temperature and no conclusion can be drawn on the other two carboxylic groups. However, in the study by Lin [42] it is suggested that all the three carboxylic groups of the TMA molecule are deprotonated. In solution the process of successive deprotonation accounts for an increase of the electrostatic energy on the molecule. On the surface the atoms underneath the molecule can stabilize the electrostatic charge though the deprotonation of three carboxylic groups requires a mechanism that cannot be simply thermal vibration. Remarkably, vibrations are excited at high temperature.

A second possibility to explain the process of deprotonation could consist in a thermal induced chemical bond distortion. In this view the C-C-O-H bridge can bend towards the surface in way such that the overlap between the O p orbitals and the d surface orbital increases. In this fashion the sp electrons could provide enough charge to break the O-H bond. As result the O atom will bridge to the surface and the H will be diffusing on the surface. It will eventually recombine with another H and desorb as H_2 . The two processes can be schematized in the following equations:



This process implies that the thermal energy should compensate the distortion energy associated with the bending of the C-C-O-H bridge and the energy spent in loosening the phenyl ring surface bond. Also, the process outlined here does not account for an ionization of the H atom but, rather for a dissociation. Dissociation seems to be a much likelier process than ionization. Besides, if the process outlined above was true the actual mobility of TMA molecules after deprotonation should be sensibly reduced as the amount of chemisorption energy per chemical bound is roughly 2 eV resulting in a 6 eV total chemisorption energy. Weckesser [173] reports the migration energy for PVBA molecule. He estimates this value to be about the 30 % of the binding energy. If the same criteria is applied to TMA, a quite high migration energy for TMA molecules at room temperature would result. However, the experimental evidence at low coverage demonstrates that molecules are still quite mobile on the surface.

Alternatively a third possible mechanism, attempting to explain the process of deprotonation at Cu(100) can be based on a simple picture of adsorbate induced dissociative chemisorption. Because of its reduced coordination the Cu adatom on the surface has a lower binding energy (roughly 1.15 eV) and a sharper d band localization. The former makes the Cu suitable for chemisorbing adsorbates. Particularly the in plane d orbitals are readily available for superposition with the p orbitals of the O atom without that any structural reordering takes place inside the TMA molecule. Furthermore, as the H atom has s spherical symmetric orbitals it can easily bond to a Cu surface atom. In this picture a Cu adatom meeting a TMA molecule on the surface, tends to interact with the O atoms weakening the O-H bond. sp electrons can provide enough charge to break the O-H bond whereas the H atom can easily attach to a Cu surface atom and eventually recombine somewhere else, on the surface, with another H atom. This picture clearly accounts for a dynamical vision of the deprotonation process. The presence of a Cu adatom becomes compulsory for the deprotonation process to take place. In this respect the hypothesis of Lin and Coworkers [42], three deprotonated carboxylic moieties, may not correspond to the reality. In fact if a Cu atom is indispensable for the deprotonation process and as the Cu complexes do not evolve in supramolecular structures, then the carboxylic groups not involved on the Cu-O bond are not deprotonated. Fig. 2.22 shows the complexes reported by Lin [42] alongside a model. It is remarkable that no longer ordering is observed even upon annealing for Cu complexes as shown in Fig. 2.22 c). This fact is different with respect to the Fe case that will be described in the next chapters. The process of deprotonation is extremely relevant for interpreting the findings in the case in which Cu is substituted with Fe. It is likely that the Fe adatom induces the O-H dissociation pro-

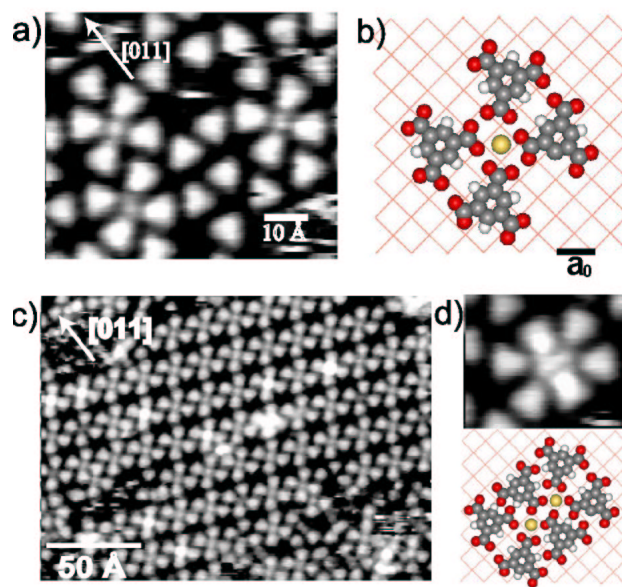


Figure 2.22: *Content: a) Detail of four member copper complexes $\text{Cu}[\text{TMA}]_4$. b) Model for $\text{Cu}[\text{TMA}]_4$. c) Four members copper complexes predominate at surfaces. No long range ordering is observed. d) Copper dimer $\text{Cu}_2[\text{TMA}]_4$ [42]*

cess in a much more robust way than Cu does resulting in a multiple linkage configuration which comprises more than one carboxylic group per molecule bound to a Fe atom at Cu(100).

The carboxylic group can bridge metal atoms in two different configurations, monodentate and bidentate, it turns to be a flexible building block for metalorganic synthesis. The threefold symmetry of the TMA molecule is particularly suited to build a number of different organometallic networks by varying the ratio between the metal and the ligand concentration [292]. On the surface the concentration of metal and ligand is defined as percentage of monolayer, respectively $[\text{L}] = 0.63$ molecules per nm^2 for the ligand and $[\text{M}] = 16$ Fe atoms per nm^2 for the metal. In UHV condition the surfaces are clean and atomically flat, no oxide or impurity layers are present. The presence of a 2D confined environment accounts for increasing steric effects connected to the absolute amount of ligand $[\text{L}]$ present on the surface. In the following, it will be described that the variation of the ratio $\frac{[\text{M}]}{[\text{L}]}$ is crucial to achieve different type of nanostructures at surfaces.

2.9 Metal-organic Synthesis at surfaces: first results

In this paragraph it is briefly described as the deposition of Fe drastically modifies the scenario described by Lin [42].

Fig. 2.23 (a) shows a typical image of the resulting scenario after Fe and TMA codeposition. Deposition is carried out at low T (100 K). There are no data revealing whether Fe is free to migrate on the Cu surface at this deposition temperature (100 K). However, comparison with Co adatoms indicates that Fe adatoms are presumably mobile on the surface upon deposition. In the examined case the Fe coverage is quite high reaching half monolayer ($[M] = 50\%$). Under the given conditions, Fe is expected to diffuse at step edges during deposition. Nevertheless, as the concentration is high, it is also possible that Cu adatoms are pumped from the step edges into the surface terrace forming small intermixed islands as reported by Dulot [186]. Fig. 2.23 (a) clearly illustrates that TMA molecules are immobilized on the surface accounting for disordered 2D structures. If the sample is annealed at 400 K, the 2D structures show a certain degree of reordering as outlined in Fig. 2.23 (b) and (c). If the order of TMA and Fe deposition is changed then it is expectable that TMA will partially inhibit the migration of Fe atoms at the step edges and generally affect its migrating dynamics. In Fig. 2.24 (a) it is shown the result of this operation. The TMA islands seem to be covered with some Fe. This may be the result of the high amount of Fe dosed ($[Fe] = 130\%$). However, even in this case annealing seems to produce a reordering of the structures as can be seen in In Fig. 2.24 (b).

In the cases illustrated so far, the ratio $\frac{[M]}{[L]}$ is quite high, 5 and 13 respectively, resulting in a strong probability that all the three carboxylic groups on the TMA molecule can be linked to diffusing adsorbates (Fe and Cu). If this ratio is further reduced (Fig. 2.24 (c,d,e,f)) to values close to $3 \div 1$ a similar scenario rises. In spite of the lower $\frac{[M]}{[L]}$ ratio, TMA molecules are still well anchored at the surface. In this case, annealing provides a quite interesting scenario where 2D disordered assemblies still prevails. Nonetheless, it is possible to recognize a tendency to form ordered 1D structures both close to the step edges Fig. 2.24 (c) and on the flat terraces Fig. 2.24 (e). This tendency to local order is also confirmed if the order of TMA and Fe deposition is changed as outlined in **Fig 2.24 (f)**.

It is possible to try to tune the ratio $\frac{[M]}{[L]}$ within the same experimental session although, the instrument characteristics do not enable the operator to perform deposition of the 2 adsorbates at the same time. Also, in UHV conditions, the surface requires preparation after 10-12 hours of investigation.

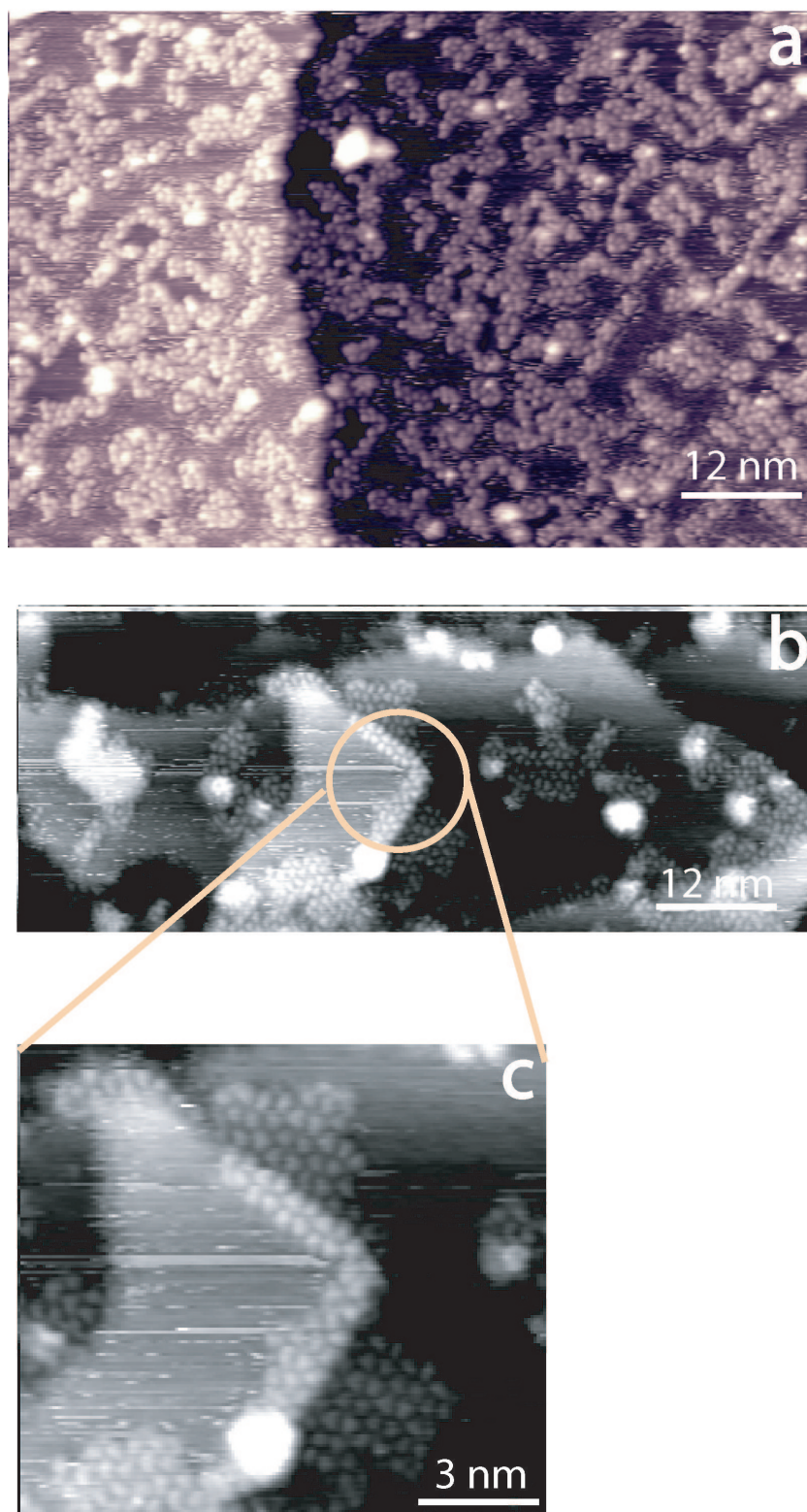


Figure 2.23: **(a)** Disordered 2D Assemblies. Substrate deposition temperature $T_s = 100\text{K}$, measured at 300 K. Deposition order Fe first then TMA. $[L]=43\%$ $\frac{[M]}{[L]}=5$. **(b)** Sample annealed to 400 K:reordering of the 2D structures induced by annealing. **(c)** Detail of the reordered assemblies at the step edges.

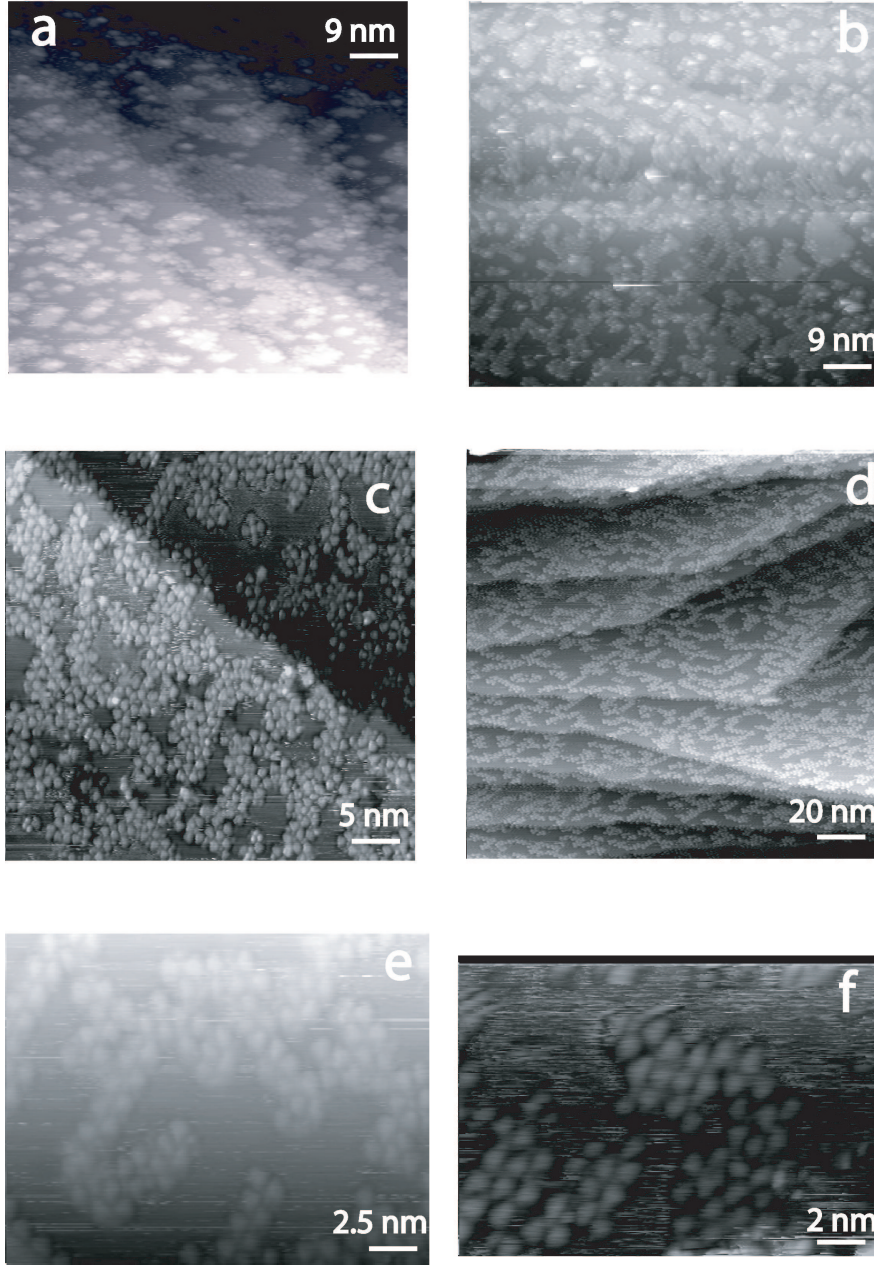


Figure 2.24: **(a)** Overdosing Fe. Substrate deposition temperature $T_s = 100\text{K}$. Deposition order TMA first then Fe. $[L] = 43\%$ $\frac{[M]}{[L]} = 13$. **(b)** Inducing reordering. Sample as in **(a)** annealed to 450 K . **(c)** Short range post annealing induced order. Substrate deposition temperature $T_s = 108\text{K}$. Deposition order Fe first than TMA . $[L] = 43\%$ $\frac{[M]}{[L]} = 1.5$. **(d)** The same as in **(c)** in a larger scale. **(e)** Detail of an chain. Same conditions as in **(c)**. **(f)** Inverting deposition order. Substrate deposition temperature $T_s = 100\text{K}$. Deposition order TMA first then Fe. $[L] = 43\%$ $\frac{[M]}{[L]} = 1.6$. Sample annealed to 450 K

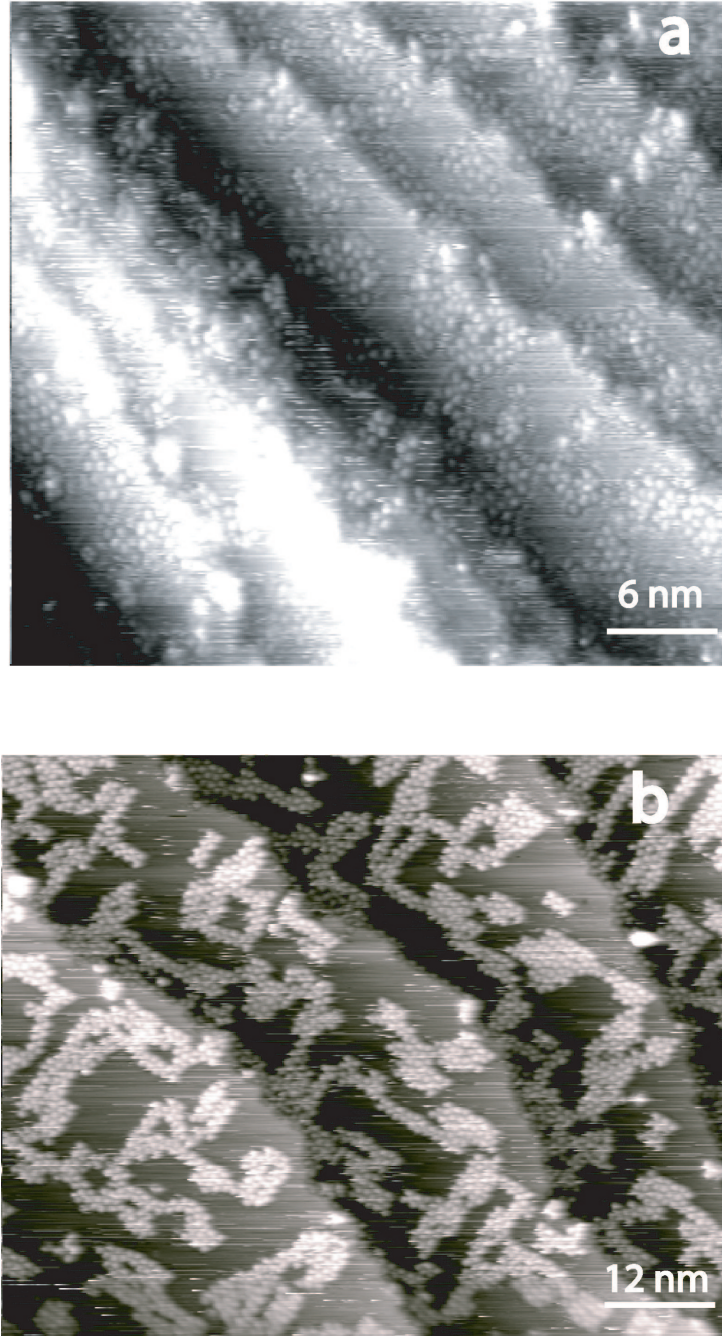


Figure 2.25: **(a)** Disordered 2D Assemblies at the step edges. Substrate deposition temperature $T_s = 108K$. Deposition order Fe first then TMA . $[L] = 43\%$ $\frac{[M]}{[L]} = 0.4$. **(b)** Effect of combined annealing and further Fe room temperature deposition. Substrate first deposition temperature $T_s = 100K$. Deposition order TMA than Fe $T_s = 300K$. $[L] = 43\%$ $\frac{[M]}{[L]} = 2.4$. Sample annealed to 400 K .

The former hinders the possibility of many depositions during the same experimental session. However Fig. 2.25 illustrates an attempt to control $\frac{[M]}{[L]}$ within the same day. As a result ordered structures appear on the surface Fig. 2.25 (b). They are easily imageable signaling that most of the TMA molecules are fixed and included in these structures. The structures are randomly distributed on the surface. They account for closed structures and for a number of long 1D aggregates. The latter features indicate the presence of coordinative bonding within the structure. In fact the directionality and the high stability of these structures can be explained only by accounting for a strong directional interaction among the molecules. As Dimitriev [41] finds completely different ordering at the same temperature for TMA deposited on Cu(100), it is understood that in the present case Fe must play a relevant role in the formation of the assemblies being described.

If the process of deposition is carried at room temperature for both adsorbates there are substantially no different changes in the results as shown in Fig. 2.26. Nevertheless in this case, the ligand coverage is quite high ($[L]=67\%$) and the steric hinderance can play a crucial role in the ordering of these structures. Moreover, the ratio $\frac{[M]}{[L]}$ is quite reduced to 0.4. The former value indicate that the amount of Fe on the surface is not sufficient to link laterally all the carboxyle moieties present.

As last preliminary result, Fig. 2.27 shows how at low $\frac{[M]}{[L]}$ it is possible to observe the formation of isolated species, similar to the Cu-TMA complexes reported from Lin [42]. These species evolve eventually, upon further deposition of Fe and annealing into 2D structures.

As summary the presence of Fe on the surface drastically modifies the scenario inspected by Lin [42]. A new type of ordering seems to emerge. Annealing seems to induce long ordering rearrangement. The ratio $\frac{[M]}{[L]}$ seems to control the lateral linkage of the TMA molecules whereas $[L]$ tends to control the steric hinderance (as it will be seen in the following also the chemical activity). In the following, it will be shown how the accurate control of all these parameters alongside with the choice of the appropriate metal atom can lead to nicely ordered 0D, 1D and 2D supramolecular structures.

2.10 Metal-organic Synthesis at surfaces: Mononuclear complexes

In this section it will be described the self assembly of mononuclear complexes as well as the behavior of adsorbates at the step edges.

As a result of deposition step edges are decorated with TMA molecules or

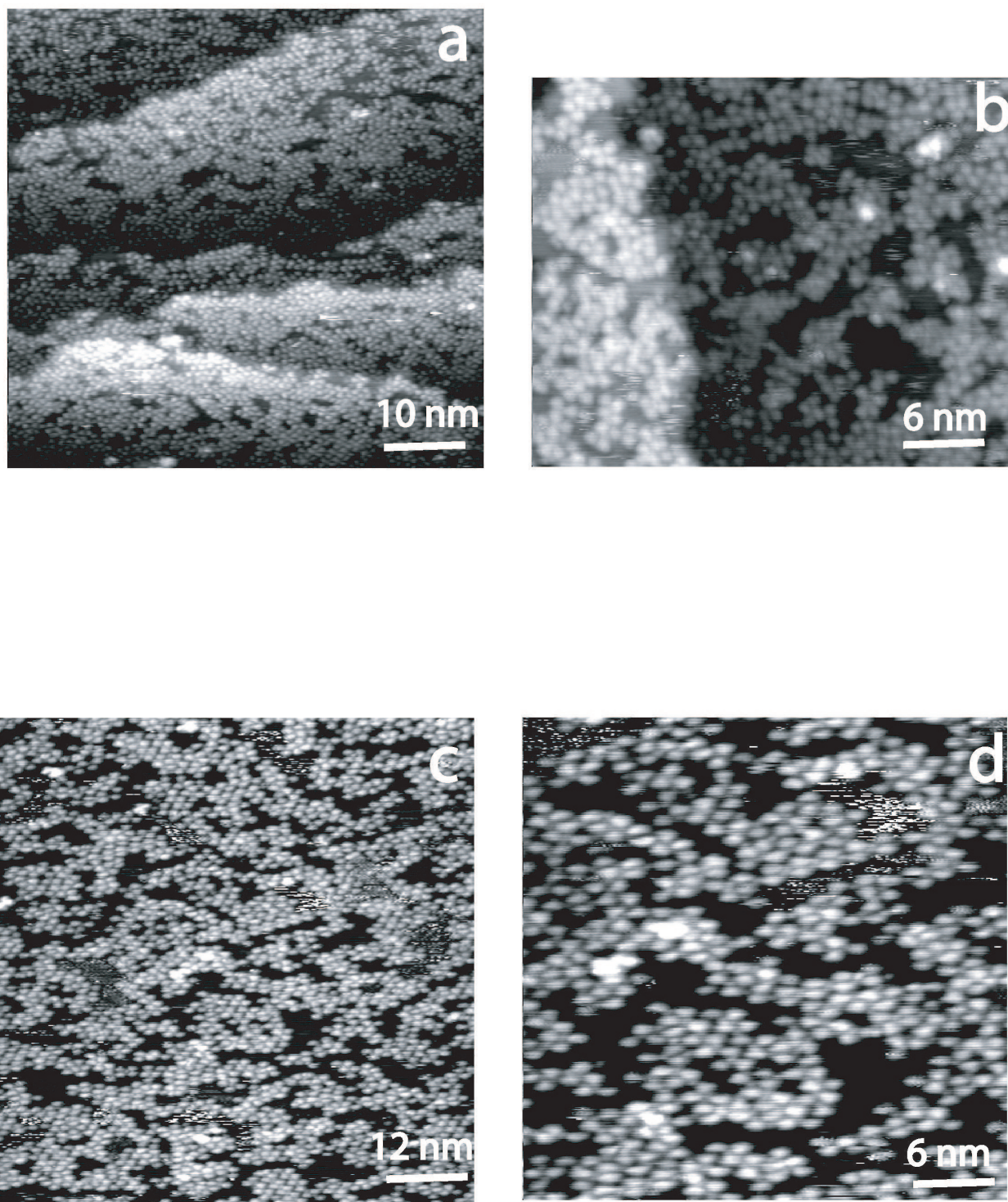


Figure 2.26: Adsorbates deposited at room temperature (a) Substrate deposition temperature $T_s = 300K$. Deposition order TMA first than Fe. $[L] = 67\% \frac{[M]}{[L]} = 0.35$ (b) Zoom in from a. (d) Sample annealed to 400K (d) Zoom in from c

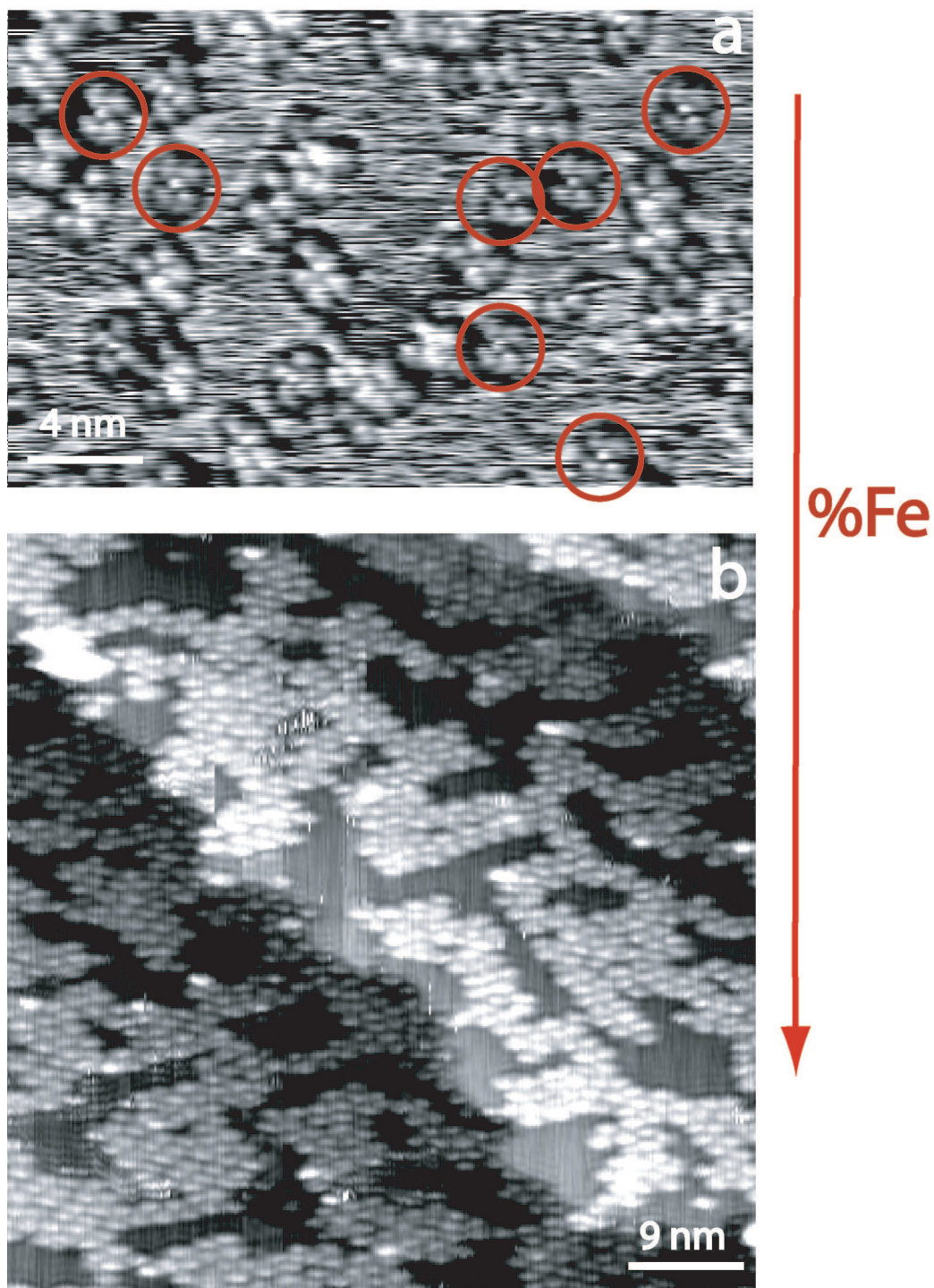
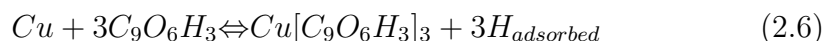
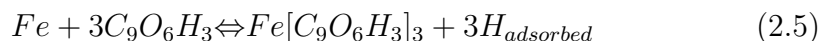


Figure 2.27: **(a)** Mononuclear complexes. Substrate deposition temperature $T_s = 100\text{K}$. Deposition order Fe first then TMA . $[L] = 57\% \frac{[M]}{[L]} = 0.19$. **(b)** Further Fe Deposition $T_s = 300\text{K}$. $[L] = 57\% \frac{[M]}{[L]} = 0.5$. Sample annealed to 400K

mostly with a species composed of three TMA molecules and possibly one Fe adatom. Fig. 2.28 illustrates the decoration of the steps at different conditions. At low TMA coverage (Fig. 2.28 **a**) the steps result mostly decorated with TMA molecules. The density of molecules at the steps is sensibly higher than the one reported previously in [41, 42]. This is presumably an effect induced from adsorbed Iron on Cu(100) step edges. In fact, Fe may diffuse at the steps and eventually offer a strong anchor site for the TMA molecules. The dense step edges decoration also support the crucial observation that Fe seems to bond TMA molecules more effectively than Cu. This signals an increased strength of the chemical bond for Fe-TMA in comparison with Cu-TMA.

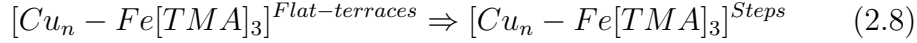
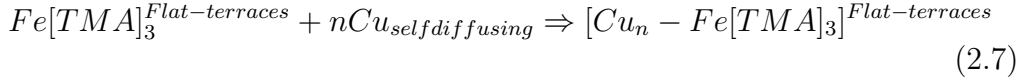
When the TMA coverage becomes appreciable ($[L] \geq 40\%$) step edges become decorated with a new species $Fe[TMA]_3$ Fig. 2.29 offers a close view of this type of structure. The presence of these species does not seem to be drastically affected neither by the sequence of TMA and Fe deposition nor by the substrate deposition temperature ($100K \leq T_s \leq 300K$). Also, the overall coverage $[L]$ as well as the ratio $\frac{[M]}{[L]}$ tend to be ineffective with respect to the presence of mononuclear $Fe[TMA]_3$ complexes as it can be inferred from the analysis of Fig. 2.28 and 2.29. These experimental findings demonstrate that the species $Fe[TMA]_3$ is quite stable and may represent a first crucial step in the development of structures of higher complexity. As stated before, on the surface there are diffusing Fe adatoms. In principle the three member complexes may be associated with two different chemical reactions 2.5:



For the reasons stated above it is suggested that the protrusion appearing in the center of the three member complexes would be Fe. Moreover, as it will be shown below, it is possible to carefully correlate the amount of Fe deposited with the number of another chemical species appearing at the flat terraces. These results indicate that the substrate protrusion seen in the images presented is Fe. Another relevant observation is that the presence of $Fe[TMA]_3$ complexes at the step edges is associated with the formation of kinks. This implies that some form of copper transportation should take place. There are two possible explanations for this process. As observed recently by Rosei [293] large molecules can capture self diffusing adatoms and create templates at the step edges. If it was assumed that free member complexes are three to move at flat terraces⁹ then, it may be possible for

⁹mobile adsorbates cannot be imaged with the STM and their presence is indicated from spikes in the tunnelling current

the complexes to transport self diffusing Cu adatoms to the step edges. This process can be simplified in the following equations:



Alternatively, the Fe atoms once bound to the TMA molecules anchored to the steps, drags it to form the complex. In this process the TMA molecule can itself drag labile Cu atoms from the step edges and induce the formation of kinks. The data shown cannot actually distinguish between these two cases. Accordingly it is not possible to draw the conclusion that there are $Fe[TMA]_3$ complexes on the flat terraces. It is suggested that a low temperature observation of the overall scenario may shed light on these issues. As a matter of fact, at low temperature even the more mobile isolated adsorbates stick on the terraces and inherently they become visible to the tip of the STM microscope.

As described in paragraph 2.9 at high values of the ratio $\frac{[M]}{[L]}$ TMA molecules tend to stick appreciably strongly at the surface developing 2D networks of well anchored molecules. This phenomenon is understood as a progressive engagement of the carboxylate moieties in later linkage with diffusing Fe adatoms at the surface. Accordingly the possibility of building mononuclear complexes at appreciable values of $\frac{[M]}{[L]}$ seems to be hindered.

In view of this effect of multiple lateral linkage, the ratio interval $0.04 \leq \frac{[M]}{[L]} \leq 0.8$ has been investigated in order to seek for mononuclear complexes at flat terraces. This investigation turns out to be difficult at room temperature as a number of adsorbates are still mobile producing spikes in the tunnelling current. Fig. 2.30 shows a typical scenario at $\frac{[M]}{[L]} = 0.25$. A species characterized from a protrusion in the middle surrounded from four TMA molecule predominates at flat terraces. This species is thermodynamically stable over different STM scans and upon annealing. The former $Cu[TMA]_4$ property is strongly different than for the mononuclear complexes presented by Lin [42]. In order to carefully associate the protrusion in the middle of the complex with Fe adatom, the determination of the number of complexes per unit area has been carried out. Several images were taken for each value of $\frac{[M]}{[L]}$ in the given interval. The images were taken on surface spots of $35 \times 35 nm^2$ at different locations. The former enables for a statistical average of the results. Fig. 2.31 illustrates the coverage of the flat terraces at different values of $\frac{[M]}{[L]}$. However, Fig. 2.32 reports the distribution of complexes on the surface as function of the nominal number of Fe adatoms deposited on the surface. The graph in blue shows the average number of complexes imaged per sur-

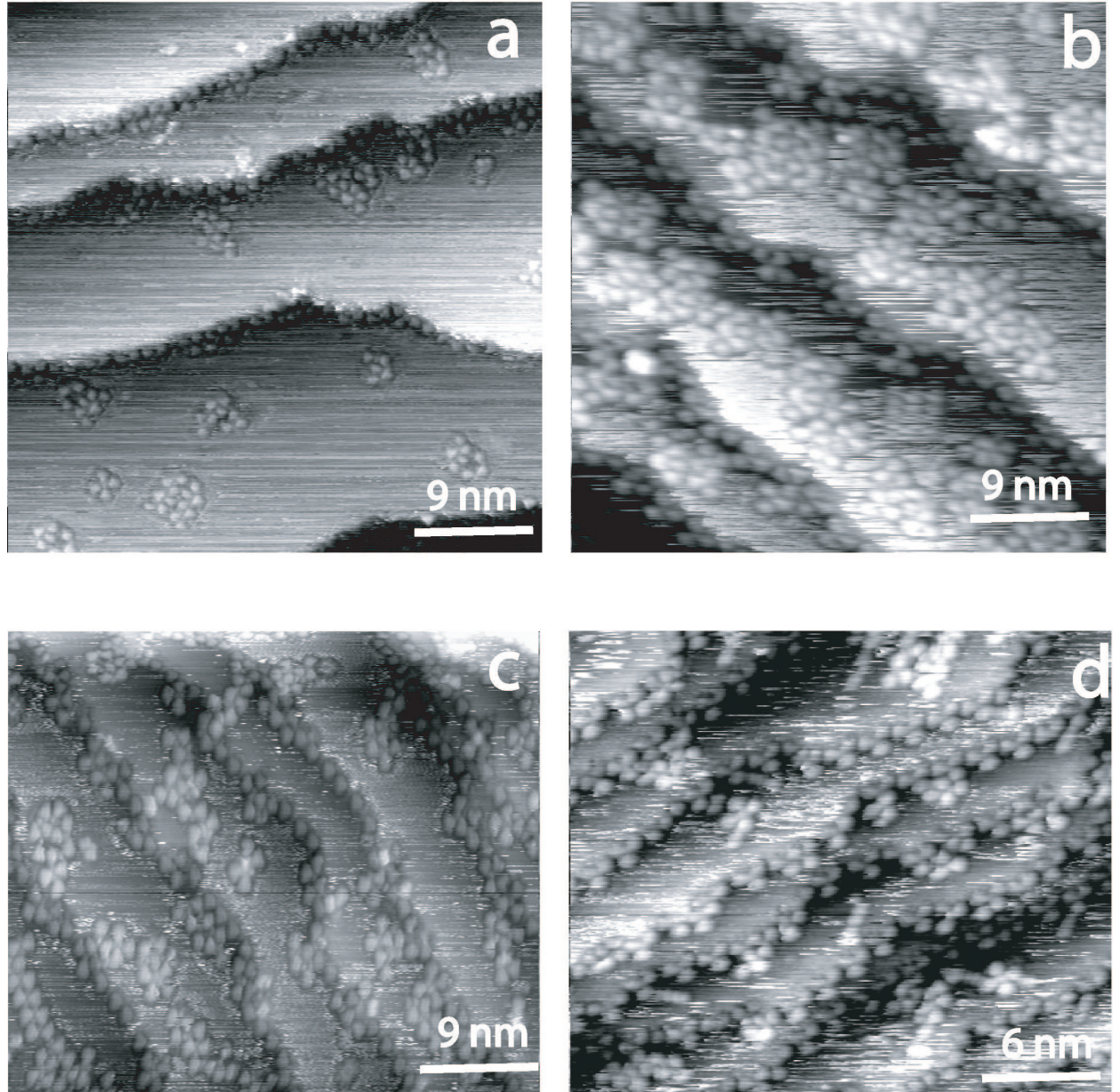


Figure 2.28: *Decoration of step edges (a) Substrate deposition temperature $T_s = 107\text{K}$. Deposition order Fe first then TMA. $[L] = 14.5\%$ $\frac{[M]}{[L]} = 1.25$ (b) Substrate deposition temperature $T_s = 100\text{K}$. Deposition order Fe first then TMA. $[L] = 43\%$ $\frac{[M]}{[L]} = 2.4$. (c) Substrate deposition temperature $T_s = 107\text{K}$. Deposition order TMA first then Fe. $[L] = 57\%$ $\frac{[M]}{[L]} = 1.5$ (d) Substrate deposition temperature $T_s = 117\text{K}$. Deposition order Fe first then TMA. $[L] = 43\%$ $\frac{[M]}{[L]} = 1$ Sample annealed to 400K for 15min .*

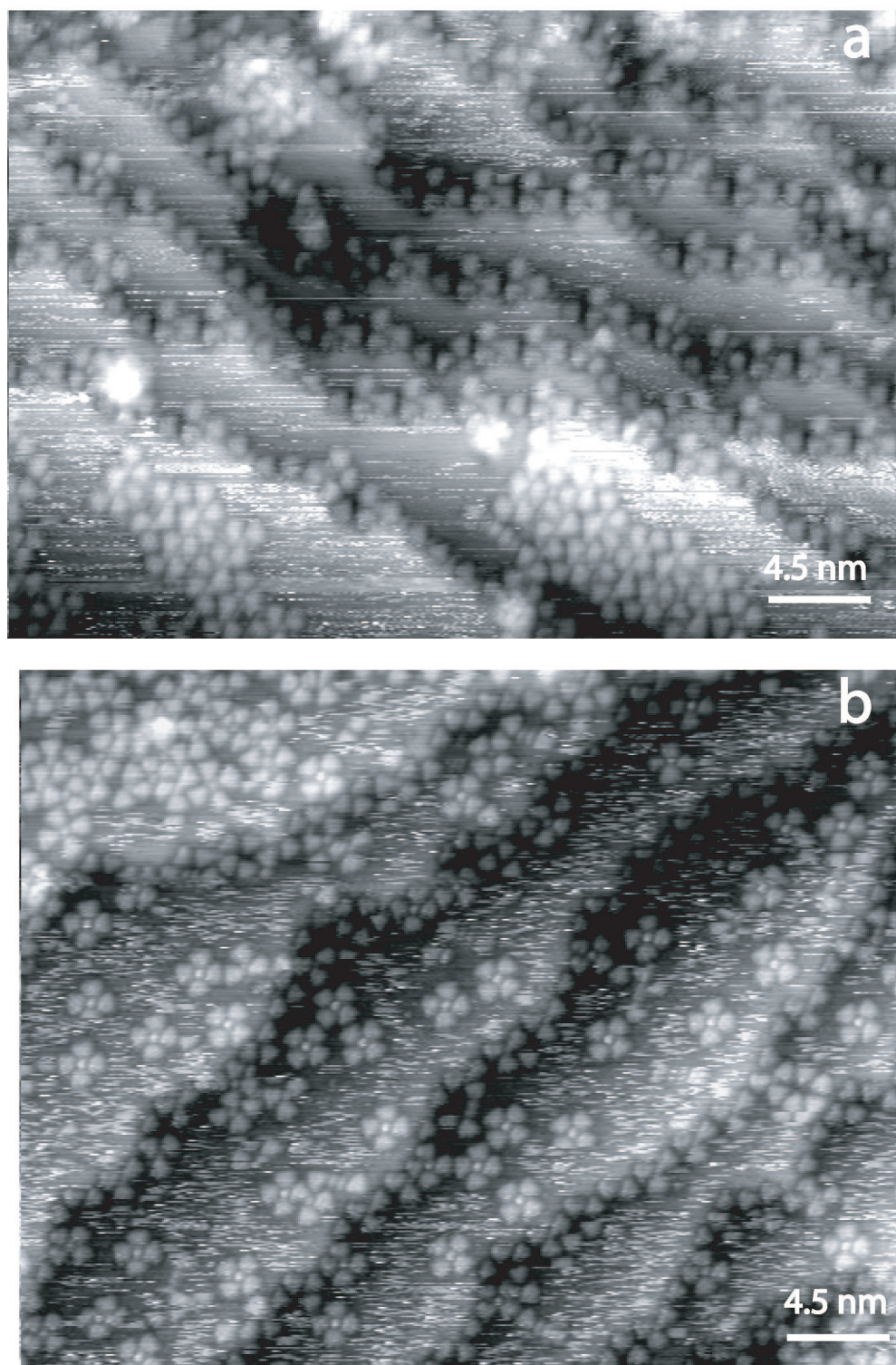


Figure 2.29: Mononuclear three member $\text{Fe}[\text{TMA}]_3$ complexes at the step edges **(a)** Substrate deposition temperature $T_s = 106\text{K}$. Deposition order Fe first then TMA. $[L] = 43\%$ $\frac{[M]}{[L]} = 0.8$ **(b)** Substrate deposition temperature $T_s = 300\text{K}$. Deposition order TMA first then Fe. $[L] = 86\%$ $\frac{[M]}{[L]} = 1.6$.

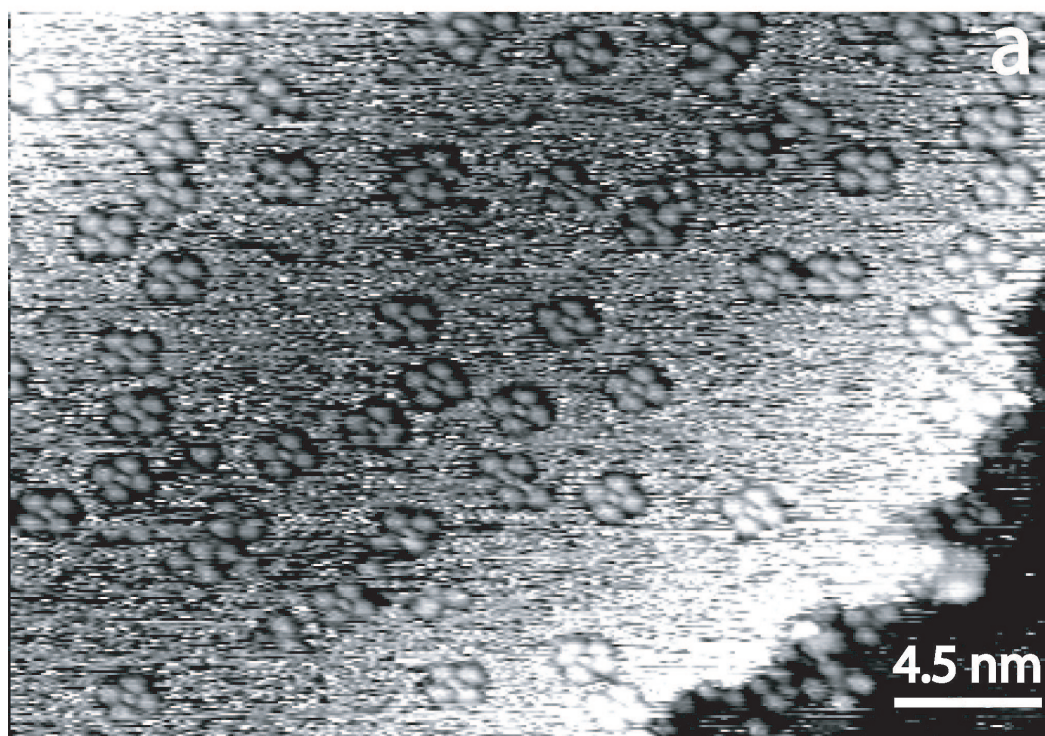


Figure 2.30: Mononuclear four member $Fe[TMA]_4$ complexes at flat terraces (a) Substrate deposition temperature $T_s = 102K$. Deposition order Fe first then TMA. $[L] = 43\%$ $\frac{[M]}{[L]} = 0.25$

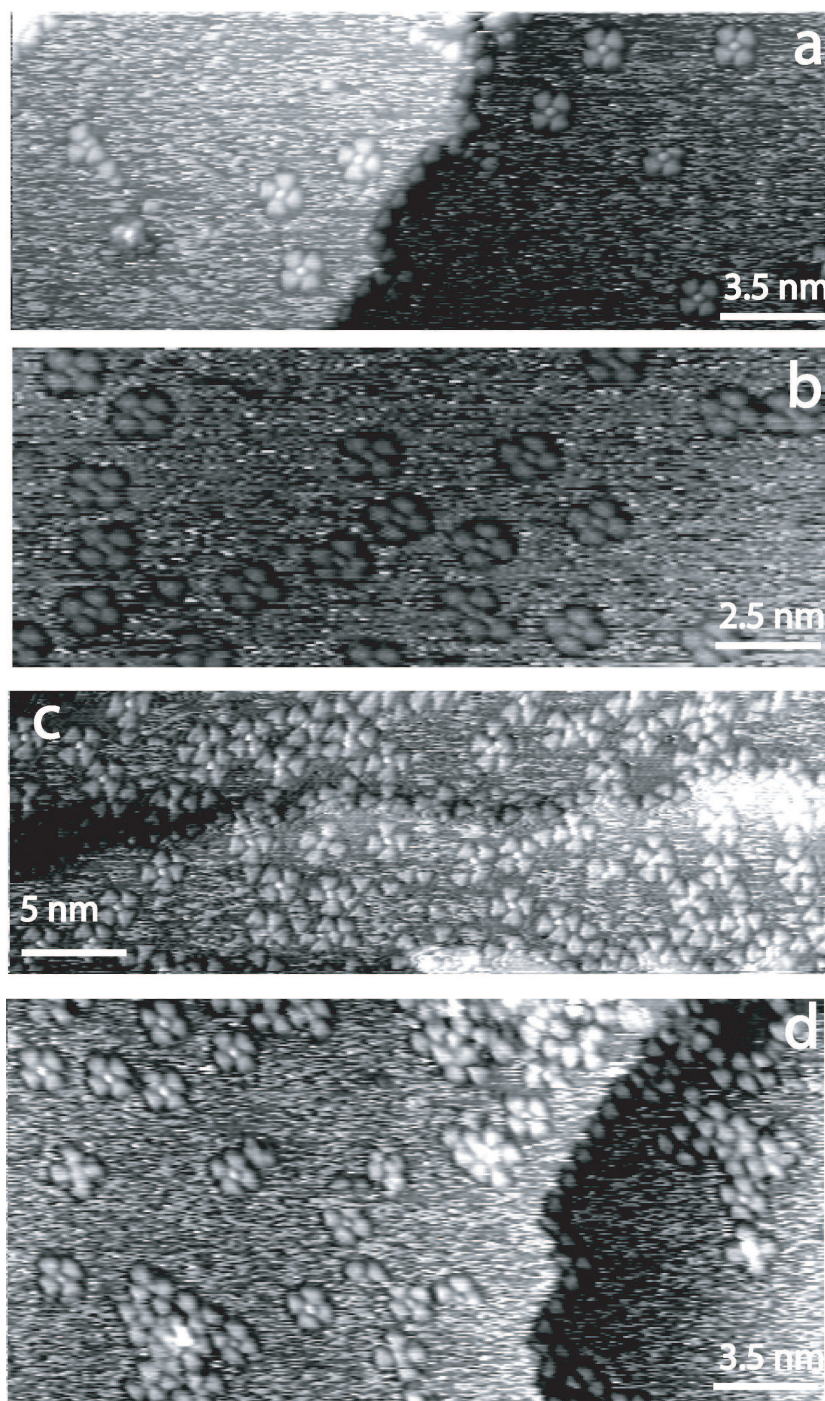


Figure 2.31: **(a)** Substrate deposition temperature $T_s = 106\text{K}$. Deposition order Fe first then TMA. $[L] = 43\%$ $\frac{[M]}{[L]} = 0.08$ **(b)** Substrate deposition temperature $T_s = 107\text{K}$. Deposition order Fe first then TMA. $[L] = 57\%$ $\frac{[M]}{[L]} = 0.3$. **(c)** Substrate deposition temperature $T_s = 103\text{K}$. Deposition order TMA first then Fe. $[L] = 43\%$ $\frac{[M]}{[L]} = 0.4$ **(d)** Substrate deposition temperature $T_s = 300\text{K}$. Deposition order Fe first then TMA. $[L] = 43\%$ $\frac{[M]}{[L]} = 0.8$ Sample annealed to 400K for 15min .

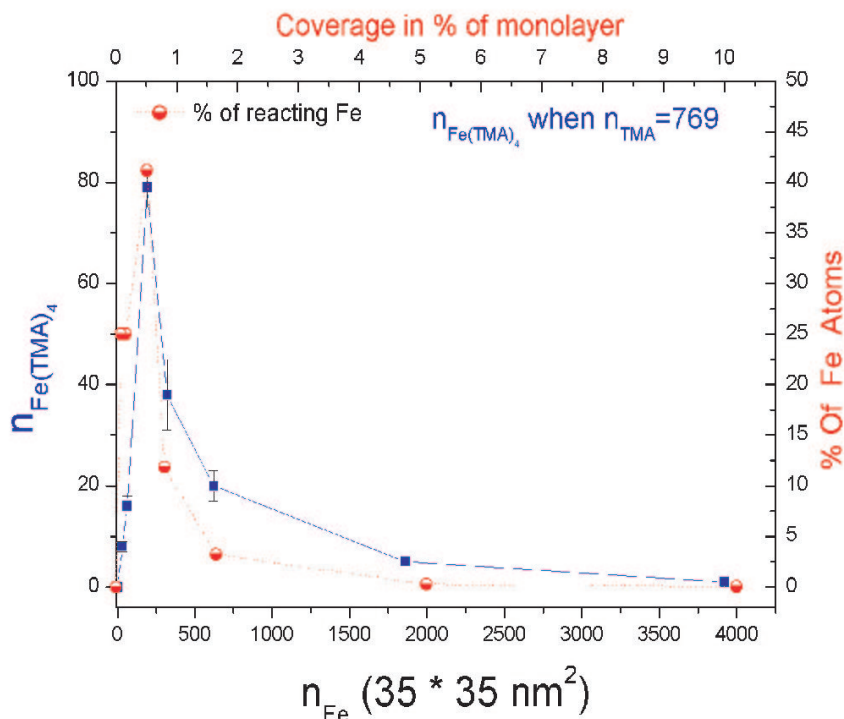


Figure 2.32: The curve in blue shows the number of complexes counted over 5-8 STM images of different surface spots. The surface spot is $35 \times 35 \text{ nm}^2$. The second curve (blue) shows the actual reaction efficiency of Fe towards formation of $\text{Fe}[\text{TMA}]_4$ complexes. The maximum is located at $\frac{[M]}{[L]} = \frac{1}{4}$.

face spot. It is straightforward to observe that the amount of complexes is correlated to the number of Fe adatoms. Besides, the maximum number of complexes is encountered for $\frac{[M]}{[L]} = 0.25$. These two observations strongly suggest that the protrusion observed within the complexes is Fe; accordingly in the following the mononuclear complexes will be referred as $\text{Fe}[\text{TMA}]_4$. The curve in red shows the percentage of deposited Fe adatoms that actively are engaged in the chemical bond within the complexes. It can easily be inferred that this percentage is quite low. It reaches a maximum of about 42% at $\frac{[M]}{[L]} = 0.25$ and then turns down at higher values. Nevertheless, the low percentage of Fe adatoms reacting at low $\frac{[M]}{[L]} = 0.25$ indicates that a relevant portion of deposited Fe adatoms are engaged in other processes rather than TMA complexation. As reported in the above, a certain amount of Fe adatoms migrate to the step edges though part of them may be engaged in the formation of chemical species at flat terraces not revealed from the STM images. In order to carefully assess how the Fe is distributed on the surface

it is suggested to repeat these measurements at low temperature.

On the basis of the analysis of the STM images a purely geometrical model can be built to illustrate the structure of a single $Fe[TMA]_4$ complex, Fig. 2.33 **a**. The Fe atom is placed at the Cu(100) hollow site for symmetric reason. From an inspection of the Fig. 2.33 **a** it can be inferred that each TMA molecule apex is not pointing directly towards the center of the protrusion. However, the axis of the triangle (TMA molecule) is rotated 22° respect to the direction connecting the center of the triangle (TMA molecule) with the center of the protrusion. This observation account for a monodentate Fe-O linkage as for the case studied from Lin [42]. Besides, from simple geometrical consideration the Fe-O bond length is estimated to be about 2\AA appreciably smaller than the one reported by Lin [42] and in line with typical Fe carboxylate bond length [294]. Inherently, the TMA molecules result placed close to the Fe adatom and their phenyl ring is placed out of the closest hollow site¹⁰. This aspect is also different from the case reported by Lin [42] were TMA molecules tend to return to the next hollow site.

In conclusion, the complexes synthesized in this section are thermodynamically stable, they show lateral bond of typical coordination compounds, the surface geometry seems not affecting the final equilibrium stage. These observations confirm the hypothesis traced in the former paragraphs. Particularly upon replacing the Cu adatom with Fe, the type of product of the chemical reaction is different. The latter is probably due to the electronic properties of Fe: it does have still 2 d empty orbitals that can accommodate electrons coming from the carboxylic group. Also, the presence of a more reactive adatom enhances the deprotonation process indicating a lateral dissociative chemisorption process for the deprotonation of the TMA carboxylic groups. Fig. 2.33 shows also that two different $Fe[TMA]_4$ complexes are present at the surface. A closer inspection shows that the two species are one the mirrored image of the other one. The complexes are inherently chiral [43]. The chirality is understood in the model shown in Fig. 2.33 as a result of the monodentate carboxylic bonding and the TMA-TMA correlation. In particular, on each complex only the right(left for S) hand side oxygen in the carboxyle group is linking the central Fe atom. The former results in to different chiral arrangements Fig. 2.33 **b**. The presence of chirality confirms that the bonding configuration is monodentate. Besides, TMA-TMA correlation may be due to hydrogen bonding. Possible hydrogen bonding between the free oxygen on the carboxyle moiety and the phenyl ring are represented with a dash line 2.33 **b**. Accordingly, chirality may be an indirect proof of the effectiveness of the hydrogen bonding between the H on the phenyl ring

¹⁰ Assuming Fe placed at the center of the hollow site

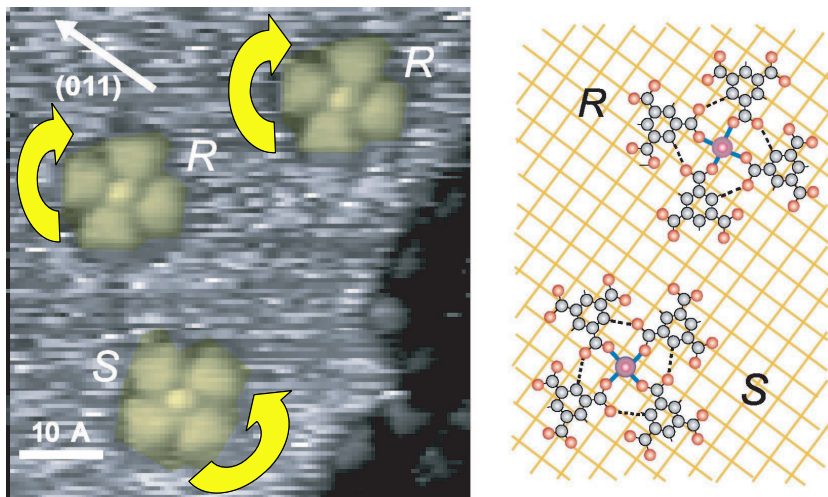


Figure 2.33: **a)** High resolution flower shaped $\text{Fe}(\text{TMA})_4$ complexes at $\text{Cu}(100)$ after deposition of Fe and TMA. Two different species are present on the surface. They are named **R** and **S**. **b)** Model for the two isomer complexes. On each complex only the right(left for **S**) hand side oxygen in the carboxylic group is linking the central Fe atom.

of the TMA molecule and the O of the carboxylic moiety of the next TMA molecule on $\text{Cu}(100)$.

2.11 Thermodynamics and kinetics of complex formation

In this paragraph a few insights on the connection of the experiments reported in the thesis and chemical thermodynamics and kinetics are addressed. As it known in chemistry [79, 295, 296, 297] the final result of a chemical reaction depends upon kinetics effects. Besides, steric and ionic effect may reduce the efficiency of a chemical reaction [298]. If the concentration of the reagents is too high their chemical affinity decreases [79]. The latter is due to the fact that molecules must meet each other in the right orientation in order to react. If the number of molecules is too high they cannot reorient themselves in the correct way. An excessive amount of molecule in solution may increase also the electrical repulsion among molecules and this prevent them from self orient in the right direction. These are well established concept in solution chemistry [299]. In order to visualize the quantitative aspects of the steric and electric hinderance some concepts of basic chemical thermodynamics are

recalled. The difference in free energy associated with a chemical reaction is equivalent to the maximum amount of effective work that can be exploited from the reaction in reversible conditions as reported in eq. 2.9:

$$\Delta G = -L_{effective} \quad (2.9)$$

This connection permits to measure ΔG from a number of electrochemical reactions. Also, the free energy is an extensive variable, meaning that it depends on the amount of reactants. At room temperature and atmospheric pressure G is equal to the **standard free energy** (G^0). For each component taking part to any chemical process it is possible to define a relation between the free energy and the **activity** 2.10:

$$nG = nG^0 + nRT \ln(a) \quad (2.10)$$

where a is defined as:

$$a = f \times c \quad (2.11)$$

In the former equation a is defined as the activity of the chemical species and f is the activity coefficient, n the number of moles and c the concentration. The activity coefficient accounts for the thermodynamic connection of the microscopic effects cited above. The free energy can be related to the equilibrium constant of the reaction through the eq 2.12:

$$\Delta G^0 = -RT \ln(K_{eq}) \quad (2.12)$$

However, if the reaction is drawn out of the standard conditions the variation of free energy is given by eq 2.14:

$$aA + bB \rightleftharpoons cC + dD \quad (2.13)$$

$$\Delta G = -RT \ln(K_{eq}) + RT \ln \frac{f_A^a[A] \times f_B^b[B]}{f_C^c[C] \times f_D^d[D]} \quad (2.14)$$

In the equation 2.14 the information concerning the variation of the chemical activity is contained in the second term. If the chemical activity of the reactants varies the free energy will vary accordingly to 2.14. This means that reducing the chemical activity of the reactants will result in an increase of the reaction free energy. In turn the degree of advancement of the chemical reaction will reduce. As a net result the amount of products decreases.

In order to check this concept in the formation of mononuclear complexes $Fe[TMA]_4$ we have investigated what happens when the Fe coverage is kept constant ($[M]=1.65\%$) and the TMA coverage($[L]$) is variable. The TMA molecule is by far the most cumbersome object on the surface as it occupies

an area equivalent to 28 Fe atoms [41]. Therefore it is better to vary $[L]$ in order to check the steric hindrance and all the combined effects leading to a variation of the activity a . Fig. 2.34 **a,b,c** shows a typical STM image at high $[L]$. Also, Fig. 2.36 **a,b** illustrates a close view of the scenario when $\frac{[M]}{[L]} = 0.25$ but, $[L] = 71.6\%$. It is possible to recognize two major differences with respect to the case reported in the previous chapter. First the number of complexes $Fe[TMA]_4$ seems smaller, second molecules are clearly imaged signaling that steric hindrance blocks them into place. The results of the counting of $Fe[TMA]_4$ measurements are reported in Fig 2.35. The number of four member complexes formed increases with the TMA coverage up to a maximum. This maximum is reached at $\frac{[M]}{[L]} = 0.3$. This result is different with respect to what shown in Fig. 2.32. This is an indication that the reaction is affected by steric effects. In fact the chemical activity of TMA is lower and inherently the ratio $\frac{[M]}{[L]}$ where the maximum amount of complexes is achieved is enhanced. The red curve in the same graph refers to the reaction efficiency Fig. 2.35. On the top x axis we report the average distance among molecules calculated simply by dividing the free space expected on the surface by the number of molecules. All the data are referred to a surface area of $35 \times 35 \text{ nm}^2$. The reaction efficiency can be found at values between 18% and 28% within a range of intermolecular distance between 0.5 nm and 1.3 nm. The results are only indicative as the counting at low coverage is difficult due to spikes in the tunnelling current. However, these experiments offer the opportunity to show that the STM can have the capability to determine the order of magnitude of thermodynamic parameters as: ΔG ΔH ΔS , associated to a chemical reaction taking place at surfaces.

The complex we observe ($Fe[TMA]_4$) could be either square planar or square pyramidal where the last ligand is one Cu atom on the surface. The former depends on the effective electron transfer from the surface. It has already been argued that the lateral coordinative linkage experienced from the Fe atom should be more pronounced in parallel to Cu with respect to the magnitude of the perpendicular linkage with the surface atoms. Accordingly, it is possible to refer to the $Fe[TMA]_4$ as square planar complexes, chemisorbed at Cu(100). It is known that in aqueous solution only Ni(II) Pd(II) Pt(II) Au(III), Rd(I) and Ir(I) give square planar Complexes [300, 301]. All these ions are characterized of an outer shell electronic configuration d^8 and the overall number of electrons taking part to the coordination bond is 16. This is a favorable situation for square planar complexes according to standard molecular orbital theory (MO) [302, 296]. The square pyramidal electronic structure follows from the former one simply allocating two more electrons in the MO. Fe is not known to give square planar complexes in any of the

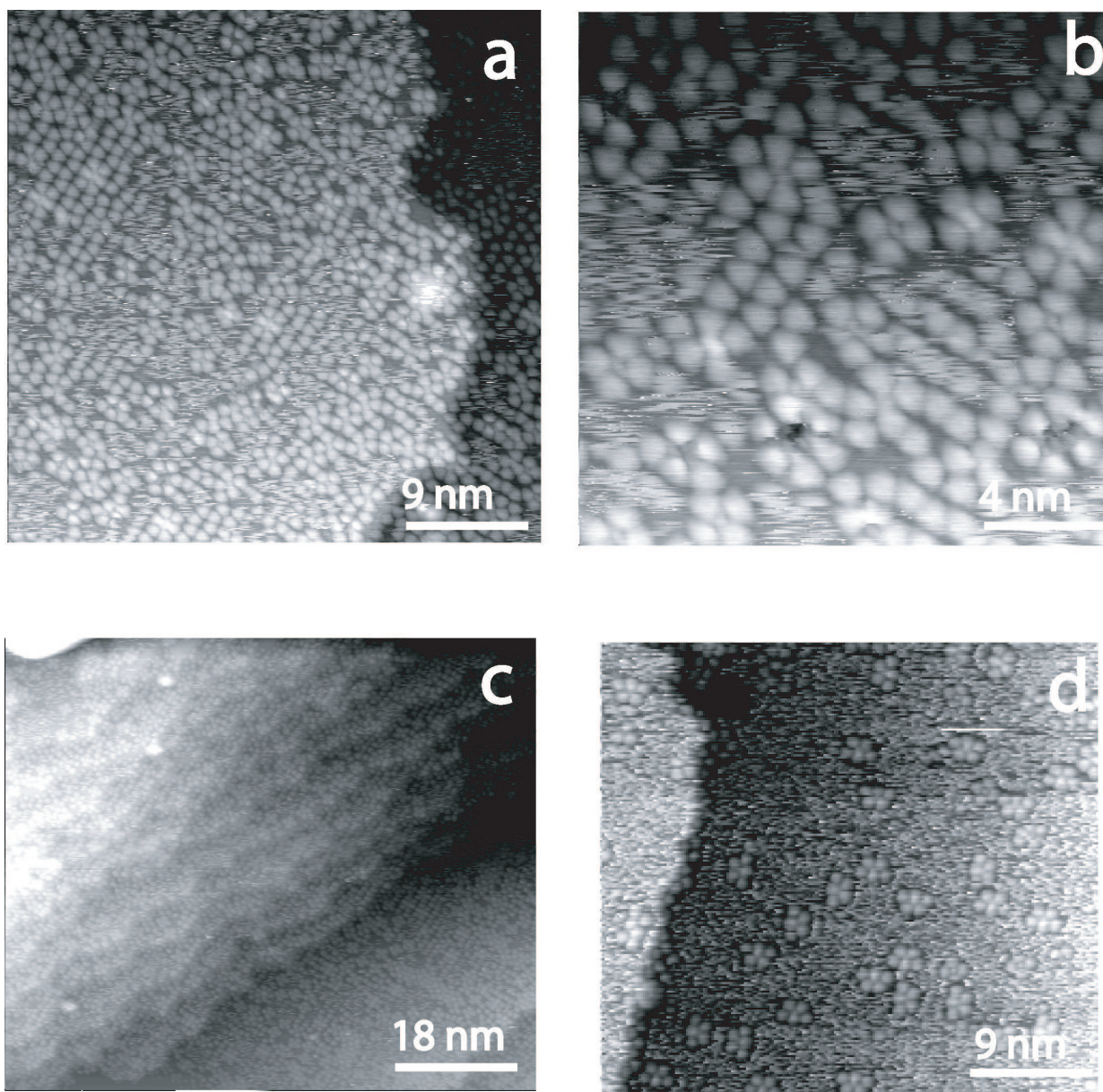


Figure 2.34: **(a)** Substrate deposition temperature $T_s = 107K$. Deposition order Fe first then TMA. $[L] = 71.6\%$ $\frac{[M]}{[L]} = 0.25$. Sample annealed to 400 k. **(b)** Same condition as in **a**. **(c)** Large view of **a**. **(d)** Substrate deposition temperature $T_s = 300K$. Deposition order TMA first then Fe. $[L] = 43\%$ $\frac{[M]}{[L]} = 0.25$

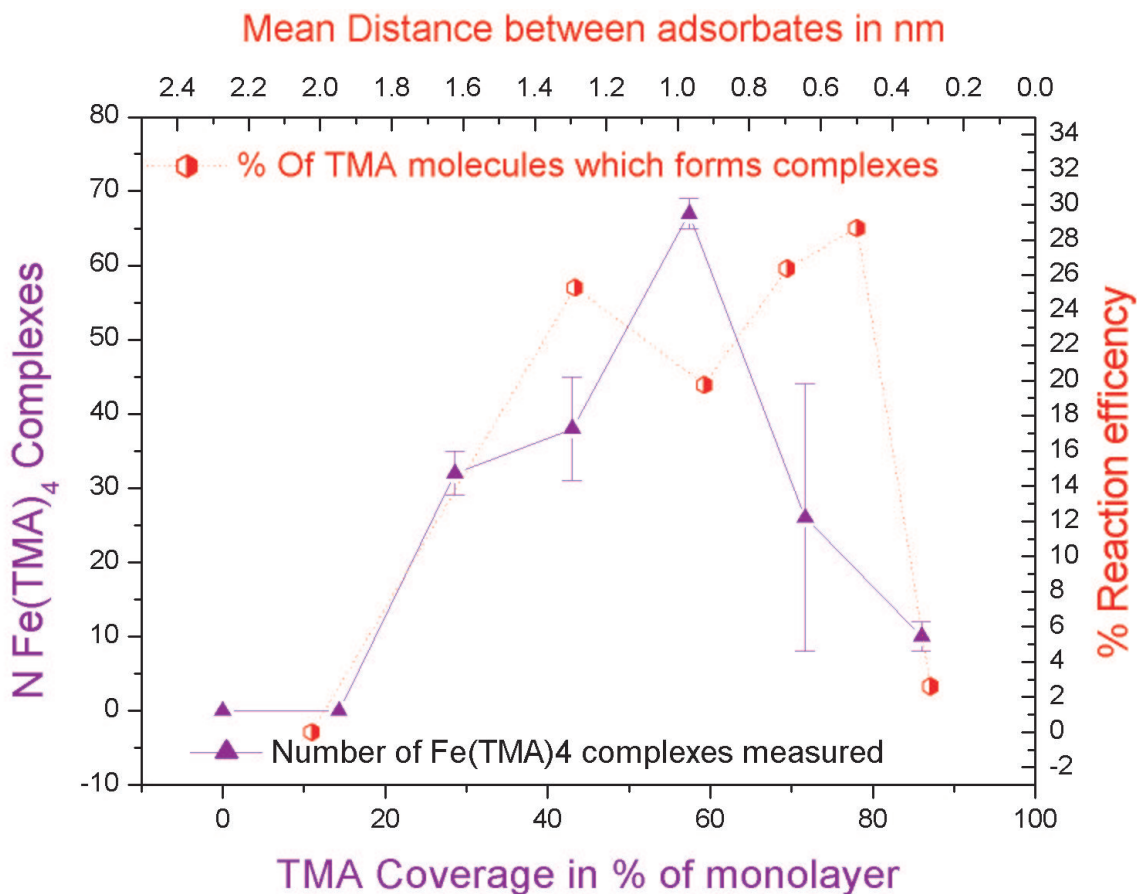


Figure 2.35: Both the pink and the red curve refer to measurement done keeping the Fe coverage constant to $[M]=1.65\%$ of monolayer. The pink curve shows that increasing the coverage of TMA the number of complexes formed first increases and then drastically decreases. The position of the peak is $\frac{[M]}{[L]} = 0.3$

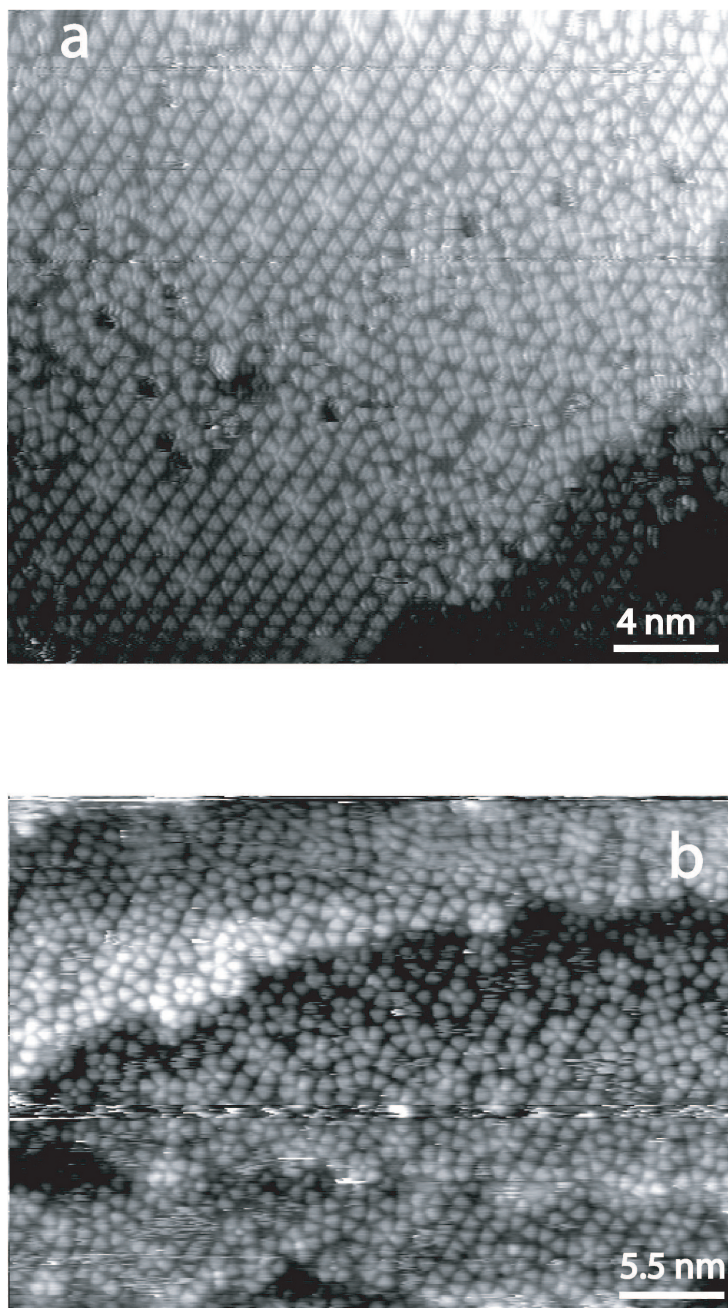


Figure 2.36: (a) Substrate deposition temperature $T_s = 105K$. Deposition order Fe first then TMA. $[L] = 71.6\%$ $\frac{[M]}{[L]} = 0.25$ (b) Same condition as in a, different location

oxidation numbers known (from -II to VI) whereas in the oxidation number I and III, d^7 , it is known to give square pyramidal complexes [294]. As mentioned in the previous paragraph, if it was assumed that Fe is in the oxidation state zero (reasonable hypothesis under the experimental conditions) then the electronic structure of Fe would resemble to the one of Ni(II) in solution signaling the possibility to form stable square planar complexes.

Different theories describe the kinetics of reactions in solution. Among these the theory of the transition state is among the most recognized[303]. According to this theory reactants spontaneously form an intermediate state which is in equilibrium with both the reactants and the products:



The speed of the chemical reaction is defined as the speed of products formations¹¹:

$$\frac{d[products]}{dt} = k^*[AB]^* = k_2 \cdot [A][B] \quad (2.16)$$

also, as the equilibrium constant for eq. 2.15 is $K^* = \frac{[AB^*]}{[A][B]}$ it is possible to rewrite 2.16 as follows:

$$\frac{d[products]}{dt} = k^* K^* \cdot [A][B] \quad (2.17)$$

Recalling the eq 2.12 the speed constant k_2 will be connected to the standard free energy of formation of the transition state ΔG_*^0 through the following relationship:

$$k_2 = k^* \exp\left(\frac{-\Delta G_*^0}{RT}\right) \quad (2.18)$$

The eq 2.18 is important as it defines a clear relationship with the transition state enthalpy of formation and entropy of formation. Clearly any increase of the ordering associated to the transition state or the esothermicity of the same will foster a quicker reaction. A bit of more algebra [303] leads to a explicit form of eq 2.18:

$$k_2 = \kappa \frac{K_b T}{h} \exp\left(\frac{-\Delta G_*^0}{RT}\right) \quad (2.19)$$

where κ is a constant between 0 and 1 and h is the Planck constant and K_b is the Boltzman constant. It is not possible to answer here to the spontaneous question on whether this theoretical implant holds for the case examined

¹¹ k^* is the speed constant for the formation of the transition state. k_2 is the speed constant for the formation of the products.

here. Another theoretical description of kinetics refers to diffusion controlled kinetics. This scenario is possible only if the probability of products formation is much higher than the probability of collision. The resulting speed of reaction in this case depends on the diffusion of reactants. This case is not treated here.

Though the approach refers to a 3D scenario it is possible to consider the constraint effect of the surface as a pressure applied to the molecule to stick on to the surface. In this case the variation of the reaction rate with respect to the pressure is related to the transition state volume variation through eq 2.16

$$\left(\frac{\partial k_2}{\partial P}\right)_T = \frac{-\Delta V_*}{RT} \quad (2.20)$$

Roughly speaking the eq 2.20 states that for a negative variation of the transition state volume the reaction speed is increased. This is what could happen at the surface, although the entropy contribution must also be taken into account.

Besides, as eq 2.16 relates the reaction rate to the equilibrium constant of the transition state it follows straightforward that the reaction rate itself is affected by the activity of the reactants:

$$k_2 = \frac{K_b T}{h} \cdot K^* \cdot \frac{f_a f_b}{f_*} \quad (2.21)$$

As it can be easily seen a variation in the activity coefficient of the reactants gives rise to a linear variation in the reaction rate. Particularly, the idea casted here is that when the activity of one of the reactants approaches zero also the reaction rate does. It is possible to artificially slow down a reaction by acting on the amount of reactants. The kinetics can inherently be followed by using the STM even if a fast scanning mode is not available. This may be the case for reaction whose speed is higher than the case shown by Lin [42]. It is known in chemistry that a chemical reaction follows different stages [296]. In particular in the case of metal organic complexes the stages usually followed by the reaction are: *Reactants/ Precursor complex /Transition state/ Successor complex/ Products*. Any steric or electrical effect on the chemical affinity acts at one of the central stages.

In the high coverage region the formation of three member complexes Y shaped is imaged clearly as depicted in Fig. 2.39. These complexes are imaged with two molecules attempting to enter the complex on the side. The shape of the $Fe[TMA]_3$ seems to indicate that the two molecule on the arms are bonding to the metal atom with the left oxygen and the right hand side oxygen of the carboxylic group. This is in strong contrast with the four member case where all the molecules bond with the right or left Oxygen of

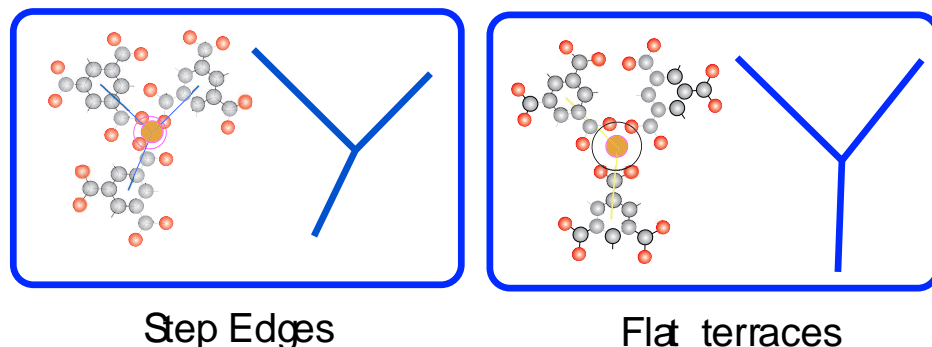


Figure 2.37: Scheme of the two possible shapes for the $\text{Fe}[\text{TMA}]_3$.

the carboxylic group Fig. 2.33. Besides, the distance between the bidentate ligand and the Fe atom is estimated to be about 2.5\AA . This means that the bond is less strong than for the four members complexes. The two molecules aside seem to stabilize this complex. The Fe atom is placed on the hollow site for symmetric reason. The three molecules result not placed on the hollow site indicating again that also in this case the energetics of the chemical bonding Fe-O is strong enough to overcome surface corrugation. The two molecule aside could also through electrostatic repulsion block this complex and avoid any intra ligands reorientation. Accounting for the high recurrence of three member complexes at step edges as well as for the slow down of the reaction rate (due to steric hinderance) at high coverage; it is suggested that the $\text{Fe}[\text{TMA}]_3$ complexes represent either an intermediate stage of reaction or a sub product. Actually, complexes at the step edges look different then the ones in Fig. 2.39. The bond length is around 3\AA for all the molecules around the Fe atom. The quality of the images does not allow for extracting a model with respect to the substrate orientation. However, two different arrangements, for $\text{Fe}[\text{TMA}]_4$ at flat surface and at step edges are shown in Fig. 2.37 Inserting a new molecule in the complex requires one molecule to rotate around its axis and the three molecules to distort their respective chemical bonds. This sequence is illustrated by a scheme Fig. 2.38 As summary, the increase of the steric hinderance proves to be a mean for imaging the reaction dynamic. A counter proof of this method to individuate transition complexes could be achieved through low $[\text{L}]$ measurements at low T.

2.12 Kinetics of adsorption processes

In the former paragraph the formation of mononuclear complexes at surfaces has been presented in view of the final equilibrium stage reached. However,

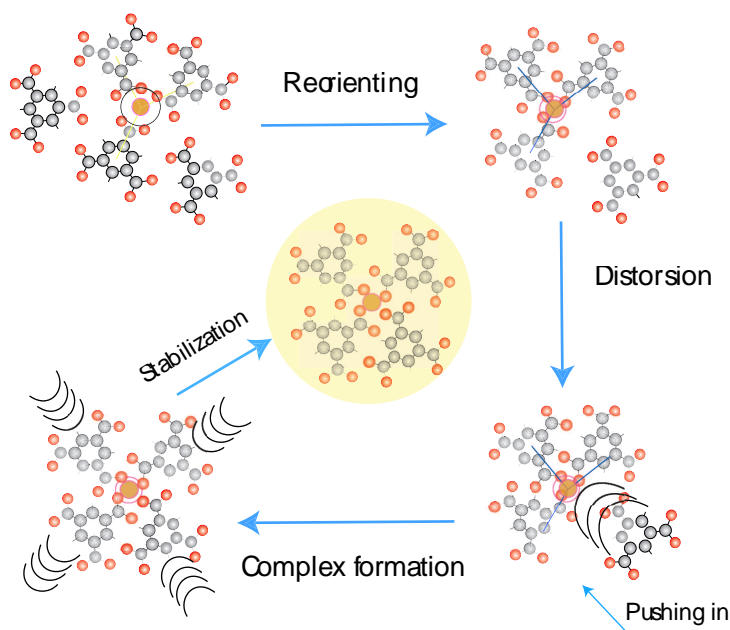


Figure 2.38: Possible sequence in the transition from three to four members complex.

the kinetics processes happening during adsorbate deposition are extremely relevant too. They effectively affect the reaction scenario. Accordingly, this section briefly presents concepts of adsorption phenomenon as well as comments on the case treated in this thesis i.e. Fe and TMA deposition.

When an adsorbate hits the surface a number of different phenomenon are possible[59]. Adsorption occurs only if the normal component of the adsorbate translation energy is high enough to avoid the molecule to be reflected. The normal component of the translational energy scales with the angle of incidence as follows:

$$E_n = E_i \cdot \cos^2 \theta \quad (2.22)$$

Fig. 2.40 illustrates the different scattering channels for a molecule incident on the surface. The scattering process can also be elastic, the adsorbate is simply reflected. The inelastic process can take place too. In this case the adsorbate exchanges part of its normal translation energy with surface phonon and leaves the surface again.

There are two different types of adsorption process, **non activated adsorption** and **activated adsorption**. The former refers to a process in which there is no energy barrier to overcome for the adsorption to take place. The latter describes those processes where an energy barrier is to be overcome for adsorbing the chemical species. In this process a transition state is formed.

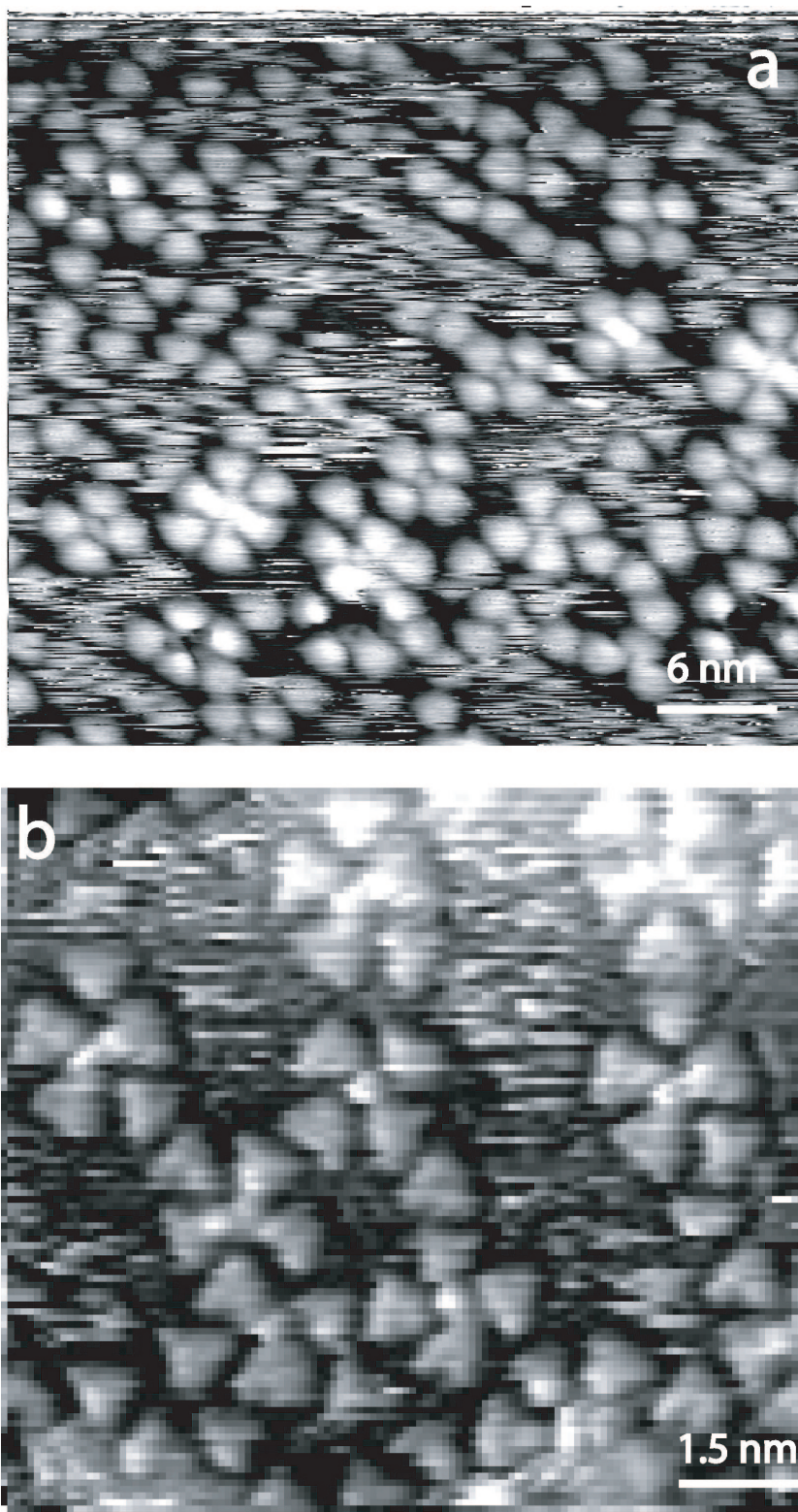


Figure 2.39: **(a)** $\text{Cu}[\text{TMA}]_6\text{D}$ Dimer. Substrate deposition temperature $T_s = 110\text{K}$. Deposition order Fe first then TMA. $[L] = 86\%$ $\frac{[M]}{[L]} = 0.2$ **(b)** Close view of three member complexes $\text{Fe}[\text{TMA}]_3$. Substrate deposition temperature $T_s = 110\text{K}$. Deposition order Fe first then TMA. $[L] = 86\%$ $\frac{[M]}{[L]} = 0.2$

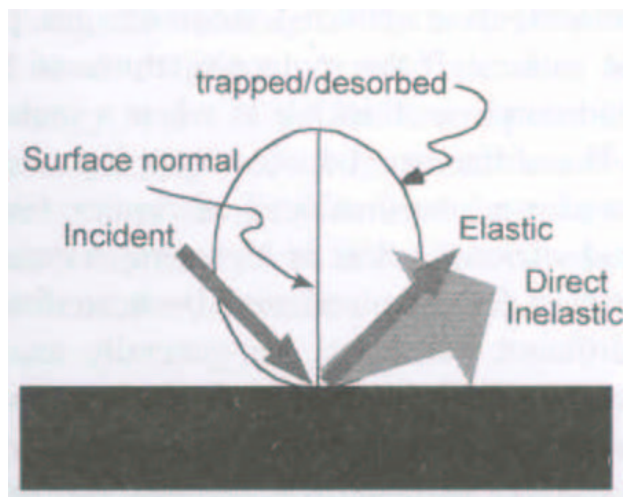


Figure 2.40: *Scattering channels for a molecule incident on a surface*[59].

The transition state is a bound adsorbate-surface state that can evolve into a final adsorbed or desorbed configuration. A molecule travelling towards the surface has got a number of degrees of freedom, namely: **rotational** and **vibrational**. Rotational levels are spaced by energies of the order of meV. This means that rotational excitation can be promoted from thermal energy and phonon coupling. However, the vibrational energies are usually of a different order of magnitude with respect to the thermal energy and the surface lattice vibrations. As the molecular mass increases vibrational levels lower in energy. Accordingly, vibrational degree of freedom can represent a further channel in which energy can be exchanged during the deposition process.

In a non activated process rotational motion can help the chemical species to stick. For instance NO on Pt(111) [304, 305, 306, 307, 308] adsorbs only with the N atom. The molecule rotates with a composed motion that can be decomposed into in plane rotation and out of plane rotation. The in plane component of this motion does not couple with the normal translational energy. However, the out of plane component does. This has a two fold effect. If the quantum rotational number J is low, the rotation can help the molecule to find the right orientation for sticking. As J increases rotational motion out of plane can hinder the sticking process. Nevertheless, in plane rotation becomes more favorable for stabilizing adsorption.

In activated adsorption rotational motion provides a tool for coupling the activation energy of the transition state with other energy degree of freedom. A case study is H_2 on Cu(100) [309, 310]. The preferential adsorption direction for adsorption of H_2 is the one in which the molecule is chemisorbed with the

main axis aligned along the surface. The reason is that this orientation provides the best charge transfer from the surface into the $2\sigma^*$ molecular orbitals. Accordingly, for $J=0$ rotation provides a tool for orienting the molecule in the right position. However, low values of J result in an hinderance of the transition state formation.

For appreciably heavy molecules a number of low energy vibrational states are available. These states can be populated during adsorption [59] resulting then in a channel in which translational energy can be diverted to.

Another import aspect of the adsorption dynamics is the sequence of deposition. When two adsorbates are to be deposited on the surface the final result of the adsorption process can vary drastically as result of the different order of adsorbate deposition. A case study is represented from CO , O_2 on Pd(111) [311, 312]. In fact, CO has an higher affinity to adsorb at Pd(111) as it can soak more electron density from the surface. If CO is deposited first, then a further deposition of O_2 will not displace CO . Conversely if O_2 is deposited first three different species appears. They are related to different adsorption configurations at different binding energies. As CO is deposited the O_2 species more strongly bound to the Pd(111) surface are displaced. The reason is that those species adsorb at the sites where CO is willing to adsorb. besides, these species can be converted to the species which bind to one single site. As the CO coverage increases the adsorption barrier increases as there are less electrons on the Pd surface to be pulled out. In this respect it becomes thermodynamically more favorable that a certain portion of sites remains covered with the upright standing chemisorbed O_2 . As it can be seen, the order of adsorbate deposition is a relevant parameter.

On the basis of the previous discussion a change in the Fe,TMA deposition order may lead to different findings, at least prior that post annealing washes out the effect. If TMA is deposited first at low T, its preferential adsorption configuration will be flat lying standing. In fact, the aromatic ring tends to establish a π bond with the surface atoms. Probably, the molecules once arrive at the surface tend to lose parallel translational energy through long jumps and activating vibrational and rotational degree of freedom. However, the presence of other molecules on the surface slightly changes the PES and new coming molecules tend to stick in the proximity of other molecules. Prior to Fe deposition it is likely that a local order is established. The adsorbate-substrate interaction will tend to order the TMA molecule with the phenyl ring at the substrate hollow sites, whereas weak lateral interaction will rotate the molecule to align one side of the triangle along the main substrate directions. When Fe is deposited the adatoms will probably undergo different processes. On the one hand they could be captured from the carboxylic group of one molecule just at the moment they arrive at the surface or they

can reach free surface sites and then migrate to meet the TMA island already formed at the surface. Such a mechanism may lead to the formation of clusters as the starting point of the synthesis are TMA islands at flat surfaces. By contrast, if Fe is deposited first the surface rugosity increases. In this condition TMA molecule can bind on four sites, the phenyl ring and the three carboxylic¹². The bonding process using the carboxylic groups is likely to be an activated adsorption. However, statistically a certain fraction of impinging TMA molecule will directly capture an Fe adatom. The resulting dimer may still be able to migrate and capture another impinging molecule. This process is probably reversible, though it may happen on a time scale small enough that a new molecule is captured before the first TMA molecule releases the translational energy and leaves the surface. This process if true would unavoidably lead to a higher number of $Fe[TMA]_3$ complexes formed during deposition with respect to the former case. As a result, statistically the number of $Fe[TMA]_3$ evolving into $Fe[TMA]_4$ would be higher than in the case in which TMA is deposited first.

In the next paragraph it will be seen that actually when TMA is deposited first the synthesis leads to the formation of polynuclear clusters rather than $Fe[TMA]_4$. The previous arguments, even though speculative, can help to figure out a possible reason.

2.13 Metal-organic synthesis at surfaces: Polynuclear complexes

In this section the synthesis of polynuclear clusters at Cu(100) is described. There are two major changes that need to be undertaken in order to produce isolated clusters. First the order of adsorbates deposition must be changed: *TMA is deposited first followed by Fe*. Second the ratio $\frac{[M]}{[L]}$ is increased with respect to the value used for producing mononuclear complexes. The second change is easily understood. As a matter of fact, in order to produce clusters the lateral linkage of TMA molecules must be increased. However, as the aim of the synthesis is to produce clusters and not long 2D arrays, not all the carboxylic groups are to be engaged in lateral linkage. Accordingly the $\frac{[M]}{[L]}$ ratio is chosen to be around one.

The first example of a polynuclear cluster is depicted in Fig. 2.41 (a). Adsorbates deposition is carried out at low T. The flat terraces appear populated with a number of TMA aggregates as large as few nm ($5 \div 10$). In order to achieve a better resolution the sample was annealed to 400 K. Anneal-

¹²Only upon deprotonation.

ing improves the measuring conditions, in fact as explained before at room temperature it is extremely difficult to resolve the structures present on the surface when the overall coverage $[L]$ is low ($[L] \leq 50\%$). For these reasons resolving the inner structure of the clusters was a difficult task. The resolution achieved was insufficient to derive a geometrical model. However, Fig. 2.41 **(b)** shows a detail of one of the clusters. A quite relevant feature is that at the middle of the cluster there is a four member complex $Fe[TMA]_4$ surrounded by a complex structure where three member complexes seem to predominate. It is not possible from the analysis of the image to establish whether the three member complexes are bonded to the central core $Fe[TMA]_4$ with bidentate carboxylate bonding or through hydrogen bonding¹³. Slightly increasing $\frac{[M]}{[L]}$ to one permits to image the polynuclear complexes without annealing the sample. This is shown in Fig. 2.42 **(b)**. The clusters are mostly composed by a core made up of a $Fe[TMA]_4$ on whose corners a three member complex $Fe[TMA]_3$ sticks. The structure of these polynuclear clusters is actually different from the single molecular magnets discussed in Par.2.5. In SMM single magnetic atoms are bridged together through oxygen or N atoms. On the contrary, here different magnetic atoms (Fe) are bridged through molecules. Nevertheless, it is still possible that a magnetic superexchange interaction takes place among the two atoms bridged [313, 314]. In fact the π electrons over the phenyl ring can constitute a communication channel through atoms. Upon annealing the clusters tend to size up and new molecules attach to them. In order to resolve the interior structure of these polynuclear clusters it is suggested to perform low temperature high resolved scanning imaging.

¹³H-bonding are unlikely due to their low thermal stability.

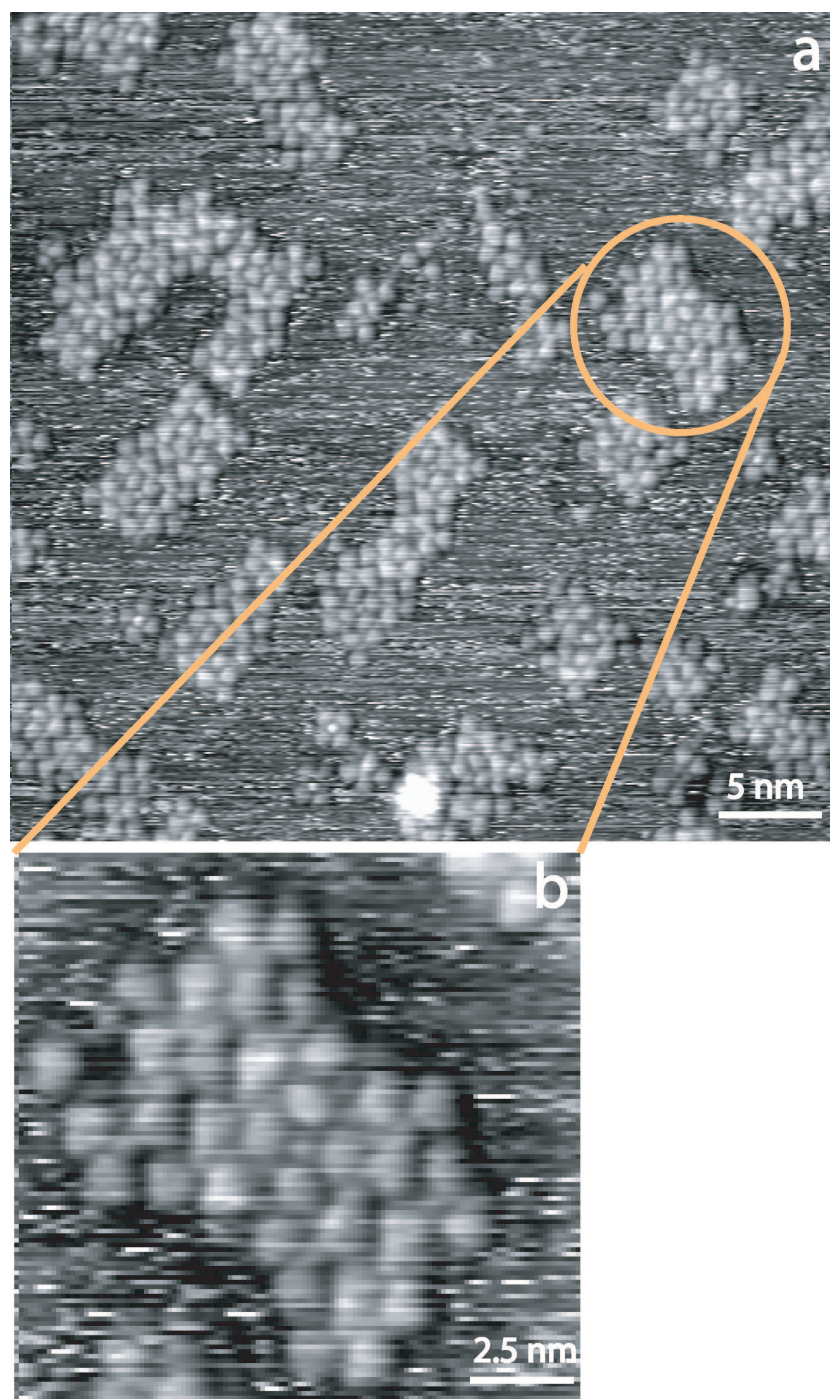


Figure 2.41: **(a)** Polynuclear complexes at flat terraces. Substrate deposition temperature $T_s = 106\text{K}$. Deposition order TMA first then Fe. $[L] = 43\%$ $\frac{[M]}{[L]} = 0.8$. Sample annealed to 400 K **(b)** Detail from a single polynuclear complex

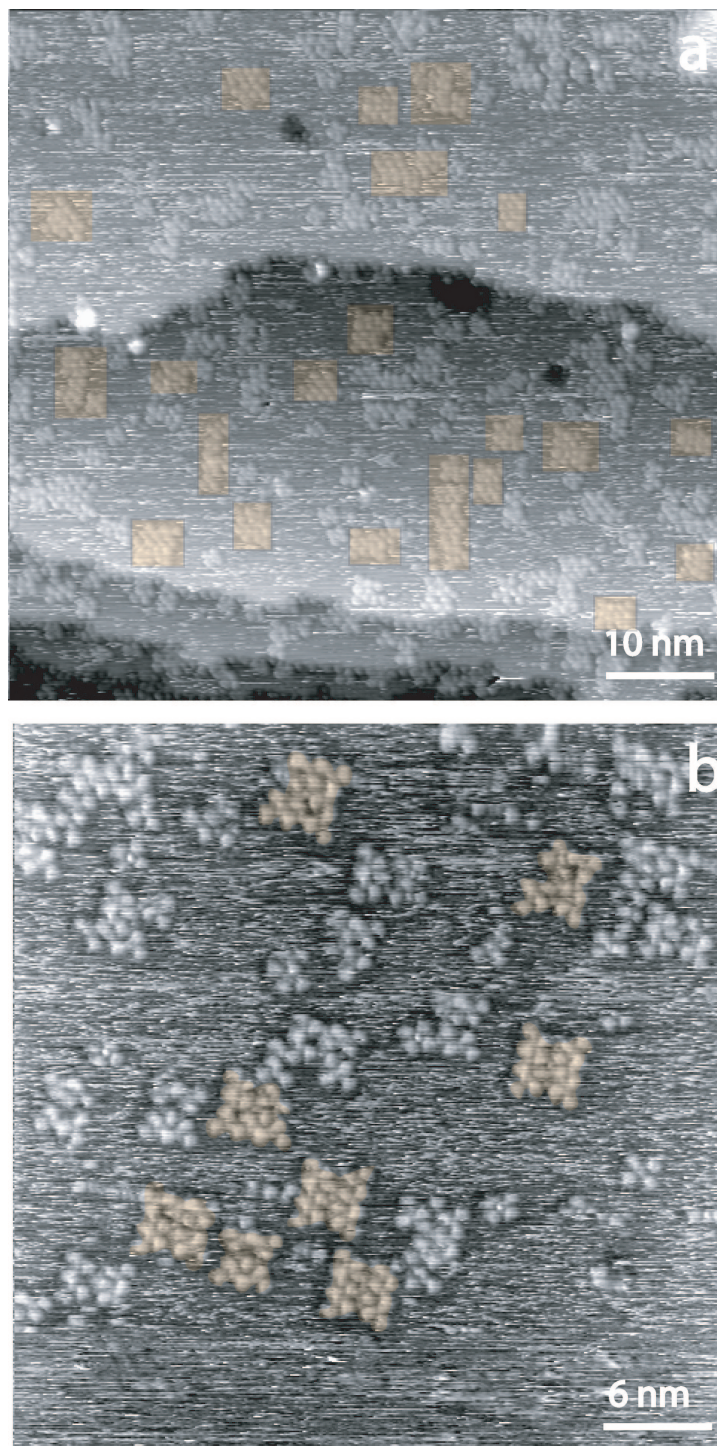


Figure 2.42: **(a)** Polynuclear complexes at flat terraces. Substrate deposition temperature $T_s = 114\text{K}$. Deposition order TMA first then Fe. $[L] = 43\%$ $\frac{[M]}{[L]} = 1$. Sample annealed to 450 K. **(b)** Substrate deposition temperature $T_s = 117\text{K}$. Deposition order TMA first then Fe. $[L] = 43\%$ $\frac{[M]}{[L]} = 1$.

2.14 Metal-organic Synthesis at surfaces: 1D and 2D structures

In this paragraph it is shown how an important external trigger, *annealing*, can act on the surface scenario after that a first chemical assembly has taken place.

If an external trigger acts on the assembling process after that it has reached the thermodynamic equilibrium the overall procedure is known as self assembly followed by post modification [202]. Fig.2.45 **a**, offers an overview of the scenario followed after deposition of TMA and Fe for appreciable $\frac{[M]}{[L]}$ i.e. $\frac{[M]}{[L]} > 1$. It can be observed that a number of aggregates are present at the surface. Their structure is not ordered. Nonetheless, it may be inferred that the structures account for multiple lateral linkage of TMA molecules.

In such a scenario the effect of annealing can be extremely relevant. Table 2.1 illustrates how the thermal energy increases while increasing the substrate temperature. Besides, the increase in the exponential part of the molecular diffusion coefficient is also reported. If the exponential part of the diffusion coefficient is considered as the number of attempts that the adsorbates does to leave its site, than it is possible to infer the following: Even if a strong chemical coordinative bond between Fe and carboxylic groups is formed (energies up to some eV) the TMA molecules and the Fe atoms within the assemblies have still some degrees¹⁴ of freedom. In fact with higher to higher temperature the probability that the molecule can slightly shift towards a better place at the surface increases. Also, the Fe atoms can reposition themselves upon annealing. The process of reordering does not involve necessarily the breaking up of the Fe-O bond. In fact this bond can stretch and distort itself upon annealing. Presumably, a fraction of Fe-O bonds are statistically broken in favor of O-H recombination¹⁵.

The mobility of high diffusing species, including the fantom $Fe[TMA]_3$, is also increased upon annealing. inherently the probability that two or more fantom species meet or fuse themselves into one object increases.

Last the evaporation of Fe atoms captured at the step edges into flat terraces is increased upon annealing. The reason is that most of the adatom at flat terraces are linked within the assemblies. Accordingly the equilibrium sketched in the reaction 2.23 is moved towards the right, and more Fe atoms reach the terraces.

¹⁴translation, partial bonding distortion and stretching, partial rotation, rotation of mononuclear complexes...

¹⁵This is a purely thermodynamical consideration.

Magnitude of thermal energy and diffusion factors			
T (K)	KT (meV)	$\frac{E_m}{KT}$	$\log\left(\frac{\exp(-\frac{E_m}{KT_{RT}})}{\exp(-\frac{E_m}{KT_{annealing}})}\right)$
300	26	31.92	0
350	31	26.77	2.38
400	35	23.71	3.5
450	39.4	21.06	4.7
500	43.7	18.99	5.6

Table 2.1: *The different values are calculated accounting for $E_m = 0.8$ eV. It is an indicative value.*

$$Fe_{steps} \rightleftharpoons Fe_{terrace} \quad (2.23)$$

In the previous paragraph it has been seen that when $\frac{[M]}{[L]} = 0.8 \div 1$ polynuclear clusters evolve. However, if the sample is annealed for a sufficiently long time ($t \geq 15min$) one dimensional structures develop[166] at flat terraces. These structures are distributed at the surface as shown in Fig. 2.43. The structures seem to depart mostly from step edges though the quality of the images in Fig.2.43 is low. In fact the amount of mobile species on the surface under the measuring conditions is still appreciable. As a result the tip picks noise up, reducing the quality of the image. As stated in section 2.5, the initial aim of the experiment described here was to achieve 1D isolated magnetic structures available for investigation with magnetic local probes. In view of this requirement, it has been attempted to reduce drastically $[L]$ while keeping $\frac{[M]}{[L]}$ constant and equal to 1. Nice isolated chains can be image at the step edges as shown in Fig. 2.44 **a**. Further increasing $\frac{[M]}{[L]}$ to 1.5, gives rise to intermixed 1D structures and polynuclear clusters upon annealing. The latter indicates that $\frac{[M]}{[L]}$ must be kept below 1.5 if 1D structures are to be observed. Surprisingly it is also possible to achieve 1D structures upon annealing if $\frac{[M]}{[L]} = 0.5$ as shown in Fig. 2.44 **c**. This is an important point. In fact this value of $\frac{[M]}{[L]}$ represents an intermediate region between the interval in which $Fe[TMA]_4$ complexes predominate and the polynuclear clusters set in. Inherently the number of monomer species $Fe[TMA]_3$ at flat terraces should be still considerable. The fact that 1D species evolve upon annealing signals that the three member complexes could be the precursor of these 1D assemblies. Besides, this is also an indication that annealing may provoke a rearrangement of the chemical bonds between Fe and O. In fact, if two complexes $Fe[TMA]_3$ meet at surfaces they need to distort themselves dras-

tically to develop a 1D structure. Moreover, if annealing is performed at 440 K degree for a longer time wider 1D structures emerge. This is illustrated in Fig. 2.44 **d**. The former indicates that the threefold symmetry of the TMA molecules can be exploited to provoke 2D well ordered arrangement.

2D ordering sets in at appreciable TMA coverage ($[L] \geq 43\%$). When the ratio $\frac{[M]}{[L]}$ is kept below 1.5 the nominal amount of Fe¹⁶ at the surface is less than necessary for engaging all the carboxylic groups present at the surface within Fe-O coordinative bonds. Accordingly, Fig. 2.45 (**b**) shows how annealing produces an intermixed scenario of 1D and 2D structures aligned along the substrate main directions. However, if $[L]$ is reduced to 43% while $\frac{[M]}{[L]}$ increased to 2.4 the amount of Fe at surface is enough to complex all the TMA molecules at surfaces. As a result islands $20 \div 30nm$ long develop at flat terraces, as shown in Fig. 2.46. Unfortunately, the STM was unable to resolve the inner structure of these assemblies. Low temperature STM observations are suggested in order to clarify this issue. However, it was possible to isolate a number of phases at high $[L]$ [166, 315]. In the framework of this thesis the focus will be on the assemblies reported in Fig. 2.48. These assemblies predominates when the deposition temperature of the adsorbates is below room temperature. This fact signals that the annealing is sensitive to a sort of memory effect. Only an accurate low temperature investigation could offer an effective overall vision of the chemical species present at surfaces.

These structures develop at Cu(100) and are composed of the 1D assemblies aligned one after the other along the substrate main directions $[011]$ and $[01-1]$. The higher is the annealing temperature the more ordered structures appear on the surface.

The example of 2D assembly reported in Fig. 2.48 is paramount evidence of the application of concepts of coordinative crystal engineering[316]. In fact, as it will be seen below, coordinative interaction is responsible for the intra chain ordering though the long range inter-chain order is mostly imputable to the weaker hydrogen bond interaction. In crystal engineering hydrogen bonding is responsible for the bending, bridging, and ordering of structures [316]. Hydrogen bonding is classified into three categories [317]:

- strong hydrogen bonding up to 1.7 eV
- moderate hydrogen bonding up to 0.63 eV
- weak hydrogen bonding up to 0.2 eV

¹⁶It is not possible to evaluate the amount of Fe adatoms stuck at the step edges

Properties of strong, moderate and weak Hydrogen bonding			
–	Strong	Moderate	Weak
A-H—B interaction	mostly covalent	mostly electrostatic	electrostatic
Bond lengths	$A-H \approx H---B$	$A-H < H---B$	$A-H \ll H---B$
H—B Å	1.2-1.5	1.5-2.2	2.2-3.2
A—B Å	2.2-2.5	2.5-3.2	3.2-4
Angles	175-180	130-180	90-150
Bond Energy eV	1.7-0.63	0.63-0.2	<0.2

As reported by Barth[252] PVBA molecules show a migration energy of about 0.83 eV on Pd(110). From this data a rough estimation of the molecular binding energy gives some 2.4 eV. If it is assumed that the binding energy for TMA is comparable to the one of PVBA then it is possible to foresee that upon annealing the reorganization of the structures will be affected by the hydrogen bond. There are two different type of hydrogen bonding that may be formed in the scenario analyzed here, O-H—O and C-H—O. The first one is known to be strong [317] though at surface the distances are stretched with respect to crystals [41]. The second one is known to be weak but, it still amounts to less 0.2 eV [317, 318].

Fig. 2.48 **a**) shows a high resolution image of the 1D structures packed into 2D arrays. Within each single 1D structure (highlighted in yellow or green) we clearly image a number of bumps associated to Fe atoms. The Fe atoms are imaged only within each single 1D structure whereas they are not imaged at the cleavage between two 1D structures. The 1D structures alternate each other in two different forms which are one the mirror image of the next one. A purely geometrical model of two chains is reported on Figure 2.48 **b**). The unit cell of the 1D structure consists of 4 Fe atoms and 2 TMA molecules. The Fe atoms are placed in two hollow sites. Giving three substrate rows (**a b c** in Figure 2.48 **b**)) the first Fe atom is placed in the hollow site between row **a** and **b** , whereas the second is placed in the hollow site between **b** and **c** column below the first one. This arrangement of atoms is repeated after one empty row (**d** in Figure 2.48 **b**)). The next two Fe atoms are positioned in the hollow sites belonging to the rows **e f g** in the same arrangement as for the latter two Fe atoms. Two Fe atoms belonging to the same column are linked by a TMA molecule. The molecule is oriented such that the axis of symmetry going through the carboxylic group pointing out of the chain is aligned along the high symmetry substrate direction [01-1]. The distance between the Fe atom and O atom is about 2 Å (red cycles around a Fe atom in Figure 2.48 **b**)) as for standard 3D coordinative bond. The

distance between the two bottom Fe atoms of the cell is estimated to be about 5.7 Å whereas, the distance between a bottom Fe atom and the next one in the chain is about 12.3 Å. The direction of the 1D structure composing the 2D array is aligned to the substrate [011] direction, though some local defects may slightly change it each 8-10 unit cells. However the presence of some defects is ascribed to the high number of assembling processes that take place in building the arrays. Errors in self assembly processes can in some cases be recovered by post assembly modification. It is important to note that the geometrical model allows for inter chain hydrogen bonding through carboxylic groups. Besides, the two oxygens of the carboxylic group are spaced unequally with respect the next chain. The former signals once more that not all the carboxylic groups are necessary deprotonated unlikely what is suggested by Lin [42]. Moreover the inter oxygen distance (O—O) is about $3 \div 3.5$ Å signaling a possible weak bonding whose energy is about 0.2 eV. If hydrogen bonding is present, the long range chiral architecture may result from this type of interaction. This is actually not surprising as such type of long ordering has been observed at metal surface [259, 40, 245].

Also, the model shows that within the chain the oxygen not bound to the Fe atom is placed about 3 Å away from the C on the next phenyl ring. This fact may indicate the presence of an intra chain hydrogen bonding. In fact C—H—O hydrogen bonding is known to manifest itself in gas, liquid and solid phase [317]. The strength of this bond is around 0.15 eV a value which could compete with the surface corrugation energy. The latter signals that intra chain hydrogen bonding may be activated upon annealing, as the position of TMA molecules varies during the annealing due to thermal activated degree of freedom.

In conclusion annealing after an assembly process induces a reordering process presumably leading the assemblies to a thermodynamically stable configuration. This configuration may be affected by the presence of hydrogen bonding interaction which defines the final geometrical 2D arrangement of coordinative 1D structures. Unlike coordinative crystal engineering, adsorbate-substrate interaction plays a key role in determining the final arrangement of the synthesized nanostructures.

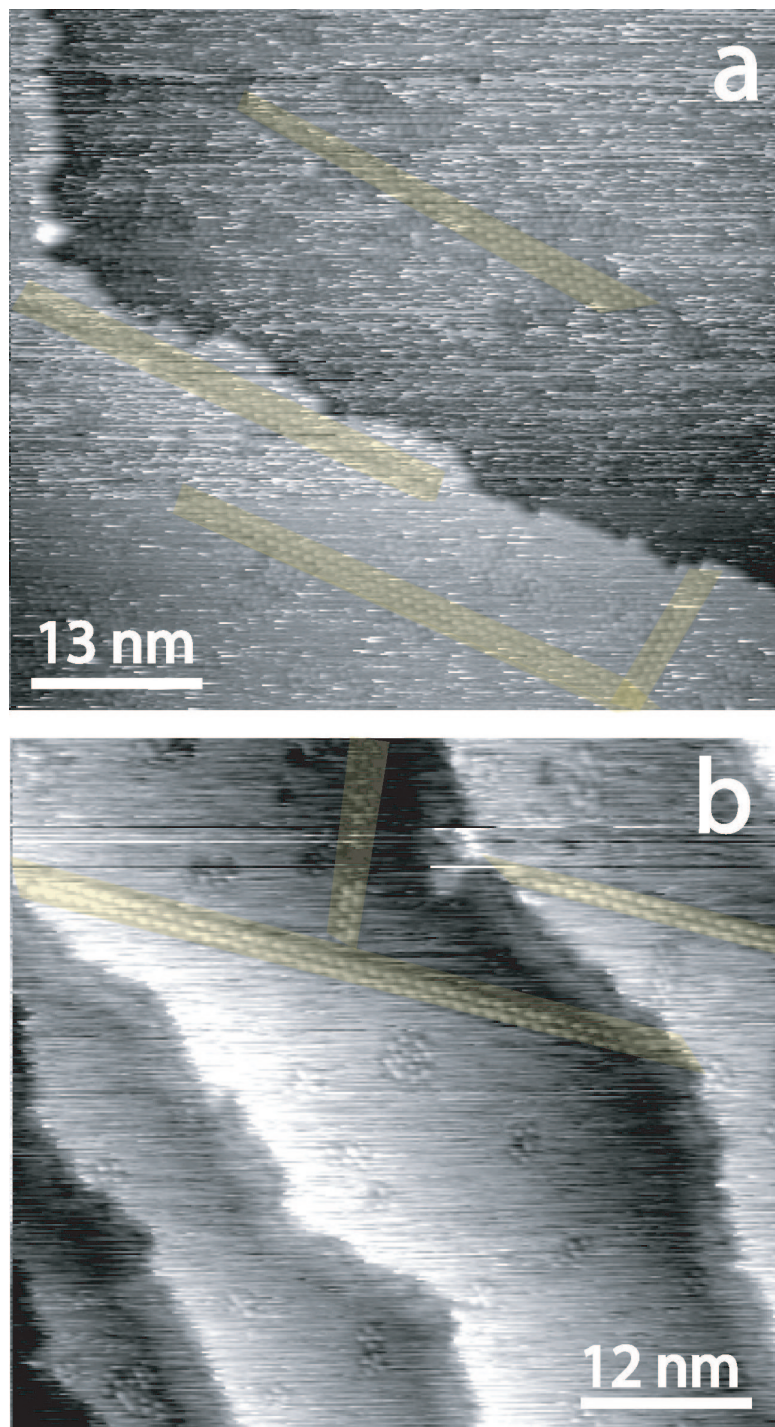


Figure 2.43: **(a)** 1D structures at flat terraces. Substrate deposition temperature $T_s = 117\text{K}$. Deposition order TMA first then Fe. $[L] = 43\%$ $\frac{[M]}{[L]} = 1$. Sample annealed to 400 K for 15 minutes. **(b)**, image taken at a different location.

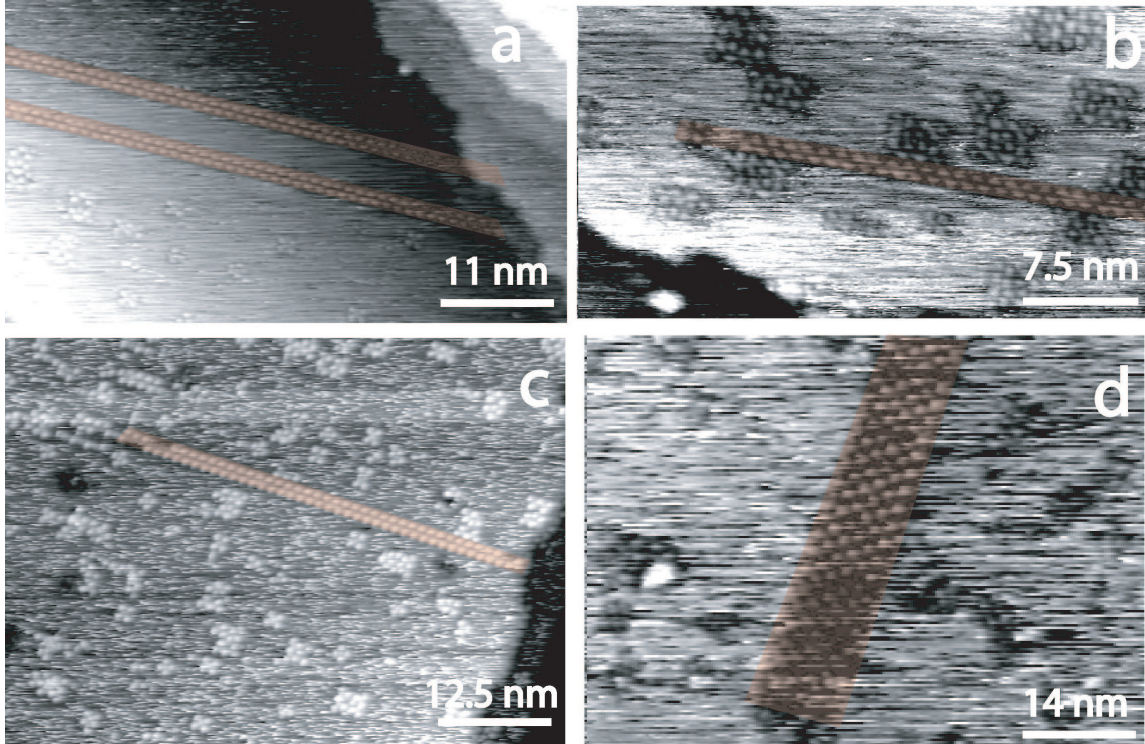


Figure 2.44: **(a)** 1D structures at flat terraces Substrate deposition temperature $T_s = 113K$. Deposition order TMA first then Fe. $[L] = 23\%$ $\frac{[M]}{[L]} = 1$. Sample annealed to 400 K for 15 minutes. **(b)** Substrate deposition temperature $T_s = 115K$. Deposition order TMA first then Fe. $[L] = 43\%$ $\frac{[M]}{[L]} = 1.5$. Sample annealed to 400 K for 15 minutes. **(c)** Substrate deposition temperature $T_s = 114.6K$. Deposition order TMA first then Fe. $[L] = 29\%$ $\frac{[M]}{[L]} = 0.5$. Sample annealed to 400 K for 15 minutes. **(d)** Substrate deposition temperature $T_s = 114.6K$. Deposition order TMA first then Fe. $[L] = 29\%$ $\frac{[M]}{[L]} = 0.5$. Sample annealed to 440 K for 60 minutes.

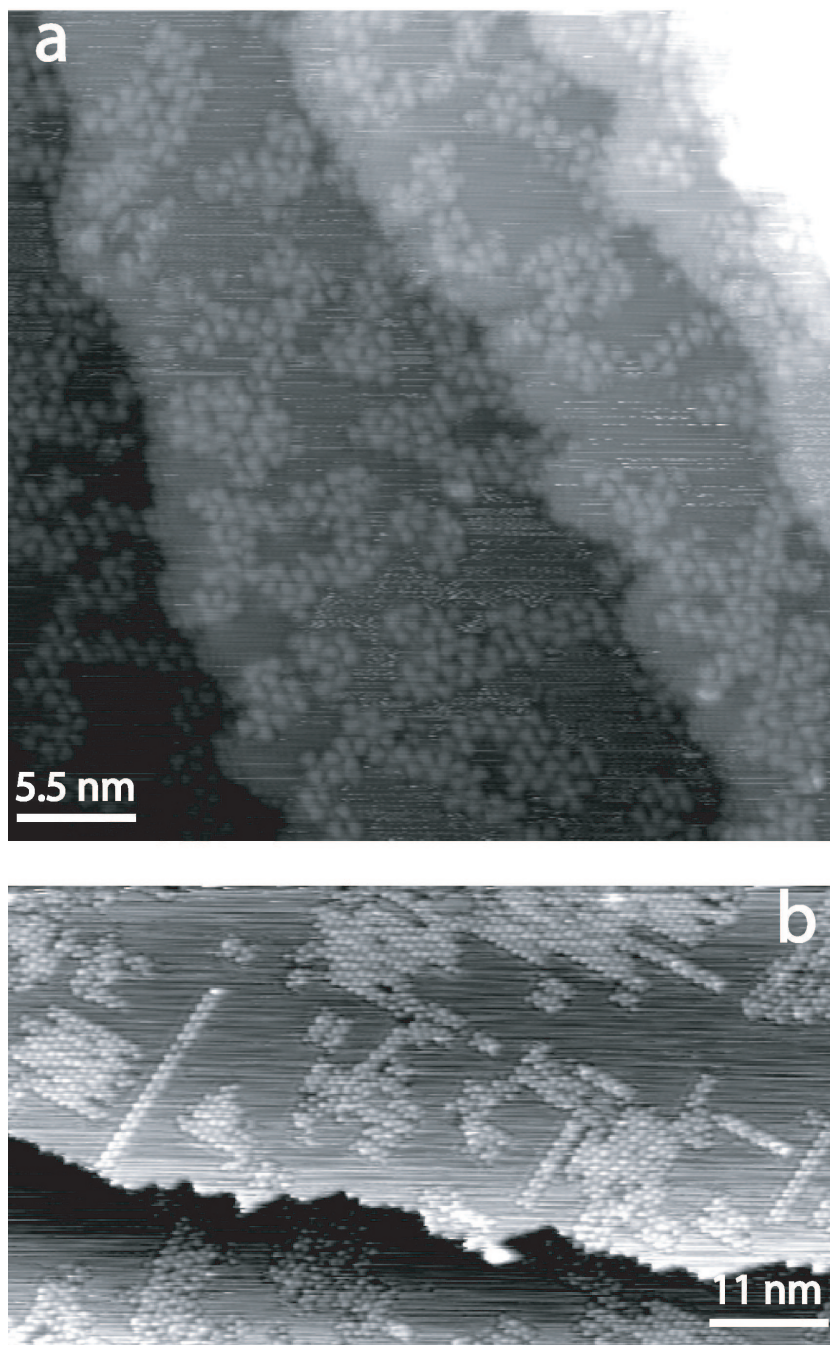


Figure 2.45: *Description: (a) Substrate deposition temperature $T_s = 112K$. Deposition order TMA first then Fe. $[L] = 57\%$ $\frac{[M]}{[L]} = 1.4$. Sample annealed to 400 K for 15 minutes. (b) Further Fe deposition temperature $T_s = 112K$. Deposition order TMA first then Fe. $[L] = 57\%$ $\frac{[M]}{[L]} = 1.4$. Sample annealed to 400 K for 15 minutes.*

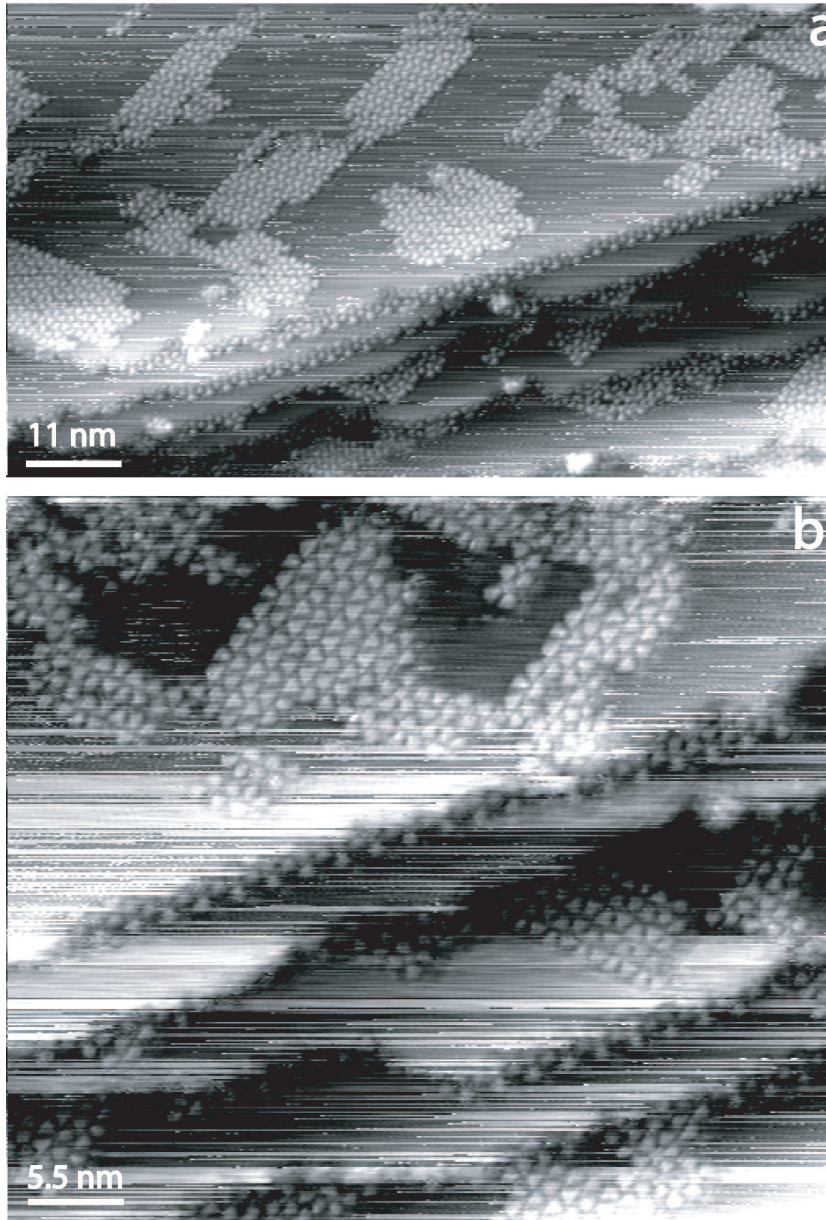


Figure 2.46: **(a)** Substrate deposition temperature $T_s = 114\text{K}$. Deposition order Fe first then TMA. $[L] = 43\%$ $\frac{[M]}{[L]} = 2.4$. Sample annealed to 400 K for 15 minutes. **(b)** Zoom in from the previous image

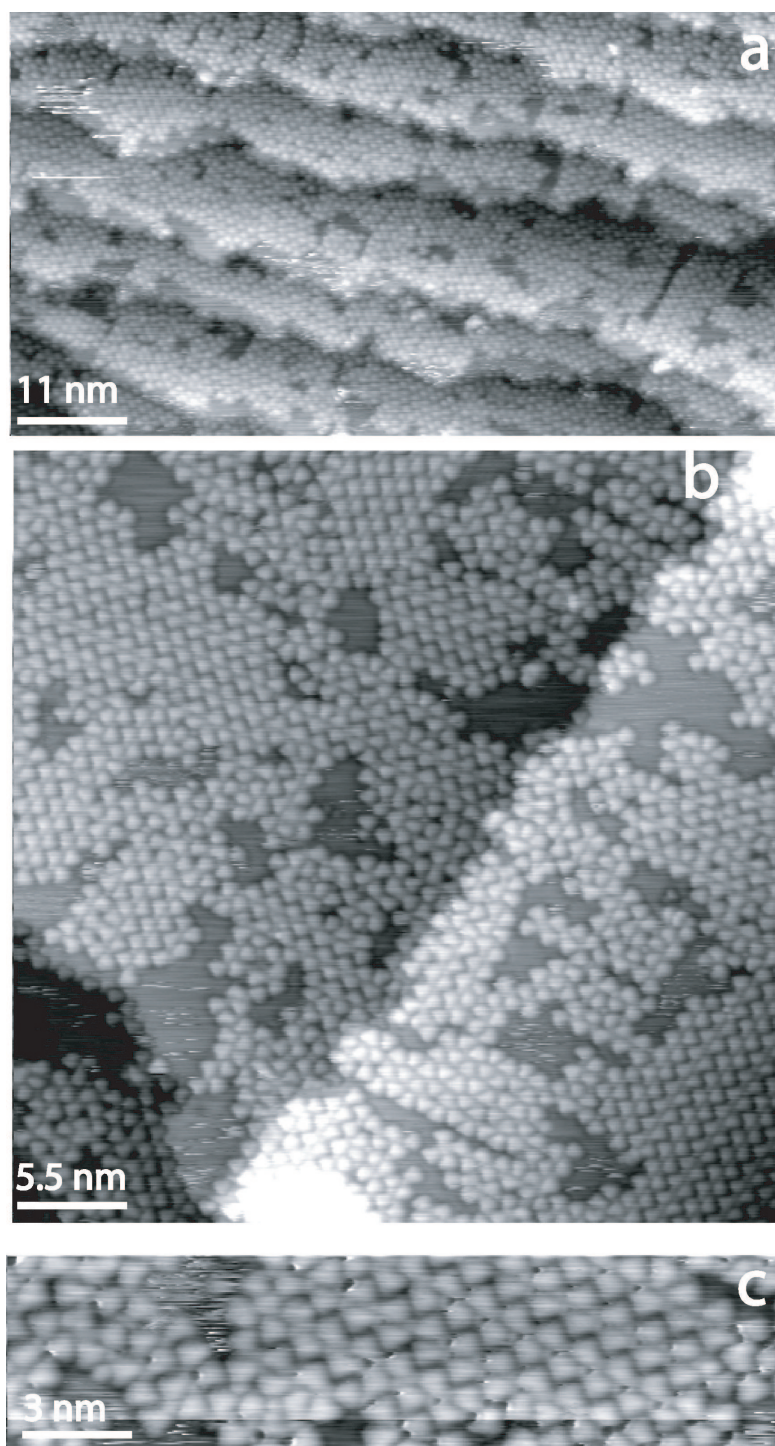


Figure 2.47: **(a)** Substrate deposition temperature $T_s = 114\text{K}$. Deposition order Fe first then TMA. $[L] = 86\%$ $\frac{[M]}{[L]} = 2.4$. Sample annealed to 450 K for 15 minutes. **(b)** Close view of the 2D assemblies oriented along the two main substrate directions $[011]$ and $[01-1]$. **(c)** Zoom in from (b). It is possible to recognize Fe atoms within the structures

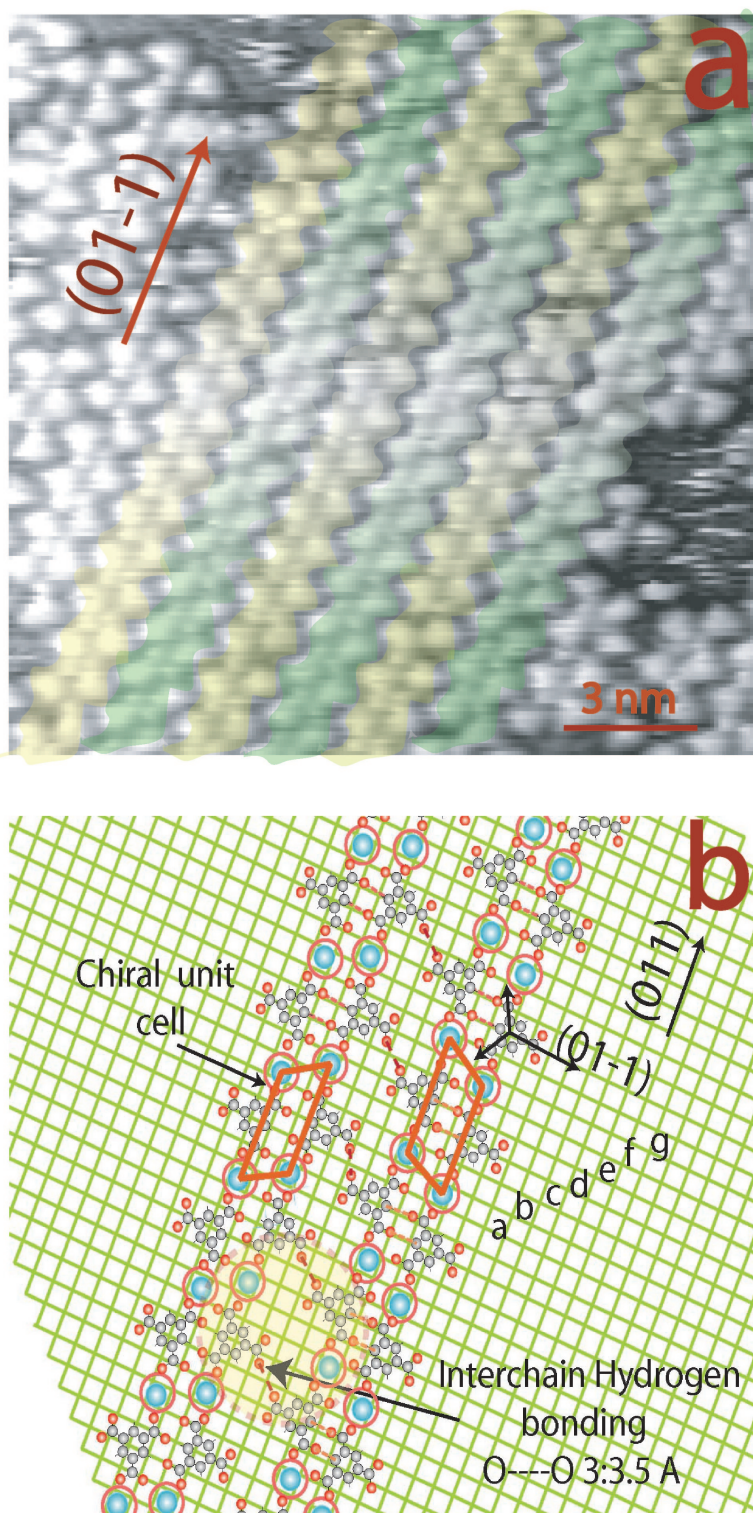


Figure 2.48: **(a)** Close view of the 2D assemblies. Two different alternating domains are imaged showing the presence of chiral ordering. **(b)** Model showing the long range ordering within and among two neighbor chains. The two chains are mirrored with respect each other. Possible intra chain and inter chain hydrogen bonding bridges are outlined.

Conclusions and Perspectives

It has been proved in this thesis that the coordinative interaction can be exploited directly on surfaces ^{footnote}Even though the measurements have been carried out on Cu(100) only, this does not affect the generality of the statement. In fact, Cu(100) has an appreciable corrugation. As weaker interactions have proven to be effective to build nanostructures on different metal surfaces, coordinative interaction can inherently be expected to do the same.. Mononuclear complexes including one Fe atom and three or four TMA molecules have been synthesized. These results are easily reproducible. Besides, polynuclear complexes including about 9 Fe atoms have been achieved too. In comparison with SMM this complexes account for Fe-Fe atoms bridged from the entire TMA molecules.

1D and 2D organometallic structures have been reliably and reproducibly synthesized too. In case of 1D assemblies, the internal structure accounts for a cell comprising 4 Fe atoms and 2 TMA molecule. 1D and 2D structures are achieved only upon annealing. With higher and higher annealing temperatures more ordered structures evolve on the surface.

I suggest to investigate further the structure of 1D chains by the use of LT-STM. Moreover, studies at low temperature can easily elucidate whether the "phantom" $Fe[TMA]_3$ complexes are an intermediate stage of reaction on the road towards $Fe[TMA]_4$ formation.

Even though the structural arrangement of the 2D assemblies differs from metal monolayers, where atomic magnetic orbitals overlap, it is suggested to check the magnetism of the assemblies built. In fact, as in the case of Co 1D chains studied by Gambardella [128], the local anisotropy, due to the presence of the surface atoms and the ligands, may lead to some form of magnetic ordering. Besides, the combined presence of a molecule and the surface linking two Fe atoms may result in a form of magnetic coupling. For these reasons I envisage XMCD measurements to elucidate the points outlined before.

As far as the understanding of the chemistry underneath the synthesis of organometallic species on surfaces is concerned, I suggest to study different

coordinative groups such as $-SH$, $-OH$ or $-CN$. Possibly electron attractor ligands are better suited than electron donor ligands to link a metal atom deposited on a surface. In fact, prior to interaction with the surface the atom is in its 0 oxidation state, therefore it does not have a strong attitude to accept a retrodonation from the ligand.

It is also important to check the effect of the metal electronic structure on the number of ligands that attach to it. In this case I suggest to use atoms like Ni or Pd that fall in between Fe and Cu in the periodic table, without changing the ligand.

The real magnitude of the adsorbate-adsorbate interaction can be inferred only if different surfaces are reliably tested. I envisage therefore the study of the reaction between Fe and TMA on different surfaces.

As for the tuning of the magnetic interaction among metal atoms within the synthesized structure, I would also try to use a ligand which is known to give rise to magnetic coupling between the metals it bridges.

Finally it has to be stated that, in order to further pursue a research project on surface magneto chemistry a different type of instrumentation is strongly on demand. I inherently sketch the major features that the appropriate instrumentation should have. Deposition of several types of atoms and molecules should be accomplished at the same time possibly in scanning conditions. UV radiation should be available at the reaction site, such to trigger the reaction itself. Also a magnetic field of appreciable magnitude (1 T) should be available at the reaction site¹⁷. The possibility to perform IR spectroscopy on the reaction site, is absolutely necessary in order to assess indisputably the nature of the different chemical bonds within the assemblies. ESR spectroscopy may be arranged in a position other than the scanning position. STM tip fast scanning is highly requested in order to follow the deposition process. The construction of a VT STM allowing all these operations is certainly a difficult task, though not prohibitive.

It is anyway a challenge that must be accepted if a real systematic study of "*spatial constraint magneto chemistry*" has to be carried out.

¹⁷This is possibly most difficult piece of equipment to incorporate in the set up described

Outlook

Chemical Atomic Manipulation

Two methods have been used so far to position atoms on surfaces[147]. The first one is lateral manipulation of atoms. In this method the tip of an STM microscope is positioned close to the adsorbate. Increasing the tunnelling current and opening the feedback loop enables the tip to come to a small distance from the adsorbates. Van der Waals interactions between the tip and the adsorbate become comparable to the migration energy of adsorbates on metal surface. The latter enables the adsorbate to follow the tip Moving on the surface. The second Method is vertical manipulation. In this method a voltage pulse is applied to the adsorbate keeping the feedback loop open. The resulting polarization of the adsorbate leads it to jump. This is possible because the attraction between Tip and adsorbate has a size comparable with the desorption energy. Here we introduce the concept of chemical manipulation e.g. we use chemical interaction to position atoms at metal surfaces and build nanostructures of nanometer size. This concept is known in 3D chemistry [316] and consists of different organic ligands and different coordinative modes used to position metal atoms on a three dimensional lattice. Chemical atomic manipulation can tune the electronic state of the metal atom as well as the interaction between two or more atoms. On metal surfaces there are three major parameters¹⁸ controlling the final result of chemical atomic manipulation: 1) The ratio between the concentration of the metal atom concentration $[M]$ and ligand concentration $[L]$. 2) The strength of the interaction between metal and surface $M-S$ compared with the strength of the interaction between metal and ligand $M-L$. 3) The shape of the organic molecule and the number of ligands that it can allocate. In this work we fix the last two parameters and we explore the range of nanostructures formed on the surface by varying the ratio $[M]/[L]$. On a different value scale of this ratio we find that some species are predominate compared with others. It has

¹⁸The relative deposition time between metal and ligands may also reveal to be a relevant parameter

to be mentioned that this form of manipulation takes place at room temperature, even though for this experiment deposition of adsorbates was carried at 100 K. So far there is only one mechanism which has been shown to be able of atomic manipulation at room temperature. The inelastic scattering of the tunnelling current can result in a vibrational excitation of adsorbates inducing a lateral motion [319]. This mechanism has been successful in moving Br atoms on Cu(100) surfaces for a few Å. However the concept we show here is that Chemical atomic manipulation is able to achieve the formation of nanostructures at room temperature even though the motion of a single atom is not directly under control.

Manipulation of the spin of the central atom

We find complexes of Fe and 4 molecules of TMA[43]. These complexes are imaged as stars with a bump in the middle. We have developed a model for the structure of the observed complexes. The model consists of a ligand metal atom distance of about 2\AA which is typical for iron carboxylate. Carboxylate group is known to link metal atoms in two different configurations: monodentate, e.g., one single oxygen bounding; bidentate, e.g., two oxygens bonding the metal atom. In the 4 member complexes all the four carboxylate group bind the metal atom in a monodentate configuration. The maximum concentration of four member complexes is found at $[\text{M}]/[\text{L}] = \frac{1}{4}$. We find 3 member complexes at step edges. They are bound to kinks. The different number of ligands attached to the metal atom offers the possibility to tune the spin state of the central atom. Due to the planar ligands the d orbital energy levels within the metal atoms may be modified. The changes manifest themselves, regardless of the effect of the surfaces on the absolute actual electronic configuration of the metal atom[239]. In a four ligand configuration, the central atom will experience a crystal field which will push the $d_{x^2-y^2}$ orbital up. In a three member complex with bidentate bond the angle between two ligands is reduced and the distance is increased to 3\AA . The former will result in a low energy of $d_{x^2-y^2}$ and in an enhanced energy of the d_{xy} orbitals. Therefore moving from monodentate 4 member complexes to 3 member complexes the relative energy difference of atomic levels change. This will affect the spin state of the central atom and different configuration will be possible: $\mathbf{S} = 0, \frac{1}{2}, 1$. The coupling between a magnetic atom and conduction electrons is known to generate a many body state. This state manifests itself in an increase of the resistance at low temperature and in a peak of the conductance at zero bias. This effect has been recently observed on a single metal complex linked to two leads through thiol bonding [320].

This experiment has shown that a single organometallic complex is suited to study the interaction through spin impurity and conduction electrons. The interaction between a magnetic impurity and the bulk electron at the surface is a phenomenon that has been elucidated in the last years.

We have evidences that the strength of the Fe TMA bond is with respect to adsorbate-substrate interaction in parallel to other cases studied [166]. This lets envisage the possibility to form complexes like this at different surfaces i.e noble metal close packed surfaces showing surface states. We have also indirect evidences that the metal surface separation is enhanced at least for the three member complexes [166]. We could therefore use the range of different complexes to probe the spin dependence of the Kondo effect. Further by tuning the crystal field splitting through ligand interaction we may probe the dependence of the Kondo feature in degenerate spin state under application of magnetic field [321]. Finally, the presence of the ligands offers the possibility to tune the portion of surface angle that the metal atom offers to surface electrons for the scattering. The presence of four or three ligands would give rise to different impinging angle for the surface electrons. The presence of three member complexes of different Y shape give a further degree of freedom in tuning the angle offered by the metal for the scattering process. The application of this concept to Kondo effect may lead to a new scattering scenario that may not be ascribable to an s wave scattering phenomenon.

Bibliography

- [1] H.C.Manoharan. Spin spotting. *Nature*, 416:24, 2002.
- [2] S.A Wolf and D.D. Awschalom et Al. Spintronics: A spin-based electronics vision for the future. *Science*, 294:1488, 2001.
- [3] D.Orgassa, G.J.Mankey, and H.Fujiwara. Spin inhection into carbon nanotubes and posossible application in spin-resolved scanning tunnelling microscopy. *Nanotechnology*, 12:281, 2001.
- [4] S.Heinze M.Bode et al. *Science*, 288:1805.
- [5] R. Wiesendanger and M. Bode. Nano- and atomic-scale magnetism studied by spin-polarized scanning tunneling microscopy and spectroscopy. *Sol.Stat.Com.*, 119:341, 2001.
- [6] Haiqiang, Et., and Al. Atomic-scale spin-polarized scanning tunneling microscopy applied to Mn₃N₂ 010. *Phy.Rev.Lett.*, 89:226101–2, 2002.
- [7] TP. Pareek and P. Bruno. Magnetic scanning tunneling microscopy with a two-terminal nonmagnetic tip: Quantitative results. *Phy.Rev.B.*, 63:165424, 2001.
- [8] D. Feinberg and G. Deutscher. Using a hybrid superconducting-ferromagnetic tip as a magnetic scanning tunneling microscope. *Physica E*, 15:88, 2002.
- [9] O.Naaman, W Teizer, and R.C.Dynes. Fluctuation dominated josephson tunnelling with a scanning tunnelling microscope. *Phy.rev.Lett*, 87:2001.
- [10] O.Naaman, W.Teizer, and R.C. Dynes. The fabrication of reproducible superconducting scanning tunnelling microscope tips. *Rev.Sci.Inst.*, 72:1688, 2001.

- [11] S.H.Pan, E.W.Hudson, , and J .C.Davis. Vacuum tunnelling of superconducting quasi particles from atomically sharp scanning tunnelling microscope tips. *App.Phy.Lett*, 73:2992, 1998.
- [12] M.Xu, Y.Takano, T.Hatano, M.Kitahara, and D.Fujita. MgB2 superconducting tips for scanning tunnelling microscopy study. *J.Supercond.*, 15:303, 2002.
- [13] R.J.Soulen and et al. *Science*, 282:85, 1998.
- [14] Ali Yazdani, * B. A. Jones, C. P. Lutz, M. F. Crommie, and D. M. Eigler. Probing the local effects of magnetic impurities on superconductivity. *Science*, 275:1767, 1997.
- [15] J.Smakov, I.Martin, and V.Balatsky. Scanning tunnelling microscopy measuraments of single spin relaxation time in superconductors. *ArXiv:cond-mat*, April, 2001.
- [16] D.Rugar, C.S.Yannoni, and J.A.Sidles. Nature. *Nature*, 360:563, 1992.
- [17] Y.Manassen and R.J. Hamers et al. Direct observation of the precession of individual paramagnetic soins on oxidazed silicon surfaces. *Phy.Rev.lett*, 62:2531, 1989.
- [18] A.V.Balatsky, Y.Manassen, and R.Salem. *Phy.Rev.B.*, 66:195416–1, 2002.
- [19] Y.Manassen, I.Mukhopadhyay, , and Ramesh Rao. Esr stm on iron atoms in silicon. *Phy.Rev.B*, 61:16223, 2000.
- [20] C.Durkan and M.E.Welland. Electronic spin detection in molecules using scanning-tunneling-microscopy-assisted electron-spin resonance. *Appl.Phys.Lett. Vol 80 and 2002*.
- [21] P.M.Lahti. *Magnetic Properties of Organic Materials*. Dekker, 1999.
- [22] J.Veciana. *Pi Greca Electron Magnetism from Molecules to Magnetic Materials*. Springer, Berlin, 2001.
- [23] J.Veciana H Iwamura. Organic magnets. *MRS Bulletin*, November 2000.
- [24] R.Sessoli, D.Gatteschi, A.Caneschi, and M.A. Novack. *Nature*, 365:141, 1993.

- [25] G.Christou D. Gatteschi et al. Single molecule magnets. *MRS Bulletin*, November:66, 2000.
- [26] A.Caneschi, D.Gatteschi, N. Lalioti, and et Al. Cobalt(II)-nitronyl nitroxide chains as molecular magnetic nanowires. *Ang.Chem.Int. Ed*, 40:1760, 2001.
- [27] W.Wernsdorfer and R.Sessoli. Quantum phase interference and parity effects in magnetic molecular clusters. *Science*, 284:5411, 1997.
- [28] H.Schinochara. Endohedral metallofullerenes. *Rep.Prog.Phys.*, 63:843, 2000.
- [29] E.Dietel, A.Hirsch, B.Pietzak, M.Waiblinger, K.Lips, et, and Al. *J. Am. Chem. Soc.*, 121:2432, 1999.
- [30] Wolfgang Harneit. A fullerene based electron spin quantum computer. *Phy.Rev.A*, 65:032322, 2002.
- [31] M.Waiblinger, K.Lips, W.Harneit, and A Weidinger. Thermal stability of the endohedral fullerenes N@C60 , N@C70 , and P@C60. *Phy.Rev.B.*, 64:159901, 2001.
- [32] B.E. Kane. A silicon based nuclear spin quantum computer. *Nature*, 393:133, 1998.
- [33] D. Loss and D.P.Devincenzo. Quantum computation with quantum dots. *Phy.Rev.A*, 57:120, 1998.
- [34] G.P.Berman, G.W.Brown, M.E.Hawley, and V.ITsifrinvich. Solid-state quantum computer based on scanning tunnelling microscopy. *Phy.Rev.Lett.*, 87:097902–1, 2001.
- [35] C.Joachim. Bonding more atoms together for a single molecule computer. *Nanotechnology*, 13:R1, 2002.
- [36] J.M.Lehn. Towards self-organization and complex matter. *Science*, 295:2400, 2002.
- [37] R.F.Service. Molecules get wired. *Science*, 294:2442, 2001.
- [38] R.F.Service. Assembling nanocircuits from the bottom up. *Science*, 293:782, 2002.
- [39] P.J.Stang and B.Olenyuk. Self-assembly and symmetry and molecular architecture. *Acc.Chem.Res.*, 30:502, 1997.

- [40] J. Weckesser, A. De Vita, J.V. Barth, C. Cai, and K. Kern. Mesoscopic correlation of supramolecular chirality in one-dimensional hydrogen-bonded assemblies. *Phy.Rev.Lett.*, 87:096101–1, 2001.
- [41] A.Dimitriev, N.Lin, J.Weckesser, J.V.Barth, and K.Kern. Supramolecular assemblies of trimesic acid on a cu(100) surface. *J.Phy.Chem.B* 106, 6907, 2002.
- [42] N.Lin, A.Dimitriev, J.Weckesser, J.V.Barth, and K.Kern. Real-time single-molecule imaging of the formation and dynamics of coordination compounds. *Ang.Chem.Int.Ed.*, 2002.
- [43] P.Messina, A.Dimitriev, N.Lin, H.Spillmann, M.Abel, J.V.Barth, and K.Kern. Single-molecule level observation of chirality generation of metal-organic complexes by achiral molecules on surfaces. *J.Am.Chem.Soc.* 124 (47): 14000 2002.
- [44] S.De.Franceschi and L.Kouwenhoven. Electronics and the single atom. *Nature*, 417:701, 2002.
- [45] W.Liang, et, and Al. Kondo resonance in a single molecule transistor. *Nature*, 417:725, 2002.
- [46] Jiwoong Park, 1, 2, 3 Abhay N. Pasupathy, 1, and 3 Jonas I. Goldsmith. Coulomb blockade and the kondo effect in single-atom transistors. *Nature*, 417:722, 2002.
- [47] G.Binnig, H.Rohrer, C.Gerber, and E.Weibel. *Phy.Rev.Lett.*, 49:57, 1982.
- [48] C.Bai. *Scanning Tunnelling Microscopy and its Applications*. Springer, 2001.
- [49] E.K.Schweizer and D.M.Eigler. *Nature*, 344:524, 1990.
- [50] B.Neu, G.Meyer, and K.Rieder. *Appl.Phys.A.*, 60:343, 1995.
- [51] Lukas Bürgi. *Scanning Tunnelling Microscopy as Local Probe of Electron Density, Dynamics, and Transport at Metal Surfaces*. PhD thesis, EPFL LAUSANNE, 1999.
- [52] O.Pietzsch, A.Kubetzaka, and D.Haude et al. A low temperature vacuum scanning tunnelling microscope with a split coil magnet and a rotary motion step.. *Rev.Sci.Inst.*, 71:434, 2000.

- [53] S.H.Pan, E.W.Hudson, and J.C.Davis. He3 refrigerator based very low temperature scanning tunneling microscope. *Rev.Sci.Ins.*, 70:1459, 1999.
- [54] M.Kugler, Ch.Renner, and O.Fischer. A he3 refrigerated scanning tunneling microscope in high magnetic fields and ultrahigh vacuum. *Rev.Sci.Ins.*, 71:1474, 2000.
- [55] A.J.Heinrich, C.P.Lutz, J.A.Gupta, and D.M.Eigler. Molecule cascades. *Science*, 298:1381, 2002.
- [56] M.Okano, K.Kajimura, S.Wakiyama, Fsakai, W.Mizutani, and M.Ono. *J. Vac.Sci. Technol.A*, 5:3313, 1987.
- [57] Andreas Hirstain. *Low Temperature Scanning Tunnelling Microscopy and Spectroscopy in Ultra UHV and High Magnetic Fields*. 1998.
- [58] J.F.OHanlon. *A Users Guide to Vacuum Technology Second Edition*. Wiley, 1989.
- [59] Kurt.W.Kolasinski. *Surface Science : Foundation of Catalysis and Nanoscience*. Wiley, 2002.
- [60] E Gemilin et al. Thermal boundary resistance of mechanical contacts.... *J.Phy.D*, 32:19, 1999.
- [61] R.C. Richardson E.N. Smith. *Experimental Techniques in Condensed Matter Physics at Low Temperatures*. 1988.
- [62] F.Barron. *Cryogenic Heat Transfer*. Taylor francis, US, 1999.
- [63] P.J. Meeson G.K.White. *Experimental Techniques in Low Temperature Physics*. Oxford, 2002.
- [64] G.Mariotto, M.DAngelo, , and I.V. Shvets. Dynamic behaviour of a piezowolker and inertial and frictional configuration. *Rev.Sci.Inst.*, 70:3651, 1999.
- [65] E.O.Doebelin. *Measurement Systems*. McGraw Hill, US, 1990.
- [66] J.A.Blakburn. *Modern Instrumentation for Scientists and Engineers*. Springer, 2001.
- [67] J.Fraden. *Handbook of Modern Sensors*. AIP Press, 1997.
- [68] Bend Seeber. Handbook of applied superconductivity. 1, 1998.

- [69] Nicholas Howard Balshaw. *Practical Cryogenics - An Introduction to Laboratory Cryogenics*.
- [70] G.Walker E.R.Bingham. *Low Capacity Cryogenic Refrigeration*. Oxford, 1994.
- [71] M.J.Yang J.B.Dottellis T.H.Chang, C.H.Yang. Cryogenic scanning tunnelling microscope for quantum dot spectroscopy. *Rew.Sci.Ins.*, 72:2989, 2001.
- [72] J.W.Lyding E.T.Foley, A.F.Kam. Cryogenic variable temperature ultrahigh vacuum scanning tunnelling microscope. *Rew.Sci.Ins.*, 71:3428, 2000.
- [73] T.Amakusa N.Shibata S.Chiba M.Iawatsuki H.Tokumoto Y.Kondo, E.T.Foley. Development of an ultrahigh vacuum scanning tunnelling microscope cooled by superfluid he4. *Rew.Sci.Ins.*, 72:2977, 2001.
- [74] H.S.Carslaw and J.C.Jeager. *Conduction of Heat in Solids*. Oxford, 1959.
- [75] B.Z.Maytal. Performance of ideal flow regulated regulated cryocooler. *Cryogenics*, 34:723, 1994.
- [76] R.Barron. *Cryogenic Systems*. McGraw Hill, 1972.
- [77] Kraus et al. Enthalpy-pressure diagram of he3 in the range... *Cryogenics*, page 29, 1974.
- [78] W.R.Wilkes. A 200 mW recirculating he3 refrigerator. *Cryogenics*, page 180, 1972.
- [79] P.W.Aktins. *Chemical Physics*. Oxford University Press, 1989.
- [80] E.N.Smith R.C.Richardson, editor. *Experimental techniques in Condensed Matter Physics at Low Temperatures*. Addison Wesley, 1988.
- [81] R.M.Gibbons and C.Mckidney. *Preliminary Thermodynamic Properties of Helium-3 Between 1 and 100*. 1974.
- [82] G.S.Sydoriak and T.R.Roberts. Thermodynamic properties of liquid helium three: Vapor pressure below 1k. *Phy.Rev.*, 106:175, 1957.
- [83] H.W.Jackson. *Phy.Rev.B.*, 26:66, 1982.
- [84] H.W.Jackson. *Phy.Rev.B.*, 28:1286, 1983.

- [85] J.G.M.Kuerten, C.A.M.Canstelijns, A.T.AA.M.Waele, and H.M.Gijsman. *Cryogenics*, 25:419, 1985.
- [86] D.S.Betts. *Cryogenics*, January:3, 1976.
- [87] F.C.Chou, C.F.Pai, S.B.Chien, and J.S.Chen. *Cryogenics*, 35:311, 1995.
- [88] B.Z.Maytal. *Cryogenics*, 35:69, 1995.
- [89] B.Z.Maytal and A.Shavit. *Cryogenics*, 37:33, 1997.
- [90] B.Z.Maytal. *Cryogenics*, 36:271, 1996.
- [91] S.B.Chien, L.T.Chen, and F.C.Chou. A study on the transient characteristics of a self-regulating joule-thompson cryocooler. *Cryogenics*, 36:979, 1996.
- [92] F.M. Asner. *High Field Superconducting Magnets*. Oxford, 1999.
- [93] Horowitz&Hill. *The Art of Electronics*. Cambridge, 1999.
- [94] National instruments white papers on GPIB systems. 2001.
- [95] R.F.Willis D.Jeon. Feedback system response in a scanning tunnelling microscope. *Rev.Sci.Instr.*, 62:1650, 1991.
- [96] G.W.Stupian B.A.Morgan. Digital feedback control loops for scanning tunnelling microscopes. *Rev.Sci.Inst.*, 62:3112, 1991.
- [97] O.V.Obyedkov V.Rostislav, L.Obyedkov. Fast acting piezoactuator and digital feedback loop for scanning tunnelling microscopes. *Rev.Sci.Instr.*, 64:2883, 1993.
- [98] Perkinelmer white papers on lockin amplifiers. 2001.
- [99] T.Matsui, H.Kambara, and H.Fukuyama. Development of a new ULT scanning tunnelling microscope. *J.Low.Temp.Phy.*, 121:803, 2000.
- [100] G.Nunes. Scanned probe microscopy at millikelvin temperatures. *Physica B*, 280:546, 2000.
- [101] O.Tegus, E.Brück, K.H.J.Buschow, F.R., de, and Boer. Transition-metal-based magnetic refrigerants for room-temperature applications. *Nature*. 415 and 150 2002.

- [102] EW. Hudson, SH. Pan, AK. Gupta, and JC. Davis. Atomic-scale quasi-particle scattering resonances in $\text{Bi}_2\text{Sr}_2\text{CaCu}_2\text{O}_{8+\delta}$. *Science*, 285 (5424): 88 1999.
- [103] SH. Pan, EW. Hudson, KM. Lang, H. Eisaki, S. Uchida, and JC. Davis. Imaging the effects of individual zinc impurity atoms on superconductivity in $\text{Bi}_2\text{Sr}_2\text{CaCu}_2\text{O}_{8+\delta}$. *Nature*, 403 (6771): 746 2000.
- [104] E.W. Hudson, K.M. Lang, V. Madhavan, S.H. Pan, H. Eisaki, S. Uchida, and J.C. Davis. Interplay of magnetism and high- T_c superconductivity at individual ni impurity atoms in $\text{Bi}_2\text{Sr}_2\text{CaCu}_2\text{O}_{8+\delta}$. *Nature*, 411 (6840): 920; 2001.
- [105] J.E.Hoffman, E.W.Hudson, K.M.Lang, V.Madhavan, S.Uchida H.Eisaki, , and J.C.Davis. A four unit cell periodic pattern of quasi-particle states surrounding vortex cores in $\text{Bi}_2\text{Sr}_2\text{CaCu}_2\text{O}_{8+}$. *Science*, 2002 295: 466.
- [106] K.M.Lang, V.Madhavan, J.E.Hoffman, E.W.Hudson, S.Uchida H.Eisaki, and J.C.Davis. Imaging the granular structure of high- T_c superconductivity in underdoped $\text{Bi}_2\text{Sr}_2\text{CaCu}_2\text{O}_{8+}$. *Nature*, 415 and 412 2002).
- [107] H. C. Manoharan, C. P. Lutz, and D. M. Eigler. Quantum mirages formed by coherent projection of electronic structure. *Nature*, 403:512, 2000.
- [108] P.S.Weiss and D.M.Eigler. Nanosoruces and manipulation of atoms In V.T.Binh, N.Garcia, and K.Dransfeld, editors, *NATO ASI Series*, page 213. Plenum, 1993.
- [109] H.P.Rust, M.Doering, and J.I.Pascual et Al. Temperature control of a liquid helium cooled eigler-style scanning tunneling microscope. *Rev.Sci.Inst.*, 72:4393, 2001.
- [110] D.Gatteschi and L.Pardi. *High Frequency EPR Spectroscopy*. Springer, 2002.
- [111] J.E.Wertz and J.R.Bolton. *Electron Spin Resonance: Elementary Theory and Practical Applications*. Mc graw Hill, 1972.
- [112] Stefan Grafström. Photoassisted scanning tunneling microscopy. *J.Appl.Phy.Lett.* 91 2002 , Ipp. 1717-1753.

- [113] M.Cyrot and D.Pavuna. *Introduction to Suerconductivity and High Tc Materials*. World Scientific, 1992.
- [114] J.Smakov, I.Martin, and V.Balatsky. Josephson scanning tunnelling microscopy. *Phy.Rev.B*, 21:6421, 2001.
- [115] K.Mullen et Al. I-v characteristics of coupled ultrasmlal capacitance normal tunnel junctions. *Phy.Rev.B*, 37:98, 1988.
- [116] K.Mullen et al. Charging effects in coupled sc tunnel junctions and their implications for tunnelling measuraments... *Phy.Rev.B*, 38:5150, 1988.
- [117] K.Mullen et Al. Combined effect of zener and quasiparticle transitions on the dynamics of mesoscopic josephson junctions. *Phy.rev.Lett.*, 60:1097, 1988.
- [118] A.Steinbach and P.Yoyez et al. Direct measurament of the josephson super current in ultra small josephson junction. *Phy.rev.Lett*, 87, 2001.
- [119] R.S.Gonnelli, A.Calzolari, D.Daghero, G.A.Ummarino, V.A.Stepanov, G.Giunchi, S.Ceresara, and G.Ripamonti. Josephson effect in MgB2 break junctions. *Phy.Rev.Lett.*, page 8709 (9): 2001.
- [120] ZZ.Li, Y.Xuan, H.J.Tao, Z.A.Ren, G.C.Che, B.R.Zhao, and Z.X.Zhao. Josephson effects in MgB2/Nb point-contacts. *Superc.Sci.Tech.*, 14 (11): 944 2001.
- [121] P. C. Canfield, D. K. Finnemore, S. L. Bud'ko, J. E. Ostenson, G. Lapertot, C. E. Cunningham, , and C. Petrovic. Superconductivity in dense MgB2 wires. *Physical Review Letters*, Physical Review Letters, March 12 and 2001.
- [122] Y.Y.Wu, B.Messer, and P.D.Yang. Superconducting MgB2 nanowires. *Adv.Mater.*, 13 (19):1487, 2001.
- [123] A.Darlinsky and J.Halbritter. On angle resolved x-ray photoelectron spectroscopy of oxides and serrations and and protrusion at interfaces. *J.Vac.Sci.*, 5 (4): 1235 1987.
- [124] A.Darlinski and J.Halbritter. Angle resolved xps studies of oxides at nbn and nbc and nb surfaces. *Sur.Interf.Analys.*, 10:223, 1987.

- [125] L.I.Johansson and H.I.P.Johansson. Core level study of NbC(100) and NbN(100) and. *Core level study of NbC(100) and NbN(100) and*, 80 1996, 237.
- [126] G.Karapetrov, M.Iavarone, W.K.Kwok, G.W.Crabtree, and D.G.Hinks. Scanning tunneling spectroscopy in MgB2. *Phy.Rev.Lett.*, 2001, 86, pp. 4374.
- [127] B.G.Rubio, H.Suderow, and S.Vieira. Tunneling spectroscopy in small grains of superconducting MgB2. *Phy.Rev.Lett.*, 86 (24): 5582 2001.
- [128] P.Gambardella, A.Dallmeyer, K.Maiti, M.C.Malagoli, W.Eberhardt, K.Kern, and C.Carbone. Ferromagnetism in one-dimensional monatomic metal chains. *Nature* 416, 301 (2002).
- [129] K. Kikuchi, 1 H. Imamura, 2 S. Takahashi, 1, and S. Maekawa1. Conductance quantization and andreev reflection in narrow ferromagnet/superconductor point contacts. *Phys. Rev. B* 65 and 020508(R) (2002).
- [130] Yu Zhu, Qing-Feng Sun, , and Tsung-Han Lin. Andreev reflection through a quantum dot coupled with two ferromagnets and a superconductor. *Phys. Rev. B* 65 and 024516 (2002).
- [131] V. V. Ryazanov, V. A. Oboznov, A. V. Veretennikov, , and A. Yu. Rusanov. Intrinsically frustrated superconducting array of superconductor-ferromagnet-superconductor junctions. *Physical Review B*, 65 and 020501 (2002).
- [132] R. E. S. Otadoy and A. Lodder. Andreev bound states and self-consistent gap functions in clean layered superconductor/normal metal systems with finite transverse width. *Physical Review B*, 65 and 024521 (2002).
- [133]
- [134] G.E.Blonder. Transition from metallic to tunnelling regimes in superconducting microconstrictions:. *Phy.Rev.B*, 25:4515, 7.
- [135] G.J.Strijkers, Y.Ji, F.Y.Yang, C.L.Chien, and J.M.Byers. Andreev reflections at metalTsUPERconductor point contacts: Measurement and analysis. *Phy.Rev.B.*, 63:104510, 2001.
- [136] C. Buzea and T. Yamashita. Review of the superconducting properties of MgB2. *Super.Sci.Tech.*, 14 (11): R115 2001.

- [137] Reinert E, Nicolay G, Eltner B, Ehm D, Schmidt S, Hufner S, Probst U, and Bucher E. Observation of a BCS spectral function in a conventional superconductor by photoelectron spectroscopy. *Phy.rev.Lett.*, 85 : 3930 2000.
- [138] Reinert F, Nicolay G, Hufner S, Probst U, and Bucher E. Investigation of the BCS density of states on a conventional superconductor by high-resolution photoelectron spectroscopy. *J.Elec.Spectr.*, 114: 615-622 2001.
- [139] T. Takeuki and K. Inoue. V3SI multifilamentary superconductor produced by a modified bronze process. *J.Appl.Phys.*, 74 (10): 6454 1993.
- [140] K. E. Kihlstrom. Tunneling α $2f(\omega)$ as a function of composition in a15 v-si. *Phys. Rev. B*, 32 and 28912894 (1985).
- [141] J. Kwo and T. H. Geballe*. Superconducting tunneling into the a15 Nb3Al thin films. *Phys. Rev. B*, 23 and 32303239 (1981).
- [142] J Muller. A15-type superconductors. *Rep.Prog.Phys.*, 43 (May 1980) 641-687.
- [143] Corrigan A, Hamard C, and Pena O. Superconducting properties of solid solutions (Mo6Se8)Pb-x and PbxB6Mo6Se8 in the ternary system pb-mo-se. *J.Alloy.Comp.*, 289 (1-2): 260 1999.
- [144] H. Suderow, E. Bascones, A. Izquierdo, F. Guinea, , and S. Vieira. Proximity effect and strong-coupling superconductivity in nanostructures built with an STM. *Physical Review B* 65, 100519 (2002) (4 pages).
- [145] P.G. de Gennes. *Superconductivity of Metals and Alloys*. W.A.Benjamin, New York, 1966.
- [146] M.Tinkham. *Introduction to Superconductivity*. R.E. Krieger Publishing Company, Malabar, 1980.
- [147] S.Gauthier. Atomic and molecular manipulation of individual adsorbates by STM. *App.Surf.Sci.*, 164:84, 2000.
- [148] A.Bencini and D.Gatteschi. *EPR of Exchange Coupled Systems*. Springer, 1990.
- [149] A.Abragam B.Bleaney. *Electron Paramagnetic Resonance of Transition Ions*. Orford, 1970.

- [150] Stephen Blundell. *Magnetism in Condensed Matter*. Oxford, 2002.
- [151] A.Caneschi et Al. *J.Mag.Magn.Mat.*, 200:182, 1999.
- [152] Y Manassen. Real time response and phase sensitive detection.....
J.Mag.Res, 126:133, 1997.
- [153] D.Sachal and Y.Manassen. Spin-orbit coupling mechanism for scanning tunneling microscopy observation of individual paramagnetic spins.
Phy.Rev.B.comm, 44:11528, 1991.
- [154] D.Shachal and Y.Manassen. Mechanism of electron-spin resonance studied with use of scanning tunneling microscopy. *Phy.Rev.B*, 46:4795, 1992.
- [155] S.N.Molotkov. On the theory of the tunneling current modulation at the larmor frequency due to the larmor frequency due to precession of an individual spin on a paramagnetic center. *Surf.Sci.*, 264:235, 1991.
- [156] A.V.Balatsky and I.Martin. Single spin detection with stm.
ArXiv:cond-mat, December 9, 2001.
- [157] Y.Manassen and E Ovanesyan et al. Esr stm experiments on thermally oxidized si(1 and 1 and 1). *Phy.Rev.B*, 48:4887, 1993.
- [158] E.Dalcanale P.Jacopozi. *Angew.Chem.Int.Ed.*, 36:613, 1997.
- [159] E.Wegelius K.Rissanen P.Cozzini E.Marastani E.Fisicaro P.Manini R.Fokkens E.Dalcanale F.Fochi, P.Jacopozi. *J.Am.Chem.Soc.*, 123:7539, 2001.
- [160] Z.Nussinov, M.F.Crommie, and V.Balatsky. *ArXiv:cond-mat/0301032*, v1, 2003.
- [161] A.V.Balatsky, Y.Manassen, and R.Salem. *Phi.Mag.B.*, 82:1291, 2002.
- [162] M.G. Richards et Al. Cryogenic GaAs FET amplifiers and their use in NMR detection. *Rev.Sci.Ins.*, 57:404, 1986.
- [163] RK. Kirschman. Cold electronics an overview. *Cryogenics 25 (3): 115-122 1985*.
- [164] R.J.Prance et Al. UHF ultra low noise cryogenic FET preamplifier. *J.Phy.E*, 15:101, 1982.

- [165] Claudio Sangregorio. *Magnetic Nanoparticles : The Sol-Gel and the Molecular Approaches*. PhD thesis, Department Of Chemistry University Of Florence Italy, 1998.
- [166] P.Messina, A.Dimitriev, N.Lin, H.Spillmann, J.V.Barth, and K.Kern. A new route to synthesize metal-organic supramolecular assemblies at metal surfaces. *In submission*.
- [167] W.Harneit, C.Meyer, A.Weidinger, D.Suter, and J.Twamley. *Phy.Stat.Sol.(b)*, 233:453, 2002.
- [168] D.Gatteschi and P.Rey. Design and synthesis and properties of nitroxide networked materials. In P.M.Lathi, editor, *Magnetic Properties of Organic Materials*, page 601. Marcel Dekker, 1999.
- [169] D.Gatteschi. Coupled transition metal ions-organic radicals. In A.Bencini and D.Gatteschi, editors, *EPR Of Exchange Coupled Systems*, page 193. Springer Verlag, 1990.
- [170] H.Brune, H.Röder, K.Bromann, and K.Kern. *Thin Solid Films*, 264:230, 1995.
- [171] Bjorn Fischer. *Nucleation and Growth in Metal-on-Metal Epitaxy: The Influence of Strain and Surface Reconstruction*. PhD thesis, EPFL Lausanne, 1998.
- [172] Karsten Bromann. *Controlling Epitaxial Morphologies On the Microscopic Scale*. PhD thesis, EPFL Lausanne, 1998.
- [173] J. Weckesser. *Atomic Scale Observation Of Large Organic Molecules at Metal* PhD thesis, EPFL Lausanne, 2000.
- [174] H.Brune. Microscopic view of epitaxial metal growth nucleation and aggregation. *Sur.Sci.Rep*, 31, 1998.
- [175] J.A.Venables, G.D.T.Spiller, and M.Hanbücken. *Rep.Prog.Phys.*, 47:399, 1984.
- [176] H.Brune, H.Röder, C.Boragno, and K.Kern. *Phy.Rev.Lett.*, 73:1955, 1994.
- [177] G.Ehrlich. *Surf.Sci.*, 246:1, 1991.
- [178] L.Hansen and P.Stolze et Al. Self-diffusion on copper surfaces. *Phy.Rev.B*, 44:6523, 1991.

- [179] U.Kurpick. Self-diffusion on (100) and (110) and (111) surfaces of ni and cu: A detailed study of prefactors and activation energies. *Phy.Rev.B* 64 (7): 075418 2001.
- [180] G.Boisvert and L.J.Lewis. Self-diffusion of adatoms and dimers and and vacancies on cu(100). *Phy.Rev.B* 56 (12): 7643 1997.
- [181] L.B.Hansen, Pstoltze, K.W. Jacobsen, and J.K NORSKOV. ACTIVATION FREE ENERGY AND ENTROPY FOR THE NORMAL EXCHANGE SELFDIFFUSION PROCESS ON cu(100). *Surf.Sci.*, 289:68–74, 1993.
- [182] B.G.Federick, M.R.Ashton, and N.V.Richardson. *Surf.Sci.*, 292:33, 1993.
- [183] B.G.Fredericka, Q.Chena, F.M.Leibslle, M.B.Lee, and N.V.Richardson K.J.Kitchinga. Long-range periodicity in c(8 2) benzoate/Cu(110): A combined STM and LEED and HREELS study. *Surf.Sci.*, 394 (1-3):1–25, 1997.
- [184] C. C. Perry, S. Haq, B. G. Frederick, and N. V. Richardson. Face specificity and the role of metal adatoms in molecular reorientation at surfaces. *Surface science*, Volume 409, Issue 3, 10 July 1998 Pages 512-520.
- [185] H Mehl, O Biham, I Furman, and et Al. Models for adatom diffusion on fcc (001) metal surfaces. *Phys.Rev.B* 60 (3): 2106-2116 JUL 15 1999.
- [186] F Dulot, B Kierren, and D Malterre. Influence of the initial step density on the growth mechanisms of the Fe/Cu(100) interface. *Surf.Sci.* 494 (3): 229-237 DEC 1 2001.
- [187] J.V.Barth and D.E.Fulwer. Low-coverage nonpseudomorphic and metastable of magnetic fe on cu(001). *Phy.Rev.B* 52 11432 (1985).
- [188] K.E.Johnson, D.D.Chambliss, R.J.Wilson, and S.Chiang. A structural model and mechanism for fe epitaxy on cu(100). *Surf.Sci.*, 313:L811, 1994.
- [189] M.W. Hosseini J-P.Sauvage. *Templating, Self Assembly, and Self - Organization, Comprehensive Supramolecular Chemistry*. Pergamon, 1996.

- [190] B.J.Holliday and C.A.Mirkin. Strategies for the construction of supramolecular compounds through coordination chemistry. *Angew.Chem.Int.Ed.*, 40:2022, 2001.
- [191] S.R.Batten and R.Robson. Interpenetrating nets. *Angew.Chem.Int.Ed.*, 37:1460, 1998.
- [192] K.Campbell, C.J.Kuehl, M.J.Fergusom, P.J.Stang, and R.R.Tykwinski. Coordination-driven self assembly: Solids with bidirectional porosity. *J.Am.Chem.Soc*, 124:7266, 2002.
- [193] A.Jeffery, C.V.Lu, and P.J.Stang. Molecular architecture via coordination. *J.Am.Chem.Soc*, 119:2524, 1997.
- [194] F.M.Tabellion, S.R.Seidal, A.M.Arif, and P.J.Stang. Discrete supramolecular architectures vs crystal engineering.... *J.Am.Chem.Soc*, 123:7740, 2001.
- [195] C.J.Kuehl, T.Yamamoto, S.R, Seidel, and P.J.Stang. Self-assembly of molecular prisms via organometallic "clip". *Org.Lett.*, 4:913, 2002.
- [196] M.D.Levin and P.J.Stang. Insights into the mechanism of coordination-directed self assembly. *J.Am.Chem.Soc*, 122:7428, 2000.
- [197] S.R.Seidel and P.J.Stang. High symmetry coordination cages via self-assembly. *Acc.Chem.Res.*, 35:972, 2002.
- [198] M.Fujita, J.Yazaki, and K.Ogura. Preparation of a macrocyclic polynuclear complex. *J.Am.Chem.Soc.*, 112:5645, 1990.
- [199] G.F.Swiegers and T.J.Malafetse. New self-assembled structural motif in coordination chemistry. *Chem.Rev.*, 100:3483, 2000.
- [200] R.Kramer, J.M.Lehn, and A.M.Rigault. *Proc.Natl.Ac.Sci.*, 90:5394, 1993.
- [201] J. Siegel J.Harrowfield B.Chevrier J.M.Lehn, A.M.Rigault. *Proc. Natl. Acad. Sci. USA*, 84:2565, 1987.
- [202] J.S.Lindsey. Self assembly in synthetic routes to molecular devices. biological principles and chemical perspectives : A review. *New.J.Chem.*, 15:153–180, 1991.

- [203] E.Breuning, M.Ruben, J.M.Lehn, F.Renz, Y.Garcia, V.Ksenofontov, P.Gutlich, E.Wegelius, and K.Rissanen. Spin crossover in a supramolecular fe-4(II) [2 x 2] grid triggered by temperature and pressure and and light. *Ang.Chem.Int.Ed.*, 39:2504, 2000.
- [204] O.Kahn and C.J.Martinez. *Science*, 279:44, 1998.
- [205] W.Fujita and K.Awaga. *Science*, 286:261, 1999.
- [206] K.J. Klabunde. *Chemistry of Free Atoms and Particles*. Academic Press, 1980.
- [207] R.Mackinzie and P.L.Timms. *and J.Chem.Comm.*, page 650, 1974.
- [208] S.Toyota, C.R.Woods, M.Benaglia, and et Al. *Angew.Chem.Int.Ed.*, 40:751, 2001.
- [209] R.E.P.Winpenny. *J.Chem.Soc.Dalton.Trans.*, 1:1, 2002.
- [210] J.Caro, J.Fraxedas, O.Jurgens, and J.Santiso. The first oriented thin films based on nitronyl nitroxide radical. *Adv.Mater.*, 10:608, 1998.
- [211] K.I.Pokhodnya, A.J.Epstein, and J.S.Miller and. *Adv.Mater.*, 12:410, 2000.
- [212] D.de Caro, M.Basso, and J.Sakah et Al. CVD-grown thin films of molecule based materials. *Chem.Mater.*, 12:587, 2000.
- [213] H.Casellas, D. de Caro, and L.Valade et Al. Molecular magnets and conductors on surfaces. *J.Phys IV*, 11:271, 2001.
- [214] H.Casellas, D.Caro, L.Valade, and P.Cassoux. A new chromium-based molecular magnet grown as a thin film by CVD. *Chem. Vap.Dep.*, 8:145, 2002.
- [215] K.I.Pokhodnya, D.Pejakovic, A.J.Epstein, and J.S.Miller. Effect of solvent on the magnetic properties of the high-temperature V(TCNE) molecule-based magnet. *Phy.Rev.B.*, 63:174408–1, 2001.
- [216] R.Sessoli, H.L.Tsai, A.R.Schake, and et Al. *J.Am.Chem.Soc.*, 115:1804, 1993.
- [217] W.Wernsdorfer and R.Sessoli. *Science*, 284:133, 1999.
- [218] Wernsdorfer, A.Caneschi, R.Sessoli, and D.Gatteschi et al. *Phy.Rev.Lett.*, 84:2965, 2000.

- [219] G.Aromi, S.M.J.Aubin, and M.A. Bolcar et al. *Polyhedron*, 17:3005, 1998.
- [220] R.E.P.Winnpenny. Serendipitous assembly of polynuclear cage compounds. *J.Chem.Soc.Dalton.Trans.*, 1:1, 2002.
- [221] R.E.P.Winnpenny. *Chem.Soc.Rev.*, 27:447, 1998.
- [222] C. M. Whelan, C. J. Barnes, C. Grégoire, and J. J. Pireaux. The influence of step sites on the bonding of benzenethiol on au surfaces. *Surface Science, Volumes 454-456 and 20 May 2000, Pages 67-72*.
- [223] X.C.Guo and R.J.Madix. Monolayer structure of phenoxy species on cu(110). *Surf.Sci.*, 341:L1065, 1995.
- [224] Junseok Lee, Sunmin Ryu, and Seong Keun Kim. The adsorption and photochemistry of phenol on ag(1 1 1). *Surface Science Volume 481, Issues 1-3 10 June 2001 Pages 163-171*.
- [225] D. C. Dender, D. Davidovic, Daniel H. Reich, , and Collin Broholm. Magnetic properties of a quasi-one-dimensional $s=1/2$ antiferromagnet: Copper benzoate. *Phys. Rev. B* 53 and 25832589 (1996).
- [226] D.C.Dender, P.R.Hammar, D.H.Reich, C.Broholm, and G.Aeppli. Direct observation of field-induced incommensurate fluctuations in a one-dimensional $s = 1/2$ antiferromagnet. *Phys. Rev. Lett.* 79 and 17501753 (1997).
- [227] T.Asano, H.Nojiri, Y.Inagaki, J.P.Boucher, T.Sakon, Y. Ajiro, and M. Motokawa. ESR investigation on the breather mode and the spinon-breather dynamical crossover in cu benzoate. *Phy. Rev. Lett.* 2000 84, Issue 25, pp. 5880.
- [228] B.Pilawa, E.Herrling, and I. Odenwald. G-factor and linewidth of the quasi-one-dimensional heisenberg antiferromagnet copper benzoate. *J.Mag.Mag.Mater.*, 226-230:417, 2001.
- [229] K.Inoue. Metal-aminoxyl-based molecular magnets. *In Electron Magnetism From Molecules to Magnetic Materials*, page 62, 2001.
- [230] A.Caneschi, D.Gatteschi, P.Rey, and R.Sessoli. *Inorg.Chem.*, 30:3936, 1991.

- [231] J.Caro, J.Fraxedas, J.Santiso, A.Figureas, J.N.B.Smith J.M.Rawson, G.Antorrena, and F.Palacio. Preparation and characterization of oriented thin films of a sulfur-nitrogen radical. *Thin.Sol.Fil.*, 352:102, 1999.
- [232] C.Rovira. Molecular compounds showing a spin ladder behaviour. *Electron Magnetism : from molecules to magnetic materials*, Structure and Bonding 100:163, 2001.
- [233] E.Dagotto, J.Riera, and D.J.Scalpino. *Phy.Rev.B.*, 45:5744, 1992.
- [234] Elbio Dagotto. Experiments on ladders reveal a complex interplay between a spin-gapped normal state and superconductivity. *Rep.Prog.Phy.*, 62:1525, 1999.
- [235] National Research Council. *Condensed Matter and Materials Physics : Basic Research for Tomorrows Technology*. National Academy Press, 1999.
- [236] J.Fraxedas, J.Caro, A.Figureas, and P.Gorostiza et al. *J.Vac.Sci.Technol.A.*, 16:2517, 1998.
- [237] J.Norskov. *Rep.Prog.Phys.*, 53:1253, 1990.
- [238] B.Hammer and J.Norskov. *Chemisorption and Reactivity on Supported Metal Clusters and Thin Films*. Kluwer, 1997.
- [239] R.Hoffmann. *Solids And Surfaces: AChemists View of Bonding in Extended Structures*. VCH, 1988.
- [240] Pietro Gambardella. *Growth and Electronic Structure and Magnetism of Supported Metal Nanowires*. PhD thesis, EPFL Lausanne (CH), 2000.
- [241] A.Fohlisch et al. *J.Chem.Phys.*, 112:1946, 2000.
- [242] K.W.Kolasinski, F.Cemic, and E.Hasselbrink. *Chem.Phys.Lett*, 219:113, 1994.
- [243] J.I.Pascual, J.J.Jackiw, K.F.Kelly, H.Conrad, H-P.Rust, and P.S.Weiss. Local electronic structural effects and measurements on the adsorption of benzene on ag(110). *Phy.Rev.B.*, 62:12632, 2000.
- [244] G.Trimarchi. Private communication, 2002.

- [245] J.Weckesser, J.V.Barth, and K.Kern. *J.Chem.Phys.*, 110:5351, 1999.
- [246] J.Weckesser, J.V.Barth, and K.Kern. *Phy.Rev.B.*, 64:161403, 2001.
- [247] Ante Bili, Jeffrey R. Reimers, , and Noel S. Hush. Adsorption of pyridine on the gold(111) surface: Implications for "alligator clips" for molecular wires. *J. Phys. Chem. B*, 106(26):6740, 2002.
- [248] M.Schunack, L.Petersen, A.Kuhnle, E.Legsgaard, I.Johannsen I.Stensgaard, and F.Besenbacher. Anchoring of organic molecules to metal surfaces: HtBDC on cu(110). *Phy.Rev.Lett.*, 86:456, 2001.
- [249] M.Schunack, F.Rosei, Y.Naitoh, P.Jiang, A.Gourdon, I.Stensgaard E.Laegsgaard, and C.Joachim. Adsorption behavior of lander molecules on cu(110) studied by scanning tunneling microscopy. *J.Chem.Phy.*, 117:6259, 2002.
- [250] F.Moresco, G.Meyer, K.H.Rieder, J.Ping, H.Tang, and C.Joachim. TBPP molecules on copper surfaces: A low temperatue scanning tunneling microscope investigation. *Surf.Sci.*, 499:94, 2002.
- [251] G.R.Darling and S.Hollaway. *Rep.Prog.phys.*, 58:1595, 1995.
- [252] J.V. Barth. Transport of adsorbates at metal surfaces: From thermal migration to hot precursors. *Surf.Sci.Rep.*, 40 (3-5):75–149, 2000.
- [253] J.L.Brand, M.V.Arena, A.A.Deckert, and S.M.George. *J.Chem.Phys.*, 92:5136, 1990.
- [254] M.Schunack, T.R.Linderroth, F.Rosei, E.Legsgaard, and F.Besenbacher I.Stensgaard. Long jumps in the surface diffusion of large molecules. *Phy.Rev.Lett.*, 88:15602–1, 2002.
- [255] F.P.Netzer, G.Ranglov, and G.Rosina and. *J.Chem.Phys.*, 89:3331, 1988.
- [256] J.Stöhr. *NEXAFS Spectroscopy and Vol.25 Springer Series in Surface Sciences*. Springer, 1991.
- [257] J. Weckesser, JV. Barth, and K. Kern. Mobility and bonding transition of c-60 on pd(110). *Phy.Rev.B.*, 64:161403, 2001.
- [258] D.G.Yablon, L.C.Giancarlo, and G.W.Flynn. Manipulating self-assembly with achiral molecules: An STM study of chiral segregation by achiral adsorbates. *J. Phys. Chem. B*, 104(32):7627–7635, 2000.

- [259] J.V.Barth, J.Wesscker, and G.Trimarchi. *J.Am.Chem.Soc.*, 2002.
- [260] T Kamikado, Y Okuno, S Mashiko, and A Yokoyama. *Nature*, 413:619, 2001.
- [261] K.W.Hipps, L.Scudiero, D.E. Barlow, and M.P. Cooke and. A self-organized 2-dimensional bifunctional structure formed by supramolecular design. *J.Am.Chem.Soc.*, 124:2126, 2001.
- [262] Shirley Chiang. Scanning tunneling microscopy imaging of small adsorbed molecules on metal surfaces in an ultrahigh vacuum environment. *Chemical Reviews*, 1997; 97(4); 1083-1096.
- [263] X.Lu, K.W.Hipps, and X.D.Wang U. Mazur. Scanning tunneling microscopy of metal phthalocyanines: d7 and d9 cases. *J. Am. Chem. Soc. 1996 and 118 and 7197-7202*.
- [264] T. A. Jung, R. R. Schlittler, J. K. Gimzewski, H. Tang, , and C. Joachim. Controlled room-temperature positioning of individual molecules: Molecular flexure and motion. *Science 1996 ; 271: 181*.
- [265] J.K.Gimzewski, T.A.Jung, M.T.Cuberes, and R.R.Schlitter. *Surf.Sci.*, 386:101, 1997.
- [266] L. Scudiero, Dan E. Barlow, and U.Mazur K. W. Hipps. Scanning tunneling microscopy and orbital-mediated tunneling spectroscopy and and ultraviolet photoelectron spectroscopy of Metal(II) tetraphenylporphyrins deposited from vapor. *J. Am. Chem. Soc. 2001 and 123 and 4073-4080*.
- [267] L.Scudiero, D.E.Barlow, U. Mazur, and K.W. Hipps and. Scanning tunneling microscopy and orbital-mediated tunneling spectroscopy and and ultraviolet photoelectron spectroscopy of Nickel(II) octaethylporphyrin deposited from. *J. Phys. Chem. B. ; 2002; 106(5); 996*.
- [268] X.Qiu, G.V.Nazin, A.Hotzel, and W.Ho. Manipulation and characterization of xenon-metalloporphyrin complexation with a scanning tunnelling microscope. *J.Am.Chem.Soc.*, 124:14804, 2002.
- [269] K.Morgenstern and K.H.Rieder. Formation of the cyclic ice hexamer via excitation of vibrational molecular modes by the scanning tunneling microscope. *J.Chem.Phy.*, 116:5746, 2002.

- [270] E.V.Tsipera, Z.G.Soos, W.Gaob, and A.Kahnb. Electronic polarization at surfaces and thin films of organic molecular crystals: PTCDA. *Chem.Phys.Lett.*, 360:47–52, 2002.
- [271] F. et al. Gilberto. A novel fluorinated Eu(III) beta-diketone complex as thin film for optical device application. *Optical Materials*, 11, 23 1998.
- [272] S.Bruck. Synthesis and structure and optical characteristics of pyridil substituted diketonates of lanthanoids. *Inorg.Chem.Comm.*, 3:666–670, 2000.
- [273] J.Batista et Al. Synthesis and x ray structure..... *Inorg.Chem*, 37:3542, 1998.
- [274] S.E.Grillo, H.Tang, C.Coudret, and S.Gauthier. STM observation of the dissociation of a chromium tris-diketonato complex on cu(1 0 0) and. *Chem.Phys.Lett.*, 355:289, 2002.
- [275] D. W. Wang, F. Tian, , and J. G. Lu. Characterization of self-assembled alkanethiol monolayers using a low-current scanning tunneling microscope. *J. Vac.Sci.Tech.B*, 20:60–64, January 2002.
- [276] U.Ziener, J.M.Lehn, A.Mourran, and M.Moller. Supramolecular assemblies of a bis(terpyridine) ligand and of its [2 x 2] grid-type zn-II and co-II complexes on highly ordered pyrolytic graphite. *Chem.A.Eur.J.*, 8:951–957, 2002.
- [277] Breuning E, Ziener U, Lehn JM, Wegelius E, and Rissanen K. Two-level self-organisation of arrays of [2x2] grid-type tetranuclear metal complexes by hydrogen bonding. *Eur. J.Inorg.Chem*, 6:1515–1521, 2001.
- [278] D.G.Kurth, K.M.Fromm, and J.M.Lehn. Hydrogen-bonding and metal-ion-mediated self-assembly of a nanoporous crystal lattice. *Eur.J.Inorg.Chem.*, 6:1523, 2001.
- [279] T.E.Jones and C.J.Baddeley. A RAIRS and STM and TPD study of the ni 1 1/r and r-tartaric acid system: Modelling the chiral modification of ni nanoparticles. *Surf.Sci.*, 513:463, 2001.
- [280] B.G.Frederick, T.S.Jones, P.Pudney, and N.V.Richardson. *J.Electron.Spectrosc.*, 64/65:115, 199.
- [281] B.G.Frederick, , M.R.Ashton, N.V.Richardson, and T.S.Jones. *Surf.Sci.*, 292:33, 1993.

- [282] Q.Chen, C.C.Perry, and B.G.Frederik et al. *Surf.Sci.*, 446:63, 2000.
- [283] K.U. Weiss, R. Dippel, K.M. Schindler, P. Gardner, V. Fritzsche, and A. M. Bradshaw. Chemical shift photoelectron diffraction from molecular adsorbates. *Phys. Rev. Lett.*, 69 and 31963199 (1992).
- [284] S.M.York, S.Haq, K.V.Kilway, J.M.Phillips, and F.M. Leibsle. STM and FTIR and quantum chemical calculation studies of acetate structures on cu(110) surfaces. *Surf.Sci.*, 522:34, 2003.
- [285] M.Bowker and R.J.Madix. *Surf.Sci.*, 102:542, 1981.
- [286] S.Haq and D.A.King. *J.Phy.Chem.*, 100:16957, 1996.
- [287] M Casarin et al. A lcao-ldf study of formate chemisorption on cu(100). *Sur.Sci.*, 307-309, 95 1994.
- [288] M.Sambi, G.Granozzo, M.Casarin, G.A.Rizzi, L.S.Caputi A.Vittadini, and G.Chiarello. Surface carboxylate species on cu(100) studied by angle-scanned photoelectron diffraction and LCAO-LDF calculations. *Surf.sci.*, 315:309, 1994.
- [289] G.Boisvert and L.J.Lewis. Self-diffusion of adatoms and dimers and and vacancies on cu(100). *Phy.Rev.B*, 56:7643, 1997.
- [290] L.HansenL, P.Stolze, K.W.Jacobsen, and J.K.Norskov. Activation free energy and entropy for the normal and exchange self diffusion processes on cu(100). *Surf.Sci.* 289 (1-2): 68-74 1993.
- [291] S.F.A.Kettle. *Physical Inorganic Chemistry*. Spektrum, 1996.
- [292] O.M.Yaghi, H.Li, C.Davis, D.Richardson, and T.L.Groy. Synthetic strategies and structure patterns and and emerging properties in the chemistry of modular porous solids. *Acc.Chem.Res.*, 31(8):474-484, 1998.
- [293] F.Rosei, M.Schunack, P.Jiang, A.Gourdon, E.Lægsgaard, I.Stensgaard, C.Joachim, and F.Besenbacher. Organic molecules acting as templates on metal surfaces. *Science*. 296,328; 2002.
- [294] R.K.Bruce. *Encyclopedia of Inorganic Chemistry*.
- [295] A.W.Adamson. *A Text Book Of Physical Chemistry*. Academic Press, 1973.

- [296] S.F.A. Kettle. *Physical Inorganic Chemistry*. Spectrum, 1996.
- [297] Douglas McDaniel. *Concepts and Models of Inorganic Chemistry*. John Wiley, 1983.
- [298] R.N. Boyd R.T. Morrison. *Organic Chemistry*. Allyn and Bacon, 1987.
- [299] S. Pasquetto and L. Patrone. *Chimica Fisica : Volume Terzo*. Masson, Milano, 1990.
- [300] L. Cattalini. *Prog. Inorg. Chem.*, 13:263, 1970.
- [301] R.J. Cross. An appraisal of square planar substitution reaction. *Advances in Inorganic Chemistry*, 34:219, 1989.
- [302] M.H. Whangbo T.A. Albright, J.K. Burdett. *Orbital Interaction in Chemistry*. John Wiley, 1984.
- [303] S.R. Logan. *Fundamentals of Chemical Kinetics*. Longman, 1995.
- [304] M.J. Cardillo. *Annu. Rev. Phy. Chem.*, 32:331, 1981.
- [305] E.W. Kuipers, M.G. Tenner, A.W. Kleyn, and S. Stolte. *Phy. Rev. Lett.*, 62:2152, 1989.
- [306] E.W. Kuipers, M.G. Tenner, A.W. Kleyn, and S. Stolte. *Nature*, 334:420, 1988.
- [307] C. Haug, W. Brenig, and T. Brunner. *Surf. Sci.*, 265:56, 1992.
- [308] A.W. Kleyn, A.C. Luntz, and D.J. Aurbach. *Surf. Sci.*, 152:99, 1985.
- [309] P.J. Feibelman. *Phy. Rev. Lett.*, 67:461, 1991.
- [310] D. Wetzig, R. Dopheide, M. Rutkoski, R. David, and H. Zacharias. *Phy. Rev. Lett.*, 76:463, 1996.
- [311] K.W. Kolasinski, F. Cemic, and E. Hesselbrink. *Chem. Phys. Lett.*, 219:113, 1994.
- [312] K.W. Kolasinski, F. Cemic, A. Meijere, and E. Hesselbrink. *Surf. Sci.*, 334:19, 1995.
- [313] Oliver Kahn, editor. *Molecular Magnetism*. Wiley, VCH, 1992.
- [314] Richard L. Carlin. Magnetochemistry: A research proposal. *Coo. Chem. Rev.*, 79:215, 1987.

- [315] H.Spillmann, P.Messina, A.Dimitriev, N.Lin, J.V.Barth, and K.Kern. *In Preparation*.
- [316] D.Braga, F.Grepioni, and G.R.Desiraju. Crystal engineering and organometallic architecture. *Chem.Rev.*, 98(4):1375, 1998.
- [317] G.A.Jeffrey. *An Introduction to Hydrogen Bonding*. Oxfor University Press, 1997.
- [318] T.Steiner. The hydrogen bond in the solid state. *Angw.Chem.Int.Ed.*, 41:48–76, 2002.
- [319] T. W. Fishlock, A. Oral, R. G. Egdell, and J. B. Pethica. Manipulation of atoms across a surface at room temperature. *Nature*, 404:743, 2000.
- [320] W.Liang, P.Matthew, M.Bockrath, and J.R.Long. Kondo resonance in a single-molecule transistor. *Nature*, 417:725, 2002.
- [321] W. G. Van der Wiel, S.De Franceschi, J.M.Elzerman, S.Tarucha, and L.P.Kouwenhoven. Two-stage kondo effect in a quantum dot at a high magnetic field. *Phys. Rev. Lett.*, 88:126803, 2002.

Curriculum vitae

Name:	Paolo Messina
Date of Birth:	August 20, 1974
Nationality	Italian
1988–1993	High School at the "Enrico Fermi" institute. Major, Chemistry and biology, Italy
1993–1998	Selected student at " <i>Collegio Borromeo</i> " Pavia, Italy
1993–1998	Undergraduate studies in physics at the University of Pavia, Italy
Junua 1998–Oct 1998	Diploma thesis in the group of Prof Dr A.Stella at the Laboratory for Solid State Physics of the University of Pavia: "Optical properties of metal nano particles emebded in dielectric matrix"
Oct 1998–Oct 1999	Research assistant in the group of Dr.S.Thomson, Spintronics at high frequencies. University of York, UK.
Oct 1999–Mar 2000	Research assistant in the group of Prof Dr K. Kern at the Institute for Experimental Physics of the Swiss Federal Institute of Technology in Lausanne.
Mar 2000–Mar 2003	Research assistant in the group of Prof Dr K. Kern at the Max Planck Institute for solid state research, Stuttgart, Germany
2003	PhD thesis: "Towards magnetic engineering at metal surfaces"

Acknowledgements

I would like to thank *Prof.Kern* for the support and the opportunity to accomplish this work. I also thank all the members of the examining commission,*Dr.Carbone, Prof.Schneider, Prof.Vogel* and the President *Prof.Meister*. A special thank to *Johannes Barth* for the useful scientific discussions and for having corrected part of this manuscript.

I' am grateful to *Wolfgang Stiepany* that has helped me in the design of the 1K microscope. To my mind he represents an example of capability and dedication at the work place.

I thank *Nian Lin* for having thought me STM alongside with *Sasha, Mateu* and *Hanness* for having welcome me in their group. I also thank *Alex Schneider* for the correction of part of the manuscript.

I' m grateful to *Ralf Vogelgesang* for all the scientific and *not scientific discussions* and for having helped me so many times with latex and related problems!

I thank *Sabine*, our group secretary, for all the assistance she gave me....a lot of work!

Thanks also to the *people in the cryogenic group* at the MPI.

I' m especially grateful to *D.M.Eigler* for his useful advice.

It is time for the friends now! Let' s start with Stuttgart . I want to mention first *Ashant* (the only Indian at this world capable to flatter girls in slovakian!). I thank him for the support and the friendship he granted to me.

MAXXXXXXXX! It is you turn now! MAX in arte "Lo zozzone". I will never forgive him for not having brought me in Poland with him."How much I will miss our....*art oriented..trips..to Prague and Bratislava!*". Max and I share one of the fundamental properties of nature: *being Terroni*¹⁹! I also thank my private *thermometer Marco from Florence* for all the time he mentioned the *temperature in Florence*!

A special thank to *Ketty, Simona, Alessandra and Silvia* for having listened to all my complains..... A thank to all the guys in Stuttgart *Marcello*,

¹⁹Southern Italians

Marco Ge, Chiara, Sabrina, Prisca Bellissima, Sandra Furilli, Mike, Angela, Kristo..., and why not "*Trombone detto Trombosterone*" *Tobias*!

Let' go to Lausanne now. I want to tank *Daniel* for reminding me I' am not the only crazy guy at this world: I miss you and your 7 languages! I thank *Tim* for all the time we spent together in Lausanne and the times he let me sleep in his living room! *Pietro* do not worry , I have not forgotten you! I thank him for all the discussions and support during these years: I will always make political public statements, it is unusefull to try to change this!

Thanks also to Elisa for being the prettiest physicist I have worked with!

Alessandro, the philosopher from Rome transplanted in the Yorkshire, my spiritual guide during my adventure abroad. Dear *Alessandro* I have not lost the Italian attitude to try finding a way *to get around rules*!

Back to Italy, I want to sincerely thank my friend *Amos* for all the support he gave me during this years. Actually he should also thank me for having introduced him ..to Prague.. and its *works of art*!

I thank *Kirstin* , the German blond giournalist, for the discussions and the visit to Colonia! Kirstin: unfortunately I have not found my *sweet lovely blond journalist*. Well , who else? I would like to thank the hundreds of people that I have met during these years and that have given me the opportunity to look at the world from different prospectives!